Doctoral Dissertation
Doctoral Program in Mechanical Engineering (33rd Cycle)

Power transmission systems: from traditional to magnetic gearboxes

Luca Dimauro
* * * * * *

Supervisors
Prof. Elvio Bonisoli, Politecnico di Torino

Doctoral Examination Committee:
Prof. Emiliano Rustighi, Referee, Università degli Studi di Trento
Prof. Matteo Massaro, Referee, Università degli Studi di Padova
Prof. Sebastiano Fichera, University of Liverpool
Prof. Paolo Di Barba, Università di Pavia
Prof. Giambattista Gruosso, Politecnico di Milano

Politecnico di Torino
September, 2021

I hereby declare that, the contents and organisation of this dissertation constitute my own original work and does not compromise in any way the rights of third parties, including those relating to the security of personal data.

…….....

Luca Dimauro

Torino, September, 2021

Acknowledgment

Pur essendo tra le prime pagine di questa tesi, la sezione dei ringraziamenti è quella a cui mi sono dedicato solo alla fine, al fine di poter trovare le giuste parole per tutte quelle persone che in diversi modi hanno contribuito al raggiungimento di questo traguardo e/o mi hanno donato momenti di spensieratezza, gioia e conforto nei momenti difficili, e alle quali spero di aver donato emozioni e ricordi positivi.

Questo lavoro di tesi rappresenta la conclusione del mio percorso di ricerca presso il Politecnico di Torino, iniziato ormai quasi 4 anni fa, e che è stato per me altamente formativo su diversi ambiti disciplinari e ricco di soddisfazioni personali.

Il mio primo pensiero va ai miei genitori: un infinito grazie per aver sempre creduto in me, per avermi sostenuto nel raggiungere questo traguardo e per essere stati al tempo stesso una fonte positiva di stress. Estendo i ringraziamenti al resto della mia famiglia (sorella, nonni, zii) per tutto l'affetto dimostrato nel corso degli anni.

Tornando all'ambiente accademico, un infinito grazie va al mio supervisor, il Prof. Elvio Bonisoli, per avermi dato l'opportunità di iniziare questo percorso, per il costante supporto e per le motivazioni datemi in questi tre anni, nonché per avermi insegnato, tramite la sua esperienza, come affrontare il mondo della ricerca e come interfacciarsi con la realtà industriale.

Un caloroso ringraziamento va anche al Prof. Maurizio Repetto che considero come un supervisor per avermi indirizzato in un ambito di ricerca ibrido tra la meccanica classica e l'elettromagnetismo, fornendo sempre spunti di riflessione interessanti per il proseguo dell'attività di ricerca. Desidero ringraziare anche il Dr. V. Cirimele per il costante supporto tecnico e i suggerimenti in ambito elettromagnetico, nonché per l'impegno profuso nel raggiungimento di obiettivi comuni.

Un sentito ringraziamento al Prof. M. Velardocchia per avermi accolto nel gruppo di ricerca di Meccanica del Veicolo e per avermi coinvolto nelle attività di ricerca accademiche e industriali del gruppo.

Vorrei inoltre ringraziare il Prof. E. Galvagno per avermi introdotto al mondo delle trasmissioni e per avermi fatto appassionare a tale settore tramite la sua esperienza e la sua conoscenza. Ringrazio anche il Prof. A. Vigliani per gli insegnamenti accademici e per i momenti di spensieratezza durante l'orario di lavoro.

Un ringraziamento va anche al Centro Interdipartimentale CARS@PoliTO per aver finanziato economicamente il mio dottorato e al referente del centro, il Prof. G. Belingardi, per aver organizzato dei momenti di confronto tra i membri di CARS, offrendo a dottorandi e ricercatori la possibilità di presentare le proprie attività di ricerca con l'opportunità di ampliare le proprie conoscenze nell'ambito della mobilità sostenibile.

Un sentito ringraziamento va agli attuali e vecchi membri del nostro gruppo di ricerca: Domenico, Simone, Angelo, Alberto, Antonio, Gianluca, Guido, Mattia, Valerio, Michele. Le chiacchiere e le risate davanti ad un buon caffè hanno reso più piacevole l'ambiente di lavoro al Politecnico.

Ringrazio tutti gli amici conosciuti a Torino durante gli ormai 10 anni di permanenza e i vari coinquilini per avermi regalato momenti di spensieratezza e di svago. Un pensiero particolare spetta anche a tutti gli amici di Augusta per i piacevoli ritrovi durante le ferie estive.

Finally, I would like to thank Prof. M.G. Tehrani, who supervise me during my research period as visiting PhD student at the ISVR (Institute of Sound and Vibration Research) of Southampton University, giving me the opportunity to widen my technical knowledge in the engineering field of active control. I would also thank all the other people I met in Southampton, for nice moments and evenings spent together.

Abstract

This dissertation addresses the development of an integrated magneto-mechanical design for the final prototyping of a magnetic gearbox transmission, integrating in a single device three different components, as clutch, gearbox, and torque limiter, to overcome the typical issues, as noise, wearing and vibrations, of mechanical power transmission systems. In the thesis, both magnetic and conventional transmission technologies are investigated with numerical, simulative, and experimental approaches.

In the first part of the dissertation, a novel methodology for the assessment of Dual Clutch Transmission vibrations during gear shifts is proposed, to predict, through numerical simulations and an offline post-processing, in a specific point of the gearbox housing its accelerations, which are used as a dynamic quantity to objectively evaluate the vibrational behaviour of gearbox inner elements during experimental tests. A sensitivity on the main geometrical parameters of gearbox has been conducted, with promising benefits in the reduction of gearshift noise.

On the other side, magnetic gears are proposed as structures able to transfer power and torques between two or more mechanical axles with a given speed ratio. They allow to transfer motion without contact between the moving parts, hence the possible adoption of a planetary magnetic gear (PMG) inside a hybrid automotive driveline has been investigated, designing a PMG able to transfer the torque needed without altering the powertrain dynamics. To handle these requirements, a multi-objective optimisation approach is carried out by a deterministic optimisation algorithm coupled to a weighted sum approach of objectives. Results are used in a transmission model developed in Simulink.

Finally, a constant effort has aimed at the development and design of several technological construction solutions, to validate the patented idea, to verify the effectiveness of the proposed system, and to highlight any possible critical aspect in different kinematic and dynamic operative conditions of the magnetic gearbox.

Contents

List of Tables

List of Figures

List of Acronyms

ICE	Internal combustion engine
MT	Manual transmission
AMT	Automated manual transmission
AT	Automatic transmission
DCT	Dual clutch transmission
DDCT	Dry dual clutch transmission
WDCT	Wet dual clutch transmission
CVT	Continuous variable transmission
FRF	Frequency response function
PMG	Planetary magnetic gear
E-CVT	Electrical continuously variable transmission
HEV	Hybrid electric vehicle
EV	Electric vehicle
DOF	Degree of freedom
SDOF	Single degree of freedom
MDOF	Multi degree of freedom
MC	Monte Carlo
FFD	Full factorial design
LHS	Latin hypercube sampling
DOE	Design of experiments
DCU	Dual clutch unit
ETCU	Electronic transmission control unit
PS	Primary shaft
SS	Secondary shaft
DMF	Dual mass flywheel
FEM	finite element model
FFT	Fast Fourier transform
IFFT	Inverse fast Fourier transform
MISO	Multiple-input single-output
RMS	Root mean square
MG	Magnetic gear
PM	Permanent magnet
PDD	Pseudo direct drive
mCVT	magnetic continuous variable transmission

eCVT	electric continuous variable transmission
HSD	Hybrid synergy drive
PSD	Power split device
FBD	Free body diagram
TVO	Throttle valve opening
PID	Proportional-integral-derivative
TRL	Technology Readiness Level
AC	Alternating current
DC	Direct current
IGBT	Insulated gate bipolar transistor
AI	Analog input
DI	Digital input

Chapter 1

1. Introduction

The power transmission system represents the main component, namely the core, of any machine in several sectors as the automotive [1,2] and aerospace [3] industries or in other application fields where a power source is connected to an utiliser to guarantee the motion transferring between the input and the output of the system.

During the last decades, a continuous improvement of power transmission systems has occurred, especially in the automotive sector, with the development of both more powerful engines [4,5] and more efficient and performing transmissions [6,7].

Due to the possible configurations of driveline, as the front-wheel drive, the rear-wheel drive or the all-wheel drive systems [8,9], and to the large number of powertrain components, the analysis of the whole power transmission is a fundamental phase during the mechanical and dynamic design [10] and, at the same time, when a mechanical problem occurs and the detection of the critical components is necessary.

In the last few years, an increasing demand for improving vehicle performance and drivability lead the automotive industry to explore new powertrain technologies, to primarily reduce fuel consumption [11,12]. At the same time, weight [13] and cost of a vehicle remain a discriminating factor in the final choice of the customer. For all these reasons, the transmission becomes increasingly important, especially in the new millennium.

In fact, for a long period, until the beginning of the 80's of the previous century, only little innovations has been applied to transmission technology since the manual transmission was the main subject of the transmission market. A considerable progress has been made in the development of automotive transmissions in the last 20 years, with an increased speed number, expanded ratio spread and an improvement of efficiency and shift quality [14]. Transmissions of cars with an internal combustion engine (ICE) are usually classified into manual transmission (MT), automated manual transmission (AMT), automatic

transmission (AT), dual-clutch transmission (DCT) and continuously variable transmission (CVT). Any vehicle with a traditional mechanical transmission is generally characterised by unavoidable and undesired issues of noise and vibrations [15,16], which both the driver and passengers would avoid for a better sensation while using the vehicle. Noise and vibrations are measured to evaluate the ride comfort and vehicle quality and reliability.

Moreover, with the increasing of vehicle electrification, the electronic control of transmission and of the gearshift phase has become an increasingly important aspect in the vehicle design. Thus, the study of an optimal control is highly related to the uncertainty on system parameters [17], since a little change on a component parameter could change the frequency response function (FRF) [18,19] of the mechanical system.

In this context, where the classical mechanical transmissions remain a key point as regards the transmission reliability, the magnetic transmission and more generally the magnetic gears represent a valid alternative to mechanical transmission to overcome noise and vibrations issues and the need of gear lubrication and cooling. Tsurumoto et al. [20] in 1987 proposed one of the first studies on this topic prototyping a magnetic gear using permanent magnets of SmCo5 material. Nevertheless, for a long time, this new technology received little interest due to the use of low-performance magnetic material leading up to low torque density. Then, in 2001, the magnetic gears appeared in a new topology as proposed by Atallah et al. [21] with the design of a planetary magnetic gears (PMG). This work has given rise to a field of research based on this new topology as regards the design [22–24], the dynamics [25–28], the optimisation [29–31], and the final prototyping [32–35] of a planetary magnetic gear. Moreover, a procedure for computing magnetic losses in coaxial magnetic gears is presented in [36] through the use of a 2D magnetic model, or power loss are evaluated by measurements [30,37], or taking into account only losses due to eddy currents [38]. This to put in evidence that the loss computation in magnetic materials is crucial to define the system performance.

Finally, the possible integration of a PMG in an electrical continuously variable transmission (E-CVT) [39] of a hybrid electric vehicle (HEV) should be further investigate, due to overall dimensions and to the transmissible torque capability, to propose a possible change of direction in the automotive transmission market.

1.1 Main contributions

The main original contributions obtained during this PhD are here presented.

Development of methodologies for power transmission systems

As regards the mechanical transmissions, a two steps methodology for the assessment of Dual Clutch Transmission vibrations during gear shifts has been developed. It is devoted to an objective evaluation of the induced vibration due to axial and rotational impacts inside the transmission by means of a single parameter, as the acceleration in an external point the gearbox housing.

Instead, as regards the magnetic transmissions, a magneto-mechanical approach is proposed to design and optimise a PMG. Firstly, an integrated tool for electromechanical simulations is developed, starting from a topological parametric model of a PMG. Then a block-oriented dynamic model of a PMG, inserted in a mechanical driveline, is developed in Simulink environment, using the results of magneto mechanical simulations, to virtually test the dynamic behaviour of magnetic transmission devices.

Realisation of an innovative magnetic gearbox prototype

An Italian patent application for a magnetic gearbox prototype has been filed. The innovative magnetic gearbox technology allow the integration of clutch, gearbox, and torque limiter in an all-in-one device.

The "Magnetic gearbox" patent has allowed to participate for a call of Proof-of-Concept project for the development of the technology with the design and construction of a two-stage (two-speed) magnetic gearbox prototype, characterised by a functional parametricity, which allows to investigate different configurations concerning the transmission ratio. In parallel with the realisation of the prototype, a devoted test bench was designed and built to explore and evaluate the magneto-mechanical characteristics of the prototype in different working conditions, through appropriate test protocols.

1.2 Organisation of the thesis

This thesis is organised as follow:

- Chapter 2: a brief introduction to different method for the study of uncertain system is presented and the analysis of uncertainty effects on the dynamic of a multi degree of freedom (MDOF) is proposed using both stochastic and deterministic approaches. Moreover, an analysis on the poles of a mechanical system is analysed to quantify the effect of uncertain parameters on the imaginary and real part of the poles.

- Chapter 3: the development of a nonlinear lumped parameter model of a Dual Clutch Transmission on Siemens/Amesim software is presented, and a sensitivity analysis is carried out on some model parameters. Moreover, a novel methodology, for the assessment of Dual Clutch Transmission vibrations during gear shifts, is proposed with an experimental validation of the simulated results.
- Chapter 4: A brief literature review on magnetic gears is presented, highlighting advantaged and drawbacks compared to traditional mechanical gears. Then a first possible integration of magnetic gears in an automotive power transmission is proposed.
- Chapter 5: Firstly, an integrated tool for electro-mechanical simulations is developed, starting from a topological parametric model of a PMG. Then, a multi-objective optimisation approach is proposed that maximises transmitted torque per unit mass of the magnetic gear, minimising, at the same time, the moment of inertia of the moving parts, to not alter the dynamic of a possible powertrain application. Finally, a block-oriented dynamic model of a driveline is modelled in Simulink environment to test the efficacy of magnetic transmissions.
- Chapter 6: The design of a PMG prototype is presented, with a progressive rise in complexity, in order to achieve quickly exchangeable configurations for different experimental tests. Three different solutions are designed highlighting advantages and drawbacks.
- Chapter 7: The PMG prototype complexity is further increased, adding a neutral position and a second PMG in order to achieve a mechanical system able to act as a magnetic gearbox with two transmission ratios. The innovative technology of magnetic gearbox is presented, proposing several constructional solutions. The kinematic analysis of the actuation system for the dis/engagement of the desired transmission ratio is analysed from an analytical and a simulative point of view, to achieve an optimal control of the engaging phase.
- Chapter 8: Development of a test rig for power transmission application using magnetic gearbox technology: several magneto-mechanical quantities are evaluated during different tests, to evaluate PMG performance and its advantages with respect to mechanical gears.
- Chapter 9: The main conclusions drawn from the work presented in the previous chapters are reported. In addition, some interesting topics for future developments will be proposed.

Chapter 2

2. Dynamic response of uncertain mechanical systems

Vibrations are one of the most common aspects of daily life. They are defined as the fluctuations of a mechanical systems about an equilibrium position. Vibrations start when an inertia element, namely a mass or a rotational element, is moved from its equilibrium position due to an external source of energy [40,41]. Thus, a restoring force or moment tends to bring the inertia element to an equilibrium position due to elastic elements of the involved mechanical system. In case of absence of nonconservative forces a continuous conversion of energy between the kinetic and potential one occurs, causing the inertia element to oscillate about its equilibrium position till a dissipative element leads to decrease the amplitude of oscillation.

A mathematical model is necessary to predict the mechanical system behaviour and to study its dynamic response under certain excitation condition since the knowledge of the system physical properties is fundamental. Therefore, the model parameters correspond to its physical properties. In a mechanical system the common parameters are mass, stiffness, and damping, which respectively describe inertial, elastic, and dissipative properties of the system.

The solution of the mathematical problem leads to an information about the vibrations. To be clear, some terms should be defined. Generally, vibration phenomena are represented using a *time history* of the system periodic oscillation about the equilibrium position. Each oscillation is completed in one *cycle* and for a simple harmonic motion the time necessary to execute a cycle is constant and it is called *period*. Moreover, the *frequency* of motion is the number of cycles in the period of one second, while the *amplitude* is defined as the maximum displacement from the equilibrium position [42].

The dynamic response of a mechanical system to a certain excitation depends on system parameters. Simpler the system mathematical model is, the easier it is to define and to predict its dynamic behaviour. It could be happening that these

mechanical systems are affected by uncertainty, due to its uncertain parameters and thus the estimation of its dynamic response is uncertainty, as well.

The topic of uncertainty was carried out, in aerospace field [43–45], to assess the propagation of structural uncertainty to linear aeroelastic stability, or in electro-mechanical field where the effects of multi-parameter aleatory uncertainties are discussed for the design and optimisation of energy harvesters [46,47]. Moreover, the study of dynamic behaviour of uncertain system is addressed in [48] as regards wind turbine drive train, and in [49] for the analysis of torsional vibrations in geared transmissions.

Only structured uncertainty, due to uncertain parameters, has been investigated in this section, although several unstructured uncertainty modeling methods [50–52] can be used to investigate the effects of unstructured uncertainty on the dynamics and control of mechanical systems. Moreover, a mixed structured and unstructured uncertainty modeling method can be used, as introduced in [53] to deal with measured frequency domain data from several servo actuators.

2.1 Methods for uncertainty estimation

During the last decades, the study of uncertain systems and of uncertainty effects on the dynamic of the system itself have been handled using deterministic or stochastic approaches. Each model has its benefits and drawbacks, which are mainly related to computational costs and accuracy of results.

The methods presented are applied for the calculation of FRFs of a simple lumped mass system with uncertain parameters, even if they could be tested using more complex systems.

The first method analysed is the complex interval analysis, whose origins date back to the last century [54,55], also treated in [18] by the author and compared with another uncertainty propagation technique, called complex affine analysis, firstly introduced in 1993 by Comba and Stolfi [56].

The advantage of these two methods is only the computational cost, since with only a calculation at each frequency it is possible to estimate together lower and upper bounds of uncertainty FRF. On the other hand, the estimation of FRF has a good accuracy within a certain percentage of uncertainty on the input parameters of the system. This maximum level of uncertainty depends on the number of uncertain parameters and on their nominal values. Moreover, the formulation of FRF should be explicit since it is not possible to apply the classical mathematical operations between complex interval matrices. In addition to this it is impossible to evaluate an explicit formulation of the frequency response functions for a system with more than 4 DOFs.

The other three methods that could be used are Monte Carlo (MC) simulations, the Full Factorial Design (FFD) or the Latin Hypercube Sampling (LHS). Using MC simulations, it is possible to choose the proper type of distribution for each uncertain parameter, namely the most suitable according to real perturbation on each parameter: in this section only normal and uniform

random distribution have been used for the model parameters. The advantage of this method is the accuracy of results, but with a very high computational cost.

In the FFD the number of simulations that should be performed to obtain an appropriate result depend on the number of uncertain parameters and on the levels of each parameter that is necessary to test. Generally, two levels for each parameter, related to an envelope of the FRF, are enough two describe accurately the effects of uncertainty. Finally, in the LHS, the random numbers, which describe the random parameters are selected in an orthogonal way, with a random distribution or using a normal distribution with covariance matrix.

The proposed methods are applied to the same test-case to prove their efficacy and limits in the analysis of uncertain systems.

2.2 Dynamics of a MDOF system with uncertain parameters

The model of a 2-DOFs lamped mass mechanical system is sketched in Figure 2.1. It is considered for the analysis on parametric uncertainty and it is characterised by two masses m_1 and m_2, by three stiffnesses k_1, k_2 and k_3, and by three viscous dampers c_1, c_2 and c_3.

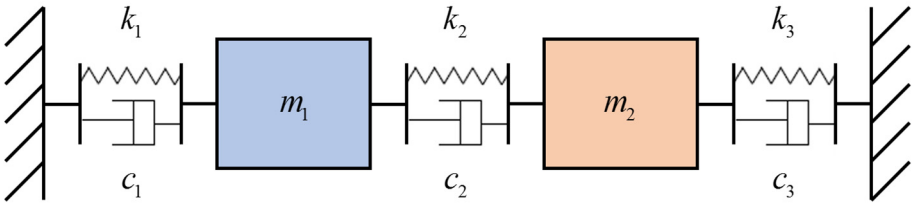

Figure 2.1 – Two DoFs lumped mass system.

The equations of motion of the system under forced vibration are written using the matrix formulation of Eq. (2.1):

$$\mathbf{M}\,\ddot{\mathbf{x}} + \mathbf{C}\,\dot{\mathbf{x}} + \mathbf{K}\,\mathbf{x} = \mathbf{f} \tag{2.1}$$

where the mass matrix $\mathbf{M}$, the damping matrix $\mathbf{C}$, and the stiffness matrix $\mathbf{K}$ are given by Eq. (2.2)

$$\mathbf{M} = \begin{bmatrix} m_1 & 0 \\ 0 & m_2 \end{bmatrix},\ \mathbf{C} = \begin{bmatrix} c_1 + c_2 & -c_2 \\ -c_2 & c_2 + c_3 \end{bmatrix},\ \text{and}\ \mathbf{K} = \begin{bmatrix} k_1 + k_2 & -k_2 \\ -k_2 & k_2 + k_3 \end{bmatrix} \tag{2.2}$$

As already said the methods are applied for the evaluation of FRFs of the uncertain mechanical system. Generally, three different FRFs can be evaluated, namely the receptance $\alpha_{j,k}$, the mobility $Y_{j,k}$ and inertance $A_{j,k}$, which are defined as the ratio in the frequency domain between the displacement, velocity

and acceleration of DOF j with respect to the external forces applied to DOF k. The receptance of a MDOF mechanical system with proportional viscous damping, is computed with modal superposition of m modes, as follows:

$$\alpha_{j,k}(\omega) = \frac{x_j(\omega)}{F_k(\omega)} = \sum_{r=1}^{m} \frac{\Phi_{j,r}\,\Phi_{k,r}}{\omega_r^2 + 2\,\mathrm{i}\,\zeta_r\,\omega_r\,\omega - \omega^2} \tag{2.3}$$

where $\Phi_{j,r}$ and $\Phi_{k,r}$ are the eigenvectors of mode r, evaluated at DOF j and DOF k, respectively, ζ_r is the damping ratio, ω_r is the natural frequency of mode r and ω is the excitation frequency.

For a 2 DOF system it could be written also in matrix form using Eq. (2.4) or Eq. (2.5):

$$\begin{bmatrix} \alpha_{1,1}(\omega) & \alpha_{1,2}(\omega) \\ \alpha_{2,1}(\omega) & \alpha_{2,2}(\omega) \end{bmatrix} = \\ = \begin{bmatrix} (k_1+k_2)+\mathrm{i}\,\omega(c_1+c_2)-m_1\omega^2 & -k_2-\mathrm{i}\,\omega c_2 \\ -k_2-\mathrm{i}\,\omega c_2 & (k_2+k_3)+\mathrm{i}\,\omega(c_2+c_3)-m_2\omega^2 \end{bmatrix}^{-1} \tag{2.4}$$

$$\begin{bmatrix} \alpha_{1,1}(\omega) & \alpha_{1,2}(\omega) \\ \alpha_{2,1}(\omega) & \alpha_{2,2}(\omega) \end{bmatrix} = \\ = \frac{1}{D(\omega)} \begin{bmatrix} (k_2+k_3)+\mathrm{i}\,\omega(c_2+c_3)-m_2\omega^2 & k_2+\mathrm{i}\,\omega c_2 \\ k_2+\mathrm{i}\,\omega c_2 & (k_1+k_2)+\mathrm{i}\,\omega(c_1+c_2)-m_1\omega^2 \end{bmatrix} \tag{2.5}$$

where $D(\omega)$ is the determinant of the matrix on the right side of Eq. (2.4) given by Eq. (2.6)

$$D(\omega) = \left((k_1+k_2)+\mathrm{i}\,\omega(c_1+c_2)-m_1\omega^2\right)\left((k_2+k_3)+\mathrm{i}\,\omega(c_2+c_3)-m_2\omega^2\right)+ \\ -\left(k_2+\mathrm{i}\,\omega c_2\right)^2 \tag{2.6}$$

The numerical values of system parameters are listed in Table 2.1.

Table 2.1 – Baseline parameters of the 2 DOFs lumped mass system.

Type	Parameter	Value
mass	m_1 [kg]	1
	m_2 [kg]	2
stiffness	k_1 [N/m]	10000
	k_2 [N/m]	20000

	k_3 [N/m]	30000
damping	c_1 [Ns/m]	10
	c_2 [Ns/m]	20
	c_3 [Ns/m]	30

Firstly, the system has been tested in nominal condition and then a random scanning analysis is performed, changing randomly all the parameters inside a range of ±1% and running the FRFs calculation 1000 times. Uniform distribution is used for all the parameters. These results are then compared with interval analysis and affine analysis briefly introduced in the following sections.

2.2.1 Complex interval analysis technique

According to the interval analysis, each real number $\mathbf{x} = \left\{ x \in \mathbb{R} \mid \underline{x} \le x \le \overline{x} \right\}$, each vector $\mathbf{y}$ of dimension n, defined as $\mathbf{y} = \left\{ y \in \mathbb{R}^n \mid \underline{y} \le y \le \overline{y} \right\}$, where $\underline{y}$ and $\overline{y}$ are real column vectors of length n, or each $m \times n$ interval matrix $\mathbf{A}$, defined as $\mathbf{A} = \left\{ A \in \mathbb{R}^{m \times n} \mid \underline{A} \le A \le \overline{A} \right\}$, where each matrix element $A_{i,j}$ is an interval number, could be written with a lower boundary and an upper boundary. Starting from the assumption that the FRFs of a mechanical system is complex, in this section only complex interval analysis is considered, even if it could be reduced to real interval analysis just not considering the imaginary part. Therefore, a complex interval number $\mathbf{x} = \mathbf{x}_r + \mathrm{i}\,\mathbf{x}_i$ is written as the sum of a real and imaginary part, where $\mathbf{x}_r$ and $\mathbf{x}_i$ are the real and imaginary interval components of the complex number. This relationship is better clarified in Eqs. (2.7)-(2.8):

$$\mathbf{x}_r = \left[\underline{x_r}, \overline{x_r} \right] = \left\{ x_r \in \mathbb{R} \mid \underline{x_r} \le x_r \le \overline{x_r} \right\} \tag{2.7}$$

$$\mathbf{x}_i = \left[\underline{x_i}, \overline{x_i} \right] = \left\{ x_i \in \mathbb{R} \mid \underline{x_i} \le x_i \le \overline{x_i} \right\} \tag{2.8}$$

Different arithmetical operations are involved in the estimation of the system FRFs and thus it is necessary define them for interval complex numbers. The idea for the extension of interval arithmetic to the complex plane, with a Cartesian representation for complex interval numbers, is attributed to Boche [57]. As in his technical report, and starting from two numbers $\mathbf{x}$ and $\mathbf{y}$, the main arithmetical operations are here defined:

$$\begin{aligned} \mathbf{x}+\mathbf{y} &= \left(\left[\underline{x_r}, \overline{x_r} \right] + \left[\underline{y_r}, \overline{y_r} \right] \right) + \mathrm{i} \left(\left[\underline{x_i}, \overline{x_i} \right] + \left[\underline{y_i}, \overline{y_i} \right] \right) = \\ &= \left(\left[\underline{x_r} + \underline{y_r}, \overline{x_r} + \overline{y_r} \right] \right) + \mathrm{i} \left(\left[\underline{x_i} + \underline{y_i}, \overline{x_i} + \overline{y_i} \right] \right) \end{aligned} \tag{2.9}$$

$$\begin{aligned}\mathbf{x}-\mathbf{y} &= \left(\left[\underline{x_r}, \overline{x_r}\right]-\left[\underline{y_r}, \overline{y_r}\right]\right)+\mathrm{i}\left(\left[\underline{x_i}, \overline{x_i}\right]-\left[\underline{y_i}, \overline{y_i}\right]\right)= \\ &= \left(\left[\underline{x_r}-\overline{y_r}, \overline{x_r}-\underline{y_r}\right]\right)+\mathrm{i}\left(\left[\underline{x_i}-\overline{y_i}, \overline{x_i}-\underline{y_i}\right]\right)\end{aligned} \tag{2.10}$$

$$\mathbf{xy} = \left(\mathbf{x}_r\mathbf{y}_r-\mathbf{x}_i\mathbf{y}_i\right)+\mathrm{i}\left(\mathbf{x}_r\mathbf{y}_i-\mathbf{x}_i\mathbf{y}_r\right) \tag{2.11}$$

$$\frac{\mathbf{x}}{\mathbf{y}} = \frac{\mathbf{x}\,\mathbf{y}^*}{\mathbf{y}\,\mathbf{y}^*} = \frac{\left(\mathbf{x}_r\mathbf{y}_r+\mathbf{x}_i\mathbf{y}_i\right)+\mathrm{i}\left(\mathbf{x}_i\mathbf{y}_r-\mathbf{x}_r\mathbf{y}_i\right)}{\mathbf{y}_r^2+\mathbf{y}_i^2} \tag{2.12}$$

Properly combining previous Eqs. (2.9)-(2.12), it is possible to evaluate the equations for the three distinct interval FRFs for calculation of receptances $\boldsymbol{\alpha}_{1,1}(\omega)$, $\boldsymbol{\alpha}_{1,2}(\omega)=\boldsymbol{\alpha}_{2,1}(\omega)$, and $\boldsymbol{\alpha}_{2,2}(\omega)$ at the desired excitation frequency ω.

$$\boldsymbol{\alpha}_{1,1}(\omega) = \frac{\left(\mathbf{k}_2+\mathbf{k}_3\right)+\mathrm{i}\,\omega\left(\mathbf{c}_2+\mathbf{c}_3\right)-\mathbf{m}_2\omega^2}{\left(\left(\mathbf{k}_1+\mathbf{k}_2\right)+\mathrm{i}\,\omega\left(\mathbf{c}_1+\mathbf{c}_2\right)-\mathbf{m}_1\omega^2\right)\left(\left(\mathbf{k}_2+\mathbf{k}_3\right)+\mathrm{i}\,\omega\left(\mathbf{c}_2+\mathbf{c}_3\right)-\mathbf{m}_2\omega^2\right)-\left(\mathbf{k}_2+\mathrm{i}\,\omega\mathbf{c}_2\right)^2} \tag{2.13}$$

$$\boldsymbol{\alpha}_{1,2}(\omega) = \frac{\mathbf{k}_2+\mathrm{i}\,\omega\,\mathbf{c}_2}{\left(\left(\mathbf{k}_1+\mathbf{k}_2\right)+\mathrm{i}\,\omega\left(\mathbf{c}_1+\mathbf{c}_2\right)-\mathbf{m}_1\omega^2\right)\left(\left(\mathbf{k}_2+\mathbf{k}_3\right)+\mathrm{i}\,\omega\left(\mathbf{c}_2+\mathbf{c}_3\right)-\mathbf{m}_2\omega^2\right)-\left(\mathbf{k}_2+\mathrm{i}\,\omega\mathbf{c}_2\right)^2} \tag{2.14}$$

$$\boldsymbol{\alpha}_{2,2}(\omega) = \frac{\left(\mathbf{k}_1+\mathbf{k}_2\right)+\mathrm{i}\,\omega\left(\mathbf{c}_1+\mathbf{c}_2\right)-\mathbf{m}_1\omega^2}{\left(\left(\mathbf{k}_1+\mathbf{k}_2\right)+\mathrm{i}\,\omega\left(\mathbf{c}_1+\mathbf{c}_2\right)-\mathbf{m}_1\omega^2\right)\left(\left(\mathbf{k}_2+\mathbf{k}_3\right)+\mathrm{i}\,\omega\left(\mathbf{c}_2+\mathbf{c}_3\right)-\mathbf{m}_2\omega^2\right)-\left(\mathbf{k}_2+\mathrm{i}\,\omega\mathbf{c}_2\right)^2} \tag{2.15}$$

In the previous equations each of system parameters is written as vector with a lower and upper bound, which difference corresponds to a range given by the nominal value and by the uncertainty percentage. By way of explanation, assuming an uncertainty amplitude of $\pm 1\%$ and considering for all the parameters the nominal values reported in Table 2.1, their lower and upper bounds are evaluated using Eq. (2.16) for masses, Eq. (2.17) for viscous damping and Eq. (2.18) for stiffnesses.

$$\begin{aligned}\mathbf{m}_1 &= \left[0.99\ ,\ 1.01\right] \\ \mathbf{m}_2 &= \left[1.98\ ,\ 2.02\right]\end{aligned} \tag{2.16}$$

$$\begin{aligned}\mathbf{c}_1 &= \left[9.9\ ,\ 10.1\right] \\ \mathbf{c}_2 &= \left[19.8\ ,\ 20.2\right] \\ \mathbf{c}_3 &= \left[29.7\ ,\ 30.3\right]\end{aligned} \tag{2.17}$$

$$\begin{aligned}\mathbf{k}_1 &= \left[0.99\times10^4\ ,\ 1.01\times10^4\right] \\ \mathbf{k}_2 &= \left[1.98\times10^4\ ,\ 2.02\times10^4\right] \\ \mathbf{k}_3 &= \left[2.97\times10^4\ ,\ 3.03\times10^4\right]\end{aligned} \tag{2.18}$$

Moreover, the FRFs, evaluated using Eqs. (2.13)-(2.15) could be written in their complex interval form using Eq. (2.19) which returns lower and upper bound of each FRF

$$\boldsymbol{\alpha}(\omega)=\left(\left[\underline{\alpha_r(\omega)},\overline{\alpha_r(\omega)}\right]\right)+\mathrm{i}\left(\left[\underline{\alpha_i(\omega)},\overline{\alpha_i(\omega)}\right]\right) \tag{2.19}$$

2.2.2 Complex affine analysis technique

The idea of affine analysis is to keep track of dependency between arithmetic operands and formulas, preserving the simplicity of interval arithmetic. There are two formulations for real and complex numbers also in the affine analysis, and in this section only the complex affine analysis is presented. Using this technique, an uncertain complex parameter x is represented by an affine form $\hat{x}$ that is a first-order polynomial, as expressed in Eq. (2.20):

$$\hat{x}=x_0+\sum_{i=1}^{n}x_i\varepsilon_i+x_{real}\varepsilon_{real}+\mathrm{i}\,x_{imag}\varepsilon_{imag} \tag{2.20}$$

where x_0 represents the central value of the affine form, x_i corresponds to the amplitude of a particular uncertainty, while ε_i are symbolic variables, whose values are unknown but lie in the range $[-1 \quad 1]$, and each of them represents one of n independent sources of uncertainty. Instead, x_{real} and x_{imag} are considered as a real and an imaginary amplitude error, respectively, and are positive and real quantities.

Considering a complex affine form $\hat{x}$, it could be translated into a complex interval number $\mathbf{x}=\mathbf{x}_r+\mathrm{i}\,\mathbf{x}_i$ using Eq. (2.21) for the bound of real part and similarly Eq. (2.22) for the imaginary ones.

$$\underline{x_r}=\mathrm{Re}(x_0)-\sum_{i=1}^{n}\left|\mathrm{Re}(x_i)\right|-x_{real}\ ,\ \overline{x_r}=\mathrm{Re}(x_0)+\sum_{i=1}^{n}\left|\mathrm{Re}(x_i)\right|+x_{real} \tag{2.21}$$

$$\underline{x_i}=\mathrm{Im}(x_0)-\sum_{i=1}^{n}\left|\mathrm{Im}(x_i)\right|-x_{imag}\ ,\ \overline{x_i}=\mathrm{Im}(x_0)+\sum_{i=1}^{n}\left|\mathrm{Im}(x_i)\right|+x_{imag} \tag{2.22}$$

On the other hand, a complex interval number $\mathbf{x}=\mathbf{x}_r+\mathrm{i}\,\mathbf{x}_i$ is converted in a new complex affine form $\hat{x}=x_0+x_{new_1}\varepsilon_{new_1}+\mathrm{i}\,x_{new_2}\varepsilon_{new_2}$ using Eq. (2.23):

$$x_0=\frac{\left(\underline{x_r}+\overline{x_r}\right)+\mathrm{i}\left(\underline{x_i}+\overline{x_i}\right)}{2}\ ,\ x_{new_1}=\frac{\left(\overline{x_r}-\underline{x_r}\right)}{2}\ ,\ x_{new_2}=\frac{\mathrm{i}\left(\overline{x_i}-\underline{x_i}\right)}{2} \tag{2.23}$$

All the basic mathematical operands for the affine technique are taken from Eqs. (38-40), (45-49), (53-55) and (59) of Manson paper [18]. Starting from these equations it is possible to estimate the FRFs of the 2-DOFs mechanical system using Eqs. (2.24)-(2.26):

$$\hat{\alpha}_{1,1}(\omega)=\frac{\left(\hat{k}_2+\hat{k}_3\right)+\mathrm{i}\omega\left(\hat{c}_2+\hat{c}_3\right)-\hat{m}_2\omega^2}{\left(\left(\hat{k}_1+\hat{k}_2\right)+\mathrm{i}\omega\left(\hat{c}_1+\hat{c}_2\right)-\hat{m}_1\omega^2\right)\left(\left(\hat{k}_2+\hat{k}_3\right)+\mathrm{i}\omega\left(\hat{c}_2+\hat{c}_3\right)-\hat{m}_2\omega^2\right)-\left(\hat{k}_2+\mathrm{i}\omega\hat{c}_2\right)^2} \tag{2.24}$$

$$\hat{\alpha}_{1,2}(\omega)=\frac{\hat{k}_2+\mathrm{i}\omega\hat{c}_2}{\left(\left(\hat{k}_1+\hat{k}_2\right)+\mathrm{i}\omega\left(\hat{c}_1+\hat{c}_2\right)-\hat{m}_1\omega^2\right)\left(\left(\hat{k}_2+\hat{k}_3\right)+\mathrm{i}\omega\left(\hat{c}_2+\hat{c}_3\right)-\hat{m}_2\omega^2\right)-\left(\hat{k}_2+\mathrm{i}\omega\hat{c}_2\right)^2} \tag{2.25}$$

$$\hat{\alpha}_{2,2}(\omega)=\frac{\left(\hat{k}_1+\hat{k}_2\right)+\mathrm{i}\omega\left(\hat{c}_1+\hat{c}_2\right)-\hat{m}_1\omega^2}{\left(\left(\hat{k}_1+\hat{k}_2\right)+\mathrm{i}\omega\left(\hat{c}_1+\hat{c}_2\right)-\hat{m}_1\omega^2\right)\left(\left(\hat{k}_2+\hat{k}_3\right)+\mathrm{i}\omega\left(\hat{c}_2+\hat{c}_3\right)-\hat{m}_2\omega^2\right)-\left(\hat{k}_2+\mathrm{i}\omega\hat{c}_2\right)^2} \tag{2.26}$$

Each of system parameters is written in the affine form as a central value plus a partial deviation term equal to 1% of the nominal value of Table 2.1. Thus all the system parameters are evaluated using Eq. (2.27) for masses, Eq. (2.28) for viscous damping and Eq. (2.29) for stiffnesses.

$$\begin{aligned}\hat{m}_1&=1+0.01\varepsilon_{m_1}\\ \hat{m}_2&=2+0.02\varepsilon_{m_2}\end{aligned} \tag{2.27}$$

$$\begin{aligned}\hat{c}_1&=10+0.1\varepsilon_{c_1}\\ \hat{c}_2&=20+0.2\varepsilon_{c_2}\\ \hat{c}_3&=30+0.3\varepsilon_{c_3}\end{aligned} \tag{2.28}$$

$$\begin{aligned}\hat{k}_1&=10^4+10^2\varepsilon_{k_1}\\ \hat{k}_2&=\left(2\times10^4\right)+\left(2\times10^2\right)\varepsilon_{k_2}\\ \hat{k}_3&=\left(3\times10^4\right)+\left(3\times10^2\right)\varepsilon_{k_3}\end{aligned} \tag{2.29}$$

Finally, the receptances, evaluated using Eqs. (2.24)-(2.26) could be written in their complex affine form using Eq. (2.30) which returns the receptance central value at each excitation frequency ω, with the partial deviation terms for all the different uncertainty contribution:

$$\hat{\alpha} = \alpha_0 + \sum_{i=1}^{n} \alpha_i \varepsilon_i + \alpha_{real} \varepsilon_{real} + \mathrm{i}\, \alpha_{imag} \varepsilon_{imag} \tag{2.30}$$

where $n = 8$ is due to the number of system parameters. Then this affine number is converted into a complex interval number using Eqs. (2.21)-(2.22) and compared with interval analysis approach.

2.2.3 Full factorial design, Latin hypercube, and Monte Carlo sampling

Design of Experiments (DOE) is a rigorous methodological approach largely used for solving different types of engineering problem [58], that applies principles and techniques at the data collection stage to ensure the generation of valid, defensible, and supportable engineering conclusions. Moreover, this kind of approach can guarantee the reduction of engineering run tests, time, and thus money. It is widely used in several engineering problem solving areas, as well as for improving or optimizing product design and manufacturing processes. If the engineer is interested in assessing whether a change in a single factor has an effect as change/improvement to the process as a whole, the DOE is used in a *comparative* way, while it is used for a *screening characterization* when the engineer is interested in understanding the process as a whole in the sense that after design and analysis he would like to know a ranked list from most important to least important factors that affect the engineering process. Moreover, the DOE is used in the *modeling* process to estimates the coefficients of a mathematical function that reproduce the model, or in the *optimising* area when the engineer is interested to determine optimal settings of the process factors; that means to determine the level of the factor that optimises the process response [59].

In other words, this means that to really understand cause-and-effect relationships in a certain system it is necessary to deliberately change the input variables to the system and observe their effects and changes in the system output, thus conducting experiments on the system. Each experimental run is a test, and a proper selection of factor levels is necessary to reduce computation costs and time in this preliminary phase of engineering design.

Therefore, in the analysis and study of an uncertain system, the screening characterisation assume a key role to assess a proper set as regards levels for each model parameter. The correct approach to dealing with two or more factors is to conduct a factorial experiment, using the FFD approach. It is based on the investigation of all possible combinations of the levels of the factors to have a complete DOE of the engineering problem. In the study of the 2 DOFs mechanical system with uncertainty of this chapter, two levels for each factor are assumed and thus, for a complete replication of all possible combinations, a 2^k factorial design is considered, with k equal to the number of factors or mechanical system parameters. As suggested in [60], the 2^k factorial design is widely used in the

preliminary stages of a DOE for a factor screening on the main uncertain input parameters that highly influence the output FRFs of the system.

On the other side, the Latin hypercube sampling, firstly introduced by McKay et al. in [61], is a sampling method to choice input parameter values for estimation of output variables. This method is generally used when the number of variables is larger and the deterministic method are difficult to use, as done in [62] for the simulation of the performance of a printer actuator.

This technique was then assumed as sampling method in the study of propagation of uncertainty in complex systems [63]. The most important characteristic of this design is that guarantee uniform samples. In an experimental design with p factors and n runs, an $n \times p$ matrix $\mathbf{D}$ is created, where the $D_{i,j}$ elements are evaluated in an orthogonal way as done in [64].

Finally, the Monte Carlo sampling method [65] is used for solving large scale stochastic problems with the drawback of very high computational costs. The selection of input parameter values could be based on a uniform or normal distribution. The Matlab command $x = rand(n,1)$ generates a vector x, which length is n, of uniformly distributed random numbers in the open interval $(0 \div 1)$, but to compare this distribution with the normal one this interval has been modified to $(-1 \div 1)$. Assuming $n = 10^5$, the histogram of x is flat as reported in Figure 2.2. Instead, the command $y = randn(n,1)$ generates a vector of normally distributed random numbers. The histogram of y looks like a normal distribution whose mean is $\mu_y = 0$ and standard deviation is $\sigma_y = 1$ and it is also reported in Figure 2.2.

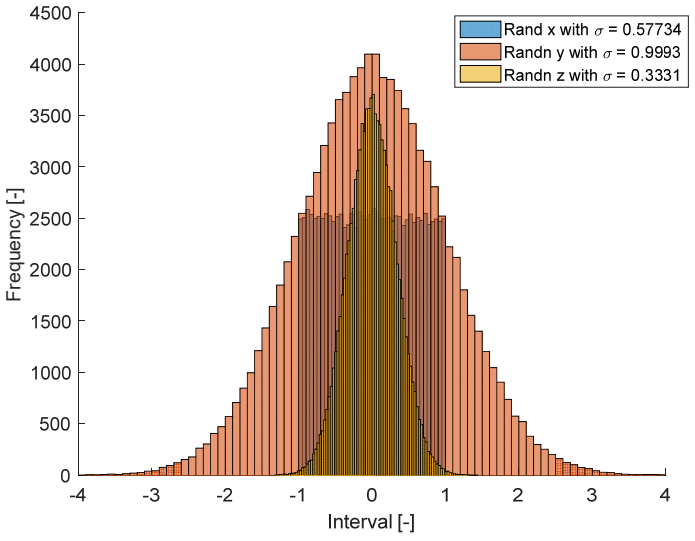

Figure 2.2 – Histogram of uniform and normal distributions.

For the study of the 2 DOFs mechanical system with uncertainty, it is necessary that random numbers lie in the range $(-1 \div 1)$ and not in the range

$(-4 \div 4)$, as happens for y histogram. Thus, a different standard deviation must be chosen to obtain normally distributed random numbers that are in the range $(-1 \div 1)$, achieving the histogram of z, with a mean $\mu_z = 0$ and a standard deviation equal to $\sigma_z = \frac{\sigma_y}{3}$. Nevertheless, with this approach there is no certainty that this range is respected as it is possible to appreciate in Figure 2.2, although the 99% of values are inside the range, hence for this reason the uniform distribution is assumed for analysis of uncertainty to replicate the same starting condition for the input uncertain parameters of other approaches. Moreover, the choice of a uniform distribution for all parameters is done to have better assessment of the extreme events, namely a higher consideration of extreme values with respect to what normally happens with Gaussian-type distributions.

2.2.4 Comparison of FRFs for different values of uncertainty

The stochastic and deterministic methods described in the previous section are used in the evaluation of receptance FRF in the 2 DOFs mechanical system with uncertain parameters. Each of the eight structural parameters are firstly considered with an uncertain lying within a range of ±1% w.r.t. their corresponding nominal values and then with smaller uncertainty to detect its different influence on the FRF. The receptances are presented both in terms of real and imaginary components and in amplitude and phase representation. The procedure consists in the evaluation of lower and upper bounds of the real and imaginary parts of FRF, at each frequency. Then, the lower and upper bound for the modulus are evaluated using Eqs. (2.31)-(2.32):

$$\min\left(\left|\alpha(\omega)\right|\right) = \sqrt{\left(\min\left(\left|Re_{max}\right|,\left|Re_{min}\right|\right)\right)^2 + \left(\min\left(\left|Im_{max}\right|,\left|Im_{min}\right|\right)\right)^2} \tag{2.31}$$

$$\max\left(\left|\alpha(\omega)\right|\right) = \sqrt{\left(\max\left(\left|Re_{max}\right|,\left|Re_{min}\right|\right)\right)^2 + \left(\max\left(\left|Im_{max}\right|,\left|Im_{min}\right|\right)\right)^2} \tag{2.32}$$

with:

$$\begin{cases} Re_{min} = \min\left(\mathrm{Re}\left(\alpha(\omega)\right)\right) \\ Re_{max} = \max\left(\mathrm{Re}\left(\alpha(\omega)\right)\right) \\ Im_{min} = \min\left(\mathrm{Im}\left(\alpha(\omega)\right)\right) \\ Im_{max} = \max\left(\mathrm{Im}\left(\alpha(\omega)\right)\right) \end{cases} \tag{2.33}$$

In this way it is not possible to be sure that the bounds include the nominal system. Therefore, the representation in modulus and phase, reported on the right

side in all figures, considers as maximum the same of Eq. (2.32), while the minimum is evaluated using the following code:

```
if abs(Re_max-Re_min)>abs(abs(Re_max)-abs(Re_min))
    Mod_min = 0;
else
    Mod_min = min([abs(Re_max) , abs(Re_min)])^2;
end
if abs(Im_max-Im_min)>abs(abs(Im_max)-abs(Im_min))
    Mod_min = Mod_min^0.5;
else
    Mod_min = (Mod_min+min([abs(Im_max) , abs(Im_min)])^2)^0.5;
end
```

Receptance $\alpha_{1,1}(\omega)$ is now evaluated using Eq. (2.3), and plotted for different levels of uncertainty in the two frequency ranges that include the two system natural frequencies ω_1 and ω_2. Assuming an uncertainty of $\pm 1\%$ on all system parameters results are reported in Figure 2.3 and Figure 2.4.

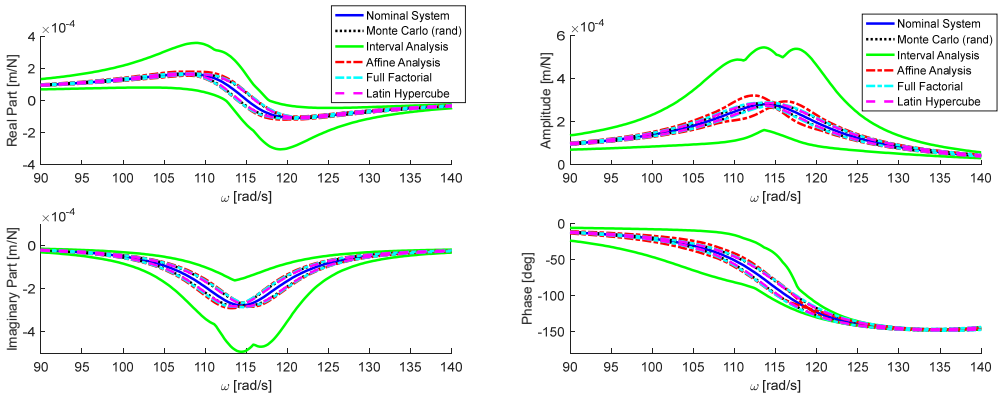

Figure 2.3 – Receptance $\alpha_{1,1}(\omega)$ in a $\Delta\omega$ including $\omega_1 = 114.69$ rad/s with an uncertainty of $\pm 1\%$.

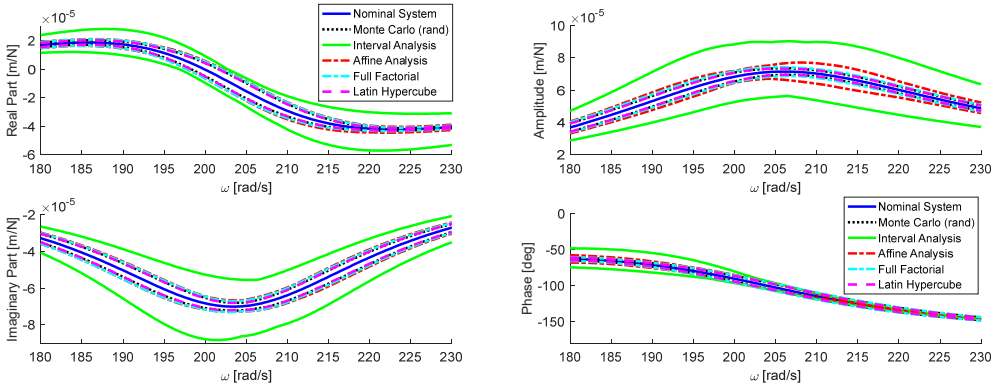

Figure 2.4 – Receptance $\alpha_{1,1}(\omega)$ in a $\Delta\omega$ including $\omega_2 = 204.14$ rad/s with an uncertainty of $\pm 1\%$.

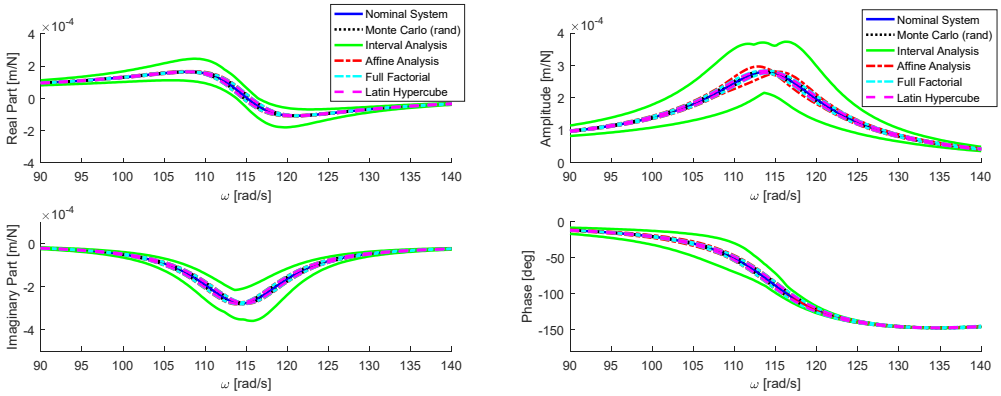

Figure 2.5 – Receptance $\alpha_{1,1}(\omega)$ in a $\Delta\omega$ including $\omega_1 = 114.69$ rad/s with an uncertainty of $\pm 0.5\%$.

Reducing the uncertainty amplitude up to $\pm 0.5\%$ the lower and upper bound of FRF are closer to the nominal system condition as illustrated in Figure 2.5 and Figure 2.6.

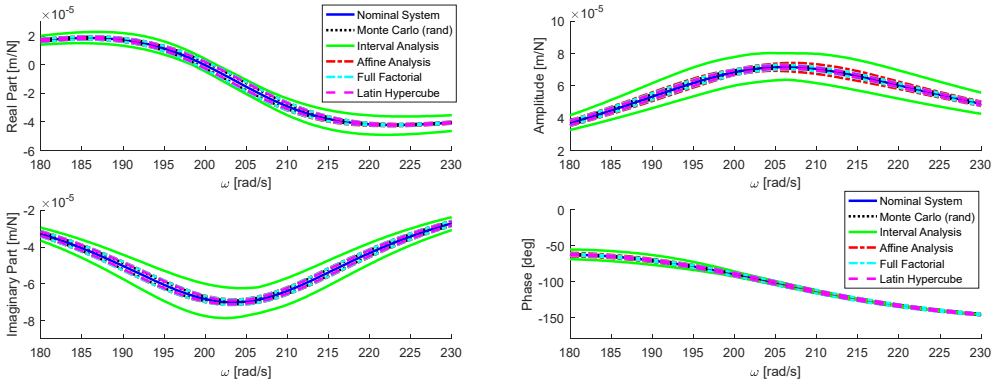

Figure 2.6 – Receptance $\alpha_{1,1}(\omega)$ in a $\Delta\omega$ including $\omega_2 = 204.14$ rad/s with an uncertainty of $\pm 0.5\%$.

Instead, an increment of uncertainty amplitude up to $\pm 1.5\%$ has an evident effect especially using the interval analysis technique as reported in Figure 2.7 and Figure 2.8.

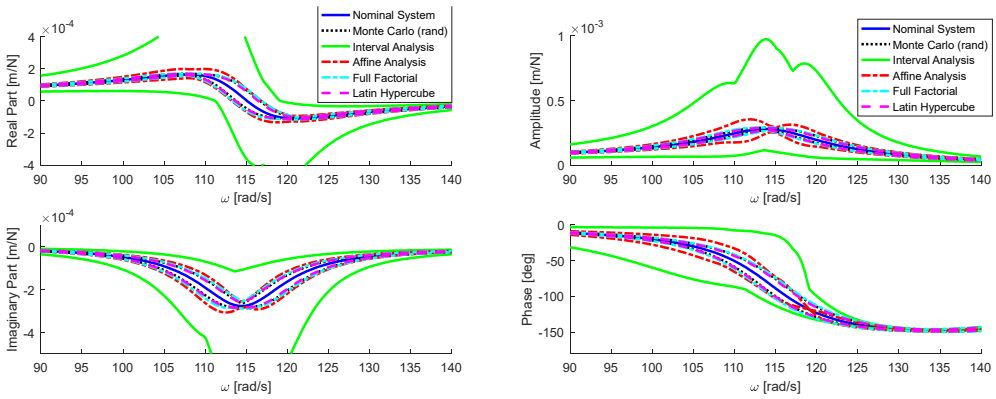

Figure 2.7 – Receptance $\alpha_{1,1}(\omega)$ in a $\Delta\omega$ including $\omega_1 = 114.69$ rad/s with an uncertainty of ±1.5%.

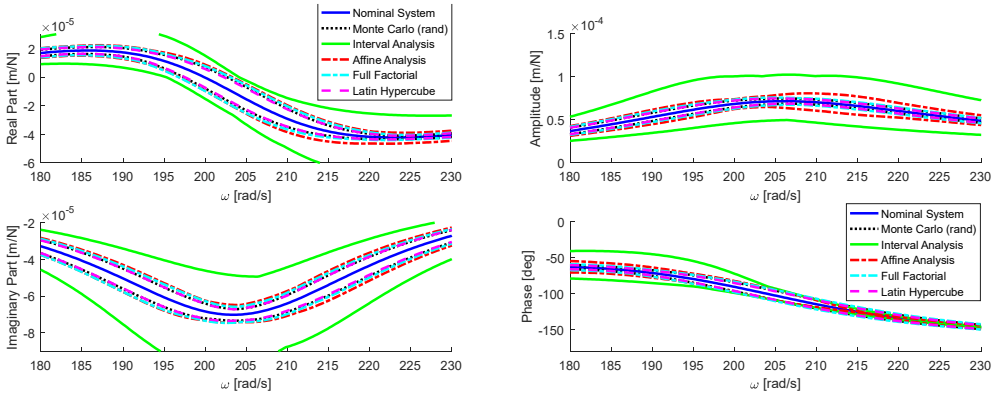

Figure 2.8 – Receptance $\alpha_{1,1}(\omega)$ in a $\Delta\omega$ including $\omega_2 = 204.14$ rad/s with an uncertainty of ±1.5%.

Finally, with an uncertainty amplitude of ±2%, uncertainty amplitude on the receptance become higher, especially using modulus and phase representation than plot with real and imaginary parts.

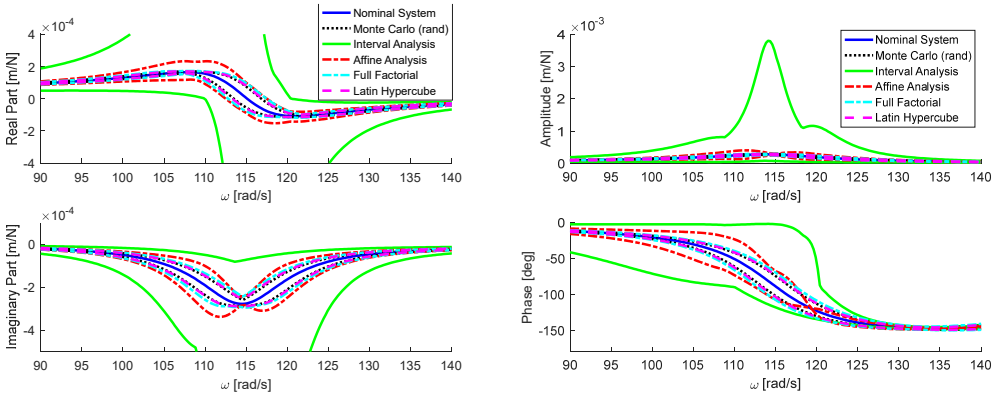

Figure 2.9 – Receptance $\alpha_{1,1}(\omega)$ in a $\Delta\omega$ including $\omega_1 = 114.69$ rad/s with an uncertainty of ±2%.

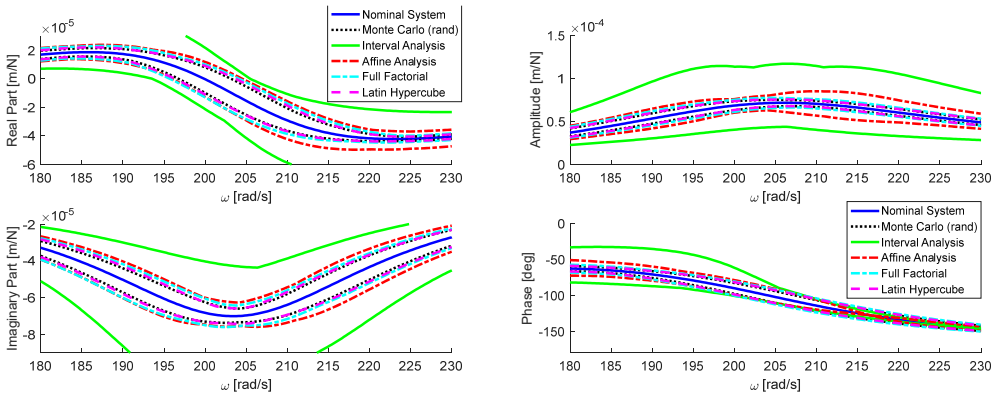

Figure 2.10 – Receptance $\alpha_{1,1}(\omega)$ in a $\Delta\omega$ including $\omega_2 = 204.14$ rad/s with an uncertainty of $\pm 2\%$.

2.2.5 Effect of uncertainty on system natural frequencies

From the previous section it is clear the effect of uncertain parameters on the FRF of a mechanical system. The higher the level of uncertainty, the greater the distance between lower and upper bound of the uncertain FRF. At the same time, it can be said that there is a maximum level of uncertainty, after which FRF bounds are too large, and the dynamic response is not clear and too far from the nominal system. This happens especially with the interval analysis approach, and it is more evident in the modulus and phase representation.

Another way to estimate the influence of uncertain parameter on a mechanical system is the analysis on the variability of system poles through the evaluation of their variances on real and imaginary parts.

Using the Monte Carlo sampling with a certain number of iterations, the system poles are evaluated at each iteration solving the eigenproblem related to dynamic problem of Eq. (2.34)

$$\mathbf{M}\,\ddot{\mathbf{x}} + \mathbf{C}\,\dot{\mathbf{x}} + \mathbf{K}\,\mathbf{x} = \mathbf{f} \tag{2.34}$$

Even if the system matrices reported in Eq. (2.2) ensure the condition of proportional viscous damping, according to Eq. (2.35), the eigenvalue problem is solved using the complex modal analysis, as in [66].

$$\mathbf{C} = \alpha\,\mathbf{M} + \beta\,\mathbf{K} \tag{2.36}$$

Hence, using the complex modal analysis, the generic model for a dynamic matrix problem is reduced to a first order problem. This form of equations of motion is also known as the ‘Duncan form’:

$$\mathbf{A}\,\dot{\mathbf{y}} + \mathbf{B}\,\mathbf{y} = \tilde{\mathbf{f}} \tag{2.37}$$

where $\mathbf{y}$, $\dot{\mathbf{y}}$ are respectively the generalised displacements and velocities $(2n\times 1)$ of the first order problem related to the only active DOFs according to:

$$\mathbf{y}=\begin{Bmatrix}\mathbf{x}\\ \dot{\mathbf{x}}\end{Bmatrix},\ \dot{\mathbf{y}}=\begin{Bmatrix}\dot{\mathbf{x}}\\ \ddot{\mathbf{x}}\end{Bmatrix} \tag{2.38}$$

$\mathbf{A}$ is a symmetric matrix $(2n\times 2n)$ given by Eq. (2.39):

$$\mathbf{A}=\begin{bmatrix}\mathbf{C} & \mathbf{M}\\ \mathbf{M} & \mathbf{0}\end{bmatrix} \tag{2.39}$$

$\mathbf{B}$ is a symmetric matrix $(2n\times 2n)$ given by Eq. (2.40):

$$\mathbf{B}=\begin{bmatrix}\mathbf{K} & \mathbf{0}\\ \mathbf{0} & -\mathbf{M}\end{bmatrix} \tag{2.40}$$

and $\mathbf{f}$ is the generalised force vector $(2n\times 1)$

$$\tilde{\mathbf{f}}=\begin{Bmatrix}\mathbf{f}\\ \mathbf{0}\end{Bmatrix} \tag{2.41}$$

Considering the homogenous equation related to Eq. (2.37):

$$\mathbf{A}\,\dot{\mathbf{y}}+\mathbf{B}\,\mathbf{y}=\mathbf{0} \tag{2.42}$$

and assuming a generalised exponential solution for $\mathbf{y}$, $\dot{\mathbf{y}}$:

$$\mathbf{y}=\mathbf{y}_0\mathrm{e}^{St} \tag{2.43}$$

$$\dot{\mathbf{y}}=S\,\mathbf{y}_0\mathrm{e}^{St} \tag{2.44}$$

the Eq. (2.42), using Eqs. (2.43)-(2.44), could be written as:

$$\left(\mathbf{B}+S\,\mathbf{A}\right)\mathbf{y}_0\mathrm{e}^{St}=\mathbf{0} \tag{2.45}$$

Hence, time is separable and erasable from the equation achieving:

$$\left(\mathbf{B}+S\,\mathbf{A}\right)\mathbf{y}_0=\mathbf{0} \tag{2.46}$$

Apart the trivial solution $\mathbf{y}_0=\mathbf{0}$ that corresponds to the static undeformed condition, Eq.(2.46) is an eigenproblem and the others interesting non-null solutions are given by the zeros of the characteristic equation by means of:

$$\det\left(\mathbf{B}+S_r\mathbf{A}\right)=0 \tag{2.47}$$

which possesses $2n$ solutions in S_r, called eigenvalues or poles of the system. The poles S_r can be real or complex conjugated. For every eigenvalue S_r a non-null corresponding eigenvector $\tilde{\boldsymbol{\psi}}_r$ can be evaluated through Eq. (2.48):

$$\left(\mathbf{B}+S_r\mathbf{A}\right)\tilde{\boldsymbol{\psi}}_r=\mathbf{0} \tag{2.48}$$

The eigenvectors $\tilde{\boldsymbol{\psi}}_r$ are then normalised according to an appropriate criterion. Instead, considering a couple of complex and conjugate eigenvalues, the relationship for underdamped eigenvalues S_r, natural frequency ω_r and damping ratio ζ_r results:

$$S_{r,r*}=\mathrm{Re}\left(S_r\right)\pm\mathrm{i}\,\mathrm{Im}\left(S_r\right)=-\zeta_r\omega_r\pm\mathrm{i}\,\omega_r\sqrt{1-\zeta_r^2} \tag{2.49}$$

Starting from Eq. (2.49), the following relationship between eigenvalues S_r, natural frequency ω_r and damping ratio ζ_r could be evaluated:

$$S_r+S_{r*}=-2\zeta_r\omega_r \tag{2.50}$$

$$S_rS_{r*}=\omega_r^2 \tag{2.51}$$

$$\omega_r=\pm\left|S_{r,r*}\right| \tag{2.52}$$

$$\zeta_r=-\frac{\mathrm{Re}\left(S_r\right)}{\left|S_{r,r*}\right|} \tag{2.53}$$

Once system poles are obtained, applying a Monte Carlo sampling with 1000 iterations, it is possible to evaluate the variability on poles when the system is affected by uncertainty. The pole variance is evaluated using Eq. (2.54):

$$\sigma=\frac{1}{n-1}\sum_{i=1}^{n}\left(Y_i-\overline{Y}\right)^2 \tag{2.54}$$

where, n is the number of poles and Y_i, $\overline{Y}$ are respectively the i^{th} pole and the average of all poles. Since poles are complex numbers, it is possible to evaluate variance on both real and imaginary components of the poles and results are summarised in Table 2.2.

Table 2.2 – Variance on complex poles for different uncertainty levels.

Level of uncertainty	**Real variance**		**Imaginary variance**	
	$S_{1,2}$	$S_{3,4}$	$S_{1,2}$	$S_{3,4}$
$\pm 0.5\%$	$\sigma_r = 3.57 \cdot 10^{-4}$	$\sigma_r = 3.5 \cdot 10^{-3}$	$\sigma_i = 2.78 \cdot 10^{-2}$	$\sigma_i = 8.62 \cdot 10^{-2}$
$\pm 1.0\%$	$\sigma_r = 1.5 \cdot 10^{-3}$	$\sigma_r = 1.6 \cdot 10^{-2}$	$\sigma_i = 1.15 \cdot 10^{-1}$	$\sigma_i = 3.48 \cdot 10^{-1}$
$\pm 1.5\%$	$\sigma_r = 3.1 \cdot 10^{-3}$	$\sigma_r = 3.16 \cdot 10^{-2}$	$\sigma_i = 2.32 \cdot 10^{-1}$	$\sigma_i = 7.97 \cdot 10^{-1}$
$\pm 2.0\%$	$\sigma_r = 6.3 \cdot 10^{-3}$	$\sigma_r = 6.42 \cdot 10^{-2}$	$\sigma_i = 4.62 \cdot 10^{-1}$	$\sigma_i = 1.59$

The poles of the 2-DOFs of this chapter are plotted in Figure 2.11 using the representation in the Argand-Gauss plane. Their distribution is similar to an ellipse, which centre correspond to the mean values of real and imaginary parts, while the length on the two semi-axes is related to the variance on real and imaginary parts.

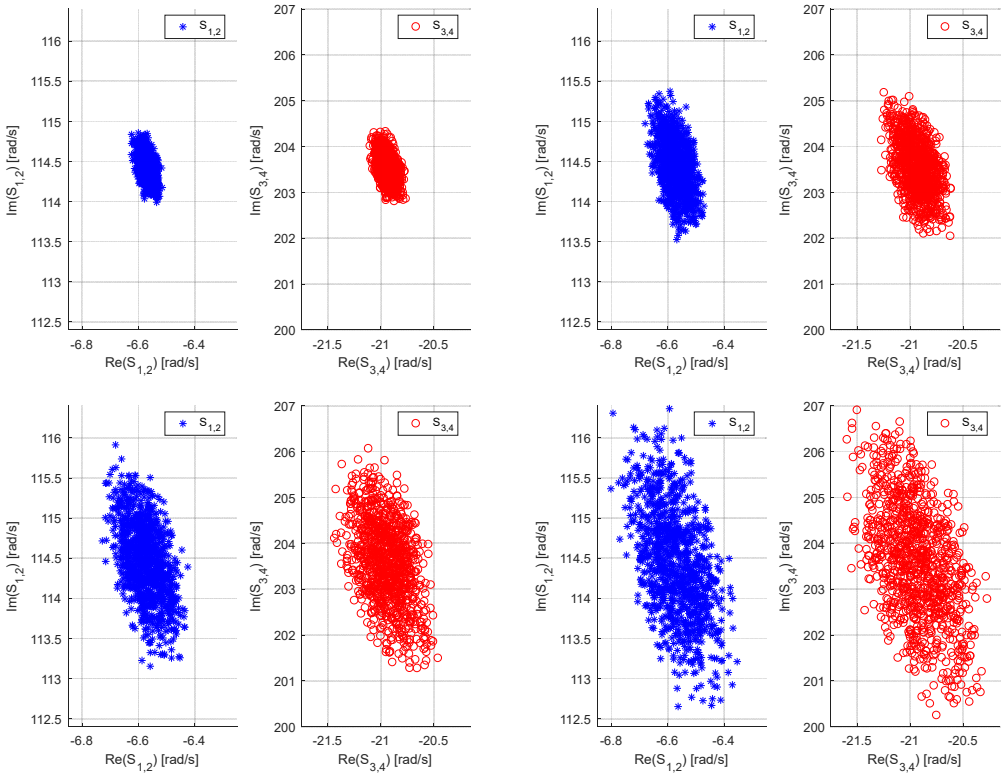

Figure 2.11 – System poles distribution for different levels of uncertainty: ±0.5% (top-left), ±1% (top-right), ±1.5% (bottom-left), ±2% (bottom-right).

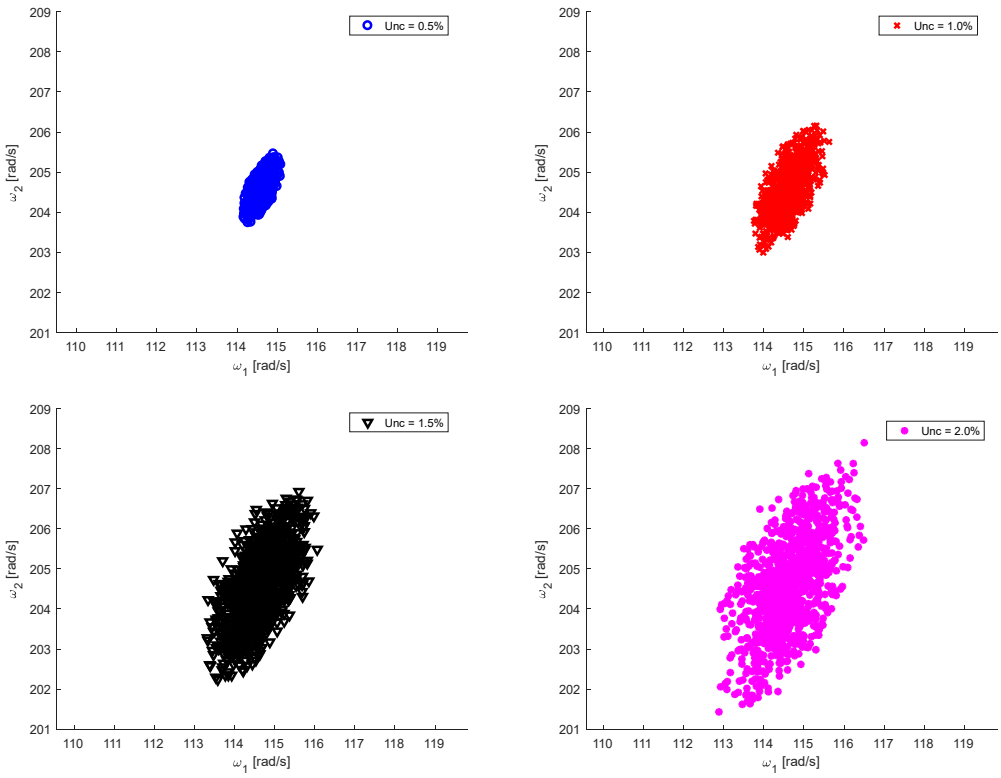

Figure 2.12 – System natural frequencies in the $\omega_1 - \omega_2$ plane for an uncertainty on system parameters from $\pm 0.5\%$ up to $\pm 2\%$.

Another way to detect the effect of parameters uncertainty on the system is to plot its natural frequencies, as proposed in [67,68], using the $\omega_1 - \omega_2$ plane. The results are proposed in Figure 2.12 for different levels of uncertainty. The centre of the ellipses correspond to the couple of ω_1 and ω_2 of the nominal system, while the two semi-axes depends on the variance of the two natural frequencies.

2.4 Conclusions

Different deterministic and stochastic methods used to study uncertain systems and their dynamic response were presented in this chapter. The advantages and drawbacks of each method have been proposed, highlighting that the number of uncertain parameters and the complexity of the analysed mechanical system are the main tiebreak factors in method selection, to avoid high computational costs without compromising the accuracy of results.

Complex interval analysis and complex affine analysis have their advantage only in the computational cost, since with only a calculation at each frequency it is possible to evaluate lower and upper FRF bounds. On the other hand, the accuracy in FRF estimation is good within a certain percentage of uncertainty, depending on the number of uncertain parameters and on their nominal values.

The FFD method can be considered as the correct approach to dealing with two or more factors, conducting a factorial experiment. However, the definition of

an appropriate DOE is one of the main aims before performing the analysis. Likewise, LHD method can be considered as a valid alternative to FFD when the number of variables is larger, and the deterministic method are difficult to use.

Finally, the Monte Carlo sampling method has the drawback of very high computational costs, but it could be very useful when the effects of uncertain parameters on the variance of imaginary and real part of system poles have to be investigated.

Chapter 3

3. Dual Clutch Transmission

The study of the dynamic behaviour of a mechanical system become more and more difficult especially when its dynamic is affected by non-linearities, or its modelling is very complex or when it is affected by uncertainties as illustrated in the previous chapter. In this context, an automotive transmission can be considered as the proper application to study the dynamics of a complex mechanical system, performing a sensitivity analysis on system parameters to assess an improvement on vehicle NVH performance.

In the last recent years, an ever-increasing number of vehicles have adopted Dual Clutch Transmission technology to ensure fast gear-shifting with uninterrupted torque transfer to the driving wheels, with the final aim of achieving high performance in terms of sportiness as well as efficiency.

In this chapter a brief review on NVH issues and modelling criteria is presented in § 3.1, before briefly illustrating in § 3.2 the mechanical architecture of a DCT gearbox. Then, in § 3.3 the modelling criteria of inner components are provided, and in § 3.4 the methodology used to analyse the gear-shift induced vibrations is presented. Finally, in § 3.5, the inputs of an experimental manoeuvre are used for a simulation and in § 3.6 the methodology is applied to a test case for the assessment of NVH performance. The PhD research activity reported in this chapter has been already published in [69].

3.1 NVH issues and modelling criteria of a DCT technology

The improvement of the NVH performance is a constantly prerogative of Research and Development (R&D) departments of several automotive companies, which spend a large portion of their budget to satisfy the needs of customers. To support this, Qatu et al. presented in [15] an overview of automotive NVH issues, describing the interior noise due to different sources, as powertrain, road-tyre

interface and wind. As far as driveline NVH is concerned, gear whine, clutch shudder and clunking noises are analysed, giving details about their frequency ranges and their possible cause.

Among NVH issues, the shudder or judder noise is mainly due to torsional oscillations during clutch engagement process and it is highly influenced by frictional characteristics [70]. If it is considered as a low frequency issue with a frequency range of 5÷20 Hz, the whine noise is a high frequency noise with a frequency range of 2÷15 kHz. Hence, it is an acoustic issue quite fastidious if it is present within the car and it is mainly correlated to transmission errors and to the variation of gears meshing stiffness [71].

Another potential NVH issue, is the clunk noise generation during gear shift, that is typical of transmission systems using the same components of a MT. It is directly perceivable in the car cabin as a metallic impact noise, and it should be carefully considered especially during the earlier transmission design stages. In details, the clunk is a metallic noise under tip-in/out condition due to impacts between gears teeth when the engine torque is suddenly applied, Moreover, it is characterised by a broad band frequency range.

More specifically, highly efficient mechanical architectures typical of AMT and Dry-DCT layouts are more subject to NVH issues due to their low level of damping and power losses, although providing better fuel economy.

Hence, it is becoming increasingly more important the integration of a reliable simulation methodology in the design process, to predict the gearshift-induced vibrations, for an optimal comparison of different design solutions. It is in this perspective that the first design step consists in the development of a detailed transmission model able to describe the inner dynamics of the gearbox transmission, highlighting the NVH phenomenon of interest. In fact, in the modelling of this type of vibration it is necessary to consider at least total transmission backlashes, driveshaft stiffnesses and gears inertias.

The clunking noise is one of NVH that requires more attention and thus it is matter of study of several works as in [72] where Gear Shift Patterns are optimized to satisfy different customers' requirements, like drivability, NVH performance, emissions and fuel consumption, or in [73] where a DCT model is developed to investigate the low frequency clunk. At the same time the experimental approach is fundamental, of course, and thus in [74] six powertrain noise and vibration troubleshooting case studies are proposed to prove techniques and engineering tools addressing a variety of drivetrain NVH issues, from an experimental point of view.

Another typical transmission vibration is the gear rattle, which consists in an impact-induced noise. It is mainly related to the torsional vibrations due to the backlashes between unloaded gear pairs excited by the engine orders. Gear rattle intensity is directly related to engine angular acceleration. It was treated by Brancati et al. from a theoretical [75] and experimental [76] point of view, discussing the squeeze effect of the oil between the gear teeth varying the lubrication mechanism, to highlight possible positive influence of oil damping factor in reducing the impacts between gears teeth and thus rattle induced

vibrations. Another way to influence the gear rattle intensity is to modify clutch stiffness parameters [77], when this issue is not caused by a vibration mode excitation of the driveline. The hysteresis seems to have an optimum range of values, with an increment of vibration level when the hysteresis is over dimensioned.

Moreover, the gear-shift noise is due to axial and rotational impacts between teeth flanks of different synchroniser elements during gear engagement.

Other research activities are conducted on gear rattle phenomenon using wavelet analysis [78] or analysing the deviation of peak force from the average value [79] to assess the rattle severity.

Due to DCT modelling complexity, a sensitivity analysis on some transmission design parameters, e.g. torsional backlash in the synchronisers or clutch disc moment of inertia, during low speed manoeuvres is proposed in [80] as a methodology for the assessment of the NVH performance of (DCTs), evaluating benefits in terms of RMS value of each bearing force time-history.

Finally, the integration of powertrain control with active braking is investigated in [81] as a feasible method to potentiality reduce noise and vibration of a vehicle transmission. The idea is to apply a torsional preload to the transmission system to avoid those external disturbances coming from the road or from the transmission shafts generate significant NVH issues.

3.2 Layout and mechanical architecture of a DCT

A DCT gearbox owes its name to the presence of two clutches, fully integrated in a Dual Clutch Unit (DCU), which could be of dry or wet-type, according to the amount of torque that must be transferred through them. So it is possible to have a Dry-DCT (DDCT) or a Wet-DCT (WDCT). In the case of a DDCT, as modelled in this chapter, the driven disk of each clutch (K1 and K2) is mounted on one of the two coaxial primary shafts, called PS1 for the odd gears and PS2 the even ones. The control unit is devoted to the management of gearshifts and engagements/disengagements of the two clutches.

The main benefit of a DCT gearbox is the possibility of a continuous traction without any interruption of the transferred torque, due to the controlled slippage of the clutches. The two clutches are alternatively engaged for even and odd gears, according to the actual gear engaged. The disengagement of the off-going clutch and the engagement of the on-coming one is managed by an electronically controlled shift process, to minimise gear-shift time.

During the DCT normal functioning, in the start-up phase, the two clutches are disengaged, the first gear is engaged, hence no torque is transferred from engine to the wheels. When the odd clutch K1 starts engaging an increasing torque is transferred from the inner primary shaft PS1 to the secondary shaft, connected to the primary shaft through the first gear pair. Meanwhile, it is possible to preselect the second gear if not already engaged, being the second even clutch K2 disengaged. The preselection of the gear, or more in general the

gear engagement takes places using a mechanical element called synchroniser, which aim is the synchronisation on rotational speed between two rotating elements.

The concept of preselection is very important allowing to perceive the great potentiality of a DCT gearbox. Indeed, it is possible to engage the corresponding synchroniser in advance with respect to the effective actuation of the next gear that is achieved engaging the corresponding clutch. The gearshift procedure is characterised by a clutch-to-clutch shift procedure together with the preselection of the new gear eliminating the dead times due to the traditional synchronisation phase of an AMT.

Moreover, the DCT compensates and overcomes the dynamic limits of an Automated Manual Transmission (AMT), reaching better dynamic performance during vehicle acceleration and more comfortable driving thanks to continuous torque transmission during the gearshifts. In contrast to AMT, a particular characteristic of DCT is that the synchronisers are mounted between two non-consecutive gears thus enabling, in case of a sequential gear-shift, the preselection of the next gear without removing the currently engaged one.

Finally, the Electronic Transmission Control Unit (ETCU) avoids the simultaneous lock of the two clutches thus preventing structural damages to the gearbox. In Figure 3.1 it is represented the layout of a DCT gearbox. The represented gearbox is characterised by four synchroniser elements, to engage up to eight gears (seven ones plus reverse gear).

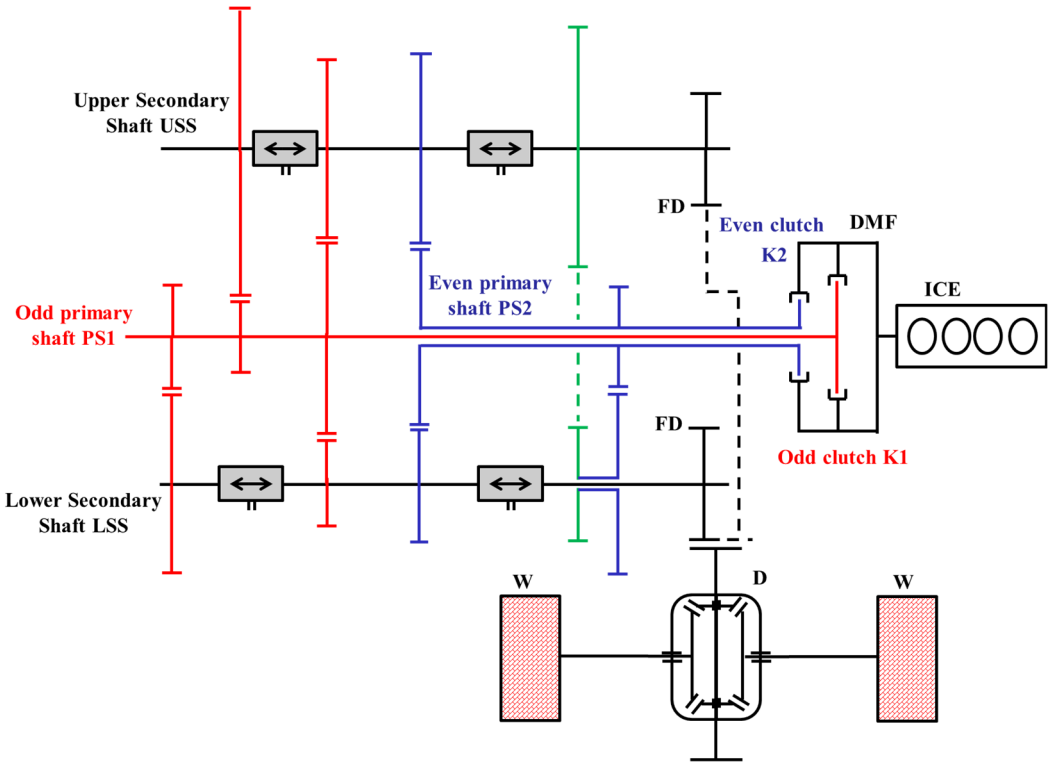

Figure 3.1 – Architecture of a DCT gearbox.

Regarding the real arrangement of primary and secondary shafts, it is important to say that, even if in Figure 3.1 the axes of the two primary shafts, of the two secondary shafts and of the differential seems to belong to the same plane, they could be arranged in the space with appropriate different angles to realise a more compact solution.

3.3 DCT modelling

The first design step to define in the modelling of a transmission, or more in general of a mechanical system, is the level of accuracy, directly correlated to the inner dynamics that should be analysed. For the study of DCT induced vibrations during the gear-shift it is firstly required an accurate simulation of the internal transmission dynamics and subsequently an offline uncoupled computation of the gearbox housing acceleration starting from the output of the simulation.

Thus, a nonlinear lumped parameter model has been developed using the software Siemens/Amesim to study the inner dynamics of a DCT gearbox and the longitudinal vehicle dynamics of a mid-size sedan.

The proposed nonlinear lumped parameter model is extremely accurate, especially in the description of gear-shift phase concerning the synchroniser dynamics, which include a customized modelling of the contact between the plunger ball and synchroniser sleeve groove.

The topic of gear synchronisation phase has been treated by Walker et al. in [82], analysing the response of a DCT using a powertrain model with lumped inertias. The performed simulations proved the highly nonlinear nature of synchroniser element and through the introduction of harmonic engine torques there was an increment of vibrations on the synchroniser sleeve, with excitations in the engaging/disengaging phase.

Moreover, even if the shift quality is not directly affected by the synchronisers, a smoother and quicker transition of gears is obviously a significant factor to achieve the final aim of fuel economy [83] and a better gear-shift performance.

The nonlinear behaviour of the transmission is mainly related to the presence of a rotational gap, called backlash, between the teeth of gears engaged on primary and secondary shafts, on the differential and in the internal elements of the synchroniser.

An overview of the developed model is presented in Figure 3.2, where different macro-blocks are highlighted. The model has the peculiarity of simulate manoeuvres with one or two synchronisers engaged at the same time and, with an accurate level of details for the synchronisation phase, which will be described in the following section of this chapter. The inputs of the model are the displacement of pistons acting on the forks during the gear-shift, the engine torque and the two clutches transmissible torques. The engine torque time history is applied to the primary mass of a Dual Mass Flywheel (DMF), which inner spring element generates a restoring torque based on the DMF characteristic, while the secondary

mass of DMF is connected to the clutch drum of DCU. Instead, the transmissible torque signals of the two clutches are connected to the friction model blocks that computes the correct clutch torque that must be transferred to the odd or even primary shafts.

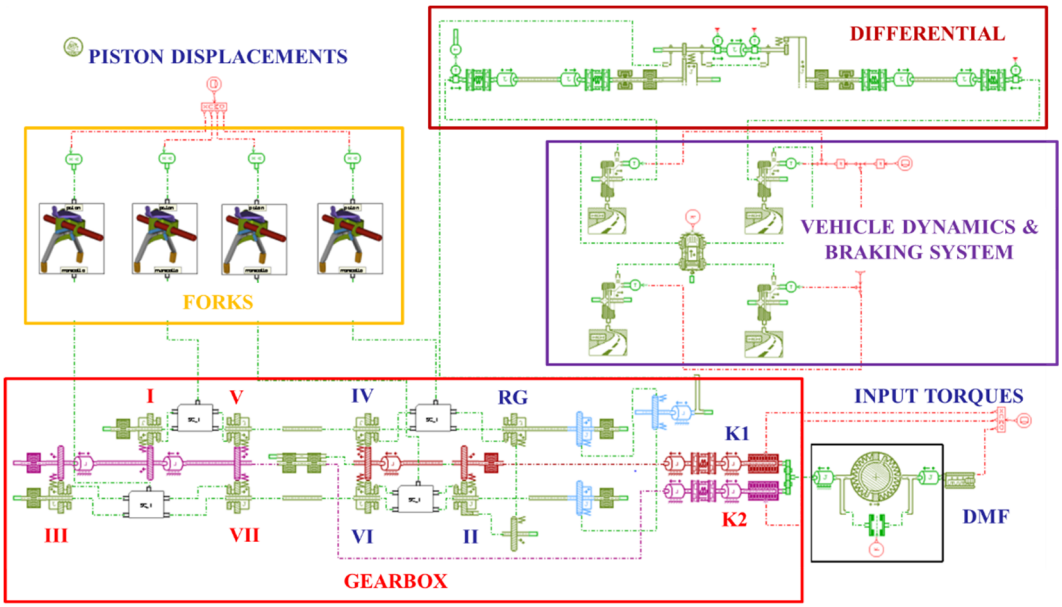

Figure 3.2 – DCT model layout on Amesim.

The model has been developed to simulate several types of experimental manoeuvres. The gear shift forks positions are related to the piston displacements and represent the inputs that control the gear engagement and disengagement during the synchronisation phase of the specific manoeuvre that must be tested. Moreover, the vehicle model is a SDOF pure longitudinal model, while each tire is modelled using a transient formulation of Pacejka's magic formulas.

The vehicle dynamic model is used to evaluate the longitudinal acceleration, velocity, and displacement of the car body. It considers viscous friction, road slope and the air resistance. The corresponding dynamic equation is reported in Eq. (3.1):

$$F_{Vehicle} = M\,a = F_{FW} + F_{RW} - F_{slope} - F_{aero} - c\,V_{Vehicle} \tag{3.1}$$

where, $F_{Vehicle}$ is the total longitudinal force acting on vehicle mass M, to produce its acceleration a. Moreover, F_{FW} and F_{RW} are the longitudinal forces on the two front and two rear wheels, respectively. In case of traction wheel their sign will be positive, while in case of breaking phase or dragged wheel their sign will be negative. Instead, the slope force F_{slope} is evaluated using Eq. (3.2):

$$F_{slope} = M\,g\sin\left(\tan^{-1}\left(\frac{\alpha_{road}}{100}\right)\right) \tag{3.2}$$

where, α_{road} is the slope of the road expressed in percentage, generating a negative force slope F_{slope} in case of uphill road and positive in case of downhill one. The aerodynamic force F_{aero} is related to vehicle dimensions according to Eq. (3.3):

$$F_{aero} = \frac{1}{2} \rho S C_x V_{wind} \tag{3.3}$$

where ρ is the air density, S in the frontal area of the vehicle, C_x is the aerodynamic drag coefficient, and V_{wind} is the relative velocity of the wind respect to car longitudinal velocity.

3.3.1 Transmission layout description

Starting from the input power source, the engine torque is applied to the DMF, which model considers the variation of the elastic and damping characteristics with the rotational speed. For both the two clutches, an angular clearance, and a lumped torsional stiffness in parallel with damping are modelled to implement the splined connection between the driven clutch hub and the primary shaft.

The torsion of the transmission shafts is considered introducing rotation stiffness and damping characteristics. Hence, primary, and secondary shafts are modelled as a series of lamped inertia, including the inertia of shaft, driving gears, and equivalent torsional stiffness elements. Instead, for the two secondary shafts the inertia of shaft is combined with the inertia of synchronisers.

The transmission includes seven gears with the driving gears (pinions) that are fixed to the primary shaft, while the driven idle gears (wheels) are mounted on the lower and upper secondary shafts. Moreover, the driven gears model includes inertia, contact stiffness and damping, clearance of the gear meshing and all geometry parameters like pitch radius, pressure and helix angles, and Young modulus are defined.

As regards the engaging mechanism, the forks model receives an input in terms of displacements of the hydraulic actuators, generating a force command to the sleeve of each synchroniser, through bending stiffness of the fork arms. And even then, a nonlinear model is considered due to the modelling of a clearance between the shift finger and the fork gate.

Then, absolute bearings models (i.e. with the external ring still fixed in the gearbox case) are mounted on primary and secondary shafts and on differential shaft considering a constant torque loss, while relative bearings are inserted between primary and secondary shafts and seal models are added the output shafts of the differential.

Finally, a nonlinear Pacejka tyre model [84] is used to model the longitudinal dynamics of the vehicle and a simple braking system with different parameters for front and rear brakes.

3.3.2 Synchroniser model description

The synchronisation phase is a common issue in the automotive transmission field. The gear engagement is usually achieved using the synchroniser, typically mounted on the secondary shafts, which elements allow the synchronisation of rotational speed between the secondary shaft, rings and idle gear of the driven gear that must be engaged. In Figure 3.3 it is reported the model of a synchroniser with its inner elements. The gear-shift is possible only when a gear is in idle conditions, namely when it is free to rotate according to the gear transmission ratio but without transmitting torque.

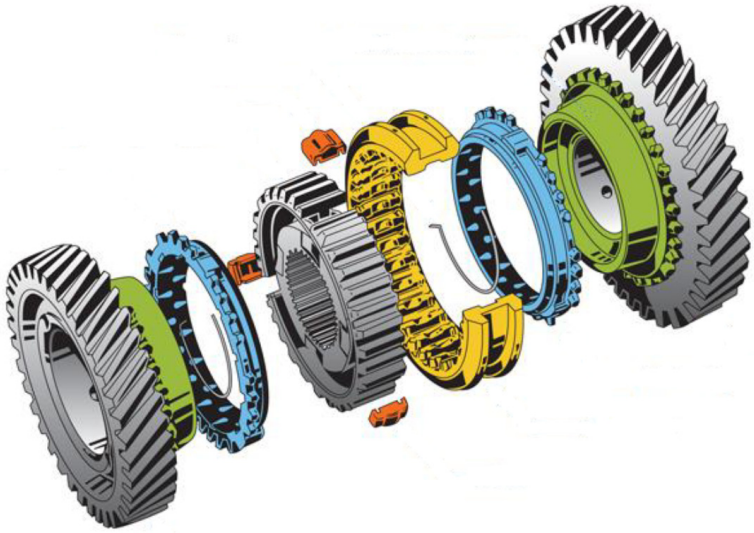

Figure 3.3 – Synchroniser elements.

Each synchroniser is connected to a different fork, which acts with an axial force on the synchroniser sleeve (in yellow in Figure 3.3) that moves pressing the plunger or struct (in orange in Figure 3.3) against the blocker ring (in blue in Figure 3.3). This phase is called pre-synchronisation phase. After that this contact is realised, a friction torque, related to the axial force, is used to accelerate or decelerate the driven gears with their small idle gears (in grey and green in Figure 3.3) synchronising its speed during the so called synchronisation phase. Then the sleeve passes through the ring until the idle gear dog teeth completing the free flying, during which possible double impacts happen and finally the lock-up phase starts obtaining the final coupling between sleeve and idle gear.

As already mentioned, the peculiarity of the developed synchroniser model is its high level of accuracy in the detection of dynamic behaviour during synchronisation phase and gear engagement. As illustrated in Figure 3.4 the synchroniser model takes into account both the torsional and the axial behaviours

of its inner elements. The equations of motion of involved elements change during each phase of engaging process and all of them could be defined starting from the free body diagrams of synchroniser inner elements.

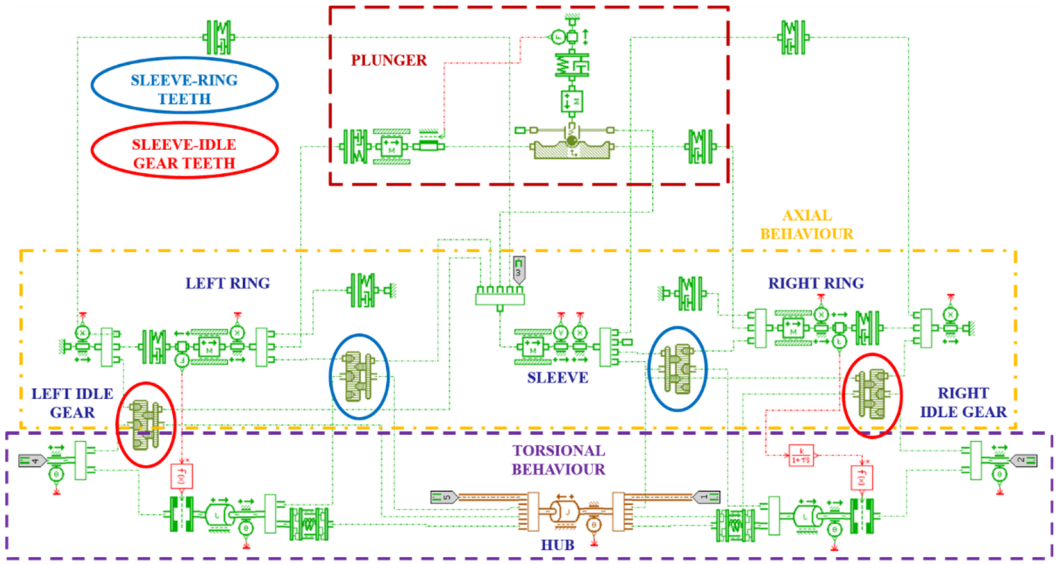

Figure 3.4 – Customised synchroniser model.

The synchronisation torque T_S developed by the friction between conical surface of the blocker ring is used to decelerate/accelerate the driven idle gear in order to reach the same speed of the secondary shaft. It is evaluated using Eq. (3.4):

$$T_S(t) = \frac{F(t)\, d_r \mu}{2 \sin \alpha_r} \tag{3.4}$$

where $F(t)$ is the axial force generated by the synchroniser sleeve against the blocker ring, d_r and α_r are respectively the mean diameter and the conical angle of the ring, and μ is the friction coefficient. Sleeve and synchroniser blocker ring pointing angle (roof angle) must be designed to maintain index torque above the drag torque in every gear position to preserve gear engagement, thus the dog teeth profiles have been defined for sleeve, rings and idle gears.

As illustrated in Figure 3.5 the preloaded ball of the plunger (or struct) moves in the axial direction towards the gear to be engaged; the plunger is dragged through the internal groove of the sleeve. During the pre-synchronisation phase the plunger ball is placed in the central position of the sleeve, which starts to move to its final position with the complete engagement of sleeve dog teeth with driven idle gears dog teeth.

The choice of using this type of cam profile contact to model the plunger/sleeve interaction ensures higher accuracy, if compared with a more standard model with a nonlinear axial stiffness and damping.

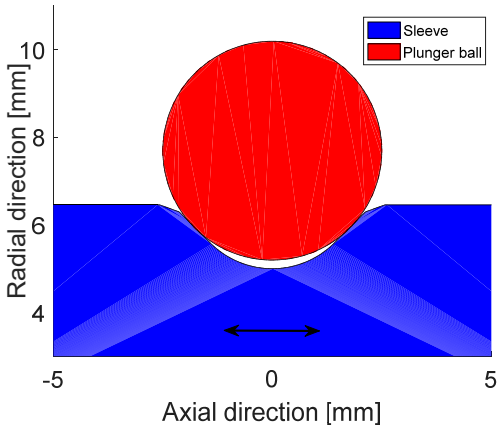

Figure 3.5 – Plunger ball and synchroniser sleeve profile.

The customised synchroniser model of Figure 3.4 count 9 DOFs, that correspond to the axial displacement of the sleeve (1), to the radial (2) and axial (3) displacements of the plunger ball, to the axial (4-5) and rotational (6-7) displacements of blocker rings on left and right side of synchroniser, and to the rotation (8-9) of the two idle gears on the two side of each synchroniser.

For all these DOFs axial and rotational clearances are considered. Hence, an axial one with relative end-stop condition is modelled between the plunger and the two rings of the synchroniser. Moreover, axial clearances are placed between blocker rings and hub, and between rings and idle gears. Finally, a torsional clearance is considered between the hub and the two blocker rings, while no torsional backlash has been modelled between hub and sleeve since it is usually very small.

3.3.3 Bearing force computation

The bearing force computation in another step to consider for the implementation of the methodology used for the assessment of DCT vibrations during gear shifts.

The process is implemented in the software, evaluating the force on each bearing of the gearbox, starting from the force exchanged between gears on primary and secondary shaft of transmission. For each gear pair radial, tangential and axial forces are considered.

As already mentioned in § 3.2, the axes of primary shaft, secondary shafts, and differential, do not belong to the same plane and thus different angles mush be considered for the correct evaluation of the forces of gearbox bearings.

Therefore, the forces between a specific gear pair, evaluated using a local reference frame must be reported to a global one, knowing the angle between unit vectors of the relative and global reference systems.

The relative position of the gearbox shafts and the reference frames (local and global) introduced for the bearing force computation is reported in Figure 3.6, where the global reference system, depicted with black arrows, is characterized by

an axial direction (X), and two perpendicular radial directions (Y and Z). the axial direction (X) is assumed parallel to the axis of all the transmission shafts.

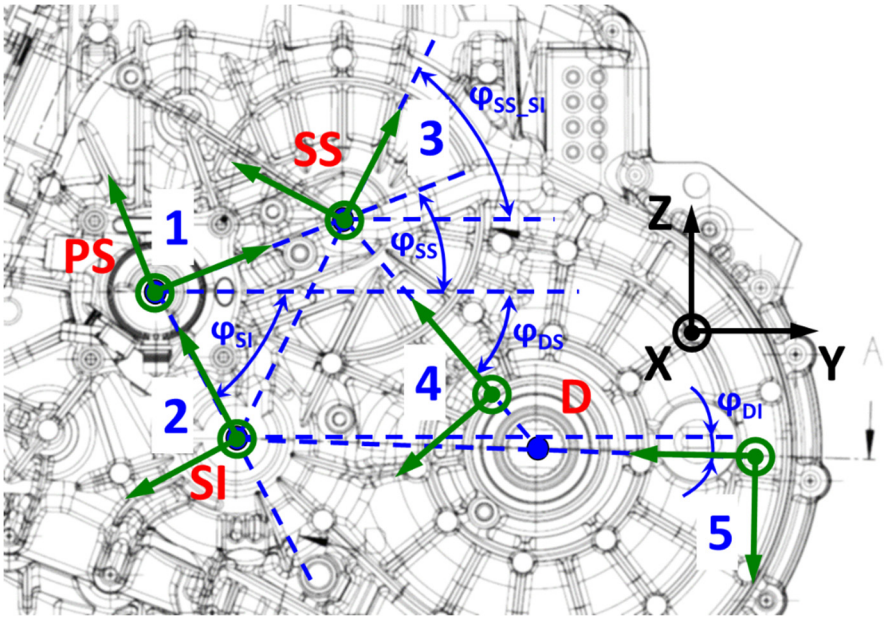

Figure 3.6 – Global (black) and local (green) reference systems.

The correct evaluation of the forces exchanged between each couple of meshing gears is ensured using five local reference systems, which in Figure 3.6 are indicated by different numbers. For each number, the following interaction are listed:

1. Primary Shaft (PS) and upper secondary shaft (SS);
2. Primary Shaft (PS) and lower secondary shaft (SI);
3. Upper secondary shaft (SS) and lower secondary shaft (SI);
4. Upper secondary shaft (SS) and Differential (D);
5. Lower secondary shaft (SI) and Differential (D).

Using these local reference frames, the axial direction is parallel to the shafts axis, the radial direction corresponds to the line connecting the axes of the two shafts involved, while the tangential direction is tangent to the pitch circumferences of the meshing gears and its versus is established by the right-handed rule to have a right-handed local reference system.

The forces exchanged by the gears are evaluated during the simulation, knowing the torque exchanged by each couple of driving and driven gears, mounted respectively on primary and secondary shaft. The meshing forces are evaluated in three different directions, and their value is evaluated using Eq. (3.5):

$$T = \frac{T_{mesh}}{r_p} \quad , \quad R = T\frac{\tan\alpha}{\cos\beta} \quad , \quad A = T\tan\beta \tag{3.5}$$

where T , R , A are the tangential, radial, and axial forces, respectively, for each couple of meshing gears. Instead, T_{mesh} is the meshing torque exchanged by the two gears, r_p is the pitch radius, α is the pressure angle, and β is the helix angle of the gear involved.

The next step in the evaluation of bearing forces consists in the computation of the two radial components of the reaction force on each bearing.

It is important to make just three brief remarks. The first one is that the two primary shafts are considered as a single shaft, due to their coaxiality, in which all the driving gears are mounted, while bearings and gearbox case are considered infinitely stiff. The second one is that the bending of gearbox shafts is neglected, and thus only torsional dynamics are considered. The last one is that the effects of temperature variations are not considered, and load dependence of bearing losses is neglected.

Finally, the process to evaluate the bearing forces must be considered the real shaft disposition in the gearbox, hence it is necessary to calculate the reaction forces on the bearings for each meshing gear couple of the shaft, applying then the superposition principle after these forces are converted from the local to the global reference frame. Thus, in the local reference system radial forces of the bearings are evaluated writing moment equilibrium equations and translation equilibrium equations for each transmission shaft as depicted in Figure 3.7.

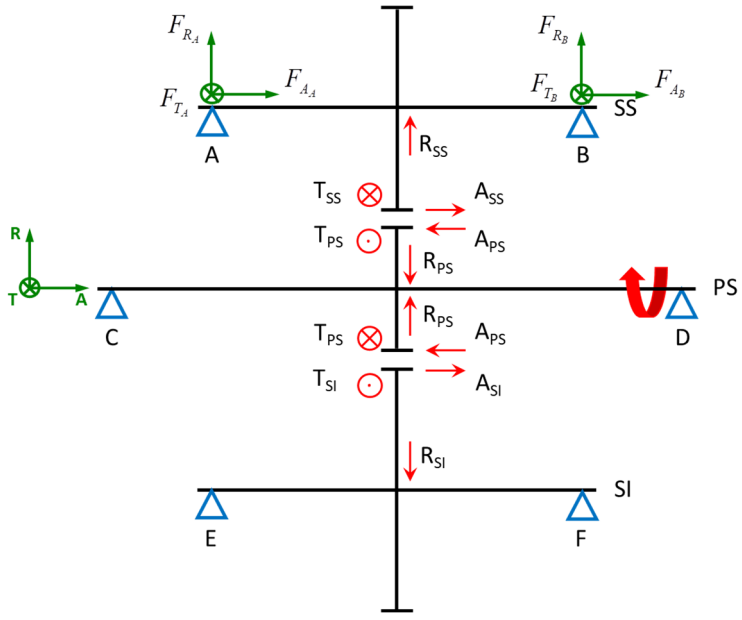

Figure 3.7 – Forces between primary and secondary shafts.

An example of the calculation process is reported below, applying it to the upper secondary shaft (SS) using the set of Eq. (3.6):

$$\begin{cases} \sum_{i=1}^{N}\left(A_{SS_i} r_{p_i} + R_{SS_i} d_i\right) + F_{R_B} l = 0 \\ \sum_{i=1}^{N}\left(R_{SS_i}\right) + F_{R_A} + F_{R_B} = 0 \\ \sum_{i=1}^{N}\left(T_{SS_i} d_i\right) + F_{T_B} l = 0 \\ \sum_{i=1}^{N}\left(T_{SS_i}\right) + F_{T_A} + F_{T_B} = 0 \end{cases} \tag{3.6}$$

where r_{p_i}, and d_i are the pitch radius and the distance between centre of the gear and the bearing on the left (called "A" in Figure 3.7), respectively, of all the gears that are mounted on the upper secondary (SS) shaft, while T_{SS_i}, R_{SS_i}, and A_{SS_i} are the forces on the i^{th} gear of the SS shaft, Finally, F_{R_A}, F_{R_B}, F_{T_A} and F_{T_B} are the reaction force of the bearing A (on the left) and B (on the right) in the two radial and tangential direction.

As regards the differential, in addition to the forces between pinions of the two secondary shafts and the differential crown, it is necessary to calculate the axial force A_{hs}, due to the bevel gears inside the differential, starting from the tangential force T_{hs}, and using Eq. (3.7)

$$T_{hs} = \frac{\left|T_{mesh_{hs}}\right|}{r_{p_{hs}}}\ ,\ A_{hs} = 2T_{hs}\tan\alpha_c \cos\gamma \tag{3.7}$$

where, $r_{p_{hs}}$ is the pitch radius, α_c is the pressure angle, and γ is the semi-pitch conical angle of the bevel gear, while $T_{mesh_{hs}}$ is the torque of each half-shaft of the vehicle, namely the torque available at the wheels.

Finally, the total axial load must be distributed among the two rolling bearing, placed on the left and right side of each shaft, and with the hypothesis of an X mounting, it has been split in accordance with the equations reported in the SKF manual for rolling bearing [85].

3.4 Methodology for gearbox housing acceleration computation

The developed methodology, for the assessment of Dual Clutch Transmission vibrations during gear shifts, is based on the capability to predict through numerical simulation a typical dynamic quantity, then used to objectively evaluate the vibrational behaviour of a gearbox during the tested manoeuvres. The acceleration of a point on the external surface of the gearbox housing is assumed as the dynamic quantity for the NVH assessment. Moreover, the proposed

methodology can be effectively used to analyse and investigate from the NVH perspective, the effect of different transmission layout (e.g. a different geometrical disposition of the transmission shafts in the gearbox or a different number and disposition of meshing gears in the space). In addition to this, also bearings location, gearbox housing design, gears macro-geometry parameters could be effected by a design change, as well as backlashes, rotating parts inertia and drag torques. Thus, using the same methodology a sensitivity analysis on some gearbox parameters could be carried out, highlighting the effects of these uncertainty paraments on the dynamic response of transmission, in terms of NVH performance.

The proposed methodology starts from the results of the Amesim simulation, namely from the three components of the bearing reaction forces, which are post processed in Matlab environment.

3.4.1 Model assumption and model FRF

The methodology is based on the knowledge of gearbox Finite Element Model (FEM) and its inertance FRFs, between the single component of acceleration, evaluated in the measurement point, in X, Y, Z directions, and the reaction forces of the bearing, in each direction of the global reference frame. Thus, the inertance $A_{j,k}(\omega)$ is evaluated using Eq. (3.8):

$$A_{j,k}(\omega) = \frac{\ddot{x}_j(\omega)}{F_k(\omega)} \tag{3.8}$$

where j correspond to the DOF where the acceleration is evaluated, and k is the DOF where the force is applied.

The FEM model, developed in Nastran by the company that produces the gearbox, includes the engine and the assembled powertrain transmission, and it is considered as a MDOF linear system, with free-free boundary conditions, that well reproduce engine mounts. This could be considered as a good approximation, in the mid to high frequency range, since engine mounts create a very soft connection between the powertrain and the vehicle chassis. About 300 modes have been detected in the frequency range 0÷4000 Hz, with 50 modes in the first 1000 Hz. Moreover, the nonlinear torsional inner dynamics of the transmission is considered as the only source of the gearbox housing vibration. Instead, the inner dynamics of the transmission is not influenced by the gearbox housing vibration. Hence, this one-way coupling ensures the application of the proposed methodology to evaluate the gearbox housing acceleration as a post-processing tool respect to the simulation results. In Figure 3.8 the measurement point (P) for the gearbox housing acceleration is depicted, and the positions of bearings on primary shaft (C-D), upper secondary shaft (A-B), lower secondary shaft (E-F), and differential (G-H) are represented, as well. The location of point P in the FE

model has been chosen by the gearbox company to have comparable data with the experimental one, already acquired in previous experimental campaign. The development of the FE model is only a further step in the detection of critical NVH issues.

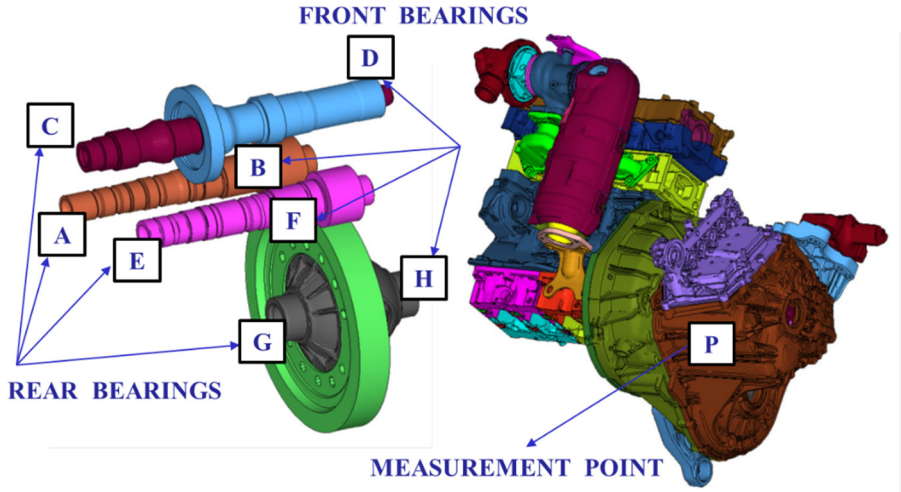

Figure 3.8 – Location of bearings and acceleration measurement point.

The right-handed global reference frame, depicted with black unitary vectors in Figure 3.6, correspond to the same reference system of the gearbox CAD model.

The auto-inertance FRFs between the X direction of the acceleration and the X direction of each bearing are represented in Figure 3.9

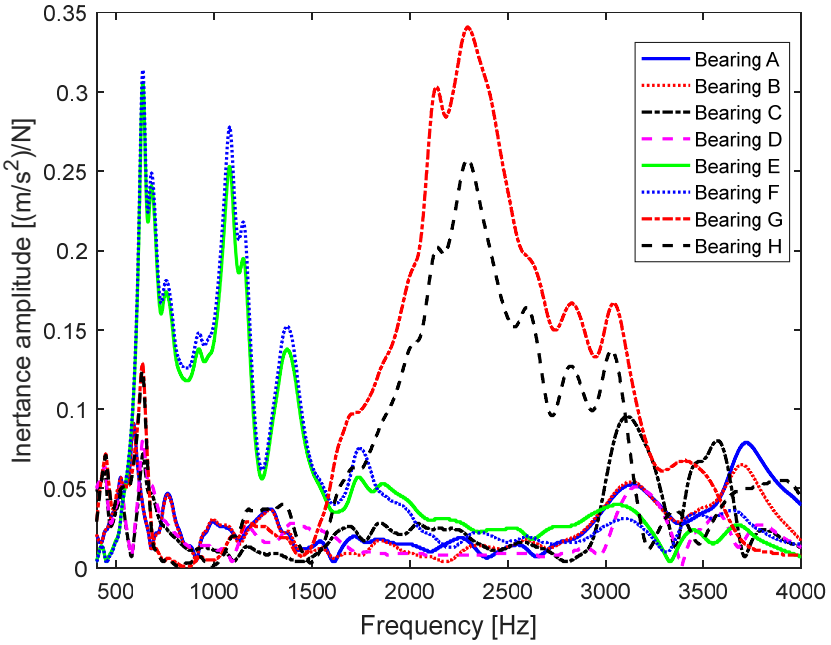

Figure 3.9 – Auto-inertances between acceleration in X direction and bearing forces in X direction.

From the auto-inertances in X direction, it is possible to get an information about the axial dynamics of the gearbox, namely about the synchronisation and gear engagement/disengagement dynamics of the transmission. In details it is possible to appreciate that the gearbox vibration in X direction mainly depends on the reaction forces of the two bearings in the lower secondary shaft (E-F), for frequencies below 1500 Hz, while at higher frequencies the reaction forces on the bearings on the differential (G-H) have a significant participation factor.

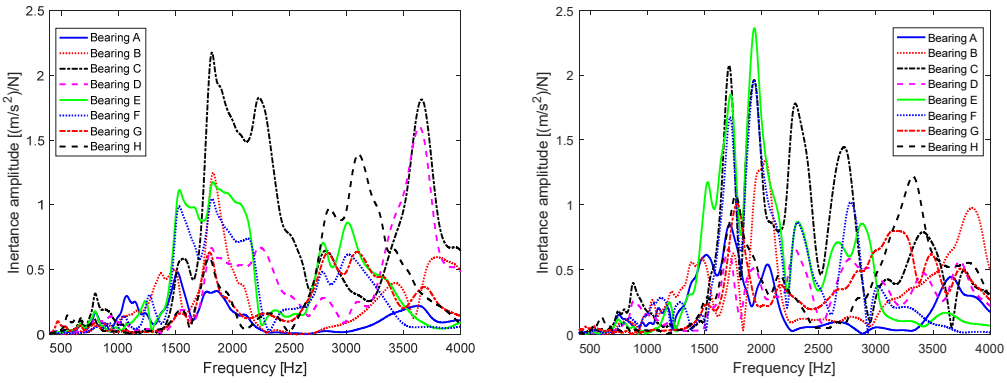

Figure 3.10 – Auto-inertances between acceleration and bearing forces in Y (left) and Z (right) directions.

Finally, in Figure 3.10, auto-inertances between acceleration and bearing forces in Y and Z direction are represented, and the trend of both FRFs reveals high peaks in the frequency range above 1500 Hz.

3.4.2 Procedure for methodology application

The aim of the described methodology is the evaluation of gearbox acceleration from inertances of the FEM powertrain model. In the previous section the FEM gearbox model has been assumed as linear, thus the response of the system can be computed through the time-domain convolution of the excitation (reaction forces on bearings) and the system impulse response (from FEM inertance FRFs). The impulse acceleration response is evaluated using the Inverse Fast Fourier Transform (IFFT) of the system inertance FRFs, as reported in Eq. (3.9), to switch from frequency to time domain:

$$\ddot{h}(t) = IFFT\left(A_{j,k}(\omega)\right) = \frac{1}{2\pi}\int_{-\infty}^{+\infty} A_{j,k}(\omega)\, e^{i\omega t} d\omega \tag{3.9}$$

where $A_{j,k}(\omega)$ is the inertance FRF and ω is the excitation frequency. Then, the time-domain convolution of the impulse acceleration response $\ddot{h}(t)$ is evaluated using Eq. (3.10):

$$a(t) = \ddot{h}(t) * F(t) = \int_0^{+\infty} \ddot{h}(\tau) \cdot F(t-\tau)\, d\tau \tag{3.10}$$

where $a(t)$ is the time history of acceleration and $F(t)$ in the time history of the bearing forces, obtained from the simulation. The procedure is applied for each direction of all eight bearings to evaluate the three components of the gearbox housing acceleration. Therefore, all the inertance FRFs, combined with the bearing forces are used to evaluate the multiple-input single-output (MISO) dynamic response of the gearbox system.

The procedure can be summarised as an application of the superposition principle since the assembled powertrain model is assumed as linear. The acceleration response is evaluated using:

$$\begin{Bmatrix} a_X \\ a_Y \\ a_Z \end{Bmatrix} = \begin{bmatrix} a_X/F_{X_A} & \cdots & a_X/F_{X_H} & a_X/F_{Y_A} & \cdots & a_X/F_{Y_H} & a_X/F_{Z_A} & \cdots & a_X/F_{Z_H} \\ a_Y/F_{X_A} & \cdots & a_Y/F_{X_H} & a_Y/F_{Y_A} & \cdots & a_Y/F_{Y_H} & a_Y/F_{Z_A} & \cdots & a_Y/F_{Z_H} \\ a_Z/F_{X_A} & \cdots & a_Z/F_{X_H} & a_Z/F_{Y_A} & \cdots & a_Z/F_{Y_H} & a_Z/F_{Z_A} & \cdots & a_Z/F_{Z_H} \end{bmatrix} \begin{Bmatrix} F_{X_A} \\ \vdots \\ F_{X_H} \\ F_{Y_A} \\ \vdots \\ F_{Y_H} \\ F_{Z_A} \\ \vdots \\ F_{Z_H} \end{Bmatrix} \tag{3.11}$$

where, a_X, a_Y, a_Z are the components of gearbox housing acceleration at measurement point, while the elements inside the matrix are related to the inertance FRFs, but are not them (since FRFs are in frequency domain), and the last vector contain all the directions of the bearing forces.

3.5 Gearshift simulated manoeuvres

The non-linear lumped parameter model developed using Siemens/Amesim software is then validated, comparing the simulation results with experimental manoeuvres, with a series of gearshifts in up-shift (from 1st to 4th gear) and in down-shift (from 4th to 1st). the model is validated using experimental runs with different levels of brake pressure and with a Gas pedal position (GPP) of 20% with respect to the full throttle condition.

As already mentioned, the input parameters of the model are the engine torque, the transmissible torques of the two clutches, the piston displacements of the gearshift hydraulic actuators, and the master cylinder pressure of the braking system. All these data are collected during dedicated experimental test and then are used for the model validation.

In the simulation analysed in this section, the experimental manoeuvre starts with the first gear engaged and both clutches open, and then it counts a series of sequential gearshifts in upshift and downshift, as depicted on the top of Figure 3.11. During the gearshift, and specifically during the cross-shift phase, two

synchronisers are simultaneously engaged: the first one for the off-going gear and the second one for the on-coming gear. In the bottom of Figure 3.11 it is possible to detect that the two trends of simulated (solid red line) and experimental (dash-dot blue line) vehicle speeds are very close each other after a certain number of tuning processes.

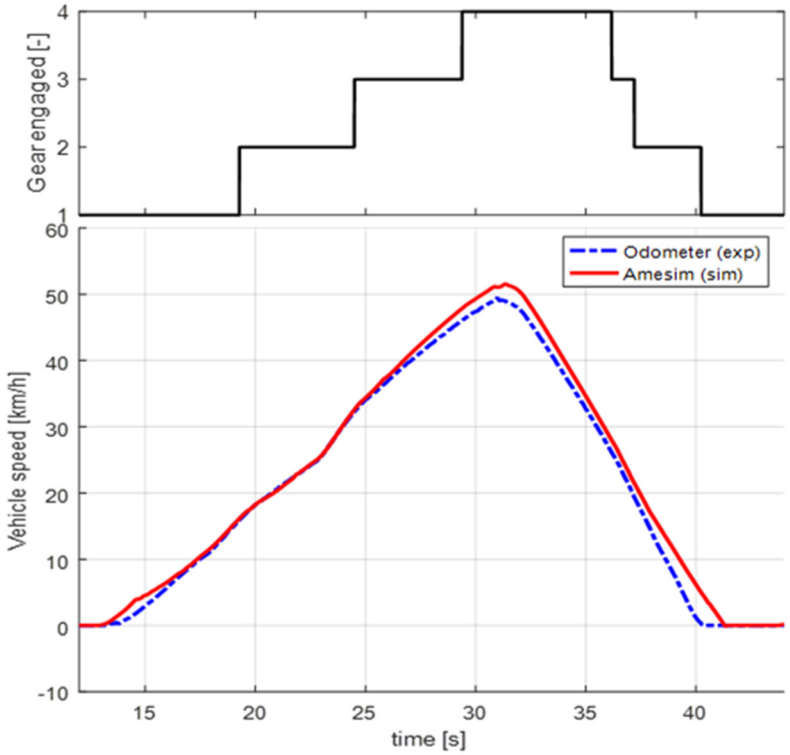

Figure 3.11 – Actual gear engaged (top) and vehicle speed (bottom) during a tested manoeuvre.

In fact, one of the first steps in the model validation was the load correlation, acting on the steady-state resistance parameters, to correctly overlap the low frequency content of simulated results with the experimental ones.

Considering the run-up phase of Figure 3.11, two possible correction way are available. The former consists in the variation of the rolling resistance parameters or of the aerodynamic coefficients, reported in vehicle dynamic equation for longitudinal behaviour of Eq. (3.1), while the latter is based in the addition of a slope road to the Amesim model. This last way is adopted to have a bidirectional constant effect (positive and negative slope depending on the necessity).

Instead, as regards the deceleration phase, the other preliminary issue was the estimation of a gain g between the master cylinder pressure p, and the total braking torque T_B applied to the wheels, due to the lack of knowledge of the exact parameters of the vehicle braking system installed on the tested car. The total braking torque on front and rear wheels is evaluated using:

$$T_B = g\,k\,p = g\left[2\mu_{dyn}N\left(A_f r_f + A_r r_r\right)\right]p \tag{3.12}$$

where, μ_{dyn} is the dynamic friction coefficient, N is the number of active friction surfaces, A and r are respectively the brake piston area and the brake mean radius for front (subscript f) and rear (subscript r) axles.

So, if the real vehicle to test changes, it is possible to quickly modify the model to adapt the simulated manoeuvre to the real experimental test case.

3.5.1 Gearshift events producing acceleration peaks

The measurement of the gearbox housing acceleration allows the detection and recognition of the main events of transmission inner dynamics. Thus, analysing the acceleration time history, the gear-shift noise can be recognised.

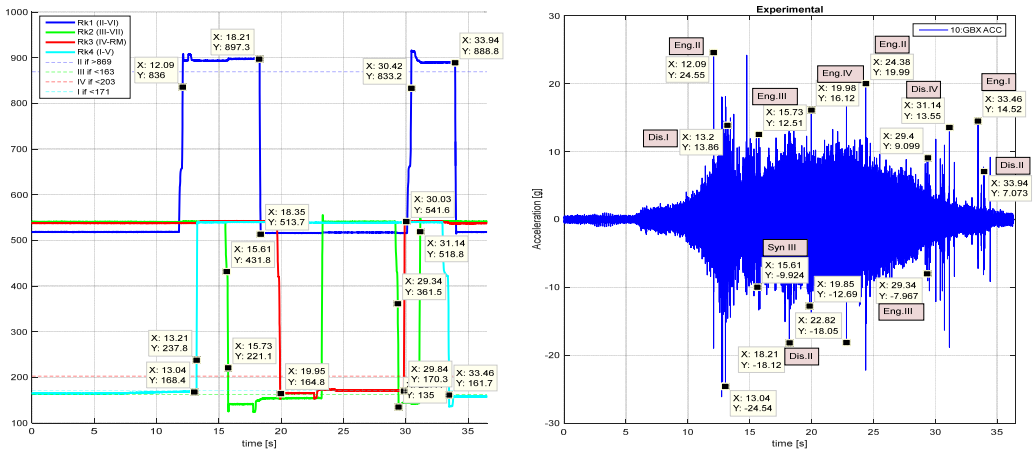

Figure 3.12 – Position of hydraulic actuators (left) and gearbox housing acceleration (right) during an experimental test run.

There are five different events that produce potential NVH issues. The higher acceleration peaks, as perceivable from Figure 3.12 (right), can be correlated to: 1) gear engagement, 2) gear disengagement. The detection of the two phenomena has been done comparing the position of the hydraulic actuators (Figure 3.12 (right)) with the time history of the acceleration, in which the labels identify the peaks associated uniquely with the gear engagement and disengagement.

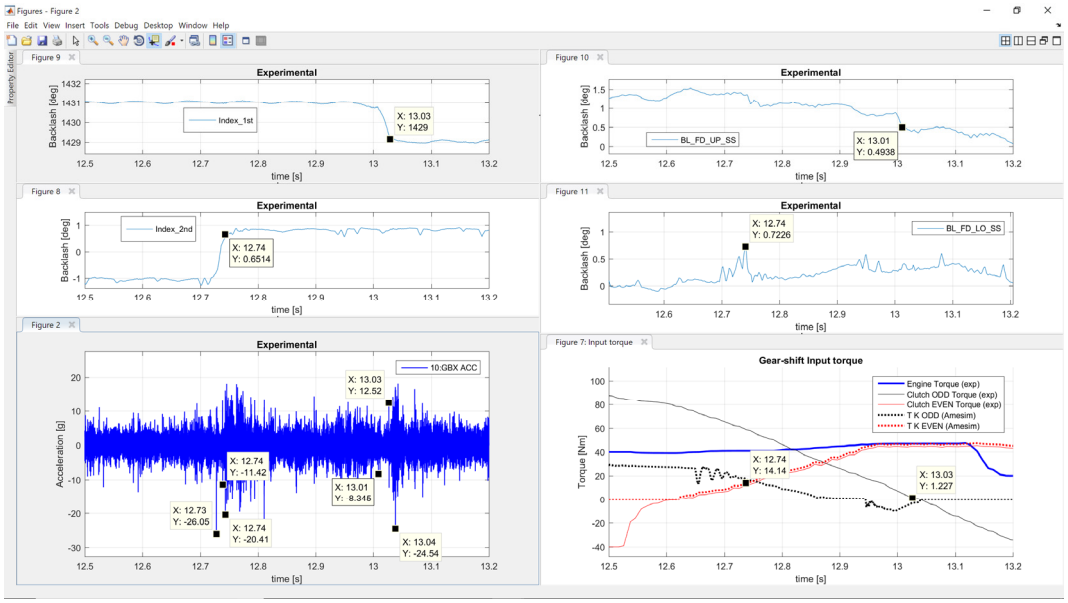

Figure 3.13 – Inner dynamics events during cross-shift from 1st to 2nd.

Instead, other smaller acceleration peaks are due to the 3) start of engagement of the on-coming clutch during cross-shift, to the 4) end of engagement of the out-going clutch during cross-shift, and to the 5) zero-crossing of torque on an active (engaged) transmission path (kiss/touch point).

In Figure 3.13, the cross-shift from 1st to 2nd gear is analysed to detect the inner dynamic events related to the smaller acceleration peaks. There is a step change in the variables *index 2nd* (a measure of the backlash in the 2nd gear synchroniser) and *index 1st* (a measure of the backlash in the 1st gear synchroniser). In detail, these steps are due to the start of loading on the on-coming transmission path (even gear clutch and primary shaft) and to the end of loading on the off-going transmission path (odd gear clutch and primary shaft).

Even if the analysis of transmission inner dynamics could be a bit complicated, it is essential for the proper evaluation of acceleration peaks.

3.5.2 Synchronisation phase: simulated results

In the previous section the acceleration peaks of an experimental test run are compared with gear engagement/disengagement and clutch engagement/ disengagement. In this section simulated events inside the synchroniser are commented and discussed.

In Figure 3.14 (left) the time histories of the synchroniser sleeve axial position, and displacements of ring and plunger, are represented, while on the right side the angular speed of secondary shaft, synchroniser ring and idle gear during the synchronisation phase are depicted.

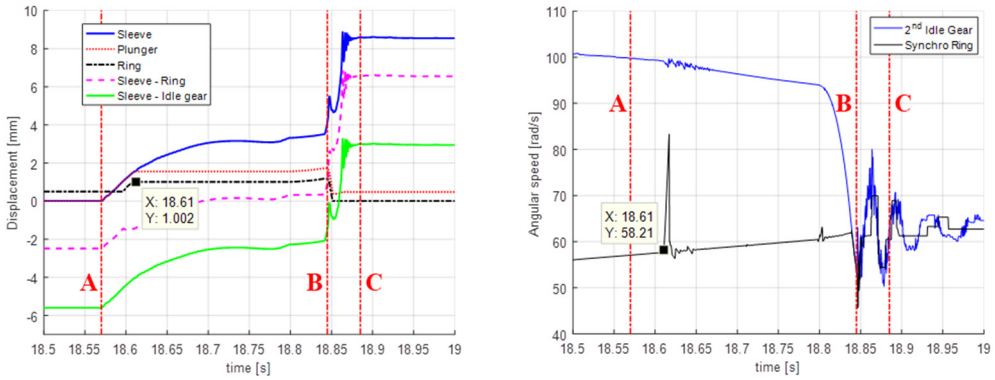

Figure 3.14 – Axial positions (left) and angular speed (right) of synchroniser elements during synchronisation phase.

Moreover, events reported in the previous Figure happen during the 2nd gear engagement, and as highlighted, the three dash-dot red vertical lines corresponds to certain moments of the synchronisation phase, marked with A, B, and C letter.

At instant A, the pre-synchronisation phase starts, and the sleeve moves the plunger against the ring, then the ring rotates under the action of the friction torque between the friction cones and start to lock the axial movement of the sleeve. Then, the synchronisation phase happens. At instant B, the free-flying starts, during which the sleeve can continue its travel towards the idle gear. This event finishes with a series of import shocks, often called “double bumps”, and the gear deviation phase can start. Finally, at instant C, there is the beginning of the lock-up phase when the sleeve dogs finish their run passing through the gear ones, achieving the gear coupling, which is preserved thanks to back angle on dogs teeth.

Meanwhile, from a torsional point of view, the synchroniser ring has a sudden acceleration, generated by the synchronisation torque, and stops when it reaches the end-stop position on the hub. Then, the idle gear angular speed starts to decrease because of the friction torque between the cones reaching the synchroniser hub rotational speed.

In Figure 3.15, the radial forces of the bearings mounted on the two secondary shafts is reported, with a specific detail of the gearshift phase, that include synchronisation and clutch engaging phases.

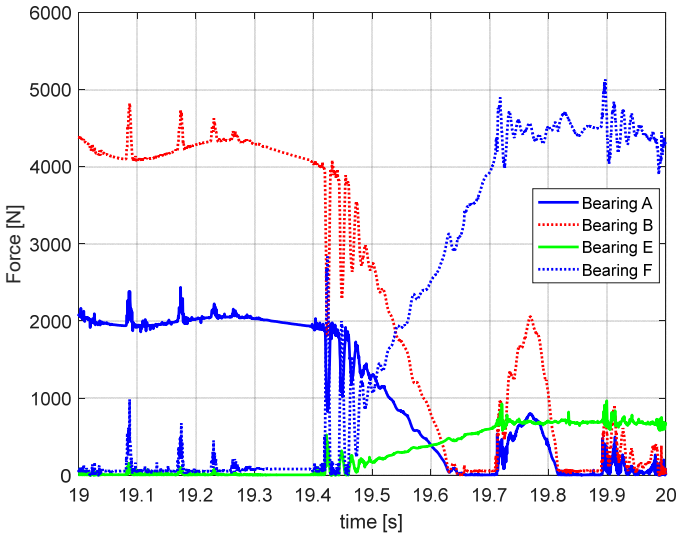

Figure 3.15 – Radial forces on bearing of upper (A-B) and lower (C-D) secondary shafts.

The intersection between bearing forces corresponds to the time instant when the cross-shift of the clutches happens. The forces generated by the assembled transmission driveline are firstly absorbed by the bearings mounted on the upper secondary shaft, where the 1st driven gear is fitted, and then by the bearing of lower secondary shaft, where the 2nd driven gear is mounted.

The methodology, described in § 3.4, for the evaluation of gearbox housing acceleration is applied to the simulated results. The acceleration time history is reported in Figure 3.16 (left), in which the main peaks are correlated to the torsional events inside the transmission during the 2nd gear engagement (red), 3rd gear engagement (green) and 4th gear engagement (yellow). The peaks of acceleration are clearly distinguishable respect to the experimental results (noise due to road and engine). The comparison for the model validation could be only qualitative, due to many uncertainties as the inertance FRFs of the gearbox, rigid hypothesis for the transmission shafts and for the open loop application of experimental inputs. Other numerical differences can be correlated to other model assumptions and simplifications, mainly adopted to reduce computational costs.

From Figure 3.16 (right), where the time history of engine, primary and secondary shafts angular speeds are represented, the higher acceleration peaks happen during the gearshift procedure as highlighted by the coloured areas. The secondary shafts angular speeds are reported to the primary shaft using the gear ratio of the corresponding gear. So, when the curve representing the PS speed is overlapped with a curve of the SS speed multiplied by the transmission ratio, it means that the gear associated to the specific ratio is engaged. For sake of clarity, the coefficients $tau(1)$, $tau(2)$ and so on, reported in the legend of Figure 3.16 (right), corresponds to the gear ratio of 1st, 2nd gears, namely to the ratio between the angular speed of the primary shaft and the speed of the corresponding secondary shaft when that gear is engaged.

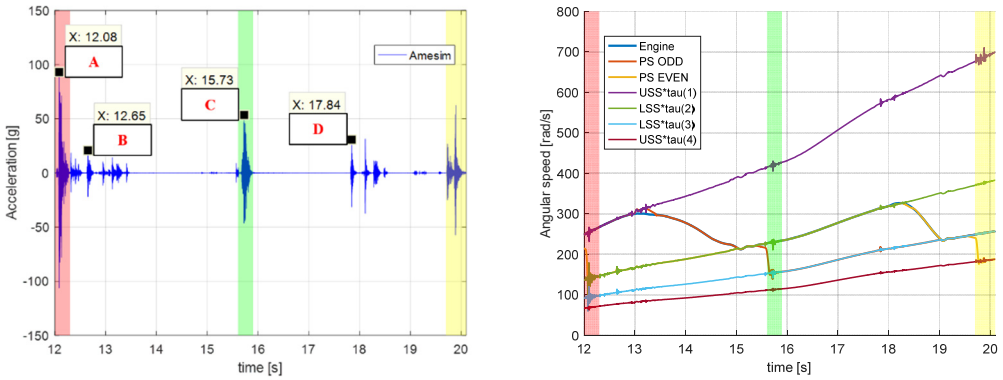

Figure 3.16 – Simulated acceleration of gearbox (left) and speed of driveline shafts (right) during up-shifts.

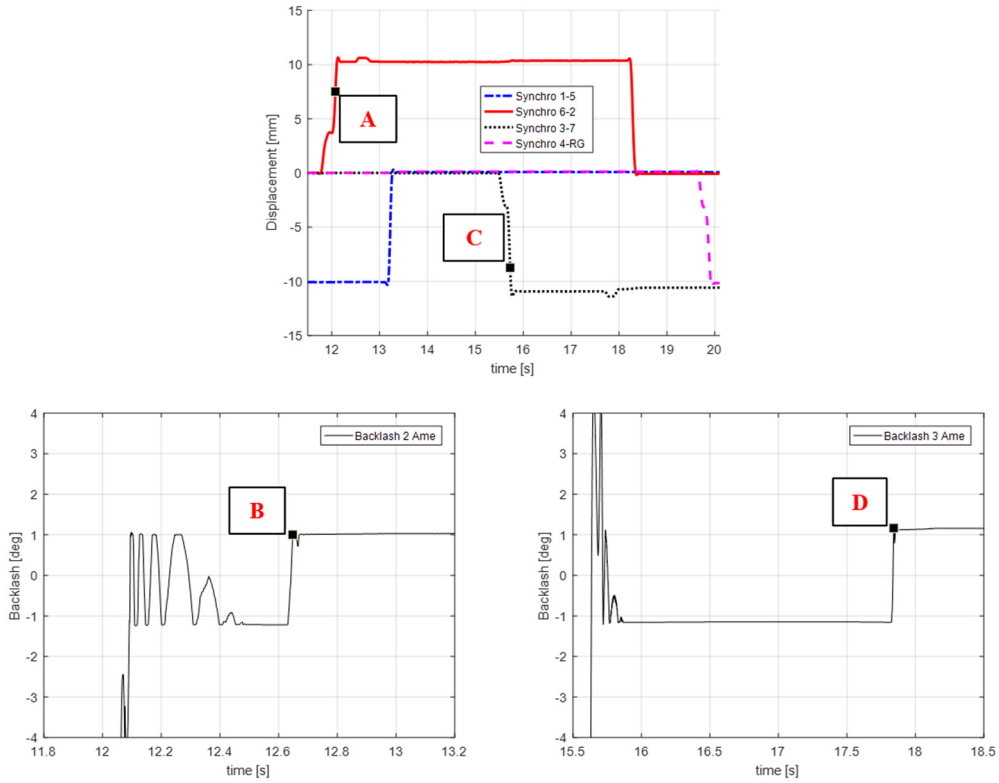

Figure 3.17 – Inner events of transmission dynamics causing acceleration peaks during up-shift manoeuvre: synchroniser displacement (top) and backlashes inside synchronisers of 2nd gear (bottom-left) and 3rd gear (bottom-right).

All the acceleration peaks are correlated to an inner event of the DCT gearbox. In fact, as regards for the main peaks, signed as A and C, they are due to gear-shift forks displacements during the gear engagement of 2nd and 3rd gears, causing axial impacts between sleeve and idle gear dog teeth.

The other two peaks, signed as B and D, are related to the recovery of the torsional backlashes in the synchroniser sleeve during the cross-shift phase, when a positive torque is applied and the contact between sleeve and idle gear occurs on the other teeth flank, as reported in Figure 3.17.

Moreover, the proposed approach could be used to analyse and estimate possible improvements in the transmission driveline, or for comparative analyses, in which different design solution are evaluated in terms of gear-shift noise.

3.6 Improvement of NVH performance: a sensitivity analysis on gear inertias

Several possible improvements of NVH performance are available acting on the transmission parameters, as on geometry parameters, backlashes, disposition of the transmission shafts inside gearbox case. The way adopted in this section consists in a sensitivity analysis on the inertia of gears. The improvements are evaluated using the proposed methodology, which is applied to the simulated results. Two different indices, as peak to peak amplitude comparison or the root mean square (RMS) of acceleration in a certain interval time, are used for the assessment of clunk severity, comparing acceleration results with the normal production (NP) ones. For the peak-to-peak amplitude comparison, only the highest peaks, inside the coloured areas of Figure 3.16 (left) representing the engaging phases, are considered. From the same Figure the most critical gear engagement is the 1st to 2nd, thus the idea is applying inertia modification on the idle gear, mounted on the secondary shaft, of 2nd gear.

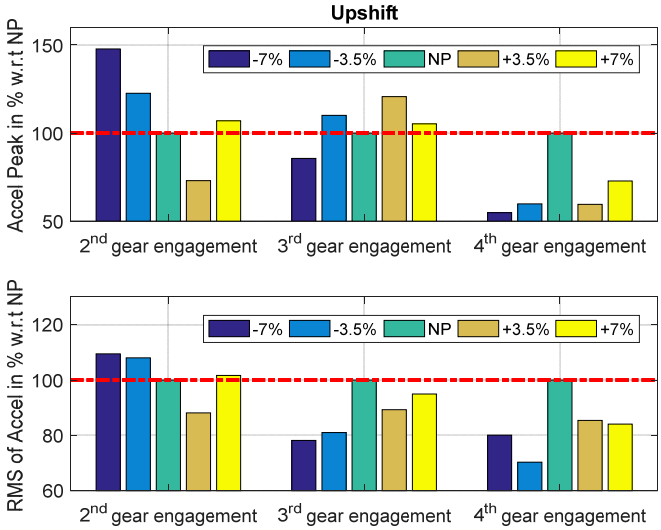

Figure 3.18 – Effects of 2nd idle gear inertia modification during up-shift phase.

All the simulation results are summarised in Figure 3.18, where it is possible to note that inertia reduction of the 2nd gear of both 7% and 3.5% improve the 2nd to 3rd and the 3rd to 4th gear-shifts worsening the 1st to 2nd gear-shift. Moreover, on the other side, an increase of inertia of 3.5% improve the 2nd and 4th gear engagement worsening the 3rd one.

Finally, an excessive inertia increment up to 7% leads to a worsening of the 2nd and 3rd gear engagement, even if an improvement in the 4th gear engagement occurs.

As already mentioned, the gear-shift from the 1st to 2nd is the more critical for the clunking noise and therefore the inertia sensitivity analysis is aimed at improving that specific gearshift. During the 4th gear engagement, the NP condition is the worst, although all the acceleration peaks are smaller than those in the others gear engagements.

The sensitivity analysis is performed for the downshift phase, as well, and results are reported in Figure 3.19. The trend of the peak analysis of 2nd gear engagement is very similar between the upshift and downshift phases, with an improvement for an inertia increase of 3.5% and a worsening for inertia reduction.

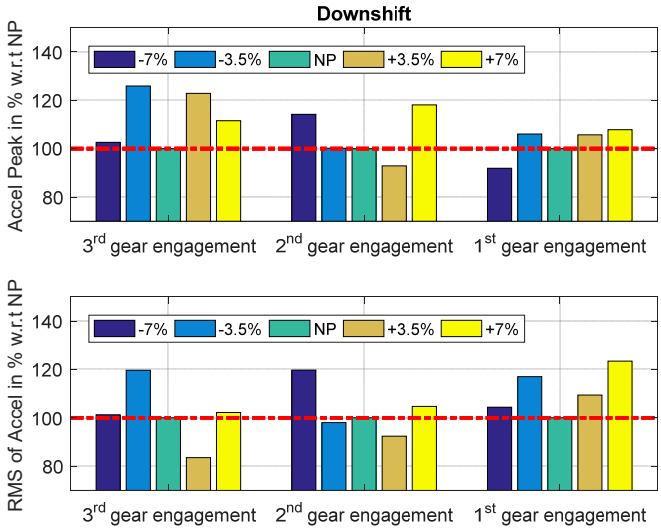

Figure 3.19 – Effects of 2nd idle gear inertia modification during down-shift phase.

Instead, as regards the 3rd gear engagement, the NP configuration is the optimal one in both manoeuvres, with a small worsening for ±3.5% inertia modification of the 2nd gear.

From a dynamic point of view, a lower inertia of the 2nd idle gear increases its mobility, thus its tendency to accelerate. Considering the end 2nd gear engagement, namely when the synchroniser sleeve impacts against the dog teeth of the lightened idle, higher rotational acceleration leads to higher velocity impacts, hence to higher gearbox housing acceleration peaks.

To give substance to the previous statement, the effect of the inertia reduction of the preselected 2nd idle gear during the engagement of 3rd gear, placed on the same secondary shaft, must be considered.

The 3rd gear engagement provokes a series of shocks, which propagate through the 3rd gear synchroniser to the lower secondary shaft. As consequence, the shaft accelerates or decelerates, and other shocks are generated and propagated to the 2nd gear synchroniser. Thus, the higher the inertia of the idle gear the

higher the risk of NVH issues because the resistance applied during impact, namely the inertia torque, becomes higher.

Instead, during a gear disengagement, the axial displacement of the sleeve is less hindered when moving from sure engaged position to the neutral one if the inertia is lower. The dynamics of the unloaded primary shaft is driven by the drag torques, so a preload in the contact between the teeth is applied and the shaft tends to decelerate in this phase. After that, when the torque is re-applied to the incoming primary shaft during cross-shift, a lower idle gear inertia implies lower energy impacts between the teeth flanks (of the driving and driven gear). The idle gear considered is the one related to the actual gear engaged.

The analysis of the gearbox inner events causing acceleration peaks, reported in Figure 3.16 (left) for the NP configuration has been performed also with the 2nd idle gear inertia reduction of 7%. Comparing the NP results with Figure 3.20, during this upshift manoeuvre an inertia reduction leads to positive benefits for the cross-shift noise, and for the 3rd gear engagement noise, even if a worsening in the 2nd gear engagement happens.

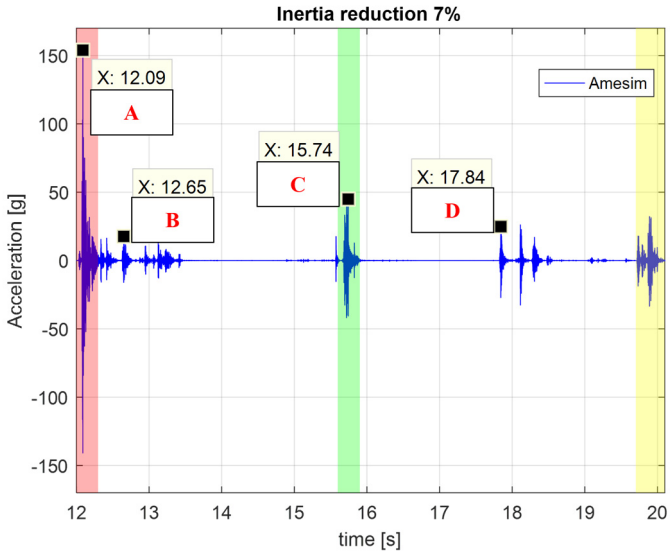

Figure 3.20 – Simulated acceleration peaks due to inner events with 2nd idle gear inertia reduction of 7%.

Moreover, the accelerations peaks in this last simulation have been compared with the experimental tests of the corresponding manoeuvre. From Figure 3.21 it is highlighted that inertia reduction of 7% has a similar effect in experimental and simulated results. The improvement over NP (normal production configuration) is more evident in the experimental data than in the simulation, except for the 2nd gear engagement, in which the worsening with respect to NP is greater in the simulated results. The good match between experimental and simulated results is primarily due to the high level of detail of the physical model, developed in Amesim, that is able to describe the main internal dynamics of the gearbox involved in the gearshift noise generation.

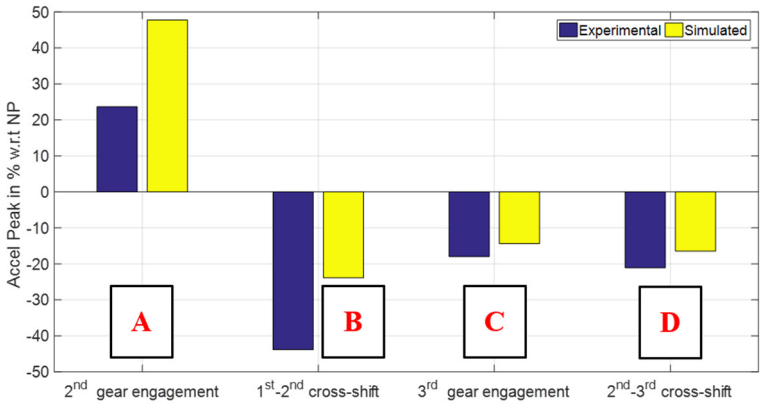

Figure 3.21 – Comparison of experimental and simulated results with 2nd idle gear inertia reduction of 7%.

Finally, improvements in NVH performance with an inertia reduction of 7% of both experimental and simulated results agree with the subjective scores given by a professional driver to the several inner events (gear engagement or cross-shift) during the experimental tests.

3.7 Conclusions

The meticulous analysis of the inner events of a transmission driveline corresponds to a root cause analysis of NVH issues and it is very important to understand how to act, during the design stage, for the improvement of transmission issues. The most critical events producing impact in the driveline are highlighted and discussed starting from experimental data and then using simulation results.

Moreover, a customised nonlinear lumped parameters model, able to detect all the main events of gear-shift events, is fundamental for the further application of the proposed methodology, used for the assessment of the gear shift noise in a Dual Clutch Transmission, but able to perform any appropriate comparison with different design solutions of a transmission.

It has been highlighted that during a gearshift manoeuvre, the noise issues are significantly affected by the gear engagement/disengagement, clutch engagement/disengagement and load reversal that produce acceleration peaks well correlated to the subjective noise perception in the car.

The post processing tool of the proposed methodology allow the evaluation of the gearbox housing acceleration starting from the bearing forces. The peak value of the acceleration time history, used as metric for the clunking noise assessment, provided a useful instrument to compare the instantaneous and localized impact in the transmission.

Finally, a sensitivity analysis on gear inertia parameter has carried out, highlighting possible improvements in NVH performance.

Chapter 4

4. From mechanical to magnetic gears

In § 3 several NVH issues of automotive transmissions have been analysed and a lumped parameter model of a DCT gearbox has been developed to analyse gearbox inner dynamics during the most critical phases, proposing a sensitivity analysis on uncertain transmission paraments, which dynamic effects are discussed in § 2, through a two-step methodology for the assessment of NVH performance.

Even if the classical transmissions maintain several advantages, regarding transmission reliability, maximum transmissible torques, the analysis of NVH issues could be considered as the main reason to explore new transmission solutions, finding a feasible alternative to mechanical transmission in the field of magnetic gears (MGs).

As for the conventional mechanical gears, the MGs are structures used for several power transmission applications, allowing torque transmission between two or more coupled movers: the former corresponds to the power source, rotating at a certain speed, while the latter is the output shaft, rotating at the same or at different angular speed, due to a certain gear ratio, depending on specific geometrical parameters.

The main advantage, deriving from the possible adoption of a MG, is the possibility to transfer torque between two mechanical axles in a contactless way, avoiding wearing of the corresponding traditional gears in contact, and necessary of lubrication. Moreover, a largely noise reduction is expected, together with the reduction of maintenance.

4.1 Review on magnetic gears

The interest in magnet gear of academic and industrial researcher rapidly increased during the new millennium, with a continuous technological development, which brings magnetic gears very close to commercial applications.

In the last two decades, different topologies have been proposed to improve performance in terms of maximum transmissible torque.

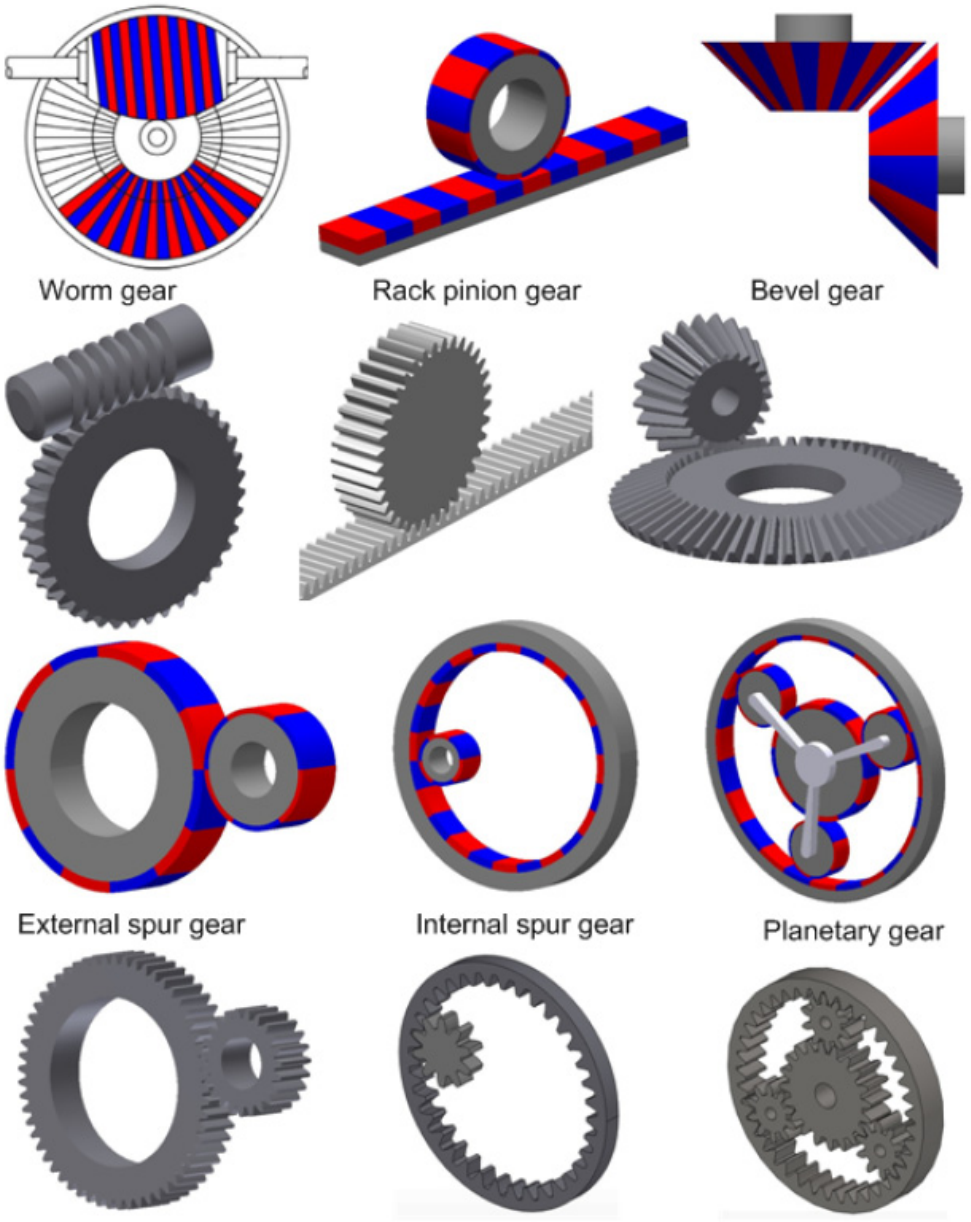

Figure 4.1 – Topological solutions of magnetic and mechanical gear.

The first ever work on the topic of MGs is Armstrong's patent [86] in 1901, in which he proposed the invention to improve power-transmitting devices, by means of magnetic forces. His idea was put coils on the teeth of a conventional mechanical gear, to generate a magnetic field, able to transfer torque between driving and driven wheel.

Instead, the first work, where the magnetism is related to permanent magnets (PMs) is dated in 1941 with Faus' patent [87] on magnetic gearing.

Moreover, in 1968 Martin proposed in his patent [88] a magnetic drive similar to a planetary mechanical gear. It was made of three elements having a common axis of revolution, namely an outer ring with PMs, an intermediate planet ring having a plurality of substantially radial magnetically permeable bars, and an inner rotor with PMs.

During these decades, the research on MGs was mainly focused on the spur type [86,87,89–92] and worm type [93,94] topologies. It can be said that for each mechanical topology, the corresponding magnetic solution could be designed and realised. A collection of the several topologies of mechanical and magnetic gears has been done by Tlali et al. in [95], which result is reported in Figure 4.1, where worm gears, bevel gears [96], rack-pinion gears, external and internal spur gears, and planetary gears [35] are represented. In this last paper the authors evaluated the torque density of the PMG, proposing a sensitivity analysis on the number of magnetic planets. From simulations, the evaluated torque density was close to 100 kNm/m^3 with six planets and about half in case of three planetary gears, namely using the MG arrangement reported in Figure 4.1 as planetary gear.

Meanwhile, other papers have reviewed MGs, as regards high-performance topologies [97], with a particular attention to computational models and design aspects of coaxial magnetic transmissions [98], or MGs application in EVs [99,100], marine [101] and wind [102] energy industries, or their integration in permanent-magnet electrical machines [103,104].

Unfortunately, the interest in this new technology was limited since their performance, especially in terms of torque density, were limited, hence MG technology was not able to compete with the traditional mechanical gears, discouraging researchers in dealing with this topic.

Finally, in 2001 Atallah's work [21] has represented the turning point in the industrial and academic research, proposing a new topological solution for a planetary magnetic gear, as reported in Figure 4.2, equipped with NdFeB magnets, and ferromagnetic poles, and characterised by a higher torque density exceeding 100 kNm/m^3.

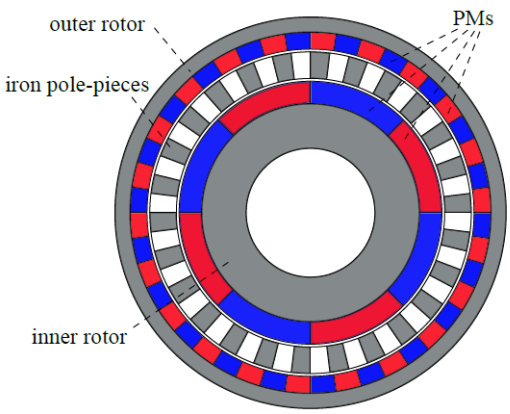

Figure 4.2 – Atallah's PMG with PMs.

Other possible topological solutions, represented in Figure 4.3, are the magnetic screw [105], proposed as a linear actuator, and the trans-rotary magnetic gear [106–108], used to convert the linear motion to rotation or vice-versa. Both rotor and translator are made of ferromagnetic iron cores equipped with skewed alternating PM poles, and the gear ratio is defined by the geometrical properties of the PMs (helix angle and width).

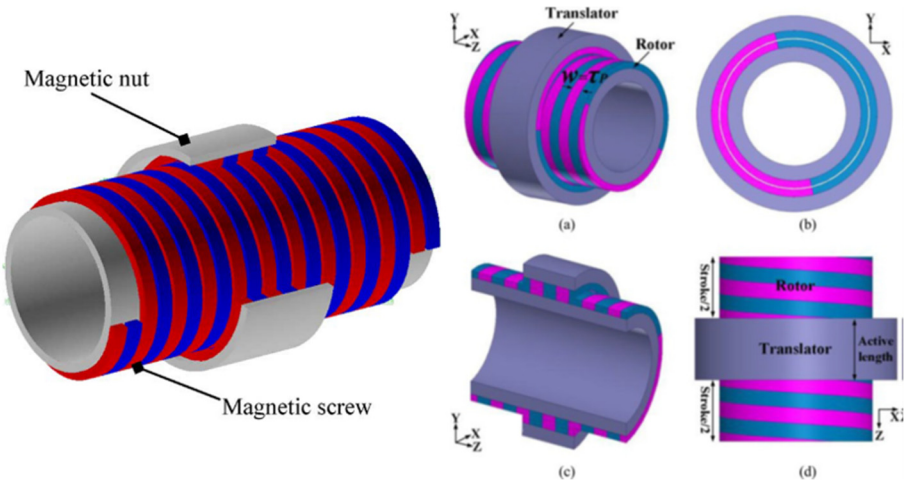

Figure 4.3 – Topology of a magnetic screw (left) and a trans-rotary MG (right).

Instead, to achieve an extreme torque density and a very high gear ratio, the cycloid MG is proposed in [109]. In Figure 4.4 (left) an example of cycloid gear is reported with 44 poles on the outer rotor and 42 poles on the inner one. Even if, the gear ratio seems to be only $44/42 \simeq 1.05$, it is possible to take advantage from the cycloid principle, achieving higher transmission ratio, properly fixing some rotation parts, as highlighted in Figure 4.5.

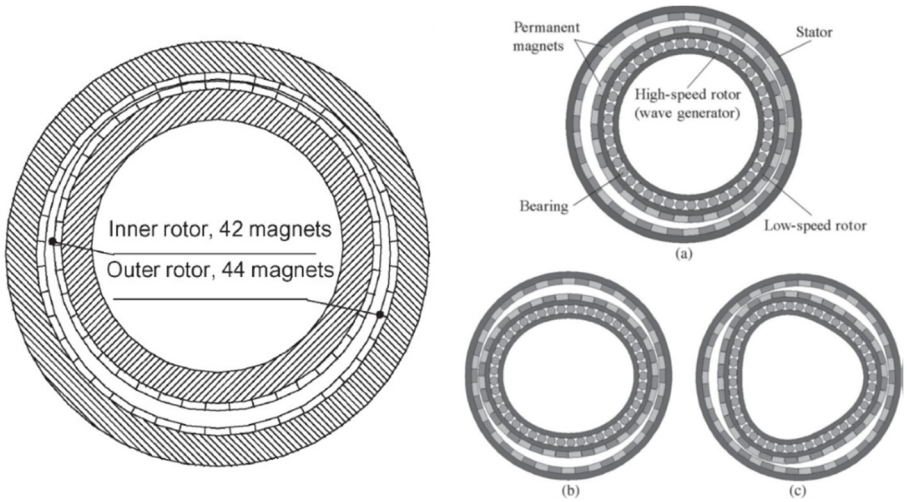

Figure 4.4 – Cycloid (left) and harmonic (right) MGs topologies.

Different solutions, using the magnetic counterpart of a mechanical harmonic gear, are reported in Figure 4.4 (right). It was firstly proposed by a patent in 1995 [110], and then its working principles were clearly explained and demonstrated in

[111]. which working principle. The harmonic MG functioning is based on a mechanism to produce time-varying, sinusoidal variation of the air-gap between a flexible low-speed PM rotor and a rigid PM stator. Even in harmonic gears, high gear ratio could be obtained.

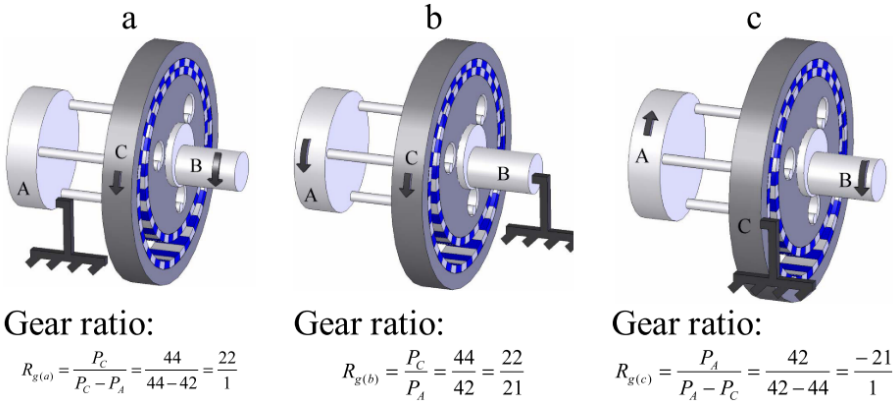

Figure 4.5 – Different working configurations for a cycloid MG.

All the previous presented topologies of MGs are characterised by a radial distribution of magnetic flux. In Figure 4.6 (left) an axial-field magnetic gear is reported. It was proposed in [112] and it is particularly suitable for applications which require a hermetic isolation between the input and output shafts. A torque density higher than 70 kNm/m^3 can be achieved, from simulation, although the axial forces are relatively low. Instead, in Figure 4.6 (right), the design of a linear concentric MG is proposed. It is used as a linear magnetic actuator [113], with a highly competitive force density, in which the inner and external elements are subjected to an axial translation.

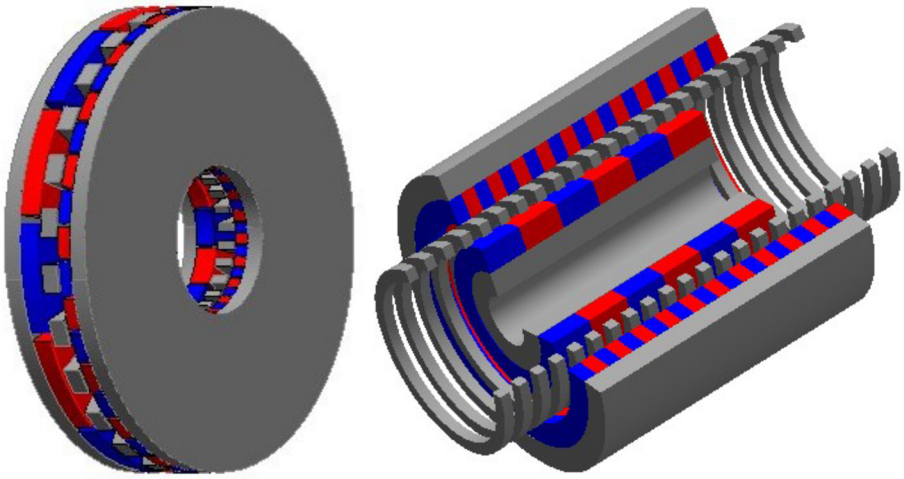

Figure 4.6 – Axial-field (left) and linear-concentric (right) MGs topologies.

For all these MGs topologies, and even for many others studied by researchers in these years, different working principle have been developed. Moreover, several design analyses approaches have been used to evaluate mechanical and electromagnetic properties of the MGs.

4.2 Mechanical and magnetic planetary gears: dynamic principles

The research activity of this PhD is based on a specific magnetic gear topology. In fact, only the planetary solution will be considered from now on, hence in this section a comparison between PMG and the mechanical counterpart is proposed, analysing the kinematic relations and dynamic principle behind mechanical and magnetic solutions. Similar comparative studies between the two solutions have been already proposed during these years [114,115].

4.2.1 Mechanical planetary gear train

Before introducing planetary gears, it is necessary to clarify which is the main difference between am ordinary gear train and a planetary gearbox. In the former the axes of the gears have always the same position in the space during their rotation, while in a planetary gear train these axes could change their spatial position during certain working conditions. An example of mechanical planetary gear train is reported in Figure 4.7. It is composed of a sun gear, a ring gear and three or more planet gears, revolving around the sun gear. The planets are typically mounted on a carrier, which rotates relatively to sun and ring gears.

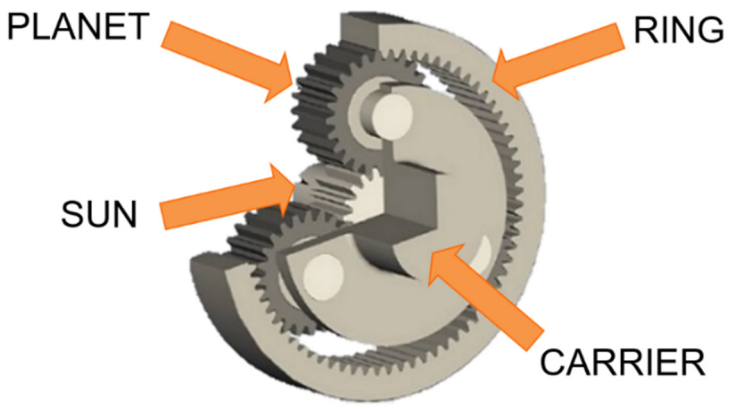

Figure 4.7 – Elements of a mechanical planetary gear train.

Planetary gear train are often used when space and weight are an issue, but a large amount of speed reduction and torque are needed. Thus, their main advantages are a high-power density, and a large gear reduction in a small volume. Several possible kinematic combinations are available, properly fixing some elements.

A planetary gear train consists of 2 DOFs, hence in order to completely define its kinematic relations it is necessary to know the rotational speed of at least two elements (for example sun and ring) and then evaluate the other velocity (carrier).

The kinematic relationship between the angular rotational speeds ω_s, ω_r, and ω_c of sun, ring and carrier, respectively, can be evaluated using a global reference system centred in the carrier. Therefore, according to this reference frame, the gear train is considered as ordinary and the gear ratio is evaluated using Willis relation for planetary mechanical gear [116]:

$$\tau = \frac{\omega_s - \omega_c}{\omega_r - \omega_c} \tag{4.1}$$

where τ is the current gear ratio. According to Eq. (4.1), it is possible have two inputs and one output or generally the gear train is consider as ordinary. In this last case, its basic value $\tau_{s/r}$, between sun and ring, is evaluated when the carrier is fixed, according to:

$$\tau_{s/r} = \tau_{s/p} \cdot \tau_{p/r} = -\frac{Z_p}{Z_s}\frac{Z_r}{Z_p} = -\frac{Z_r}{Z_s} \tag{4.2}$$

where $\tau_{s/p}$ is the gear ration between sun and planets and $\tau_{p/r}$ is the gear ratio between planets and ring. The basic gear ratio $\tau_{s/r}$ depends on the geometrical properties of the gears, namely from the number of teeth of the sun gear Z_s and of the ring gear Z_r. The minus sign means that sun and ring rotates at two opposite rotational speeds. Moreover, for any planetary system with three planets the following relation between gear teeth must be satisfied:

$$Z_r = Z_s + 2Z_p \tag{4.3}$$

where Z_p is the number of teeth of the planet gear. As already mentioned, a planetary gear train system has different operating modes, which depends on the input and the output elements. All the six possible configurations are listed in Table 4.1..

Table 4.1 – Planetary gear train configurations.

Gear ratio $\tau_{in/out} = \omega_{in}/\omega_{out}$	**Input**	**Output**	**Fixed**
$\tau_{s/r} = \tau$	sun	ring	carrier
$\tau_{r/s} = 1/\tau$	ring	sun	carrier
$\tau_{s/c} = 1 - \tau$	sun	carrier	ring
$\tau_{c/s} = 1/(1-\tau)$	carrier	sun	ring
$\tau_{c/r} = \tau/(\tau - 1)$	carrier	ring	sun
$\tau_{r/c} = (\tau - 1)/\tau$	ring	carrier	sun

From Eqs.(4.2)-(4.3), the range for τ, for a single stage mechanical planetary gear is defined by Eq. (4.4):

$$-\infty < \tau < -1 \tag{4.4}$$

4.2.2 Magnetic planetary gear

The introduction of a magnetic gear in a power transmission driveline offers several potential benefits, including the physical isolation between the prime mover and the secondary one, reduction of noise and vibration levels, protection against overload and mainly contactless torque transmission.

The magnetic equivalent of the mechanical planetary gear train is shown in Figure 4.8. It consists of an inner rotor with n_s permanent magnets pole pairs, an outer rotor with n_r pole pairs, and an intermediate rotor with q ferromagnetic steel poles. The three rotors are respectively the equivalent of sun, ring, and carrier of the mechanical planetary gear train. Moreover, in a PMG the contact of the teeth of gears in the mechanical counterpart is replaced by the modulation of the magnetic fields generated by the inner and outer magnetic rotors through the carrier element.

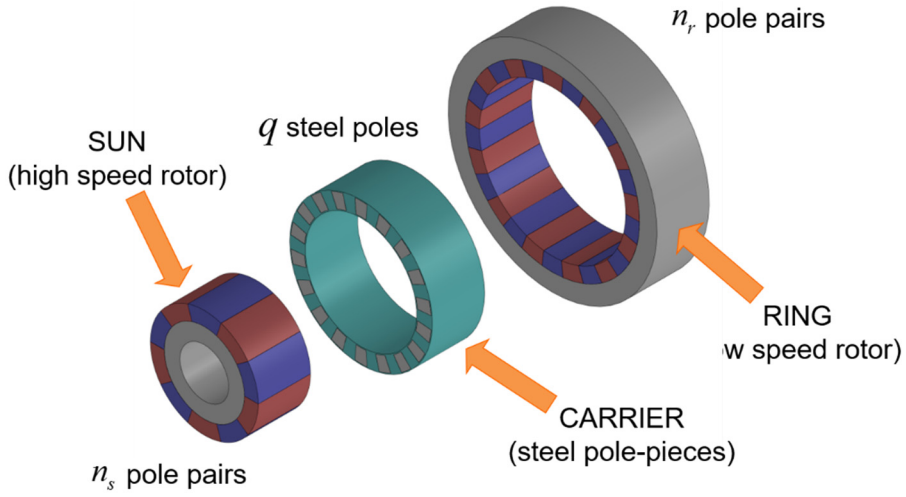

Figure 4.8 – Elements of a planetary magnetic gear.

It has been proved by Atallah et al. [22] that the highest torque transmission capability, between two rotors at a different rotational speed, is achieved when:

$$q = n_s + n_r \tag{4.5}$$

The PMG ratio between inner and outer rotor is given by:

$$G_{s/r} = \frac{\omega_s - \omega_c}{\omega_r - \omega_c} = -\frac{q - n_s}{n_s} = -\frac{n_r}{n_s} \tag{4.6}$$

As for the mechanical planetary gear train, several operating modes are available for the PMG, properly fixing one of the three elements. All the six possible configurations are listed in Table 4.2.

Table 4.2 – Planetary magnetic gear configurations.

Gear ratio $G_{in/out} = \omega_{in} / \omega_{out}$	**Input**	**Output**	**Fixed**
$G_{s/r} = -\frac{n_r}{n_s}$	sun	ring	carrier
$G_{r/s} = -\frac{n_s}{n_r}$	ring	sun	carrier
$G_{s/c} = \frac{q}{n_s}$	sun	carrier	ring
$G_{c/s} = \frac{n_s}{q}$	carrier	sun	ring
$G_{c/r} = -\frac{q}{n_r}$	carrier	ring	sun
$G_{r/c} = -\frac{n_r}{q}$	ring	carrier	sun

Hence, in PMGs the number of PMs pole pairs and the number of ferromagnetic steel poles assume the same role of number of teeth, in mechanical gear train, to define the gear ratio.

4.3 PMG applications

The magnetic gears have a large market for their application. They could be used in several sector where it is necessary to replicate a mechanical gear train with a magnetic one.

4.3.1 Pseudo direct drive

One of the most interesting application is their implementation in low speed electrical machine application, where it is common to connect a high-speed machine together with a mechanical gearbox, due to weight/size and cost effective. In this application, MGs can be used in replacing of the mechanical gearbox, or they can be integrated in an electrical machine to create a pseudo direct drive (PDD) machine, as proposed by Atallah et al. in [117].

In a PDD the external PMs pole pairs are mounted on the internal bore of the stator of an electrical brushless machine, while the magnetic fields generated by the windings are used to move the high-speed inner rotor, where the inner PMs pole pairs are mounted. The torque generated by the inner rotor is then increased

through the magnetic gear and transported out by the low-speed ferromagnetic rotor. In Figure 4.9 the integrated magnetic gear in a brushless machine is reported.

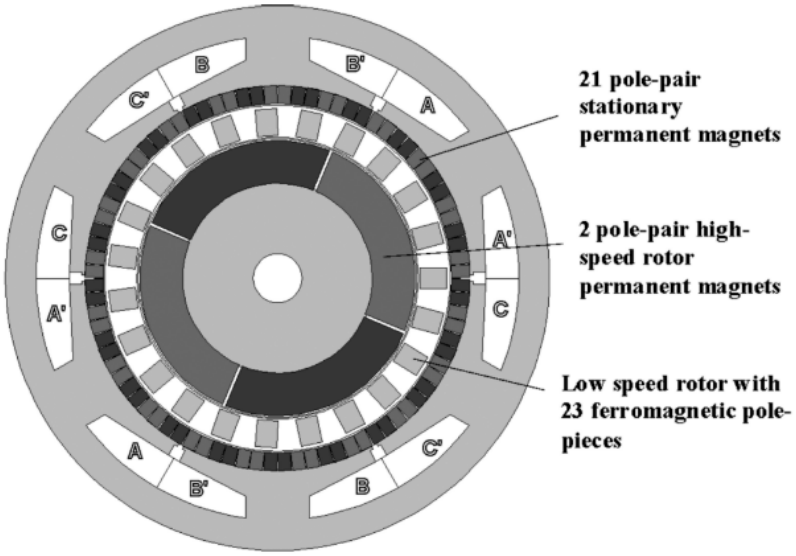

Figure 4.9 – Pseudo direct drive machine.

Finally, Atallah has shown that a torque density over 60 kNm/m^3 could be achieved from a naturally air-cooled machine, with a power factor of 0.9 or higher.

4.3.2 Continuous variable transmission

The PMGs consist of three concentric rotors. In Table 4.2, it has been seen that the PMG act in a fixed-ratio mode, locking usually the permanent-magnet rotor having the higher number of poles, namely the outer rotor, or the ferromagnetic rotor, in order to maintain the inner rotor as high-speed rotor.

However, another way to use the PMGs is varying the speed of the third rotor [118–120], achieving a magnetic continuous variable transmission (mCVT). Atallah et al. proposed in [39] a magnetic power split device, integrated with a brushless permanent-magnet machine, which works as a mCVT. It is proposed for different application, as a component of a wind turbine drivetrain or as component of a hybrid vehicle driveline.

The possible implementation of a mCVT has been also investigate by Mao et al. in [121], proposing a multi-objective optimisation tool to improve torque, energy efficiency and torque ripple of the mCVT implemented in the hybrid driveline.

4.3.3 Power split device of Toyota Prius

The Toyota Prius is a full hybrid electric vehicle developed by Toyota and manufactured by the company since 1997 with different release. In particular, the production of the first release occurred in years ranging from 1997-2003, while the second generation was developed and produced in the years from 2004-2009, coming to the third-generation production in 2010.

Before introducing the description of Toyota Prius drivetrain, it can be useful provide a brief overview of the main common configuration used for HEVs, as proposed in a review on topological architectures for HEVs [122] by Emadi et al.

In HEVs, two or more sources of power/energy are combined to achieve the required power necessary to propel the vehicle. These vehicles combine the ICE power with an electric traction motor, which is powered by an energy storage device, generally known as battery pack. The most common configurations to couple the two different power sources are generally the parallel hybrid, the series hybrid, and a combined series-parallel architecture.

In a series configuration the ICE generally run at an optimal efficiency point to drive the generator and charge the battery pack. When the state of charge (SOC) of the battery is at the fixed minimum, the ICE turns on recharging the battery. It is important to note that in this case the ICE is not connected to the wheel and so the power is supplied to the wheels only by the electric motor. A simplified scheme is reported in Figure 4.10

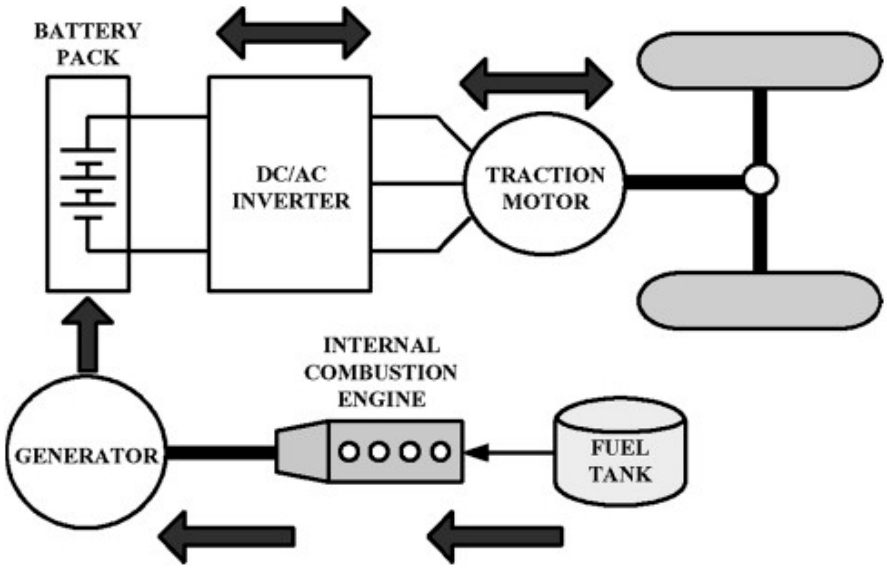

Figure 4.10 – Layout of a series HEV drive train.

In a parallel configuration both ICE and electric motor, as depicted in Figure 4.11, are connected with the transmission and thus it is possible to choose the best combination in order to have the required amount of torque at any given time. The most common strategy in this configuration is to use the motor alone at low speeds since it is more efficient than the ICE, while use only the ICE at higher

speeds A parallel HEV can also equipped with a CVT, instead of a fixed transmission.

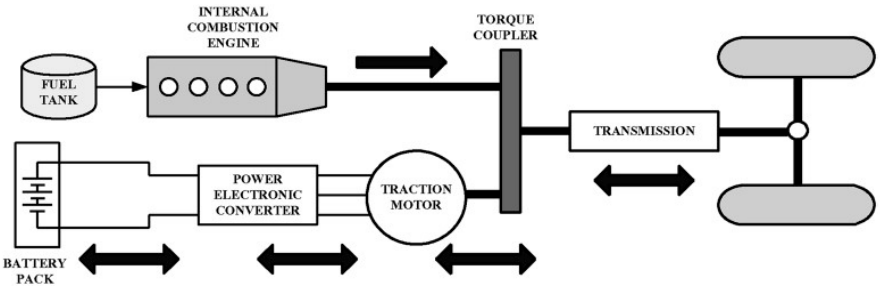

Figure 4.11 – Layout of a parallel HEV drive train.

The configuration of major interest is reported in Figure 4.12 and it consists in a combination of series and parallel architectures. The heart of the Hybrid Synergy Drive (HSD) is a simple little device called Power Split Device (PSD), which is the connection element of this configuration and allows to combine the advantages of both series and parallel HEV layout. The electrical motor is used to give power to the wheel, especially at low vehicle velocity, while at higher velocity different contribution of the two sources of power are possible.

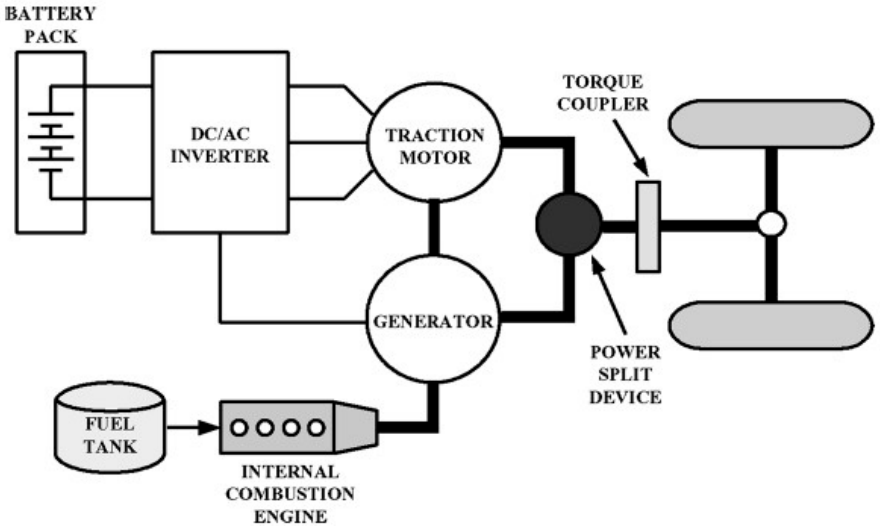

Figure 4.12 – Layout of a Series-Parallel combined HEV drive train.

Coming back to Toyota HEVs, the PSD is a planetary gear set that acts as a CVT but with a fixed gear ratio. The overall functionality of the 2010 Prius eCVT, shown in Figure 4.13, is similar to the 2004 Prius, even if there are significant differences on the number of planetary gear set involved. In both systems the sun gear of the planetary gear is connected to the generator with a hollow rotor shaft, through which a shaft connected to the ICE passes and connects to the planetary carrier. The ring of the planetary gear is connected directly to the motor output in the 2004 Prius, and to the motor through a high-speed reduction gear in the 2010 Prius. More information on the two different

architectures are reported in the technical reports of the two vehicle releases [123,124].

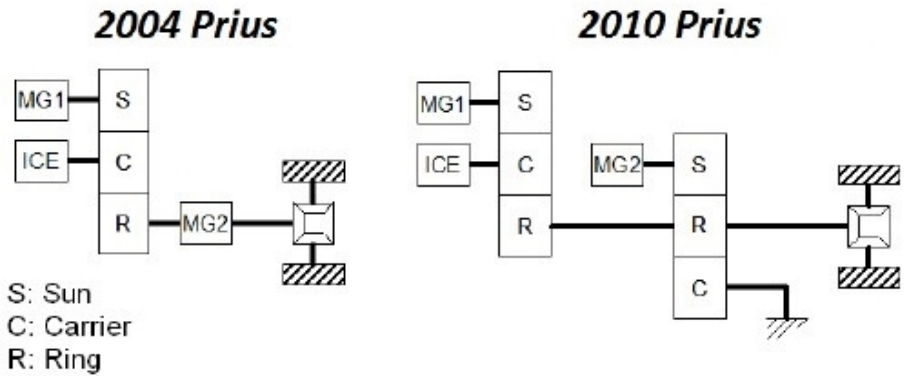

Figure 4.13 – Mechanical diagram of 2004 Prius, 2010 Prius gear systems.

In this section only the 2004 Toyota Prius HSD is investigated to analyse the possible integration of a PMG in his driveline.

The PSD planetary gear train consists of three inputs/outputs: the ICE, the generator that is a permanent magnet synchronous machine called MG1 and a motor/generator called MG2 that is connected to the wheels through reduction gears and differential. In the Prius driveline, the sun gear generally rotates at high speeds and is connected to the rotor of the MG1 generator. Moreover, the planetary carrier is connected to the ICE, while the outer ring, that is the output of the device, is connected to the MG2 motor and thus to the wheels.

Finally, the PSD even allows the smaller between the two Motor/Generators, namely MG1, to act as a starter for the ICE, eliminating another component of a traditional gasoline engine. In Figure 4.14 more details about the number of teeth of the gears are presented.

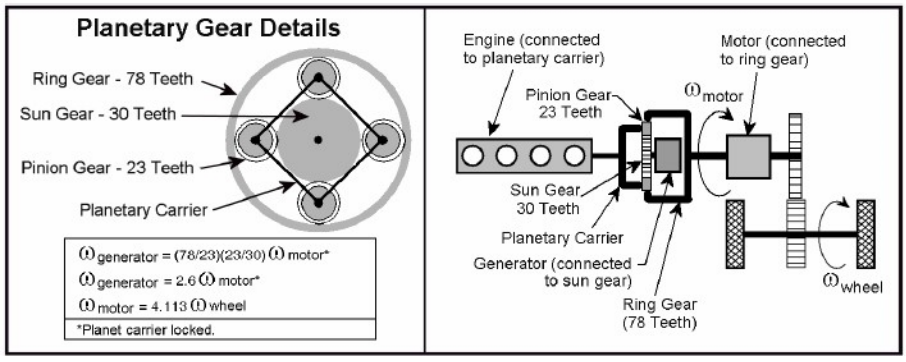

Figure 4.14 – Diagram of the 2004 Prius power split device.

It could be interesting present also an overview about the specification of the main components of Toyota Prius highlighting the differences and the developments between 2004 and 2010 generation. Technical data are listed in Table 4.3.

Table 4.3 – Specification for Toyota Prius components.

Component	Property	Value Prius 2004	Value Prius 2010
Engine	Type	1.5 Liter gasoline	1.8 Liter 4-cylinder
	Maximum output	57 kW @ 5000 rpm	73 kW
	Maximum torque	115 Nm @ 4200 rpm	-
Battery	Type	Nickel-metal hydride	Nickel-metal hydride
	Voltage, amperage	201.6 V, 6.5 Ah	201.6 V, 6.5 Ah
	Power output	20 kW	27 kW
Traction motor	Maximum output	50 kW @ 1200-1540 rpm	60 kW
	Maximum torque	400 Nm @ 0-1540 rpm	207 Nm
System	Maximum output	82 kW @ 85 km/h and higher	100 kW
	Maximum torque	478 Nm @ 22 km/h or lower	-

In the Toyota Prius eCVT only an increasing of the MG2 rotational speed has a resulting effect in changing the vehicle speed, considering the gear ratio between MG2 and the wheels. On the other side, an ICE speed variation does not directly affect the wheel speed. The ICE can rotates faster or slower, depending on how much power is needed, and the car can always reach the desired speed properly combining the speed of ICE, MG1 and MG2 keeping the ICE running at the most efficient rate possible. Instead, MG1 has a maximum rate of 10.000 rpm in either direction (positive or negative) but is limited to a maximum of 6.500 rpm. ICE rotation is limited to speeds between 1.000 rpm and 4.500 rpm. It can also stop completely, but anything between 0 and 1 000 will force the slider up or down. This happens because the internal combustion engine cannot effectively operate below that speed. The hybrid control logic stop the ICE when the driver does not need more power and start it again when he needs more power, or higher speed from MG1.

Another important step is to understand the working principle of the PSD, proposing a kinematic and dynamic study. An HEV is subjected to several operating modes during its use. Hence, assuming that that the ICE is connected to the carrier, the electric motor MG2 to the ring and the generator MG1 to the sun, the power and the torque available for the wheel are evaluated using the Eqs. (4.7) -(4.8) and also considering the appropriate transmission gear ratios:

$$T_C + T_R - T_S = T_{wheel} \tag{4.7}$$

$$P_C + P_R - P_S = P_{wheel} \tag{4.8}$$

where the different subscripts are referred to the three elements of PSD: sun, carrier, and ring. Instead, all the operating modes are summarised in Table 4.4.

Table 4.4 – Operating mode of PSD in a HEV.

Configuration	**Speed** ω			**Torque** T			**Power** P		
	S	**C**	**R**	**S**	**C**	**R**	**S**	**C**	**R**
Full Electric	$\neq 0$	$=0$	$\neq 0$	$=0$	$\neq 0$	$+T_R$	$=0$	$=0$	$+P_R$
Full ICE	$=0$	$\neq 0$	$\neq 0$	$\neq 0$	$+T_C$	$=0$	$=0$	$+P_C$	$=0$
Battery Re-charge	$\neq 0$	$\neq 0$	$=0$	$-T_S$	$+T_C$	$\neq 0$	$-P_S$	$+P_C$	$=0$
Hybrid (Electric+ICE)	$\neq 0$	$\neq 0$	$\neq 0$	$-T_S$	$+T_C$	$+T_R$	$-P_S$	$+P_C$	$+P_R$
Regeneration	$\neq 0$	$=0$	$\neq 0$	$=0$	$\neq 0$	$-T_R$	$=0$	$=0$	$-P_R$
Startup	$\neq 0$	$\neq 0$	$=0$	$+T_S$	$-T_C$	$\neq 0$	$+P_S$	$-P_C$	$=0$

The possible adoption of a PMG in the mechanical transmission driveline leads to several advantages and some drawbacks.

The first advantage is related to the possibility of transferring torque in a contactless way, avoiding wearing of the mechanical parts in contact, reducing noise and other negative effects. In addition, the absence of contact removes the need of a clutch device limiting the maximum stress acting on the system. Moreover, the efficiency of the MGs is theoretically higher than using mechanical gear train.

On the other hand, to get the same mechanical performance, in terms of torque transfer capability, the volumes of mechanical and magnetic gears are different: mechanical gears are compact due to the high local force values between teeth while magnetic counterparts must rely of higher lever arm values to transfer torque, so they are usually larger than the classical ones.

A preliminary analysis of the Toyota Prius gearbox has been done to detect its overall dimensions and the dimensions of the PSD. In Figure 4.15 the main components of Prius gearbox are represented with a detail of PSD, which include the crown of the Electric motor MG2.

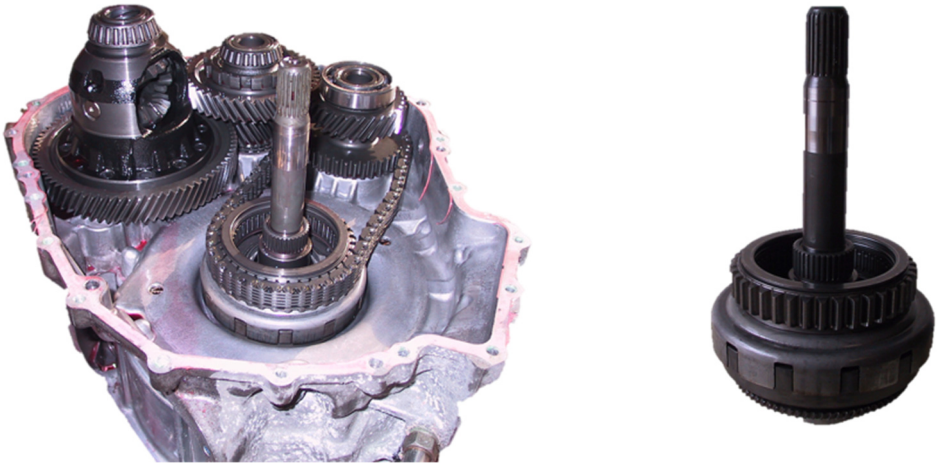

Figure 4.15 – Toyota Prius gearbox (left) with a detail of
PSD and MG2 crown (right).

In Figure 4.16 the assembled PSD is reported, with a detail of the PSD external ring.

Figure 4.16 – Toyota Prius PSD (left) and ring of PSD (right).

Finally, in Figure 4.17, two details of carrier with the four planets and of the sun gear are reported.

Figure 4.17 – Carrier (left) and sun (right) of Toyota Prius PSD.

After the dimensioning analysis, as already stated, a substitution one to one of the mechanical planetary gear train is very hard to achieve. Indeed, as it is possible to note from Figure 4.18, the dimensions of a preliminary magnetic gear that is able to transfer more or less the same torque of the PSD are higher than the corresponding mechanical counterpart.

Figure 4.18 – Comparison of mechanical and magnetic planetary gear dimensions.

The result reported in the previous figure will be described in the following chapter, where the design process of a PMG, its optimisation, and its dynamic behaviour will be further investigated.

4.4 Conclusions

The magnetic gears have been proposed in this chapter as a non-conventional technology for the torque transmission inside a driveline.

Firstly, several magnetic gears topologies, according to the state-of-art have been presented, highlighting that for each type of classical mechanical transmission it could exist the magnetic counterpart with a largely noise reduction, due to torque transmission in contactless way, together with the reduction of maintenance.

Planetary magnetic gears have been considered as the best topological solution to replicate a mechanical gearing device, including the possibility to have different configuration, so different arrangements as regards the power input/output.

Different possible uses of MGs with already existing applications, as a pseudo direct drive of a mCVT, have been presents.

Moreover, a preliminary analysis on the possible replacement of the power split device of a hybrid vehicle has been performed, concluding that the PMG can transmit the torque requested by the vehicle but, on the other hand this can be done only if a complete redesign of the power transmission driveline is performed. Dimensions and masses of the magnetic gear are in fact, larger than the classical one and must be accommodated in a way different from the present layout.

Chapter 5

5. Design, optimisation, and dynamic simulations of a PMG for powertrain applications

As briefly introduced in section § 4.2.2, the operation principle of the magnetic gear is based on the modulation of the magnetic field, produced by the PMs pole pairs mounted on the inner and outer rotors, using the ferromagnetic poles of the middle rotor.

In this chapter the dynamic and analytical design of a PMG is carried out, to better investigate the possible adoption of magnetic gears in an automotive transmission driveline.

In § 5.1 a planetary magnetic gear with three moving rotors is analysed, in terms of modulation effect, describing its principle of operation.

Then, § 5.2 an optimisation process is carried out maximise the transmitted torque while minimising at the same time the moment of inertia of the rotating parts.

Finally, in § 5.3 torque maps of the optimised PMG are implemented in a block-oriented dynamic model to perform dynamic simulation of a driveline, including a PMG.

5.1 Principle of operation and design

The magnetic gear analysed in this section in reported in Figure 5.1. The number of PMs on sun and ring is chosen to have the same gear ratio $G_r = -5/13 = -2.6$ of Toyota Prius PSD, according to its details reported in Figure 4.14.

The flux density distributions, produced by PMs on both sun and ring rotors at a radial distance r can be written, according to [22], as:

$$B_r(r,\vartheta)=\left(\sum_{m=1,3,5,\ldots} b_{rm}(r)\cos\left(mp\left(\vartheta-\omega_{s,r}t\right)+mp\vartheta_0\right)\right)\times\left(\lambda_{r0}(r)+\sum_{j=1,2,3,\ldots}\lambda_{rj}(r)\cos\left(jq\left(\vartheta-\omega_c t\right)\right)\right) \tag{5.1}$$

for the radial component, while for the circumferential component:

$$B_\vartheta(r,\vartheta)=\left(\sum_{m=1,3,5,\ldots} b_{\vartheta m}(r)\sin\left(mp\left(\vartheta-\omega_{s,r}t\right)+mp\vartheta_0\right)\right)\times\left(\lambda_{\vartheta 0}(r)+\sum_{j=1,2,3,\ldots}\lambda_{\vartheta j}(r)\cos\left(jq\left(\vartheta-\omega_c t\right)\right)\right) \tag{5.2}$$

where p is the generic number of PMs pole pairs, since Eqs. (5.1)-(5.2) can be applied to both sun and ring rotors, q is the number of ferromagnetic poles in the carrier modulating rotor, while $\omega_{s,r}$ and ω_c are the rotational speeds of one of the PMs rotor and of carrier rotor, respectively. Moreover, b_{rm} and $b_{\vartheta m}$ are the Fourier coefficients of the flux density distribution without ferromagnetic poles, while λ_{rj} and $\lambda_{\vartheta j}$ are the Fourier coefficients for the modulating functions of the radial and circumferential components of flux density distribution.

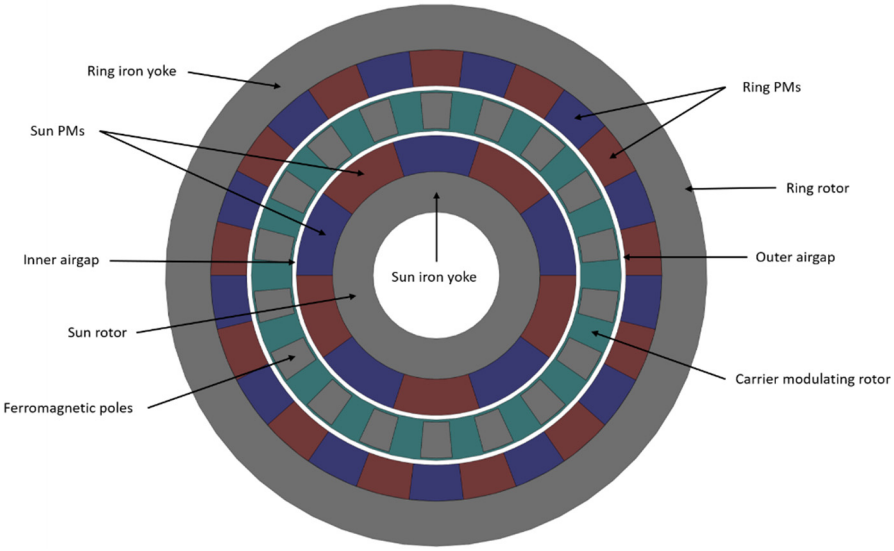

Figure 5.1 – Coaxial planetary magnetic gear structure.

Developing the equations further, the number of pole pairs in the space harmonic flux density distribution can be evaluated from:

$$p_{m,k}=\left|mp+kq\right| \tag{5.3}$$

$$m=1,3,5,\ldots,\infty \tag{5.4}$$

$$k=0,\pm1,\pm2,\pm3,\ldots,\pm\infty \tag{5.5}$$

The Eq. (5.3) is used inside density flux distribution equations to evaluate the modulated field of the inner rotor (with $p = n_s$) or the outer rotor (with $p = n_r$).

As already written in the previous chapter, the number of ferromagnetic poles q, and the number of PMs on sun n_s and ring n_r are linked together by Eq. (5.3).

5.1.1 FEM design

The planetary magnetic gear of Figure 5.1 is sketched and implemented in FEM software, defining all material properties, to evaluate the maximum transmissible torque.

The software used for the design of magnetic problem is FEMM, which is a suite of programs for solving low-frequency electromagnetic problems using 2D planar or axisymmetric domains [125]. The software is made of three different parts, which are better described below.

Pre and post processing tool

The first part of FEMM software is devoted to lay out the geometry of the problem to be solved and for defining material properties and boundary conditions. Moreover, field solutions can be represented using contour and density plots, ad it is possible evaluate different quantities and integrals by a proper user's selection of a region or a point. As it is possible to appreciate from Figure 5.2, where the 2D planar model of the proposed PMG is reported, all material properties of magnets and electrical steel for yokes and ferromagnetic poles are defined. Moreover, the magnetisation direction for PMs on inner and outer rotors is defined.

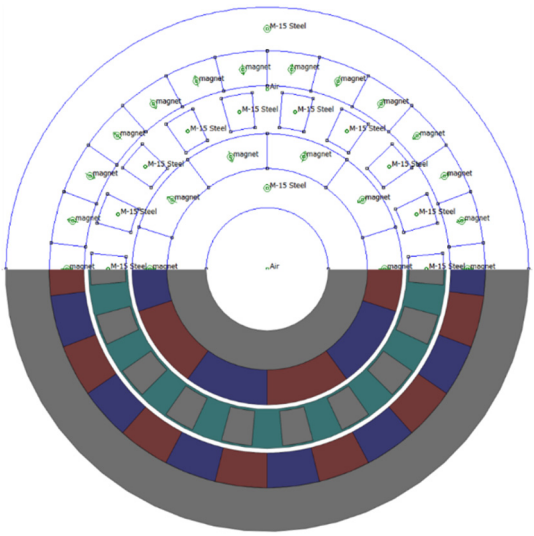

Figure 5.2 – Sketch on FEMM (top) and CAD model (bottom) of a PMG.

Meshing tool

The second part of FEMM is instead related to mesh creation, starting from the geometry sketched in the previous part. Different triangle dimensions can be chosen to properly mesh the different regions of the PMG. As it is clear in Figure 5.3 the size mesh in the inner and outer air gap is finer than in the PMs and in the yokes. This is a suggested requirement for a more accurate evolution of the torque transmitted by the magnetic gear, which procedure will be later described.

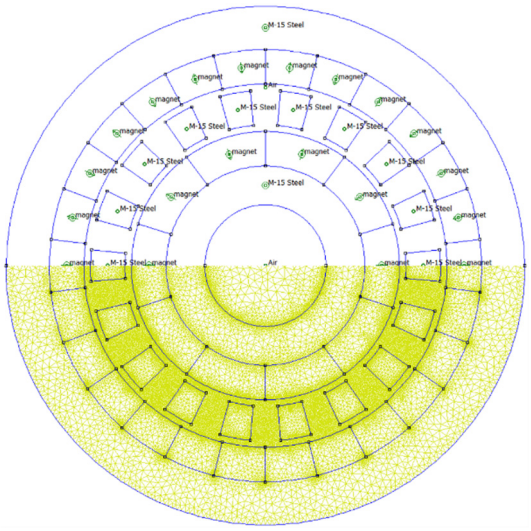

Figure 5.3 – Geometry (top) and mesh (bottom) on FEMM.

Solver tool

The last part of FEMM is devoted to the analysis and solution of magnetics problems. In Figure 5.4, the 2D planar problem has been solved and the magnetic flux density is evaluated.

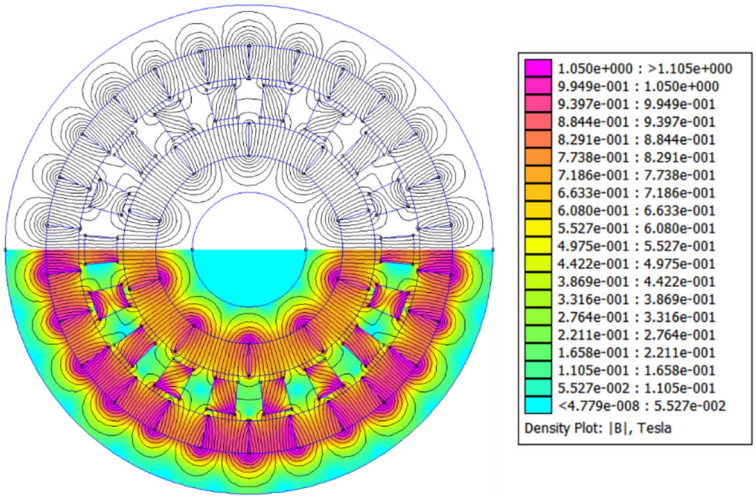

Figure 5.4 – Contour plot (top) and density plot (bottom) of magnetic flux density.

The software evaluate magnetostatic problems, namely problems where the fields are time invariant. In this condition both the Gauss's law for magnetism, in Eq. (5.6), and the ampere's law, in Eq. (5.7), are respected:

$$\nabla \cdot \mathbf{B} = 0 \tag{5.6}$$

$$\nabla \times \mathbf{H} = \mathbf{J} \tag{5.7}$$

where the divergence is applied to vector $\mathbf{B}$, which represents the magnetic flux density, while the curl vector operator is applied to the magnetic field intensity $\mathbf{H}$ evaluating the current density $\mathbf{J}$. The relation between the magnetic flux density and the field density is defined by:

$$\mathbf{B} = \mu \mathbf{H} = \mu_0 \mu_r \mathbf{H} \tag{5.8}$$

where μ_0, and μ_r are the vacuum and relative permeabilities of each material. Instead, in case of nonlinear materials, the permeability is a function of $\mathbf{B}$ according to Eq. (5.9):

$$\mu = \frac{\mathbf{B}}{\mathbf{H}(\mathbf{B})} \tag{5.9}$$

The torque capability of the magnetic gear is evaluated using a volume integral. In fact, it is necessary to select the blocks upon which force, or torque must be computed, evaluating the integral. The only trick to use for the torque evaluation using the weighted stress tensor volume integral is that the regions upon which the force is being computed must be surrounded by air. For this reason, a finer mesh help to achieve a more accurate result.

5.1.2 Torque ripple

Magnetic gears, as all the electrical machines, must be designed to transmit torque with the lowest possible torque ripple. The torque ripple is the effect on torque transmission which is caused by a particular phenomenon consisting in the interaction of permanent magnets rotor with the ferromagnetic poles, namely called cogging torque. In [126] Niguchi et al. presented a detailed analysis on cogging torque, with a particular attention to the harmonic spectra of the cogging torque of a magnetic gear.

In these last years, researchers usually use the cogging torque tactor C_f as indicator for the cogging torque severity. This factor, defined as in Eq. (5.10), was firstly introduced in [127] ad since then it is used in the design of magnetic gears:

$$C_f = \frac{2n_{s,r}\, q}{LCM\left(2n_{s,r}, q\right)} \tag{5.10}$$

where $n_{s,r}$ is the number of PMs pole pairs on sun or ring rotor, q represents the number of ferromagnetic poles, and LCM stands for least common multiple. It is preferred to have a unity cogging factor, which leads to a lower cogging torque. Therefore, a fractional gear ratio is suggested to have a higher LCM, hence a lowest is the cogging factor. Moreover, a unity cogging factor can be achieved only with an odd number of ferromagnetic poles, while the minimum cogging factor in case of even ferromagnetic poles is two.

5.1.3 Dynamic design

The dynamics of a PMG is very similar to the dynamics of a mechanical planetary gear train. The contact stiffness, which is responsible for the torque transmission, is replaced by a magnetic contactless stiffness, that guarantees the torque transmission between the three rotors of a PMG in a contactless way. In Figure 5.5 the free body diagram (FBD) of a planetary magnetic gear, made of sun, carrier, and ring rotors, is shown. The corresponding absolute angular velocities of sun ring and carrier are assumed concordant with respect to external torques.

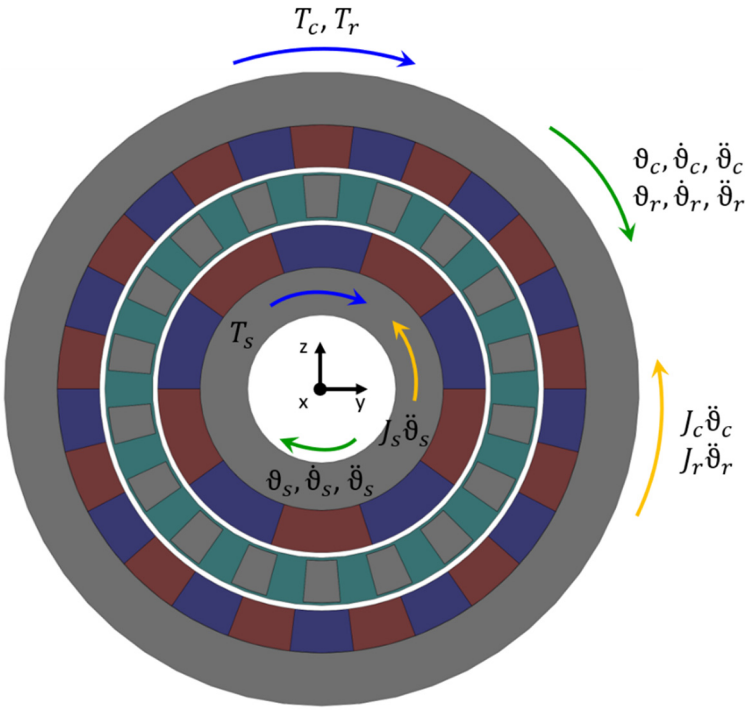

Figure 5.5 – Free body diagram of a planetary magnetic gear.

The equations of motion of the 3 DOFs planetary magnetic gear are defined starting from the free body diagrams of sun, carrier, and ring, which are analysed in Figure 5.6. For the sake of clarity, dissipative terms such as bearing and seals torques, are not considered for the three rotors, and will be later studied. Anyway, these possible contributions can be added to the FBDs with a discordant versus

with respect to the corresponding angular velocities. Moreover, inertias effects of inner, outer and middle rotors, together with magnetic torques are considered for the free body equilibrium.

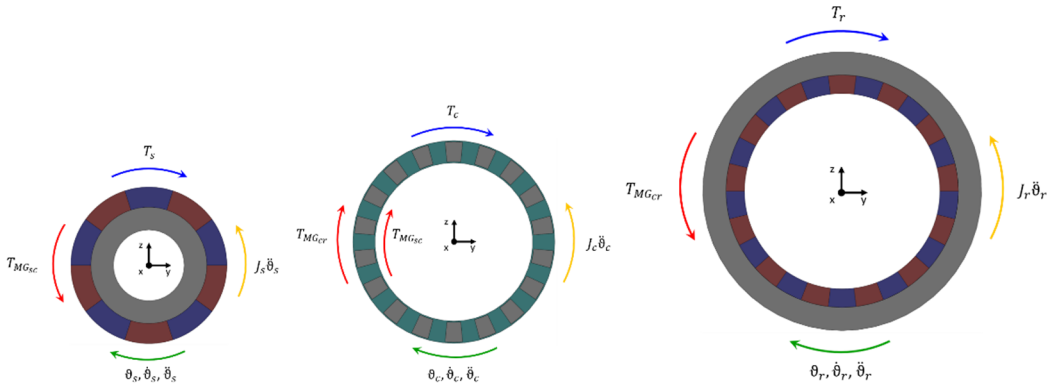

Figure 5.6 – FBDs of PMG sun (left), carrier (centre) and ring (right) rotors.

According to Figure 5.6, the equations of motion can be written using Eq. (5.11):

$$\begin{cases} J_s\ddot{\vartheta}_s = T_s - T_{MG_{sc}} \\ J_c\ddot{\vartheta}_c = T_c + T_{MG_{sc}} + T_{MG_{cr}} \\ J_r\ddot{\vartheta}_r = T_r - T_{MG_{cr}} \end{cases} \tag{5.11}$$

that in a matrix way is written as in Eq. (5.12):

$$\begin{bmatrix} J_s & & \\ & J_c & \\ & & J_r \end{bmatrix} \begin{Bmatrix} \ddot{\vartheta}_s \\ \ddot{\vartheta}_c \\ \ddot{\vartheta}_r \end{Bmatrix} = \begin{Bmatrix} T_s \\ T_c \\ T_r \end{Bmatrix} + \begin{Bmatrix} -T_{MG_{sc}} \\ T_{MG_{sc}} + T_{MG_{cr}} \\ -T_{MG_{cr}} \end{Bmatrix} \tag{5.12}$$

where J is the moment of inertia of each rotor, T is the mechanical torque on the three rotors, while $T_{MG_{sc}}$ and $T_{MG_{cr}}$ are respectively the magnetic torques generated by the magnetic flux between sun and carrier and between carrier and ring. Therefore, keeping the carrier fixed, if the sun is connected to a motor, T_s will be the torque provided by the motor and T_r will be the resistive torque on the ring rotor, which is assumed as the output rotor.

5.1.4 Evaluation of transmitted torque

The performance of a magnetic gear, in terms of transmissible torque, can be evaluated by the 2D FEM software, previously described, taking into account nonlinearities of the ferromagnetic regions of the gear. The analysis is performed by means of a magneto-static solution of the structure, even if the relative motion

of the rotors should call for a dynamic solution as time-varying magnetic flux can induce eddy currents in conductive parts and losses in ferromagnetic materials. In a preliminary study, these phenomena can be neglected [128]. On the other side, nonlinearity in ferromagnetic phenomena is instead correctly considered due to the primary importance of this effect. In fact, the saturation can be critical in ferromagnetic yokes since their magnetic reluctance influences the magnetic flux magnitude created by the permanent magnets and, consequently, the torque.

The torque transmitted between the rotating elements of the PMG is computed through the Maxwell's stress tensor, in the post-processing phase. Torque is evaluated along different shell-paths on the two air-gap of the machine and results are then averaged [129]. For each different angular position, a FEM analysis is performed with the evaluation of the transmitted torque.

The torque value depends on the relative position of the three rotors and hence its characteristic must be evaluated in a significant number of angular positions. If the ferromagnetic poles are fixed, the torque is transmitted from the inner rotor to the outer rotor according to the torque maps reported in Figure 5.7.

Each configuration, used to define the torque map, is identified by the angle of sun ϑ_s, and ring ϑ_r. The discretization of the two angles should be tiny enough to have a good reconstruction of the map. These torque maps are characterised by sloped iso-torque lines. The slope of each curve at constant torque depends on the gear ratio of the magnetic gear between outer and inner rotor, and thus it depends on the number of PMs poles on the two rotors according to Eq. (4.6). In this case the gear ratio $G_r = 2.6$ is the same of the mechanical PSD of Toyota Prius, as already written in the previous sections.

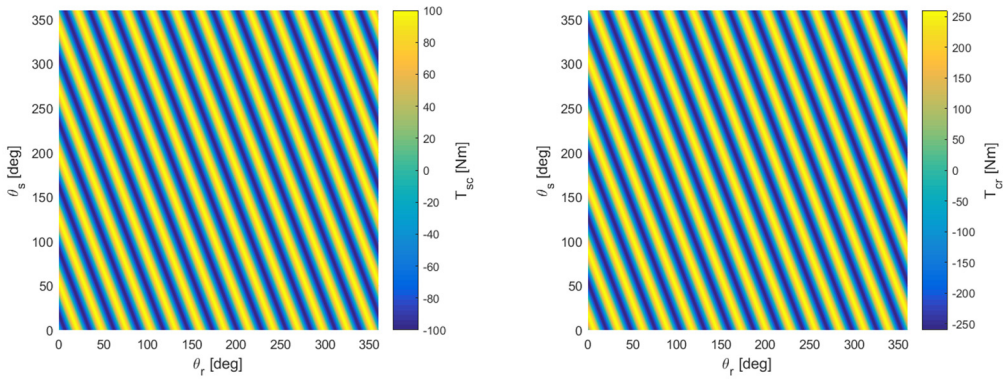

Figure 5.7 – Torque on sun rotor (left) and on ring rotor (right) w.r.t. rotors angular position.

As it is possible to note from the previous figures, PMG periodicity can be analysed to reduce the number of FEM simulations necessary to evaluate the torque in any of the possible angular positions. From Figure 5.8 (left) it is possible to detect how each point at the same torque is repeated with a periodicity $\tau_s = 360°/n_s = 72°$ along the y axis of the figure, and a periodicity $\tau_r = 360°/n_r = 27.69°$ along the x axis. The torque at the point P_1 is the same of

that of points P' and P^*, highlighted in the figure, hence it is possible to reconstruct the overall map starting from one point and rotating the rotor with an highest number of permanent magnet poles in order to have a smaller interval for the periodicity.

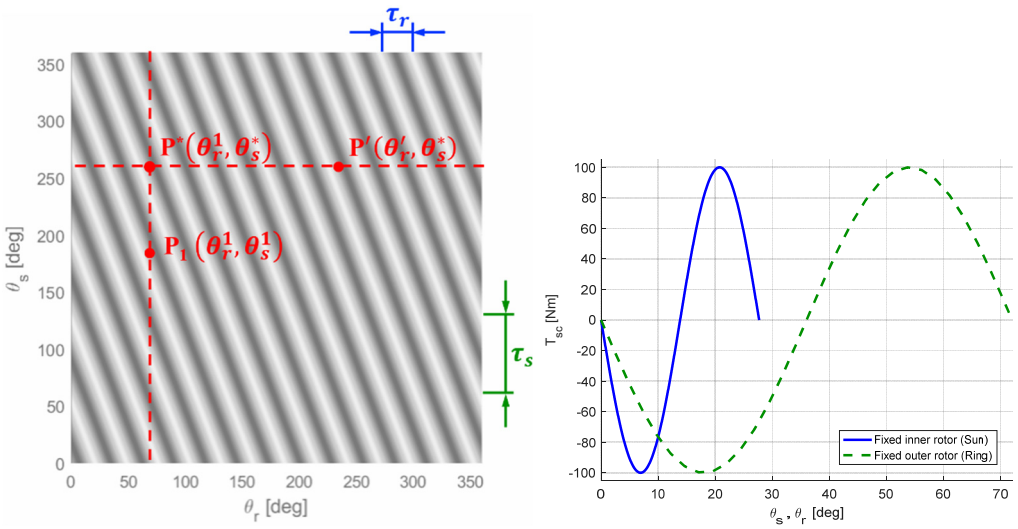

Figure 5.8 – Greyscale map of the PMG torque to highlight the periodicity along τ_s and τ_r (left) maintaining fixed the position of one of the two rotors (right).

If the topology of the magnetic gear does not change, to get the maximum torque value, only one FEM simulation is necessary, with the two rotors relative positions that return that torque maximum value, since the torque trend is a sine function, and it can be easily replicated.

5.2 Multi-objective optimisation

In § 4.3.3 the possible adoption of magnetic gears in an automotive application has been investigated. The replacement of the mechanical PSD with a PMG should not alter the transmission dynamics; hence the new PMG have to satisfy torque requirements, without compromising the moment of inertia. Therefore, a multi-objective optimisation approach is proposed to cope with these requirements, to maximise the transmitted torque minimising the moment of inertia. The optimisation process has been carried out by a deterministic algorithm exploiting a weighted sum of the two objectives, due to the computational costs, with a subsequent exploration of the Pareto front is performed by changing the weights [130] of torque and inertia. Once the geometric parameters of PMG are defined, its moment of inertia can be computed by considering the areas occupied by different materials and assigning to each of them the related mass density. An equivalent moment of inertia of the whole machine is computed by considering the different angular velocities of the parts that are related by the gear ratio G_r.

Therefore, if the carrier is kept fixed the equivalent moment of inertia is computed using Eq. (5.13):

$$J_{eq} = J_s + \frac{J_r}{G_r} \tag{5.13}$$

where J_s is the sun moment of inertia and J_r is the ring one. Instead, the moment of inertia of the middle rotor containing the iron poles is not considered, assuming that this rotor is kept fixed.

5.2.1 Preliminary optimisation

A preliminary parametric investigation of the objectives changing some geometric parameters has been carried out to have an idea on the objective functions landscapes and to detect also the boundary constrains of the parameters involved in the optimisation process.

Once the gear ratio is defined, all the parameters of the magnetic gear are evaluated to have a comparable torque capability with respect to the mechanical PSD counterpart. They are listed in Table 5.1, where parameters in bolt are kept fixed during the optimization process.

Table 5.1 – Magnetic gear parameters.

Parameter	Value	Unit
Sun PM thickness $th_{PM,s}$	8	mm
Ring PM thickness $th_{PM,r}$	8	mm
Steel poles thickness th_{poles}	8	mm
Sun yoke thickness $th_{yoke,s}$	10	mm
Ring yoke thickness $th_{yoke,r}$	10	mm
Gear external radius R_{ext}	125	mm
Gear axial length L	200	mm
Sun PMs pole pairs n_s	5	-
Ring PMs pole pairs n_r	13	-
Carrier steel poles q	18	-

In this preliminary analysis the PMs thickness is assumed the same for both inner and outer rotor. The colourmaps of the optimisation goals domains are obtained changing this parameter together with the thickness of steel poles, while all the other parameters listed in Table 5.1 are kept constant. The behaviour of the variables considered appears to be quite regular and well behaved. Results are depicted in Figure 5.9.

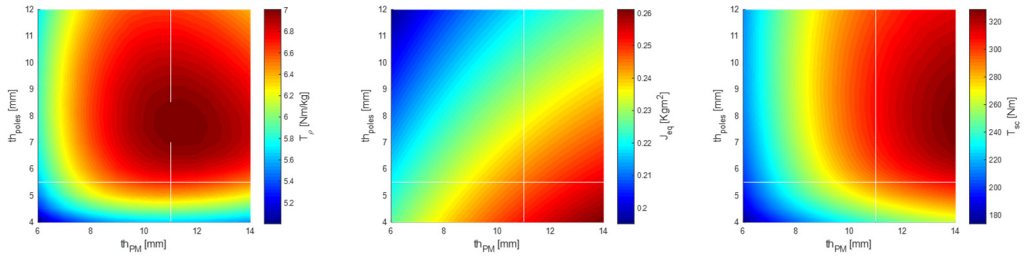

Figure 5.9 – Colourmaps of the optimisation goals domains for 2 variables parametric analysis (poles and PMs thickness): torque density (left), equivalent moment of inertia (centre) and transmissible torque on inner rotor (right).

In Figure 5.10 is instead reported the trend of the variable previously analysed, namely torque density, equivalent moment of inertia and the transmissible torque at the inner rotor of the magnetic gear, changing the thickness of sun and ring rotors, while all the other parameters of Table 5.1 are kept constant. Results of this last optimisation are very regular, as in the previous case.

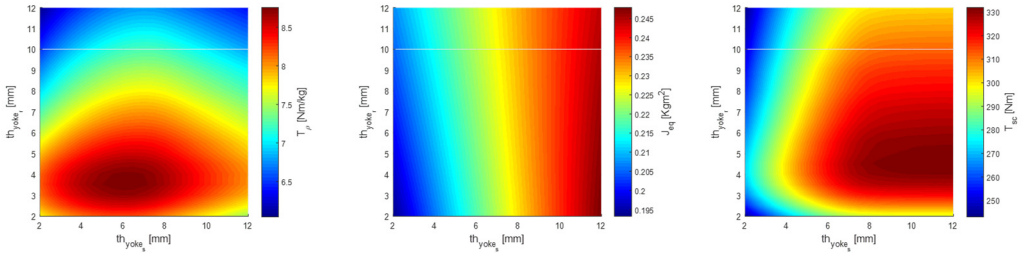

Figure 5.10 – Colourmaps of the optimisation goals domains for 2 variables parametric analysis (sun and ring yoke thickness): torque density (left), equivalent moment of inertia (centre) and transmissible torque on inner rotor (right).

5.2.2 Optimisation with “fmincon” and “Pattern Search”

The next step in the optimisation process was the implementation of an optimisation algorithm that allow to change five different parameters, with the aim of maximising the torque minimising the equivalent moment of inertia of the magnetic gear J_{eq}. These two objectives are contrasting each other: higher torque values require a larger amount of permanent magnets and this is leading to a large value of the equivalent moment of inertia. Moreover, instead of using the maximum torque value at the inner rotor T_{sc} as objective, the ratio between the maximum transmissible torque at the inner rotor and the mass of the structure is used, namely a torque density T_{ρ}. This choice puts a larger effort in optimising the exploitation of the magnetic materials inside the structure.

Two different algorithms are used to find the Pareto front: the first one is the “fmincon” Matlab function, based on the gradient of the objective function, while the second one is “Pattern Search” routine, that does not make use of any gradient of the objective function with respect to degrees of freedom.

In addition, even if there is no theoretical proof of convexity of the objective functions, the optimisation procedure has been run several ways by changing the starting point of the search and, in all cases tested, the procedure converged at the same minimum point.

The multi-objective optimisation is reduced to a single objective one by means of a weighted sum of the two objectives, using the parameter α that can vary between 0 and 1, according to Eq. (5.14):

$$of\left(T_\rho, J_{eq}\right) = \max\left[\alpha\frac{T_\rho}{T_{\rho,ref}} - \left(1-\alpha\right)\frac{J_{eq}}{J_{eq,ref}}\right] \tag{5.14}$$

where the two parameters $T_{\rho,ref}$ and $J_{eq,ref}$ are used to normalise the two components of the objective function and are evaluated at the first iteration of the optimisation process.

First optimisation

The first optimisation was done using both "fmincon" and "Pattern Search", with the aim of compare the results of the two algorithms.

For the two analyses the boundary constrains for the five parameters and the starting value are reported in Table 5.2, where *LB* and *UB*, respectively indicate the lower and upper boundary for each parameter involved in the optimisation process, while *Ref* indicated the value of each parameter at the first iteration, used to evaluated $T_{\rho,ref}$ and $J_{eq,ref}$, in Eq. (5.14).

Table 5.2 – Parameter constraints.

Parameter	LB	Ref	UB	Unit
Sun PM thickness $th_{PM,s}$	6	6.5	14	mm
Ring PM thickness $th_{PM,r}$	6	13.5	14	mm
Steel poles thickness th_{poles}	4	11.5	12	mm
Sun yoke thickness $th_{yoke,s}$	2	2.5	12	mm
Ring yoke thickness $th_{yoke,r}$	2	11.5	12	mm

In Figure 5.11 the Pareto front using two different algorithms is reported. The two variables analysed to create the Pareto front are the torque density T_ρ and the equivalent moment of inertia J_{eq}. It is possible to notice that using the "Pattern Search" algorithm (red line) a wider region is obtained. The utopia point correspond to the lowest possible value of equivalent moment of inertia and to the highest torque density value, therefore it is placed in the bottom right corner of the figure.

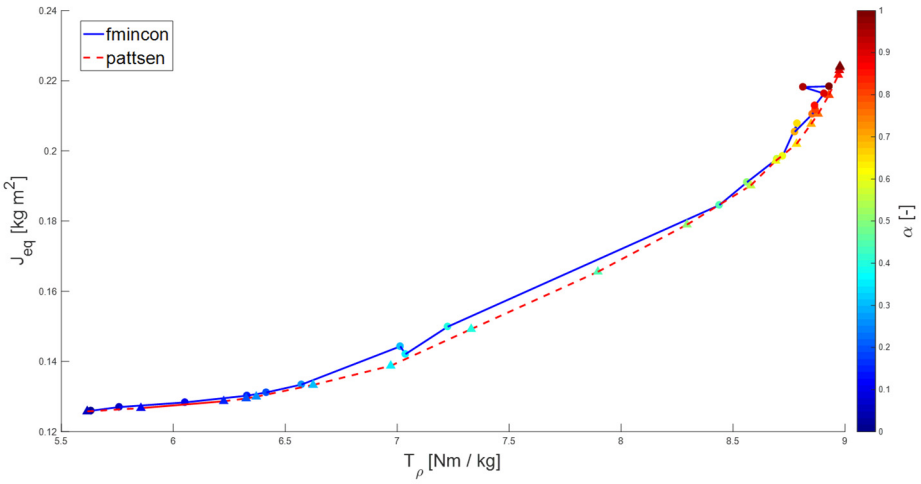

Figure 5.11 – Pareto front for the two optimisation algorithms.

In Figure 5.12 the final value of the objective function using the two different algorithms is reported. It is possible to notice that "Pattern Search" returns higher values respect to "fmincon" algorithm, except for $\alpha = 0.6$. This result agrees with the Pareto front reported in Figure 5.11.

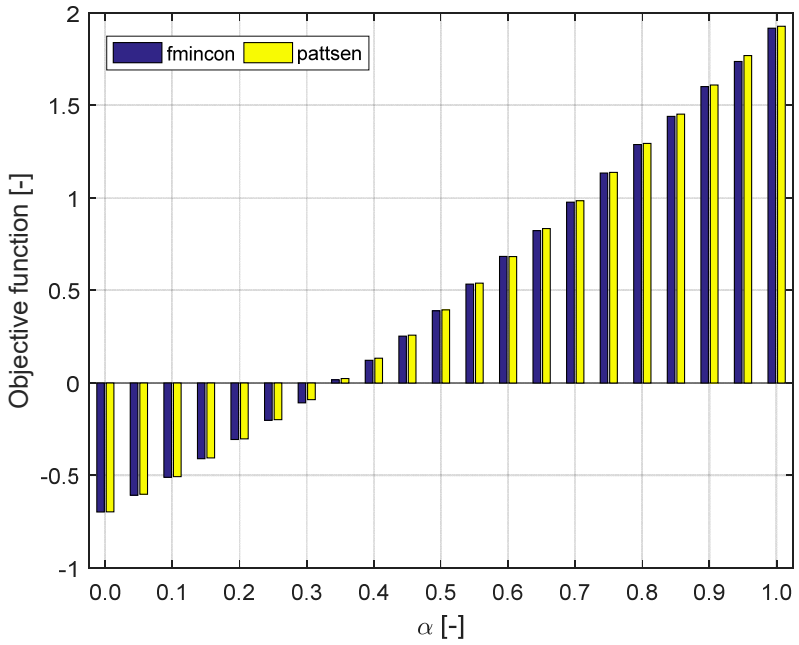

Figure 5.12 – Final objective function value for the two optimisation algorithms.

According to the results of the previous figures the "Pattern Search" algorithm can be assumed as the optimal one for this optimisation problem. Hence, in Figure 5.13 the Pareto front for different values of the weight α is shown together with maximum torque at the inner rotor T_{sc} and mass M of the magnetic gear.

The same results, for both optimisation algorithm, are illustrated in Figure 5.14 as mass and moment of inertia with respect to transmissible torque. Using

this representation, it is clear that to achieve a higher transmissible torque it is necessary to increase the overall dimensions of the magnetic gear, increasing its moment of inertia, as well.

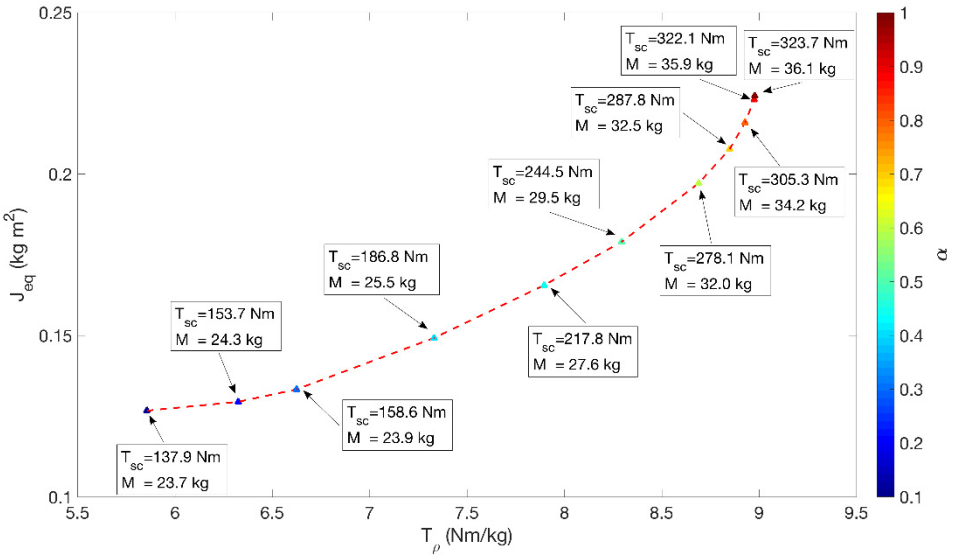

Figure 5.13 – Pareto front for different values of the weight α using "Pattern Search".

For each point of the Pareto front also the corresponding values of mass M and torque T_{sc} are indicated.

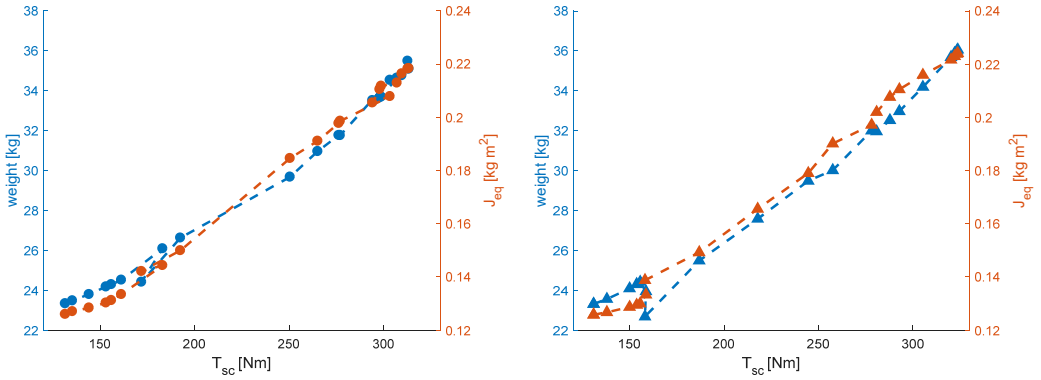

Figure 5.14 – Results of optimised magnetic gear for different value of α using "fmincon" (left) and "Pattern Search" (right).

After the optimisation process, the following step is to decide which value of the parameter α to choose in the prototyping phase of the magnetic gear. The two parameters that could be analysed are the ratio between the torque density and the equivalent moment of inertia T_ρ / J_{eq}, which trend is reported in Figure 5.15 (left), or the ratio between the transmissible torque on inner rotor and the equivalent moment of inertia T_{sc} / J_{eq}, which trend is reported in Figure 5.15 (right), that

correspond to an angular acceleration. These two parameters are linked by the weight of the magnetic gear, which trend is reported in Figure 5.16.

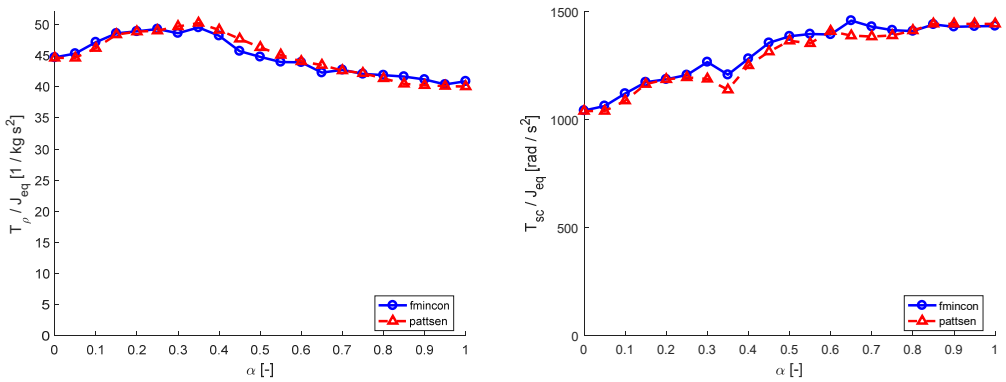

Figure 5.15 – Torque density over equivalent moment of inertia (left) and angular acceleration (right) of the magnetic gear w.r.t. α.

The choice of the appropriate parameter will give different results since the weight of the magnetic gear has a higher impact respect to the equivalent moment of inertia. If the ratio between the torque density and the equivalent moment of inertia T_ρ / J_{eq} is chosen as the appropriate parameter, the magnetic gear must be realised according to the optimal design using $\alpha = 0.35$. Instead, if the angular acceleration is defined as the appropriate one, the optimal design can be achieved with $\alpha \geq 0.65$.

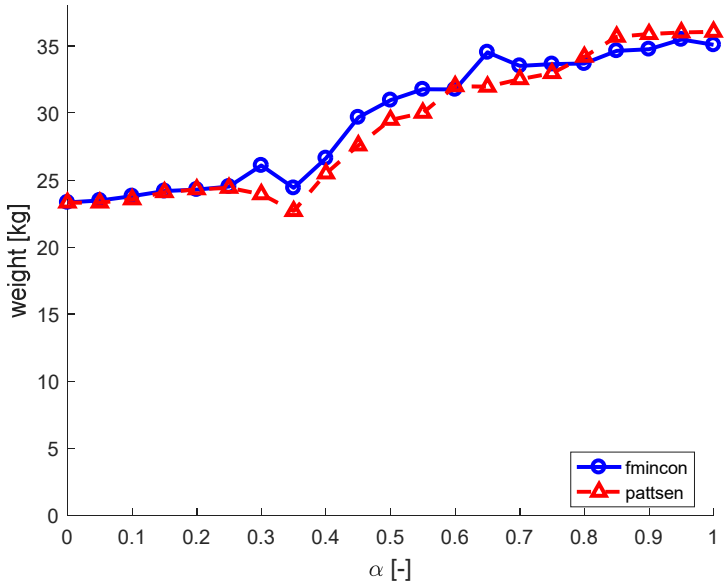

Figure 5.16 – Weight of magnetic gear w.r.t. α.

In Figure 5.17 it is possible to notice how the aspect ratio changes if more importance is given to the equivalent moment of inertia or to the torque density during the optimisation process.

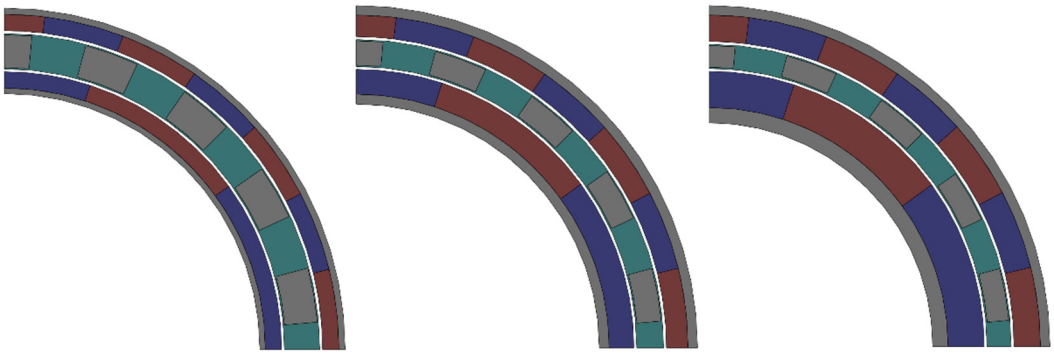

Figure 5.17 – Appearance of the optimised magnetic gear using "Pattern Search" for: $\alpha = 0.1$ (left), $\alpha = 0.5$ (middle), $\alpha = 0.9$ (right).

Finally, the trend of the magnetic gear parameters involved in the optimisation algorithm for different values of α and using "fmincon" and "Pattern Search" optimisation algorithms are reported in Figure 5.18-Figure 5.20.

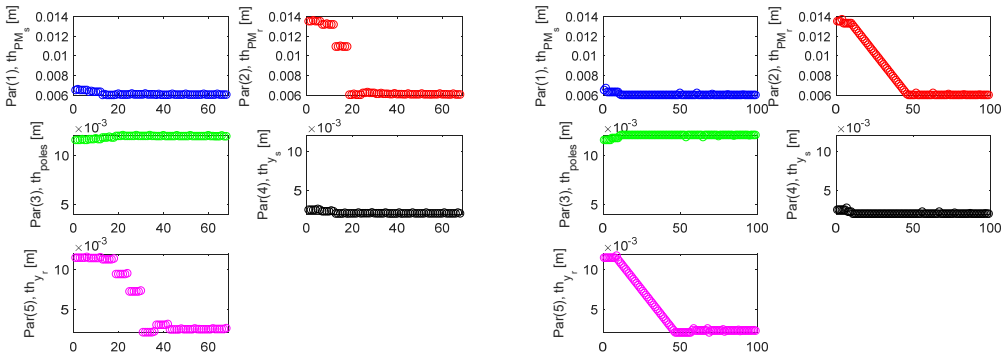

Figure 5.18 – Parameter trend using "fmincon" (left) and "Pattern Search" (right) for $\alpha = 0.1$.

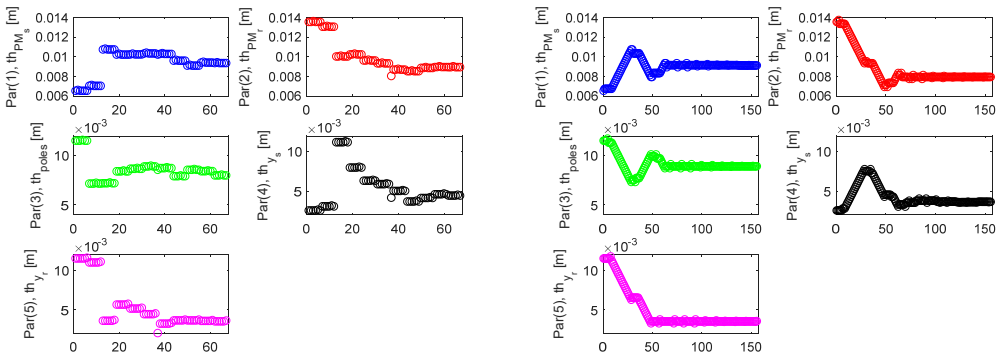

Figure 5.19 – Parameter trend using "fmincon" (left) and "Pattern Search" (right) for $\alpha = 0.5$.

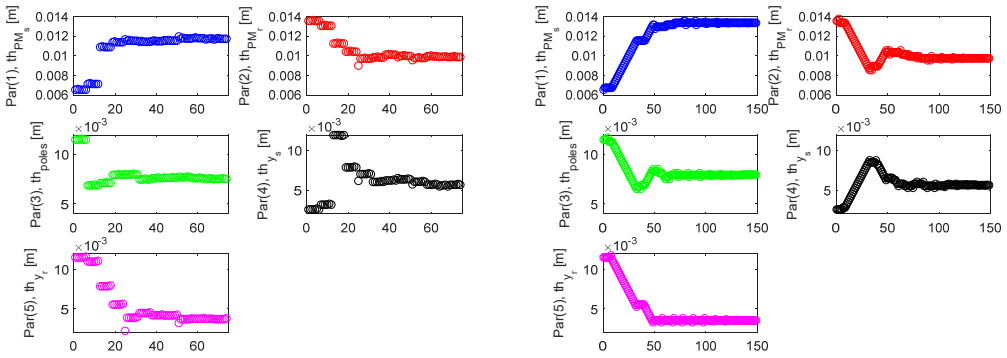

Figure 5.20 – Parameter trend using “fmincon” (left) and “Pattern Search” (right) for $\alpha = 0.9$.

The first optimisation algorithm (“fmincon”) finds the maximum of the objective function in a number of iterations that is around the half of iteration necessary for the second algorithm (“Pattern Search”). The simulation phases have required an average computational time of 29.6 seconds, for each run, on a workstation equipped with an Intel Core i7-3770 at 3.4 GHz and 32 GB of RAM.

Second optimisation

After the first optimisation process, where the Pareto front is found for both optimisation algorithms, it could be interesting to start a new optimisation process in which the reference value for all the parameters is chosen w.r.t. parameter α that returns the highest value of ratio between torque density and equivalent moment of inertia, as illustrated in Figure 5.15 (left). Therefore, a value of $\alpha = 0.35$ is chosen for both the optimisation algorithms “fmincon” and “Pattern Search”. Then, boundary constrains are fixed respect to the first optimisation while the starting value depends on the optimisation algorithm and their values are reported in Table 5.3.

Table 5.3 – Parameter constraints of second optimisation step.

Parameter	LB	Ref “fmincon”	Ref “Pattern Search”	UB	Unit
Sun PM thickness $th_{PM,s}$	6	6.4006	6.05	14	mm
Ring PM thickness $th_{PM,r}$	6	6.1215	6.00	14	mm
Steel poles thickness th_{poles}	4	9.6756	8.10	12	mm
Sun yoke thickness $th_{yoke,s}$	2	2.5367	2.00	12	mm
Ring yoke thickness $th_{yoke,r}$	2	3.1483	3.00	12	mm

In Figure 5.21 the two Pareto front using “fmincon” of the first and second optimisation iterations are reported. The optimisation function is the same for both optimisation process as reported in Eq. (5.14).

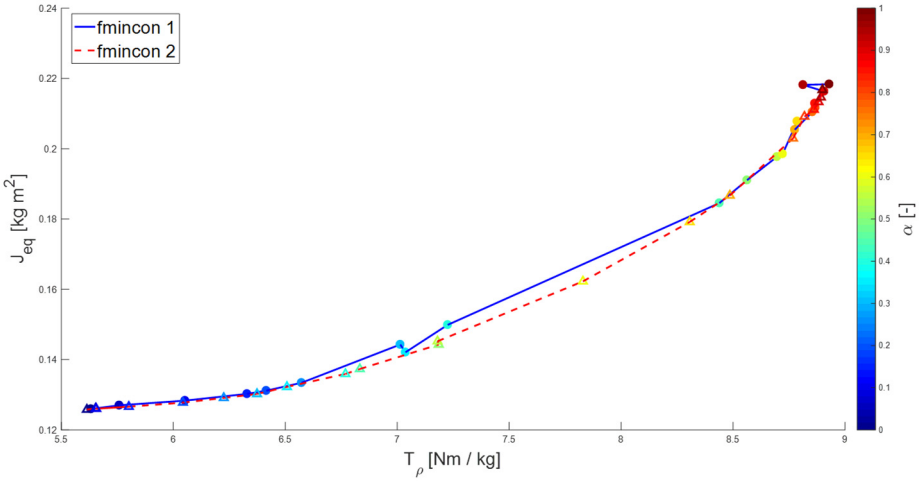

Figure 5.21 – Pareto front using “fmincon” for the two optimisation iterations.

As it is possible to notice in the central region the Pareto front of the second optimisation iteration is wider, although for high values of parameter α, the optimised torque density value T_ρ is lower than in the first iteration. The same assumptions could be done using the “Pattern Search” algorithm, which results are illustrated in Figure 5.22.

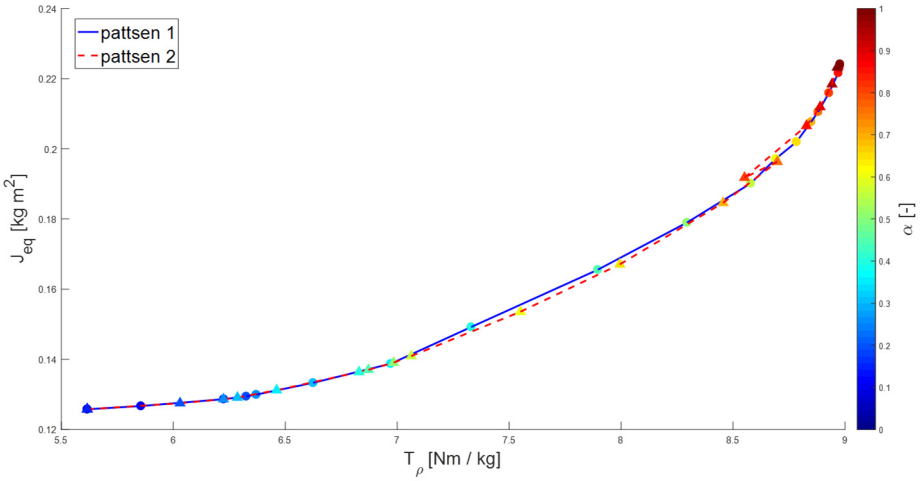

Figure 5.22 – Pareto front using “Pattern Search”
for the two optimisation iterations.

In Figure 5.23 the ratio between the torque density and the equivalent moment of inertia together with the weight of the optimised magnetic gear are reported after the two optimisation steps using two different algorithms. The magnetic gear

parameters that should be chosen for the prototype correspond to a value of parameter $\alpha = 0.4$ for "fmincon" and to $\alpha = 0.5$ for "Pattern Search".

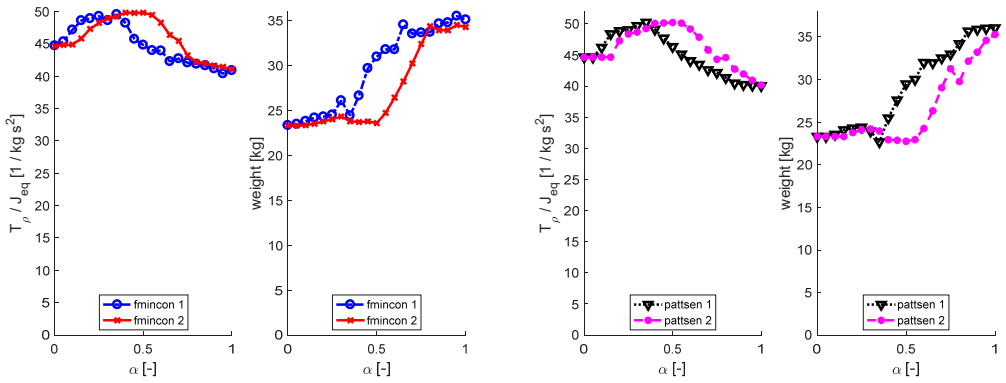

Figure 5.23 – Torque density over equivalent moment of inertia and weight of the magnetic gear using "fmincon" (left) and "Pattern Search" (right) algorithms w.r.t. α.

Meantime, from the weight analysis it is possible to appreciate how the optimisation algorithm tends to maintain an almost constant weight for low values of parameter α, with a sudden weight growth for values $0.4 < \alpha < 0.8$, as illustrated in Figure 5.23. Therefore, the hypothesis of choosing as optimal configuration the one returns the highest ratio between torque density and moment of inertia also leads to a minimum weight of the magnetic gear.

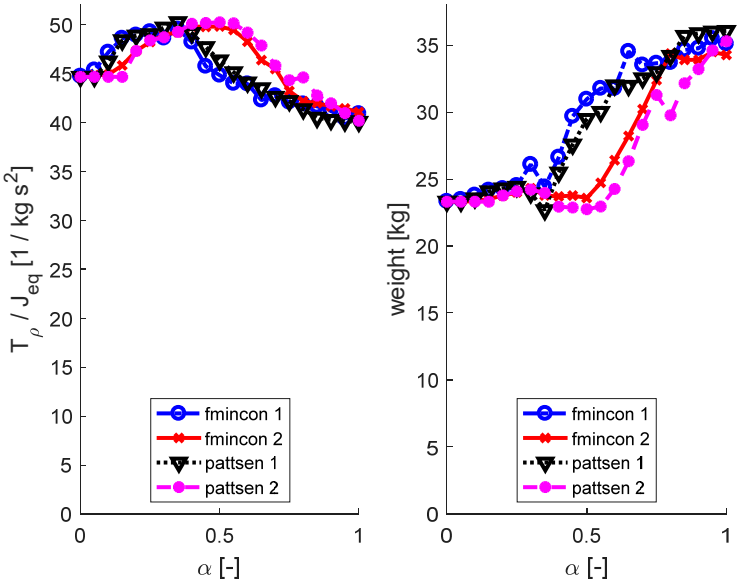

Figure 5.24 – Torque density over equivalent moment of inertia and weight of the magnetic gear using different algorithms w.r.t. α.

The differences between the first and the second optimisation steps are more evident in Figure 5.24, in which the second step for both the optimisation algorithms is moved to higher value of parameter α. Instead, the appropriate

choice of α parameter changes if the angular acceleration is considered as objective function, as reported in Figure 5.25.

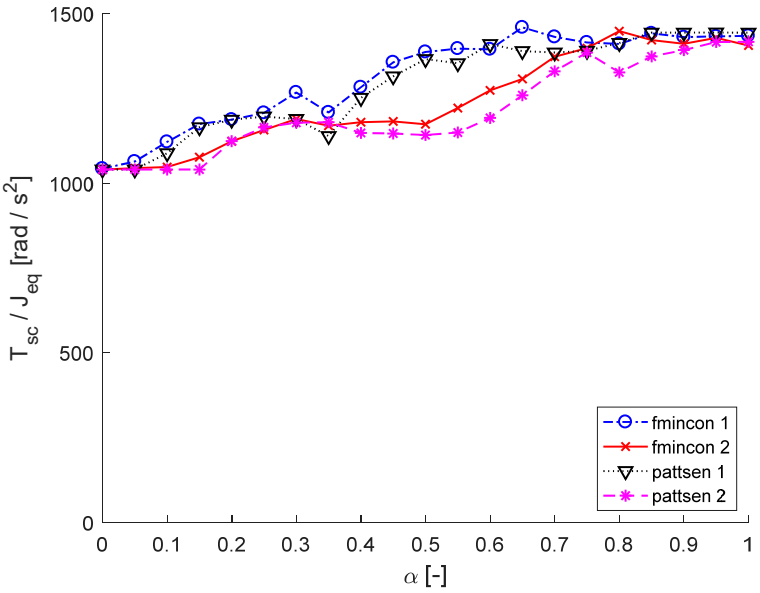

Figure 5.25 – Angular acceleration of the magnetic gear w.r.t. α.

If higher angular acceleration are desired, the highest values of parameter α must be chosen. This has a dual effect on the dynamics of a magnetic gear, since it has the advantage of a faster dynamic response during a transition phase, with the drawback of higher possible oscillations and vibrations to the transmission driveline.

5.3 Dynamic analysis on Matlab/Simulink

The software Simulink, integrated in Matlab, is used to create a simplified model of driveline using the concept of magnetic gear transmission. The driveline model, shown in Figure 5.26, is modelled by means of block-oriented approach [131,132].

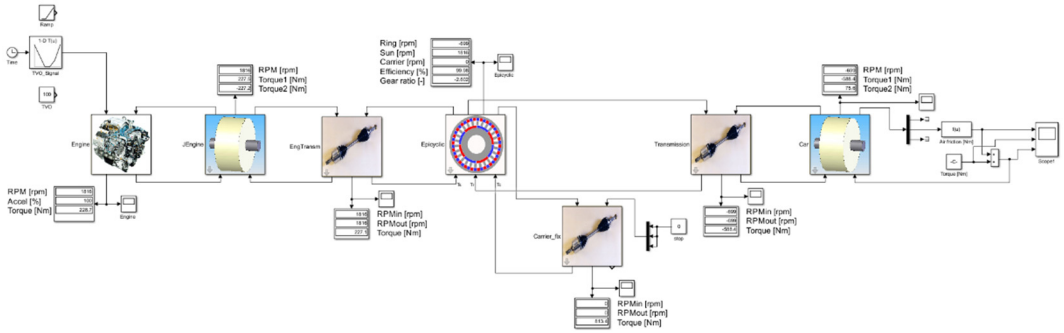

Figure 5.26 – Simplified model of driveline using magnetic gear transmission.

Using this approach, the driveline is split in its main components, which include kinematic and dynamic relationships. Moreover, this approach allow to put in evidence the correlation between each block of the model and the correspondent physical system, highlighting input/output relations between components and their interactions on system behaviour.

A high level of flexibility in the development of the Simulink model is unsured, using a multi-sharing component library and adopting a user-friendly graphical interface.

For all the system components it is necessary to define the dynamic laws by means of mechanical equilibrium principles, imposing the initial condition and defining dynamic constants and constraints.

In Figure 5.26, the engine is connected to the sun of the PMG trough an inertia block, which include engine, clutch and DMF inertias, the carrier is kept fixed, while the ring of the PMG is connected to another inertia representing vehicle load resistance. The model is thus characterised by three degrees of freedom: engine speed (equal to the first inertia speed and to the PMG sun speed), the carrier speed (that in this case is equal to zero), and the ring speed (equal to the last inertia of the system).

In the model the driver acts on the throttle valve opening (TVO) causing a transition phase, namely an acceleration or deceleration on the driveline.

The engine torque is mapped by means of experimental data and depends on the engine angular velocity and to the TVO, according to Eq.

$$T_{ICE} = T_{ICE}\left(n_{ICE}, TVO\right) \tag{5.15}$$

Finally, different numerical integration approaches have been tested to achieve numerically stability of solutions and to improve convergence velocity of the simulation.

The magnetic transmission model has been tested in both transient and steady-state conditions. The main dynamic parameters of the driveline are reported in Table 5.4.

Table 5.4 – Parameters of the transmission driveline with a PMG.

Type	**Parameter**	**Value**
Inertia	J_M [kg m^2]	0.025
	J_R [kg m^2]	130
Rolling resistance	f_0 [Nm]	10
	f_2 [Nms^2/rad^2]	0.0123
Transmission gear ratio	τ [-]	-13/5 = -2.6

According to system parameters, the inertia J_R, representing the vehicle, is evaluated as $J_R = MR^2$, where M is the vehicle mass and R is the tyre radius. Moreover, the resistive torque is evaluated using Eq. (5.16):

$$T_R = f_0 + f_2 \dot{\vartheta}_R{}^2 + T_{B_R} \tag{5.16}$$

where f_0 and $f_2 = 0.5\,\rho\, C_d\, A_f\, R^3$ are two constant terms depending on tyres and vehicle dimensions, air density and drag coefficient, while T_{B_R}, representing the dissipation torques related to the bearings of the second part of the transmission, is assumed equal to zero. Since the TVO is the input of the model, different simulations can be performed changing the trend of TVO during the simulation. At a first instance, Figure 5.27 (left), the driver is simulating a condition with 100% of gas pedal, hence the speed of the inner rotor, namely the speed of the ICE, is continuously increasing. The torque is instead progressively reduced due to the torque map of the ICE, which depends on its speed and on TVO. Moreover, the ICE speeds starts from 700 rpm, which is considered as the minimum condition for the engine.

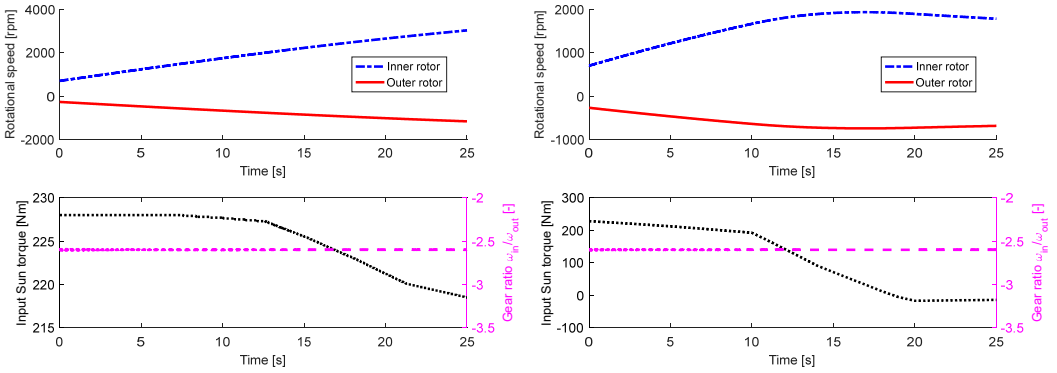

Figure 5.27 – Speeds and torque of magnetic gear rotors with a TVO of 100% (left) and with a decreasing TVO (right).

In the second simulation, as illustrated in Figure 5.27 (right), the TVO starts from 100% and then it is linearly reduced up to zero at the simulation time of 20 s. However, the rotational speed increases since the TVO is higher than zero. After this first phase, namely from 20 s to 25 s it is set equal to zero, hence a negative resistive torque is applied to the inner rotor of the magnetic gear.

Finally, in the last simulation, as in Figure 5.28, the TVO assumes a generic profile depending on the simulation time. If the TVO is positive, the ICE usually provides a positive torque to the sun rotor, according to the torque map, depending at the same time on the engine rotational speed. Moreover, the gear ratio of the PMG is always respected both in transient and in steady-state conditions.

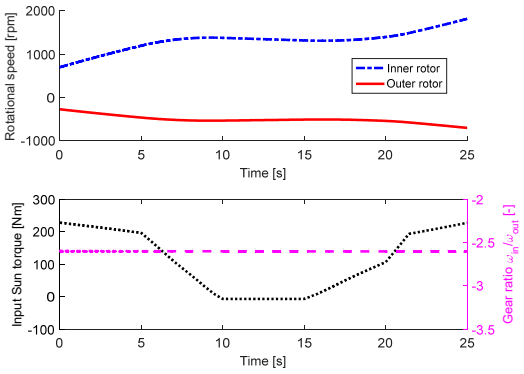

Figure 5.28 – Speeds and torque of magnetic gear rotors with a generic TVO.

This Simulink model will be again considered in the following chapters for other tests on the transmission, which level of detail will be further increase.

5.4 Conclusions

In this chapter, the main guidelines for the dynamic and analytical design of a magnetic gear, for power transmission application, have been drawn. In particular, the working principles of a PMG are presented to explain the influence of the number of ferromagnetic poles on the radial and circumferential magnetic induction distributions inside the device.

The dynamic equations of a PMG are written using the classical approach of applied mechanics, based on the equilibrium laws of free body diagrams.

The different tools of software FEMM are presented to clarify how sketch, mesh and solve the magnetic problem for the design and analysis of a magnetic gear.

Moreover, maps of the transmitted torque of the PMG are evaluated for different positions of inner and outer rotors of the device, keeping the carrier fixed. It has been noted a periodicity in the torque map, depending on the number of PMs pole pairs on the two rotors and a particular trend linked to the transmission ratio.

The dynamic design has been integrated with a multi-objective optimisation problem, based on a weighting average of two objectives: the maximisation of PMG torque density and the minimisation of its equivalent moment of inertia, presenting a Pareto front. Two different optimisation algorithms are carried out in two different steps of the optimisation, proposing different points of view in the choice of appropriate constructional parameters of the PMG.

Finally, the torque maps of the optimised PMG and its dynamic equations are integrated in a customised and simplified model of transmission to assess the possible adoption of a magnetic transmission inside an automotive driveline.

Chapter 6

6. Design of PMG prototype

This chapter presents the CAD modelling activity in the design process of a PMG to achieve a prototype for experimental testing. In § 5 a magneto-mechanical approach has been proposed to design a magnetic gear, together with a multi-objective optimisation process to improve mechanical and dynamic properties of the magnetic gear. Several releases of the PMG prototype are proposed, with a progressive rise in complexity, to achieve quickly exchangeable configurations for different experimental tests. The software *Solidworks* has been used for the design of the proposed CAD models. In § 6.1 the choice of the appropriate sizing will be discussed, while in § 6.2 the characteristics of the three proposed solutions are investigated.

6.1 Sizing and design assumptions

The appropriate sizing of the prototype is chosen according to maximum overall dimensions and analysing results of the optimisation process. In details, two different values of parameter α, which links the torque density and the equivalent moment of inertia of the planetary magnetic gear, are chosen in order to investigate possible improvements and design solutions for the prototyping phase. All the dimensions of the identified PMG have been halved, except for the air gap, that remains the same due to constructive reasons. Moreover, other two configurations starting from the same values of α are tested increasing the yokes thickness, as reported in Figure 6.1, while in

Table 6.1 the numerical values for the optimised parameters are indicated. The possibility to increase the yokes thickness is analysed to highlight their effects on the transmissible torque, although a structural stiffening could be obtained using a non-ferromagnetic material. The two values of $\alpha = 0.5$ and $\alpha = 0.9$ have been chosen in accordance with Figure 5.24 and Figure 5.25,

maximising the quantity T_ρ / J_{eq} in the first case, and the quantity T_{sc} / J_{eq}, namely an equivalent angular acceleration, in the second case.

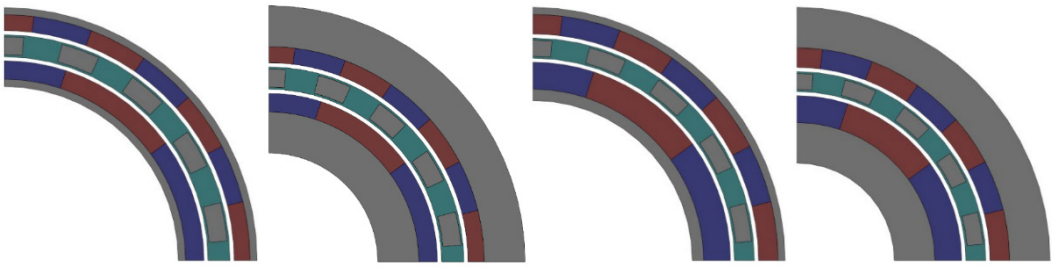

Figure 6.1 – Appearance of the optimised magnetic gear using "Pattern Search" for: $\alpha = 0.5$ (left), $\alpha = 0.5$ with thicker yokes (centre-left), $\alpha = 0.9$ (centre-right), $\alpha = 0.9$ with thicker yokes (right).

Table 6.1 – Magnetic gear parameters w.r.t. configurations.

Parameter	$\alpha = 0.5$	$\alpha = 0.5$ **thicker yokes**	$\alpha = 0.9$	$\alpha = 0.9$ **thicker yokes**	**Unit**
	Value				
Sun PM thickness $th_{PM,s}$	4.55	4.55	6.65	6.65	mm
Ring PM thickness $th_{PM,r}$	3.95	3.95	4.85	4.85	mm
Steel poles thickness th_{poles}	4.45	4.45	3.95	3.95	mm
Sun yoke thickness $th_{yoke,s}$	1.80	10	2.8	10	mm
Ring yoke thickness $th_{yoke,r}$	1.75	10	1.75	10	mm
Air gap	1.5				mm
Gear external radius R_{ext}	125				mm
Gear axial length L	100				mm
Sun PMs pole pairs n_s	5				-
Ring PMs pole pairs n_r	13				-
Carrier steel poles q	18				-

For each configuration, four different analyses have been carried out, analysing the mechanical and magnetic properties at the PMG inner rotor, according to Figure 6.2:

- the first one corresponds to the classical geometry in which all the permanent magnets are in contact each other;
- in the second one a gap of 1 mm between PMs with opposite magnetisation direction is assumed;

- in the third one the gap of 1 mm is still considered and each PM is segmented in 3 parts along the circumferential direction considering 0.3 mm of gap between these parts;
- the last one still considers the gap of 1 mm between PMs of opposite magnetisation direction and any gap between the three segmented parts.

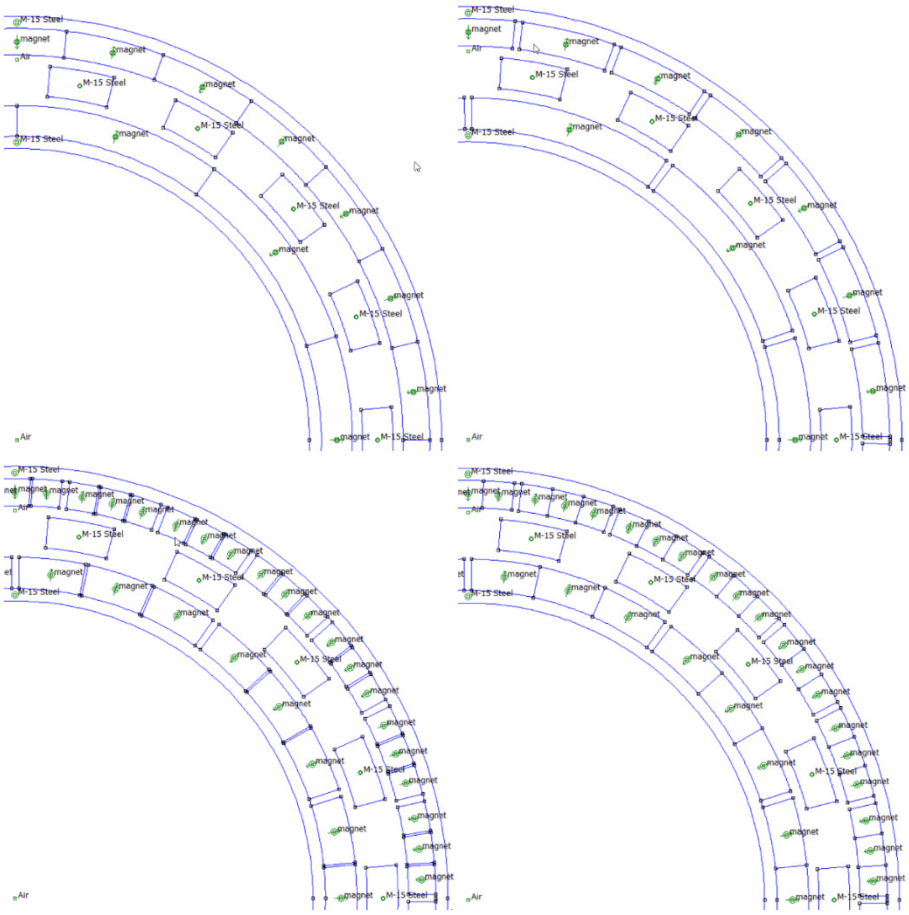

Figure 6.2 – Magnetic gear FEMM model in four different design starting from Figure 6.1 (left): standard (top-left), gap between magnets (top-right), gap between magnets segmented in three parts with gap (bottom-left), gap between magnets segmented in three parts without gap (bottom-right).

As stated in [36] the segmentation of PMs could be considered as a factor to consider in the design phase to increase the magnetic transmission efficiency in magnetic gears. The main effect of PMs segmentation consists in the reduction of the PMs conductivity through lower levels of eddy current losses. This aim is usually achieved with segmentation in both circumferential and axial direction. It has been highlighted that the effect of PMs segmentation is higher at the outer rotor, where the eddy current is equally distributed in the segments, while at the inner rotor PMs the eddy currents distribution locally concentrates in correspondence of the stationary ferromagnetic poles.

The maximum transmissible torque at inner rotor, as reported in Table 6.2, is the highest for the standard configuration, as expected. However, the introduction of a circumferential gap between PMs has a lower effect on the transmissible torque and the PMs segmentation does not influence the transmissible torque in a critical way, since its effect is more evident in the power losses due to eddy currents.

Table 6.2 – Transmissible torque at inner rotor of PMG.

Analysis	$\alpha = 0.5$	$\alpha = 0.5$ **thicker yokes**	$\alpha = 0.9$	$\alpha = 0.9$ **thicker yokes**	**Unit**
	Value				
1 – standard	23.43	20.74	30.94	24.36	Nm
2 – gap PMs	23.40	20.59	30.88	24.12	
3 – gap PMs & gap seg.	20.60	18.30	27.33	21.03	
4 – gap PMs & no gap seg.	22.48	20.37	29.81	23.49	

Table 6.3 – Weight of PMG.

Analysis	$\alpha = 0.5$	$\alpha = 0.5$ **thicker yokes**	$\alpha = 0.9$	$\alpha = 0.9$ **thicker yokes**	**Unit**
	Value				
1 – standard	3.63	6.61	4.41	6.99	kg
2 – gap PMs	3.52	6.49	4.26	6.83	
3 – gap PMs & gap seg.	3.44	6.42	4.16	6.73	
4 – gap PMs & no gap seg.	3.52	6.49	4.26	6.83	

Table 6.4 – Torque density.

Analysis	$\alpha = 0.5$	$\alpha = 0.5$ **thicker yokes**	$\alpha = 0.9$	$\alpha = 0.9$ **thicker yokes**	**Unit**
	Value				
1 – standard	6.45	3.14	7.01	3.49	Nm
2 – gap PMs	6.66	3.17	7.25	3.53	
3 – gap PMs & gap seg.	5.98	2.85	6.57	3.12	
4 – gap PMs & no gap seg.	6.39	3.14	7.00	3.44	

Instead, the second solution with only a gap between magnets has a positive effect on the torque density of the planetary magnetic gear, since its weight is reduced, and the maximum transmissible torque is quite similar to the standard configuration.

6.2 Prototype dimensions

The prototype sizing proposed in the previous section considers a T_{sc}, namely the transmissible torque at the inner rotor between sun and carrier, between in the range between 20 Nm and 30 Nm. Since the PMG is used as a speed reducer, the torque at the external rotor and at the middle rotor will be greater, according to the transmission ratio defined by the number of magnetic pole pairs. Hence, with a gear transmission ratio between inner and outer rotor $\tau_{s/r} = -2.6$, and a gear ratio between sun and carrier $\tau_{s/c} = 3.6$, the transmitted torque will be between 46 Nm and 108 Nm. Therefore, appropriate electric motors will be necessary to be able to transmit the mentioned torques. This reason leads to the choice of reducing much more only the axial length of the PMG, keeping constant all the other dimensional parameters, in order to be able to realise a test bench with the magnetic gear protype and two electrical motors, which must be connected to the input and output shafts of the PMG prototype.

Table 6.5 – PMG prototype dimensions and results.

Parameter	**Value**	**Unit**
Sun PM thickness $th_{PM,s}$	6.75	mm
Ring PM thickness $th_{PM,r}$	5	mm
Steel poles thickness th_{poles}	4.25	mm
Sun yoke thickness $th_{yoke,s}$	13	mm
Ring yoke thickness $th_{yoke,r}$	11	mm
Air gap	1.5	mm
Gear external radius R_{ext}	62.5	mm
Gear axial length L	10	mm
Sun PMs pole pairs n_s	5	-
Ring PMs pole pairs n_r	13	-
Carrier steel poles q	18	-
Gear transmission ratio $\tau_{s/r}$	-2.6	-
Results	**Value**	**Unit**
Torque inner rotor (sun) T_{sc}	2.29	Nm
Torque outer rotor (ring) T_{cr}	5.95	Nm
Torque carrier T_c	-8.24	Nm
Weight m_{PMG}	0.73	kg
Torque density T_ρ	3.13	Nm/kg

After the appropriate sizing has been defined the first release of the PMG prototype has been designed using Solidworks software, as better illustrated in the next section.

6.2.1 First release of a PMG prototype

The first release for the PMG prototype include both an active part, able to transmit torque between the three rotors and a passive part, necessary to connect the system with the external environment. In Figure 6.3 the active part of the PMG prototype is reported. The sun of PMG is connected to the input shaft of the prototype by means of four parallel keys, which number avoids a dynamic unbalance of the rotor at high rotational speeds. The PMs are then fixed to the sun and ring rotors using glue and the two rotor shoulders together with the spacers of the assembly guarantee their correct axial position. Instead, the carrier is made of resin material, which structure houses the ferromagnetic poles.

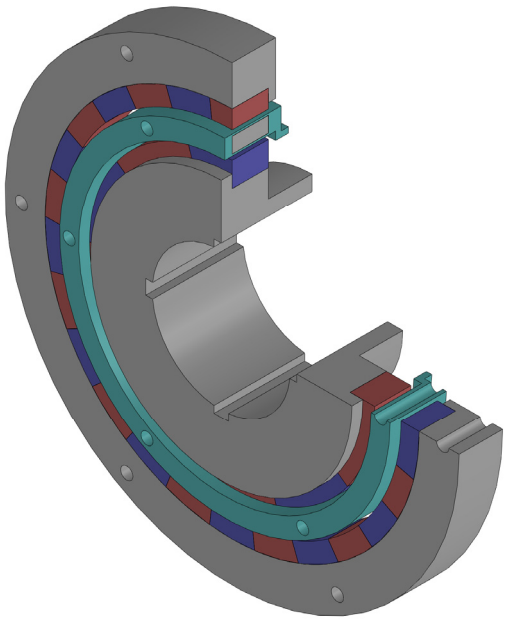

Figure 6.3 – Active part of PMG prototype.

The active PMG is then mounted inside the assembly proposed in Figure 6.4 in two different configurations. In the former (left), the carrier is fixed to the bottom plate using some screws while the ring rotor is connected through a flange to the output shaft. In the latter (right) the ring is fixed, and the carrier is connected to the output. Instead, in both arrangements the input shaft is always connected to the sun rotor. The idea to test the magnetic gear in a dual way derives from the concept of epicyclic gears which ensure different configurations for the input/output of external power.

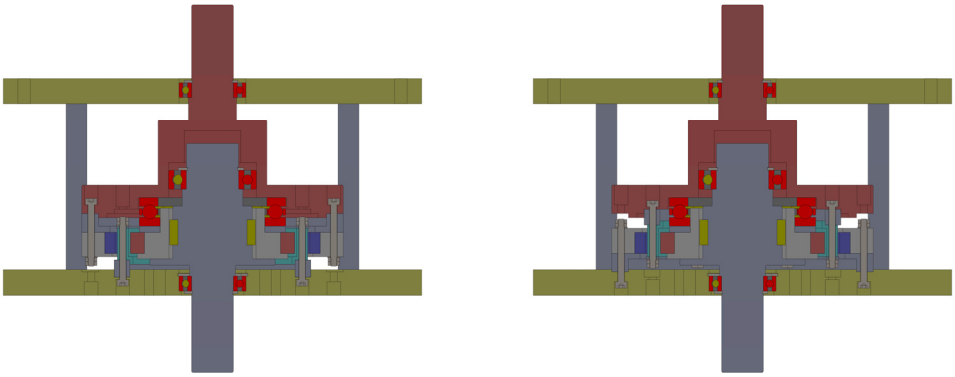

Figure 6.4 – First release of magnetic gear assembly in two different operative conditions: carrier fixed (left) and ring fixed (right).

The advantages of this prototype release are mainly linked to its simplicity, given by a limited number of components in addition to the active PMG, which guarantees a low weight of the system. But its simplicity likewise leads to several drawbacks, due to the difficulty of assembling the prototype and to the possibility of changing the configuration, but in a very invasive way, with the issue of replicating the concentricity of magnetic rotors once the prototype has been disassembled. Hence, the prototype design moved to a second release with fewest downsides.

6.2.2 Second release of a PMG prototype

The new proposed version consists of an external structure, which include the active PMG, and the procedure for configuration modification is realised in a simpler way, just exchanging only some screw connections of the prototype. Both configurations are illustrated in Figure 6.5, where on the left side the external ring is fixed to the bottom plate and the carrier is connected to the output shaft through a connecting flange. Likewise, on the right, the carrier is fixed to the bottom plate and the ring rotates together with the output shaft. Moreover, a conical coupling is chosen to connect the input shaft of the prototype with the inner rotor of the active PMG, adopting a solution cheaper than using four parallel keys and avoiding at the same time the issue of dynamic unbalance.

The main advantages of this release are mainly related to the possibility of changing configuration in a quickly way, just switching some screws. Moreover the magnetic gear prototype can be considered as a device completely independent from the test bench, which have to be realise for the experimental tests. On the other side, the presence of a higher number of radial and axial bearings causes more dissipation, reducing the mechanical efficiency between input and output of the system, even if the magnetic properties and the maximum transmissible torque between the magnetic rotors is still the same if compared with the active PMG of the first release.

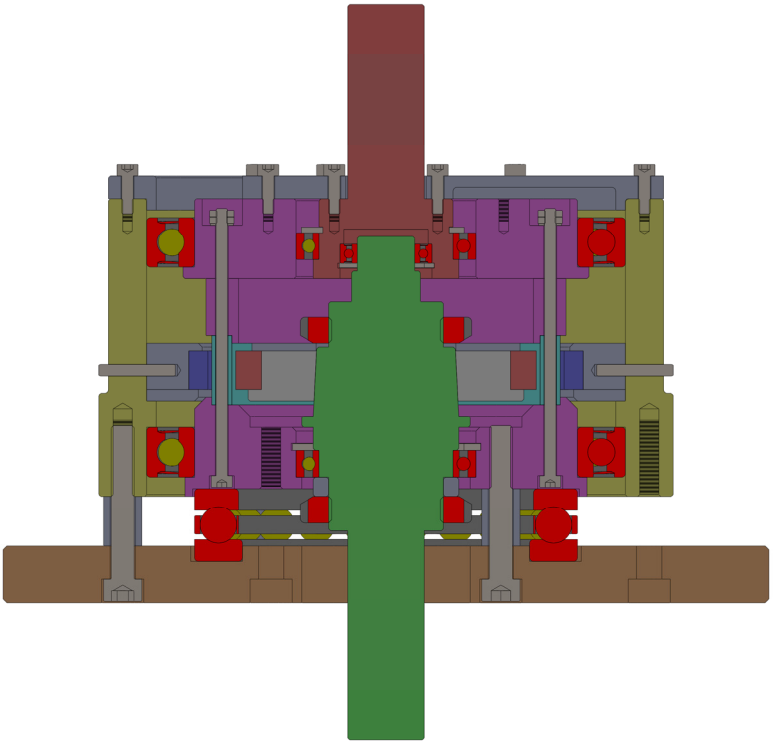

Figure 6.5 – Second release of magnetic gear prototype.

Other drawbacks are instead related to the cost for realisation of prototype since the presence of rare-earth customised PMs requires the adoption of components in titanium, which is a paramagnetic and non-conductive material, to avoid its magnetisation and eddy currents.

6.2.3 Third release of a PMG prototype

The third designed release is based on the main topological assumptions of the second release. Hence the parametric properties of the model are still retained, ensuring the possibility of different configuration between power input and power output. The primary difference versus the previous release concerns the active part of the magnetic gear prototype, reported in Figure 6.6. In fact, a low-cost solution with commercial rare-earth PMs and commercial ferrite poles is proposed with the possible adoption of plastic material for the PMG and for the external components to realise with 3D printing. Even if the overall dimension of the prototype are similar to the previous version, the torque density of the PMG is lower due to the presence of larger air gaps between the PMs of inner and outer rotors and the ferrite poles of the middle rotor.

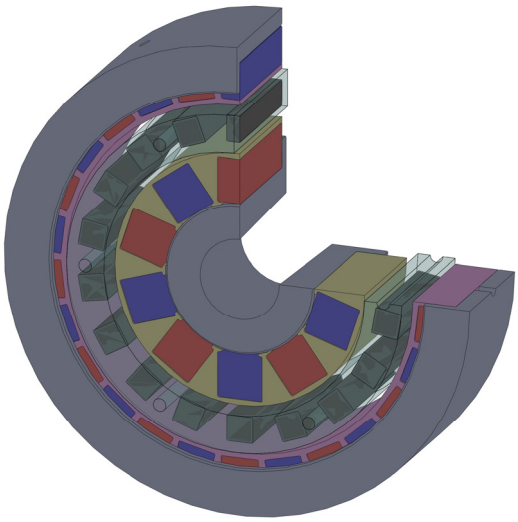

Figure 6.6 – Active part of third release PMG prototype.

The adoption of this low-cost solution could be useful to realise a demonstrator for didactical applications, while the second release is preferred to experimentally test the mechanical and magnetic properties of the prototype in order to validate the simulative results.

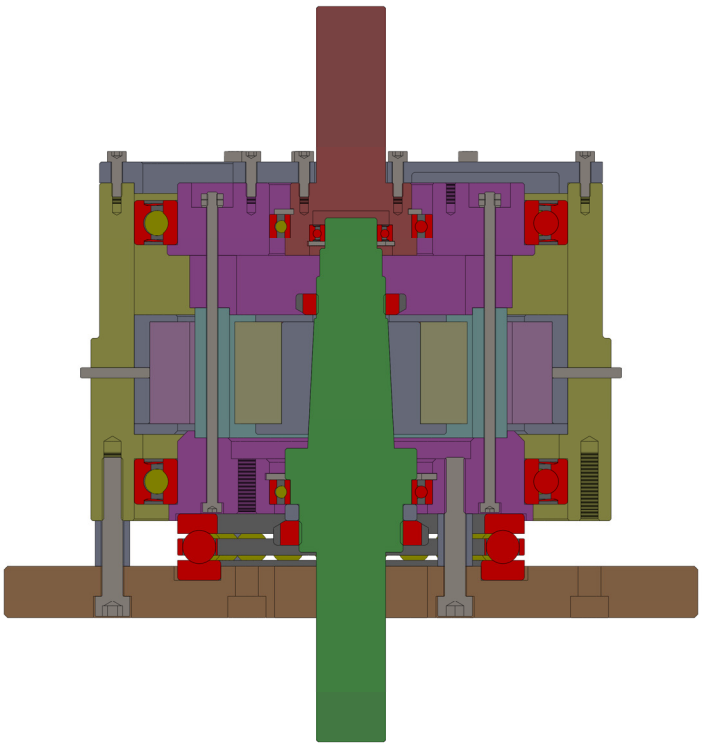

Figure 6.7 – Third release of magnetic gear prototype.

6.3 Conclusions

This chapter the CAD design of a PMG prototype has been addressed.

A preliminary activity has concerned the analysis on FEMM of four different arrangements of PMs on inner and outer rotors: in particular, the effect of their segmentation on the transmissible torque capability and PMG torque density has been investigated to reduce the thermal dissipations due to eddy currents, since the segmentation reduces the PMs conductivity.

After then the main constructional parameters of a PMG have been defined and three different releases of PMG prototype have been proposed, highlighting advantages and drawbacks of each solution. One of the main criteria in the design of the prototype was its parametricity, hence it has been made possible to change the configuration to have different input/output solution with carrier or ring fixed.

Chapter 7

7. The concept of a magnetic gearbox: from the working principles to the prototype

Nowadays the automotive world is facing a new challenge. In fact, with the increasing of vehicle electrification, the automotive companies are moving to green technologies to satisfy the market demand. On the other hand, there is a continuous research of high-performance transmissions in terms of sportiness and efficiency, which is conducting to new mechanical transmission technologies to ensure fast gear-shifting with uninterrupted torque transfer to the driving wheels.

In § 3 a methodology for the objective evaluation of induced vibrations during gearshift in a DCT gearbox has been proposed, with a sensitivity analysis on model parameters to improve NVH performance. In § 4-5 magnetic gears have been proposed as a feasible technology respect to the mechanical counterpart, since recent magnets, based on rare-earth materials, show strong physical properties that could be very attractive for large new markets and applications.

According to a mechanical epicyclic gearing device sketch, there are some different solutions to modulate the mechanical input with respect to get a power transmission conversion in terms of angular velocities and torques. If fact, it is possible to block the carrier connecting the output to the ring, or it is possible to switch the configuration, blocking the ring and having the output power connected to the carrier. The final aim is to have typically larger torques and reduced velocities in the output, using different gear ratios. The most common applications for the concept of gear ratio are car gearboxes for changing the rotational speed between the engine and the wheels, or the automotive differentials to allow steering between left and right wheel. And furthermore, in everyday life there are many applications of the gear ratio concept like washing machines and mixers.

The state-of-the-art gearshift systems are generally composed of a set of mechanical gears as gear wheels, pinions, racks, etc, which are properly arranged

in order to take on a plurality of configurations according to the desired transmission gear ratio. However, presently there are no consolidated technologies of magnetic gearboxes and hence the invention proposed by the author of this PhD thesis and by the other inventors [133] is totally innovative.

Nowadays, in the automotive field the gearbox is an essential component of vehicle power transmission and is made up of classical mechanical gears requiring the use of a clutch to allow the decoupling of rotating elements during gearshifts. Moreover, a fundamental target of the industries is the reduction of system complexity. Considering the classical sketch of an automotive power transmission, it includes the engine, with different solutions, according to the vehicle type such as traditional internal combustion engine solution, hybrid layout or full electric vehicle, then one or more clutches, a mechanical gearbox, and in case a torque limiter.

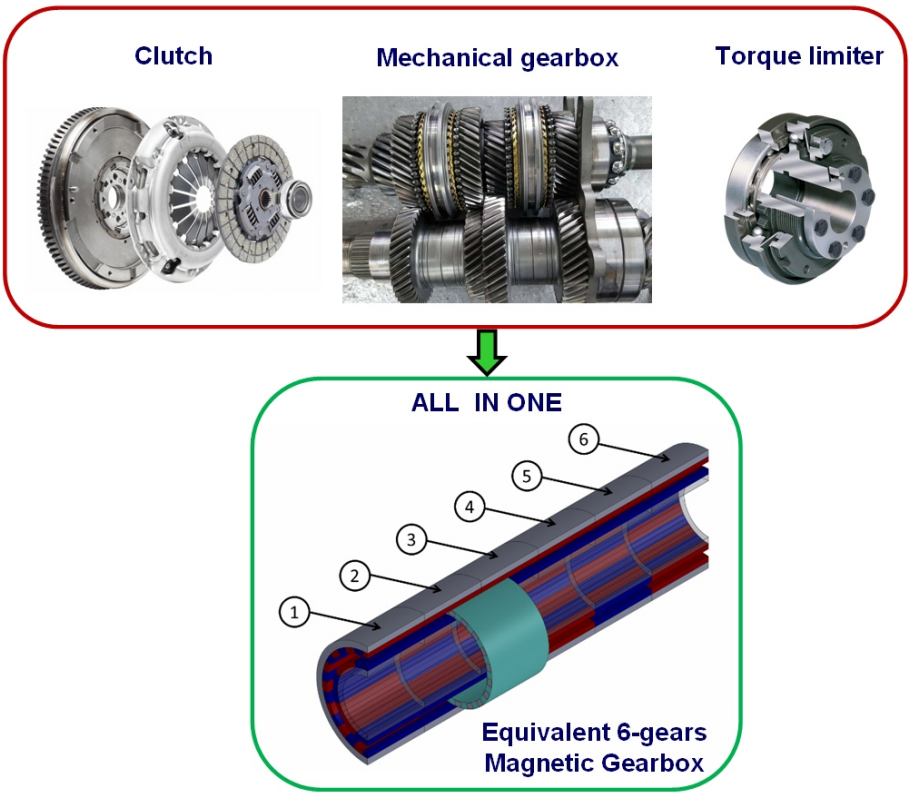

Figure 7.1 – System complexity reduction with magnetic gearbox solution.

The proposed invention, based on the principle of power transmission through magnetic gears, which are characterised by high performance and reliability, enables the integration of the clutch and of torque limiter functions inside the gearbox itself, avoiding the implementation of other mechanical components which are particularly subject to wear, as illustrated in Figure 7.1 with the proposed all-in-one solution. The invention also solves the problem of gear engagement noise, which is typical of traditional mechanical gearboxes, allowing the torque transfer between input and output without contact between mechanical components. Finally, the absence of contact between the mechanical components

avoids wearing and the necessity of lubricant oils, enhancing failure resistance, ensuring a longer life to the system, and introducing an environmental benefit with the reduction of polluting materials.

7.1 Magnetic gearbox description

The proposed magnetic gearbox is an innovative technology, which belongs to the sector of power transmission systems transferring the mechanical power generated by a power input source to a specific application user. For the sake of clarity, it is useful to briefly explain the technology of a traditional gearbox, comparing it to the proposed magnetic solution.

A gearbox system is a device, usually of a mechanical type, characterised by discrete gear ratios, with a minimum of two gear ratios, for instance a chain drive, which can be considered constant or variable, but with a non-zero constant average; it is used to change the transmission ratio between the output of the power source and the input of the user device. In the automotive field, the gearbox systems is used to properly vary the torque transferred from the engine to the vehicle wheels through a transmission driveline. Similarly, gearbox systems are notoriously used in other different industrial fields as, for example, in electrical tools, in surgical instruments, and in energy transformers by means of wind turbine, or other devices.

In general, a magnetic gearbox system can be used with several advantages in all the application fields where it is necessary to vary the transmission ratio between the output of a mechanical power source and the input of a generic user device, hence modulating the transmitted power as a product of torque and rotation speed.

In the automotive field, the clutch is a necessary component to ensure gearshifts, allowing the engine and gearbox elements to be decoupled. Furthermore, by means of the shifter, the drivers activate a particular element inside the gearbox, called synchroniser, whose function is to synchronise the rotational speeds between specific gear wheels inside the gearbox, thus establishing a defined transmission ratio between input and output of the gearbox. the gearshift procedure has been better described in § 3.3. In summary, during any gearshift, the following phases shall be taken into account: clutch disengagement, choice of synchroniser using the shifter, gear synchronisation, gradual clutch engagement, motion of the vehicle with the new gear engaged.

In addition to the constructive and design complexity, mechanical gearbox systems have further disadvantages, such as the necessity to use the clutch which is device subjected to wear. Furthermore, in their basic configuration, the mechanical gearbox systems are not designed to automatically include the function of torque limiter. A further drawback of traditional gearboxes is represented by the contact between the gears of transmission. This feature, in addition to gear wearing phenomenon, requires a periodic maintenance of the

gearbox to refill the lubricant oil, which is necessary for the correct functioning of the transmission gearbox.

In this context, the main purpose of the magnetic gearbox invention is to overcome the mentioned drawbacks present in "state-of-the-art" mechanical gearbox systems. In particular, the proposed invention allows to limit or eliminate the contact areas between the gears of the system. In addition, this technology allows the gearshift, namely the discrete changing of transmission ratio without the aid of additional components subject to wear such as a clutch. The absence of contacts eliminates the consequent need for lubrication which is limited to the bearings only. Finally, the invention allows to limit the torque transferred between the gears of the system without the aid of additional components, like a torque limiter.

The proposed multiple gear ratios magnetic gearbox is based on the principle of power transmission through magnetic gears and consists of a number of coaxial magnetic gears equals to the number of desired gear ratios.

In a possible arrangement the internal rotor is driven by the power source and the external rotor is connected to the user and rotates at a speed determined by the transmission ratio of the selected gear. The intermediate element, containing ferromagnetic poles, creates the torque transfer. By moving its axial position, it can engage with different magnetic rotors allowing the torque transfer between inner and outer rotors with the desired transmission ratio.

Dimensions of the magnetic gearbox and of its inner elements (magnets, ferromagnetic poles, airgaps) are optimised minimising the overall dimensions and maximising the torque transfer capability between input and output. In the following sections several architectures for a mechanical gearbox will be presented and discussed.

7.1.1 Magnetic gearbox with moving carrier

One of the first possible arrangements for a magnetic gearbox is the solution with the carrier subjected to an axial displacement in order to engage with the appropriate gear to transmit torque between input and output at a specific transmission ratio. This proposed solution is reported in Figure 7.2, where a configuration with six transmission ratios is chosen, adapting the magnetic gearbox to an automotive use. The presence of the moving carrier implies that the number of ferromagnetic poles is constant, and thus the number of PMs pole pairs on inner and outer rotors should properly change for each gear to respect one of the fundamental equations of magnetic gears, namely that the number of ferromagnetic poles q must be equal to the sum of inner n_s and outer rotors n_r PMs pole pairs. In the proposed arrangement, the neutral position is not considered, yet. In the same figure it is possible to notice how the carrier moves axially inside the magnetic gearbox engaging with the third gear, with the assumption that the first gear is on the left and the sixth on the right part of the figure.

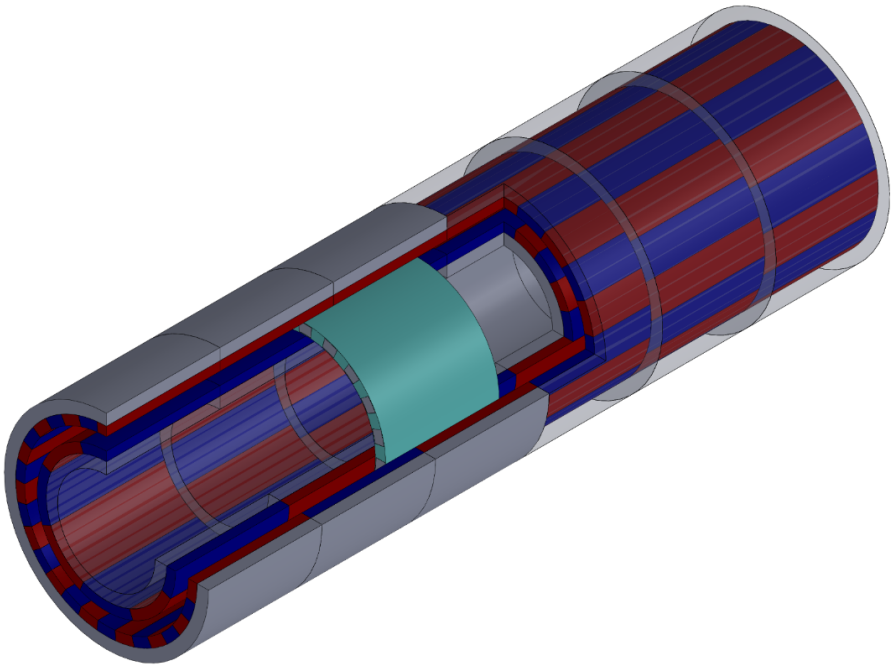

Figure 7.2 – Magnetic gearbox solution with a moving carrier.

The transition phase between the disengagement of the off-going gear and the engagement of the on-coming gear requires to understand what the effects are on speed and torque transmitted between inner and outer rotors and the required time to synchronise the two rotors according to the new transmission ratio of the magnetic gearbox, depending on the number of PMs pole pairs of the magnetic gear is going to be used.

As already mentioned, the use of the clutch can be avoided with the proposed invention of magnetic gearbox, although it is badly needed in a mechanical gearbox. In fact, by means of an adequate control of the input motor speed, during the new gear engagement, the carrier is moved with any interruption of the motion transmission between the involved rotors. Moreover, unlike what happens in the mechanical counterpart, the translation of the carrier is not hindered by the presence of constraints deriving from the mechanical contact between the rotating elements.

7.1.2 Magnetic gearbox with moving ring

A further possible solution for a magnetic gearbox, covered by the same patent, consists in having the outer rotor, namely the ring, as the common element of the gearbox, instead of the intermediate rotor, namely the carrier. The proposed solution is represented in Figure 7.3. According to this second configuration, the number of PMs pole pairs for the common outer rotor remains constant while, unlike the previous configuration, the number of ferromagnetic poles of the carrier varies, to fulfil the equation on the proper number of PMs and ferromagnetic

poles. On the other side, the number of PMs pole pairs on the inner rotor is instead different for each of the single magnetic gears that make up the magnetic gearbox.

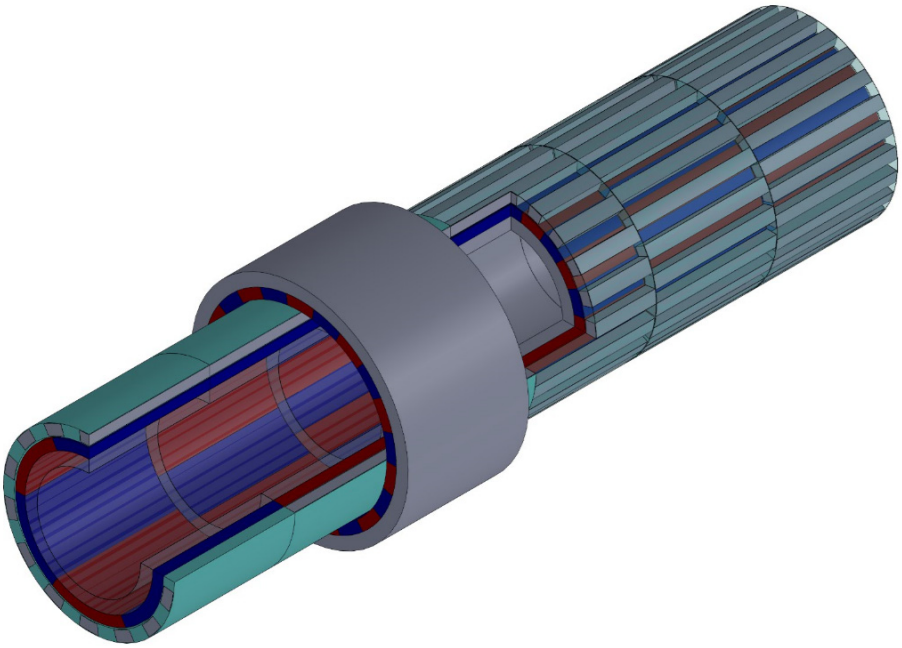

Figure 7.3 – Magnetic gearbox solution with a moving ring.

Therefore, the relationship $q = n_s + n_r$ is still valid for each stage of the gearbox, although the implementation solution is different. This configuration is particularly advantageous from an economic point of view, since the costs related to the construction of the permanent magnets on the outer rotor is significantly reduced. According to this solution, a possible arrangement could be with the power source connected to the inner rotor, while the utiliser can be connected both to the external ring or to the intermediate rotor. In the first case, the outer rotor will be subjected to a roto-translation, especially during the gear engagement, rotating in opposite direction with respect to the inner rotor, while the ferromagnetic rotor has only the function of concatenating the magnetic flux between PMs of inner and outer rotors. Instead, as regards the second case, the outer rotor will be devoted only to the axial translation, while the intermediate rotor will be connected to the output, rotating in the same direction of the input shaft.

7.1.3 Magnetic gearbox with moving sun

Another innovative solution for a magnetic gearbox, in contrast with the previous one, consists in having the inner rotor, namely the sun, as the common element of the magnetic gearbox. The proposed solution is reported in Figure 7.4. According to this third possible configuration, the number of PMs pole pairs for the common inner rotor remains constant while the number of ferromagnetic poles

of the carrier and of the PMs on the outer rotor varies to fulfil the equation $q = n_s + n_r$.

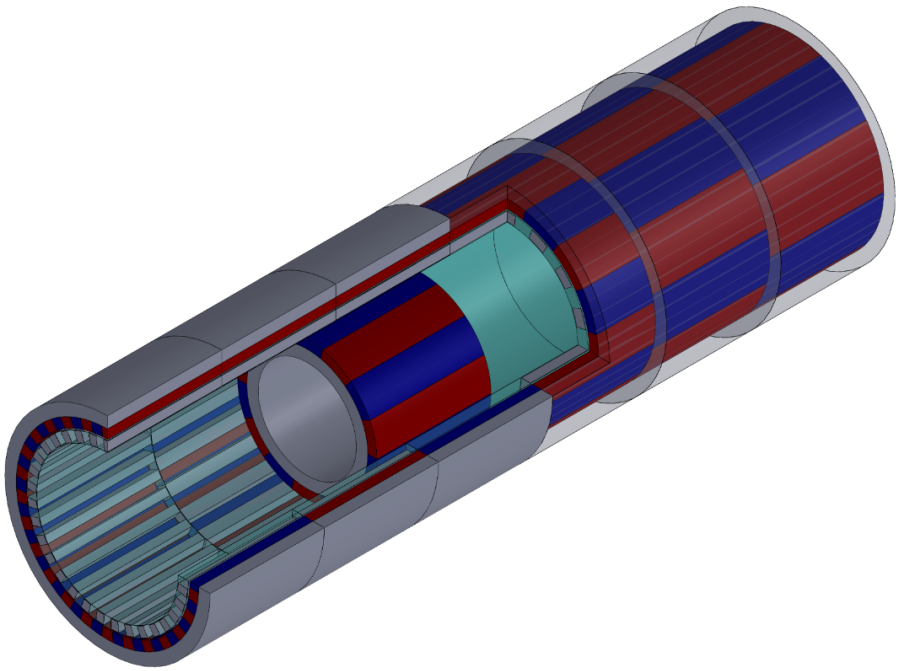

Figure 7.4 – Magnetic gearbox solution with a moving sun.

For this solution, as for the previous one, two possible arrangements could be proposed: in the former the inner rotor will be subjected to a roto-translation, especially during the gear engagement, while in the latter it is devoted only to the axial translation. To be clear, different combinations of input/output can be arranged with the three rotors, to ensure the desired transmission ratio and the desired rotation direction for the shafts of the magnetic gearbox.

7.1.4 Two stages magnetic gearbox with two moving carrier

A more compact innovative solution can be achieved with a multi-stage magnetic gearbox. In Figure 7.5 a two-stage magnetic gearbox is reported. It is made of three rotors, namely inner, middle, and outer rotors and two moving carriers, which are necessary for the magnetic interaction between other rotating elements. In this new arrangement, the relation $q = n_s + n_r$ is still respected both for the coupling between inner and middle rotor through the inner carrier and for the interaction between middle and outer rotor by means of the external carrier.

This proposed solution can be used in two different ways. In the former, the two stages are used to amplify the transmission gear ratio of the single stage, so it is possible to combine the axial positions of the two carriers to achieve several different transmission ratios, which number depends on the stage number and on the number of magnetic gears for the single stage. Hence, assuming for this case a

stage number of $n_{stage} = 2$ and setting the number of magnetic gears equal to $n_{MG} = 3$, the total number of transmission gear ratios is $n_{tau} = n_{MG}^{\ n_{stage}} = 9$.

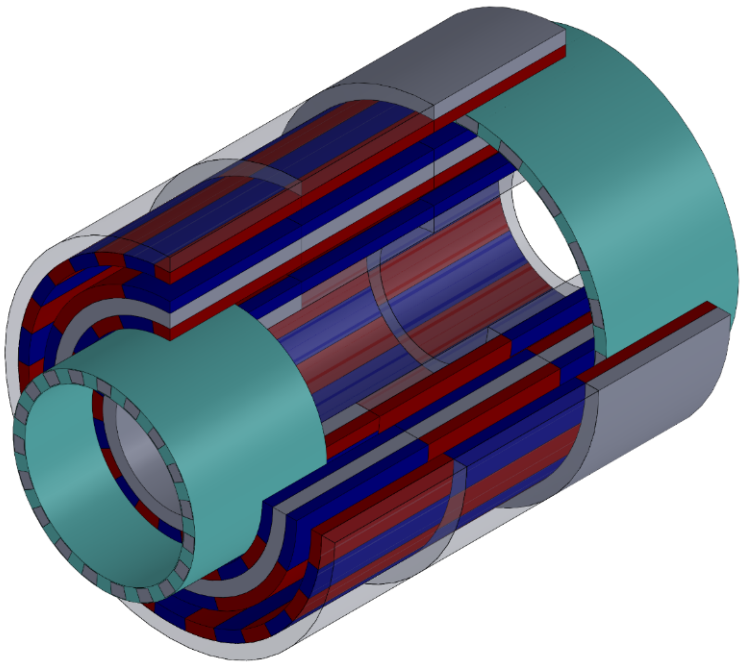

Figure 7.5 – Multi-stage magnetic gearbox solution with two moving carriers.

Instead, in the latter operating condition, and in similarity with the DCT gearbox analysed in § 3, the power input can be connected to the middle rotor, while the inner and outer rotors can be considered as the two secondary shafts of a DCT transmission. Therefore, for a six-gear gearbox, the outer rotor can be used for the first three gears, namely from 1st to 3rd, which require a higher torque than the input shaft, since the torque capability of a magnetic gear depends on some geometrical parameters and in particular it is proportional to the circumferential length. On the other side, the inner rotor will be used for the gears from 4th to 6th, which require a lower torque and higher rotational speeds than the input shaft.

7.1.5 Applications and overcome of other previous patented solutions

The proposed invention finds a possible application in several sectors of the industrial world. The automotive field is certainly the closest for the development and marketing of the proposed technology, with its possible implementation in vehicles with internal combustion engines, in hybrid vehicles, and in fully electric vehicles. Other sectors that may be strongly affected by this technology are automation and robotics, aerospace, military, and wind energy.

As already mentioned in § 4.3.2, Atallah proposes in [118] a variable magnetic gear in which the carrier is connected to an auxiliary motor in order to regulate the transmission ratio between sun and ring, acting as a continuous

variable magnetic transmission. Instead, as regards the magnetic gearbox object of my research activity, there is not a motor devoted to the rotation of the carrier, which is subjected only to an axial translation. This aspect reduces the complexity of the magnetic gearbox and of its control during experimental activities.

The variable gear ratio magnetic gearbox, proposed by Montgomery in [134], is made of inner and outer magnetic rotors, with the coupling element, namely the carrier, which comprises a plurality of magnetisable lamellae. Each interpole is formed from a group of neighbouring lamellae. Selected lamellae can be disabled to provide boundaries between adjacent interpoles. This allows different numbers and arrangements of interpoles to be formed, to provide different gear ratios between the first and second gear members. Moreover, Montgomery's solution proposed as second option the construction of an array of ferromagnetic poles connected by springs with a system of insertion and disarming of the poles, and as third option of using auxiliary windings on the ferromagnetic poles of the internal rotor to regulate their saturation and their effect on the transmission ratio. On the contrary, our solution does not require any type of auxiliary winding and relative power supply converter. In addition to this, the Montgomery's proposed solutions for activation/deactivation by saturation and/or connection/disconnection do not allow to maintain a fixed ratio between ferromagnetic and magnetic poles, compromising the performance in terms of efficiency and torque oscillations (torque ripple). Instead, our patent always guarantees compliance with this condition, allowing us to operate in optimal conditions. Finally, the magnetic gearbox patented by Cruden in [135] requires a system of mechanical gears coupled to a magnetic gear in order to adjust the gear ratio, acting with a mechanism similar to a synchroniser to engage the proper transmission ratio to put in rotation the carrier of the magnetic gear, hence operating as a continuous variable transmission. As previously stated, in our magnetic gearbox the carrier is subjected only to an axial translation.

For sake of clarity, other several patents on magnetic gears are available, and other patents on magnetic gearbox acting as a variable transmission, with the three rotors in simultaneous rotations have been analysed to highlight and put in evidence the advantaged of our solution. The three patents here mentioned are those more exhaustive and complete, although quite different from our proposed technology.

7.2 Study of gearshift procedure with analytical approach

The dynamic analysis of the transition phase during the gear engagement of a different PMG in a magnetic gearbox is an essential step for the appropriate control of a test-bench for power transmission application, which include a magnetic gearbox. Firstly, a simple dynamic model, representing a motor connected to the vehicle load through a magnetic gearbox is considered. Then, five different manoeuvres are considered to switch from the first gear ratio to the

second one, including two acceleration phases to achieve the stationary condition at a certain gear ratio and three phases to manage the upshift phase.

7.2.1 Dynamic model

As previously told, in a transmission driveline it is very important to study the dynamic behaviour of its inner components, especially in the transition phases, which happen during upshifts or downshifts. In this section an analytical approach is used to study the transition phase, integrating the system motion equation. Alternatively, when it is impossible to solve the dynamic equations using simple integrals, the system differential equation is solved using Matlab function `ode45`. The system analysed is represented in Figure 7.6, where at one side a motor is connected to the planetary magnetic gear of the magnetic gearbox, while on the other side the load, namely a rotating inertia, represents the vehicle resistance.

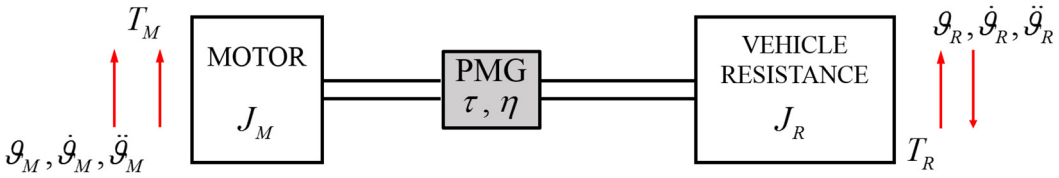

Figure 7.6 – Schematic diagram of a system with motor, gearbox, and load.

The system is divided into three subsystems to write the dynamic equations, according to Figure 7.7. The actual PGM of the gearbox is characterised by a given gear ratio τ and by an efficiency η.

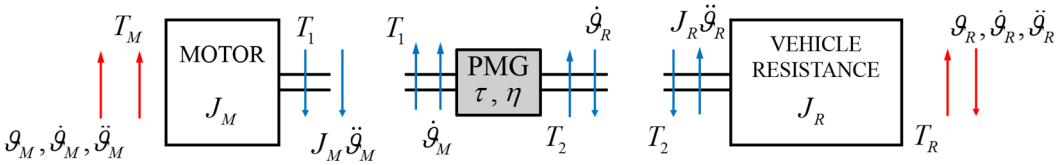

Figure 7.7 – Schematic diagram of the three subsystems.

For the first subsystem, namely the input motor, the equation is written as:

$$T_M - T_1 - J_M \frac{d\dot{\vartheta}_M}{dt} \tag{7.1}$$

where T_M and T_1 are the motor torque and the internal torque between motor and PMG, respectively, while J_M in the motor moment of inertia. Instead, for the second subsystem, that is the planetary magnetic gear the set of equations in Eq. (7.2) is written:

$$\eta = \frac{P_{out}}{P_{in}} = \frac{T_2 \dot{\vartheta}_R}{T_1 \dot{\vartheta}_M} = \frac{T_2}{\tau T_1}$$
$$T_2 = \eta \tau T_1 \tag{7.2}$$

where $\tau = \frac{\dot{\vartheta}_M}{\dot{\vartheta}_R}$ is the gear ratio between input and output rotational speeds. For the third subsystem, which represents the vehicle load Eq. (7.3) is written:

$$T_2 - T_R - J_R \frac{d\dot{\vartheta}_R}{dt} \tag{7.3}$$

where T_R and T_2 are the resistive torque and the internal torque between load and PMG, respectively, while J_R in the moment of inertia that represents the vehicle.

It is now possible to write the dynamic equation of an equivalent system, where rotational acceleration and speeds are evaluated at the input motor as done for resistive torque and moments of inertia. The characteristic equation of the equivalent system is here reported:

$$T_M - T_R' - J_{eq} \frac{d\dot{\vartheta}_M}{dt} = 0 \tag{7.4}$$

where T_R' is the resistive torque evaluated at the input motor and $J_{eq} = J_M + \frac{J_R}{\eta \tau^2}$ is the equivalent moment of inertia of the global system.

7.2.2 Gearshift procedure

The magnetic gearbox, analysed in this section, consists of two different PMG with a different gear ratio. Therefore, a torque profile for the input motor that depends on the rotational speed and two different resistive torque, evaluated for each gear ratio of the magnetic gearbox, is obtained in Figure 7.8.

The motor torque law is given by Eq. (7.5):

$$T_M = T_{M_0} - k_M \dot{\vartheta}_M - T_{B_M} \tag{7.5}$$

where k_M is a constant related to the slope of the dash-dotted blue line in the previous figure, which represents a simplified linear torque characteristic for an electric motor, T_{M_0} is the maximum torque at null engine speed, while T_{B_M} are the dissipation torques related to the vehicle utilities and to the bearings on the first part of the driveline. The two resistive torques (red and black lines) are instead related to the vehicle rolling resistance and it could be written as Eq. (7.6):

$$T_R = f_0 + f_2 \dot{\vartheta}_R^{\,2} + T_{B_R} \tag{7.6}$$

where f_0 and $f_2 = 0.5\,\rho\,C_d\,A_f\,R^3$ are two constant terms depending on tyres and vehicle dimensions, air density and drag coefficient, while T_{B_R} represents the dissipation torques related to the bearings on the second part of the transmission driveline.

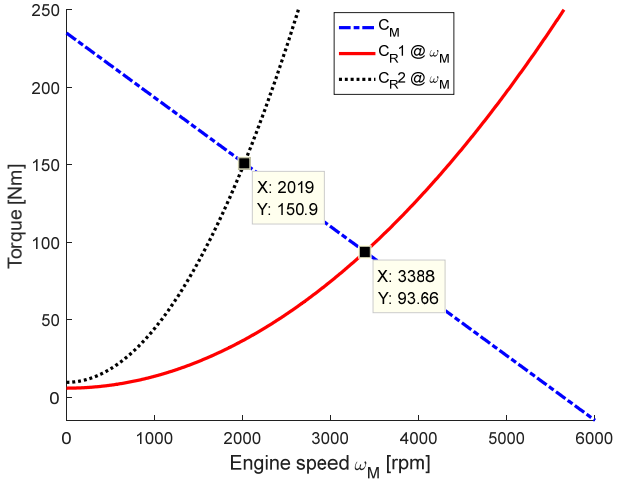

Figure 7.8 – Operative torque characteristic of a magnetic gearbox driveline.

As written previously, the resistive torque is evaluated at the input motor using the transmission gear ratio. The intersection of the blue line with the two resistive torques returns the stationary condition for each of the transmission gear ratios. In Table 7.1 some reasonable values for the system parameters are listed.

Table 7.1 – Parameters of the transmission driveline with a magnetic gearbox.

Type	Parameter	Value
Inertia	J_M [kg m2]	0.025
	J_R [kg m2]	130
Bearing torque	T_{B_M} [Nm]	15
	T_{B_R} [Nm]	5
Rolling resistance	f_0 [Nm]	10
	f_2 [Nms2/rad2]	0.0123
Transmission gear ratio	τ_1 [-]	-13/5 = -2.6
	τ_2 [-]	-11/7 = -1.57
Motor	k_M [Nm/rad]	0.398
Gearshift time	t_{CM} [s]	2

The first phase of the simulated manoeuvre represents an acceleration starting from a non-zero rotational speed of the rotating parts. In Figure 2.2 the magnetic

gearbox in working with the first gear ratio τ_1 given by the number of permanent magnets on inner and outer rotors of the corresponding planetary magnetic gear.

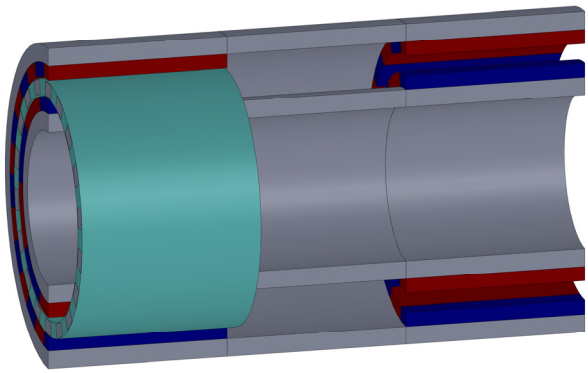

Figure 7.9 – Magnetic gearbox working at first gear ratio τ_1

In this condition it is necessary to solve Eq. (7.7):

$$\frac{d\dot{\vartheta}_M}{dt} = \frac{T_M - T_R{}'}{J_{eq}} = \frac{T_{M_0} - k_M \dot{\vartheta}_M - T_{B_M} - \left(f_0 + \frac{f_2}{\tau_1^3 \eta} \dot{\vartheta}_M{}^2 + \frac{T_{B_R}}{\tau_1 \eta} \right)}{J_{eq}} \tag{7.7}$$

This phase allows the system to get the first stationary condition. After that the disengaging phase occurs. The input motor torque is linearly reduced and the system is in a configuration like that reported in Figure 7.10 (left).

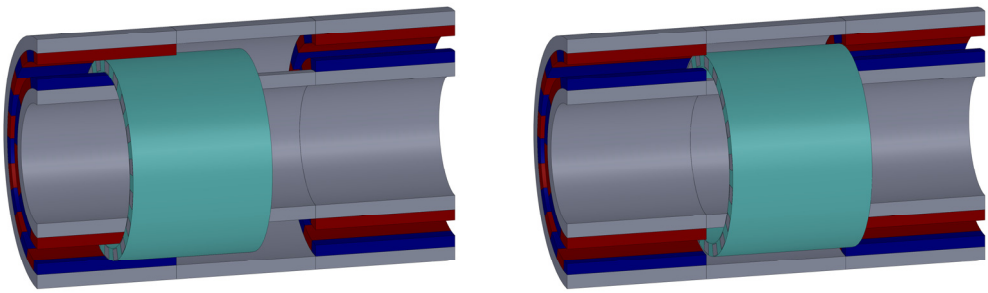

Figure 7.10 – Magnetic gearbox during disengaging (left) and in neutral position (right).

The input torque in this phase is written as:

$$T_{M,2} = T_M\left(1 - x_{CM}\right) = T_M\left(1 - \frac{2\left(t - t_1\right)}{t_{CM}}\right) \tag{7.8}$$

where $T_{M,2}$ is the input torque in the second phase, $0 \le x_{CM} \le 1$ is the axial displacement of the carrier inside the PMG from the engaged position (1) to the neutral one (0). Then, t_{CM} is the total time for disengaging and engaging and t_1 is the time at the end of the first acceleration phase. Therefore, it is necessary to solve the differential equation reported in Eq. (7.9):

$$\frac{d\dot{\vartheta}_M}{dt} = \frac{T_M - T_R{}'}{J_{eq}} = \frac{\left(T_{M_0} - k_M\dot{\vartheta}_M\right)\left(1 - \frac{2\left(t - t_1\right)}{t_{CM}}\right) - T_{B_M} - \left(f_0 + \frac{f_2}{\tau_1^3\eta}\dot{\vartheta}_M{}^2 + \frac{T_{B_R}}{\tau_1\eta}\right)}{J_{eq}} \tag{7.9}$$

In the third phase the input motor and the vehicle load are uncoupled in order to suddenly reduce motor speed to correctly complete the engaging phase. The governing equations of this phase are reported in Eq. (7.10):

$$\begin{aligned} \frac{d\dot{\vartheta}_M}{dt} &= \frac{-T_{B_M}}{J_M} \\ \frac{d\dot{\vartheta}_R}{dt} &= \frac{-\left(f_0 + f_2\dot{\vartheta}_R{}^2 + T_{B_R}\right)}{J_R} \end{aligned} \tag{7.10}$$

This phase continues until time t_3 when the $\vartheta_M = \tau_2\,\vartheta_R$ and then the engaging phase begins, followed by another acceleration phase, which are represented in Figure 7.11.

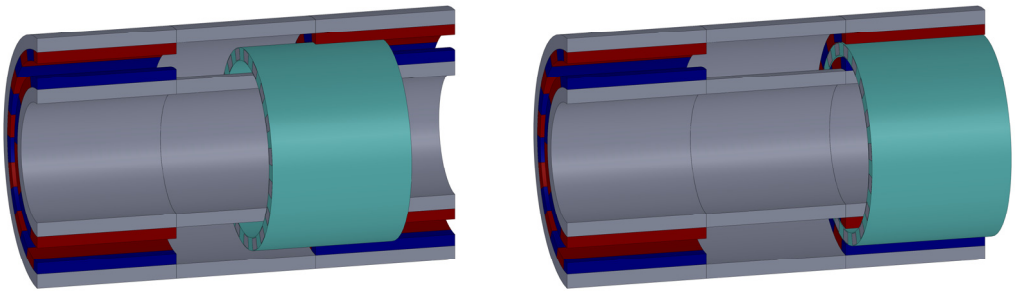

Figure 7.11 – Magnetic gearbox during engaging (left) and working at second gear ratio τ_2 (right).

During the engaging phase the system governing equation is reported in Eq. (7.11), that is the same of Eq. (7.9) but with τ_2 instead of τ_1:

$$\frac{d\dot{\vartheta}_M}{dt} = \frac{T_M - T_R'}{J_{eq}} = \frac{\left(T_{M_0} - k_M \dot{\vartheta}_M\right)\left(\frac{2(t-t_3)}{t_{CM}}\right) - T_{B_M} - \left(f_0 + \frac{f_2}{\tau_2^3 \eta}\dot{\vartheta}_M{}^2 + \frac{T_{B_R}}{\tau_2 \eta}\right)}{J_{eq}} \quad (7.11)$$

Finally in the last acceleration phase the system equation is the same of Eq. (7.7), but with τ_2 instead of τ_1 as in Eq. (7.12):

$$\frac{d\dot{\vartheta}_M}{dt} = \frac{T_M - T_R'}{J_{eq}} = \frac{T_{M_0} - k_M \dot{\vartheta}_M - T_{B_M} - \left(f_0 + \frac{f_2}{\tau_2^3 \eta}\dot{\vartheta}_M{}^2 + \frac{T_{B_R}}{\tau_2 \eta}\right)}{J_{eq}} \quad (7.12)$$

The rotational speeds of the input motor and of the output shaft are reported in Figure 7.12. The four dashed vertical black lines separate the five different phases of the upshift manoeuvre.

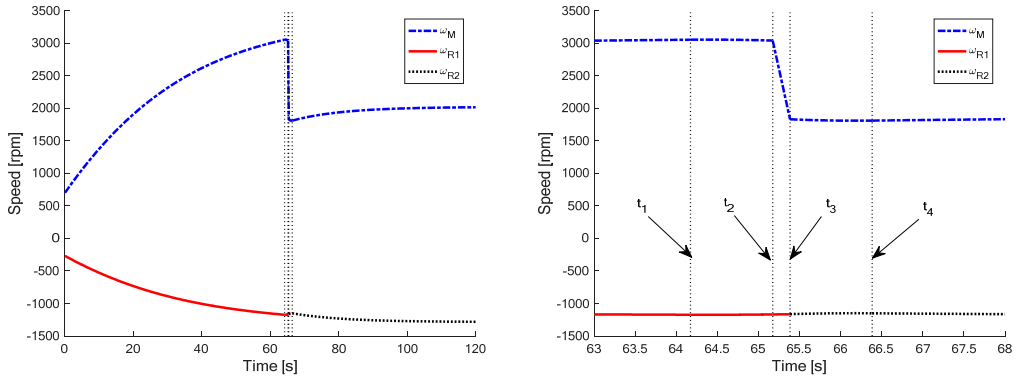

Figure 7.12 – Input motor and output speeds.

The time in neutral position at time $t_2 \le t \le t_3$ is necessary to decrease the engine speed up to the new rotational speed, determined by the new transmission gear ratio τ_2. To conclude, in Figure 7.13 the trend of the input motor torque is reported.

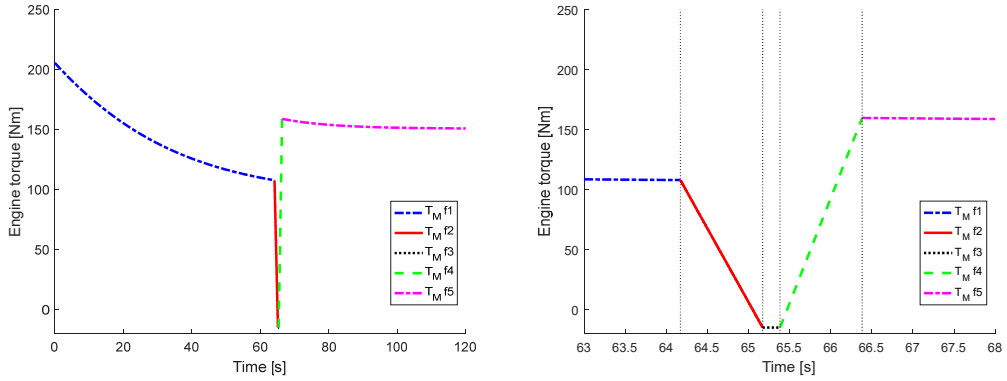

Figure 7.13 – Motor torque.

During the disengaging and the new engaging phase the magnetic gear acts as a torque limiter with a linear decrement of the transmitted torque, depending on the axial translation law of the ferromagnetic carrier.

7.3 PID controller

A proportional-integral-derivative (PID) controller [136] is a closed loop feedback algorithm. It is used where a continuous modulated control is required. In Figure 7.14 the block diagram of a PID controller is reported.

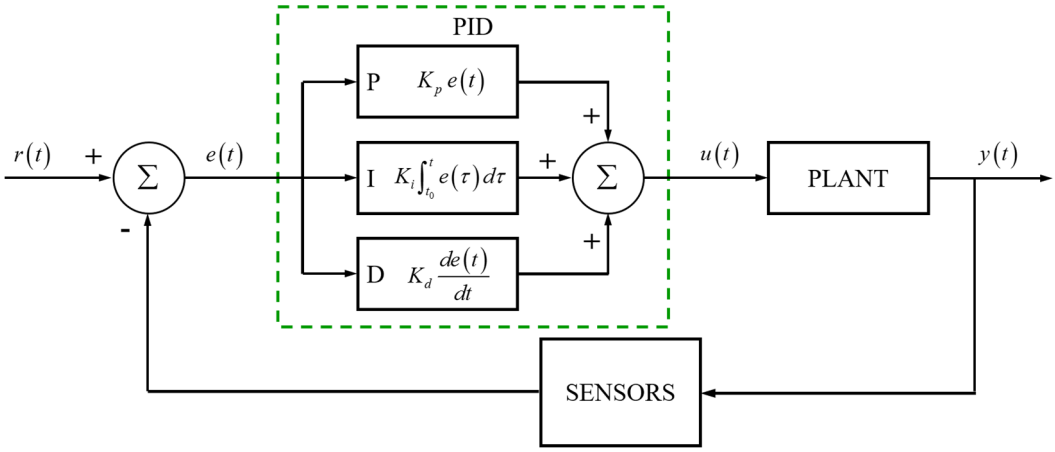

Figure 7.14 – Block diagram of PID controller in a feedback loop.

It calculates an error $e(t)$, then applies a responsive correction to control function based on proportional, integral and derivative terms. The error $e(t)$, namely the input of the PID is given by Eq. (7.13):

$$e(t) = r(t) - y(t) \tag{7.13}$$

where $r(t)$ is the desired setpoint, or reference, and $y(t)$ is the output variable of the system that should be controlled. The PID controller acts on the error $e(t)$ acting a correction based on three different gains. The mathematical form in time domain is given by Eq. (7.14):

$$u(t) = K_p\, e(t) + K_i \int_{t_0}^{t} e(\tau)\, d\tau + K_d \frac{de(t)}{dt} \tag{7.14}$$

while in Laplace domain it is given by Eq. (7.15):

$$C(s) = K_p + \frac{K_i}{s} + K_d\, s \tag{7.15}$$

where K_p, K_i, K_d represents gains for the proportional, integral and derivative actions of the PID controller. The block diagram of a PID controller in the Laplace domain is reported in Figure 7.15.

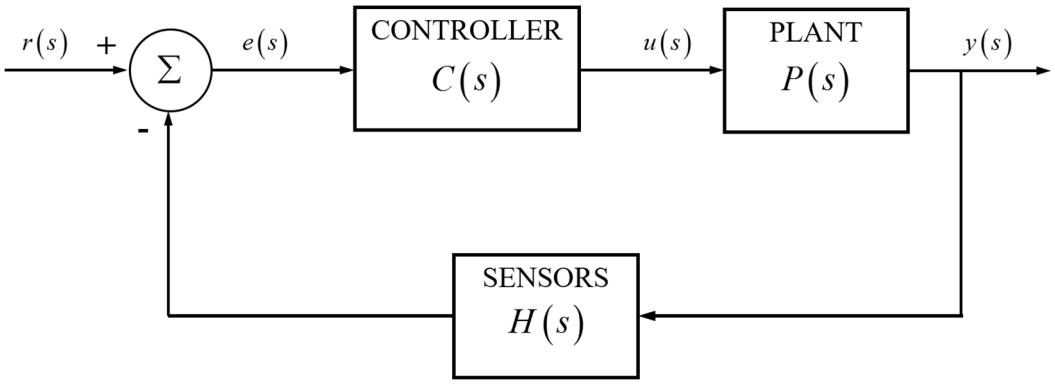

Figure 7.15 – Block diagram of PID controller in Laplace domain.

The Eq. (7.14) could be written as Eq. (7.16):

$$u(t) = K_p\left(e(t) + \frac{1}{T_i}\int_{t_0}^{t} e(\tau)\,d\tau + T_d\frac{de(t)}{dt}\right) \tag{7.16}$$

where T_i, T_d are the time constant of integral and derivative PID actions. These two parameters are correlated with K_i, K_d by Eq. (7.17):

$$K_i = \frac{K_p}{T_i} \quad , \; K_d = K_p T_d \tag{7.17}$$

A PID algorithm includes an only proportional (P) controller, a proportional-integral (PI) controller or a proportional-derivative (PD) controller. In Table 7.2 different type of PID controller are summarised.

Table 7.2 – PID controllers.

PID type	**Parameters**		
P	$K_p \neq 0$	$T_i \to \infty$	$T_d = 0$
PI	$K_p \neq 0$	$T_i \to \infty$	$T_d \neq 0$
PD	$K_p \neq 0$	$T_i \neq 0$	$T_d = 0$
PID	$K_p \neq 0$	$T_i \neq 0$	$T_d \neq 0$

In a PID controller each gain has a specific function:

- K_p, namely the proportional gain, directly changes the magnitude of the input, this means that if the system has a non-null steady-state error, it will be proportionally magnified;

- K_i, namely the integral gain, is commonly considered linked to error of the time history and practically its effect is much more powerful if the integral of the error is larger, while it decreases in effect when the integral of error is low. This is the usual reason why in the asymptotic stable system the integral gain is very low or neglected;
- K_d, namely the derivative gain, is based on the rate of change of the error: if the error rapidly increases, then derivative action will be stronger. This term adds the ability of the controller to anticipate the error and this anticipation tends to add damping to the system, thereby decreasing overshoot. This term has no effect on the steady-state error.

The transfer function of a PID controller depends on the three gains of the controller itself. Its transfer function is given by Eq. (7.18):

$$C(s) = K_p + \frac{K_i}{s} + K_d\, s = \frac{K_d\, s^2 + K_p\, s + K_i}{s} \tag{7.18}$$

Now, a simple mass-spring-damper system, as reported in Figure 7.16, is considered.

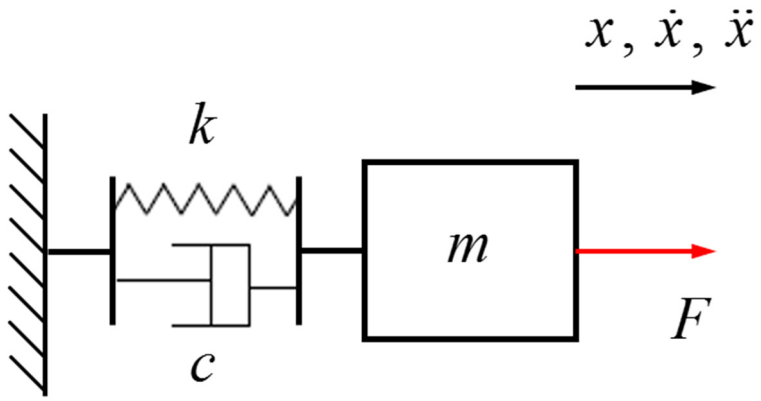

Figure 7.16 – One DOF mechanical system.

The governing equation of the system above is:

$$m\ddot{x} + c\dot{x} + k\,x = F \tag{7.19}$$

that in Laplace domain becomes:

$$m\,s^2 x(s) + c\,s\,x(s) + k\,x(s) = F(s) \tag{7.20}$$

The transfer function between the input force $F(s)$ and the output displacement $x(s)$ is given by:

$$P(s)=\frac{x(s)}{F(s)}=\frac{1}{m\,s^2+c\,s+k} \tag{7.21}$$

Considering the block diagram reported in Figure 7.15 the transfer function of the system with unity-feedback ($H(s)=1$) is given by:

$$T(s)=\frac{y(s)}{r(s)}=\frac{C(s)P(s)}{1+C(s)P(s)}=\frac{K_d\,s^2+K_p\,s+K_i}{m\,s^3+(c+K_d)s^2+(k+K_p)s+K_i} \tag{7.22}$$

Another possible layout for a PID controller is reported in Figure 7.17, where an input gain compensation [137] is considered.

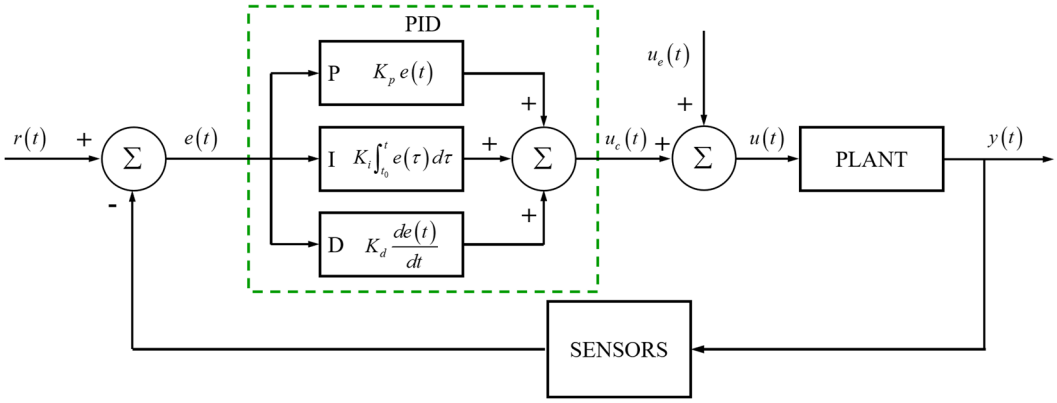

Figure 7.17 – Block diagram of PID controller with input compensation.

A simple PID controller will be used in the next section to control the disengaging and engaging phases during a gearshift in a magnetic gearbox.

7.4 Simulink model of a magnetic gearbox

The same simplified driveline model, already discussed in § 5.3, is used now to study the dynamic of a magnetic gearbox with a block-oriented approach. Indeed, a control logic is applied to a magnetic gearbox transmission system, based on planetary magnetic gear technology, to study its behaviour both in steady-state and in transition conditions. The updated model of transmission, including a magnetic gearbox with two PMG, is reported in Figure 7.18.

The ICE has been replaced by an electric motor, characterised by the linear torque trend reported in Figure 7.8. Instead, the central part of the driveline is composed by the magnetic gearbox, which contains inside two PMG with two different gear ratios. The ring of the magnetic gearbox, as previously, is connected to an inertia representing vehicle load resistance, while the driver manoeuvre is simulated through the TVO command, which acts on the torque characteristic of the electric motor.

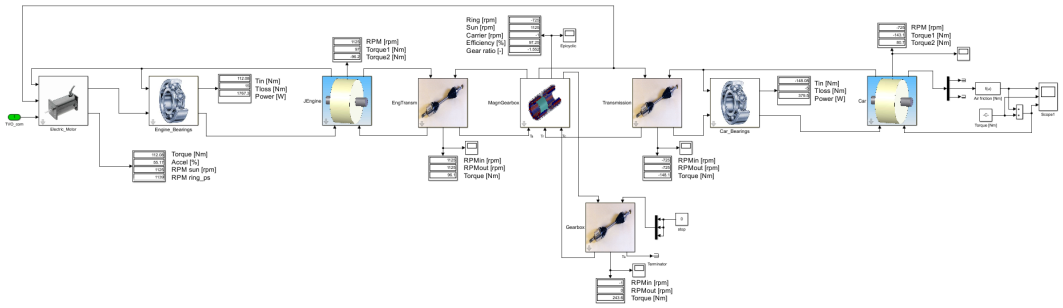

Figure 7.18 – Model of driveline transmission with magnetic gearbox.

All the transmission parameters are the same reported in Table 7.1. A PID controller is used to control the gearshift phase. Using this model different gearshift conditions have been analysed, but to be concise, only three different cases, namely three different control logic, will be discussed in this section.

7.4.1 Test # 1

In this first test, the controller acts on the TVO, which is directly operated by the driver through the gas pedal. All the timing parameters to manage the gearshift phase are listed in Table 7.3

Table 7.3 – Time parameters during gearshift (test # 1).

Description	Parameter	Value
Starting time of gearshift	t_s [s]	15
Time in neutral position	t_N [s]	0.2
Time in control phase	t_c [s]	0.8
Time for disengaging+engaging	t_{CM} [s]	1
Starting time for disengaging	$t_1 = t_s$ [s]	15
Starting time of neutral position	$t_2 = t_1 + \frac{t_{CM}}{2}$ [s]	15.5
Starting time of control phase	$t_3 = t_2 + t_N$ [s]	15.7
Starting time of engaging	$t_4 = t_3 + t_c$ [s]	16.5
Gearshift completed	$t_5 = t_4 + \frac{t_{CM}}{2}$ [s]	17

Firstly, an only proportional controller is used. Then a PI is used to reduce the steady-state error, increasing the P term, as well. The values for the two gains are determined in order to avoid a saturation of the TVO during the control phase.

In Figure 7.19 the speed of the input shaft (solid red line) and of the secondary shaft (dash-dot blue and dot-dot black lines), which is reported to the primary shaft, for both the gear ratios, are represented. During the control phase,

at time $t_3 \le t \le t_4$, a steady-state error occurs due to the integrative gain that is equal to zero.

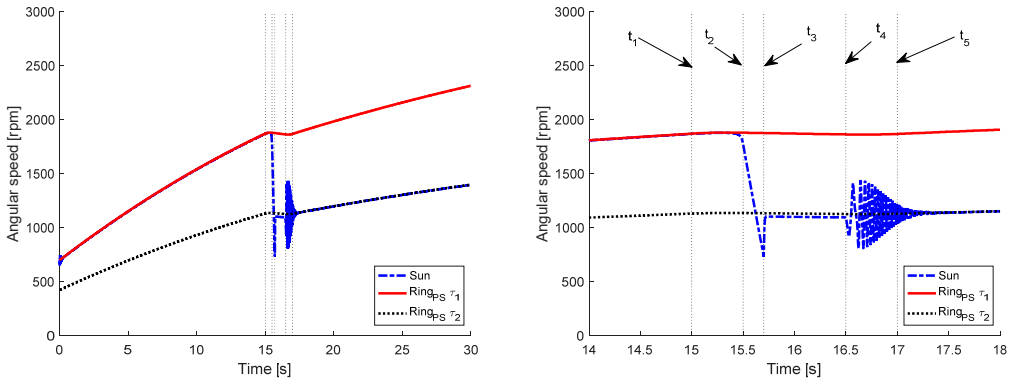

Figure 7.19 – Sun and ring (reported to primary shaft) speeds during the simulation (left) and gearshift period (right).

In Figure 7.20 is reported the torque provided by the electric motor connected to the sun of the PMG, the TVO of driver and the TVO command, that is the input of the electric motor; the motor takes into account the TVO request during the control phase. The following PID gains are considered: $\begin{bmatrix} K_p & K_i & K_d \end{bmatrix} = \frac{216}{400}\begin{bmatrix} 1 & 0 & 0 \end{bmatrix}$.

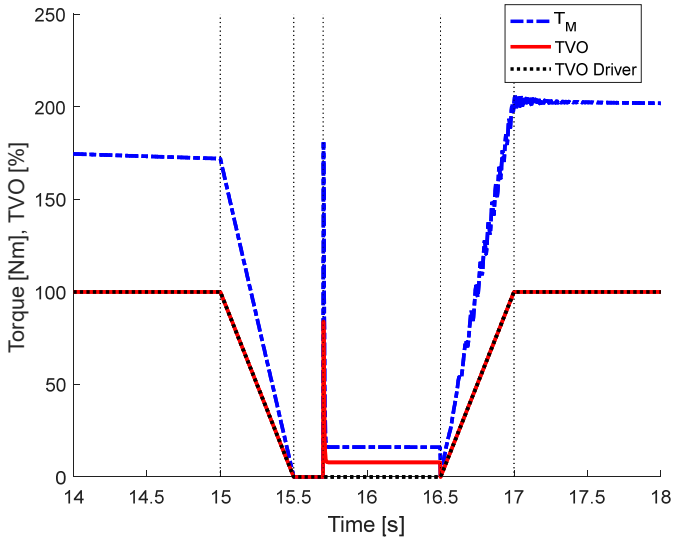

Figure 7.20 – Input torque and TVO command during the gearshift phase.

The value $K_p = \frac{216}{400}$ is calculated using Eq. (7.23):

$$K_p = \frac{T_M\big|_{(n_r \cdot \tau_2)}}{\left(n_s - n_r \cdot \tau_2\right)} \tag{7.23}$$

where $T_M\big|_{(n_r\cdot\tau_2)}$ is the torque that must be provided by the electric motor at the new rotational speed, which depends on the transmission gear ratio of the second PMG, while $(n_s - n_r\cdot\tau_2)$ is the speed gap that have to be fill with the use of an only proportional control during the gearshift phase.

Then the proportional gain is increased, and a non-null integral gain is considered. As it is possible to appreciate from the two figures below, the steady-state error in reduced with an overshoot at the beginning of the control phase due to the increment of the proportional gain. In this way a saturation at the value of 100% occurs at the beginning of the control time. The following PID gains are considered: $\begin{bmatrix} K_p & K_i & K_d \end{bmatrix} = \frac{216}{400}\begin{bmatrix} 5 & 2 & 0 \end{bmatrix}$.

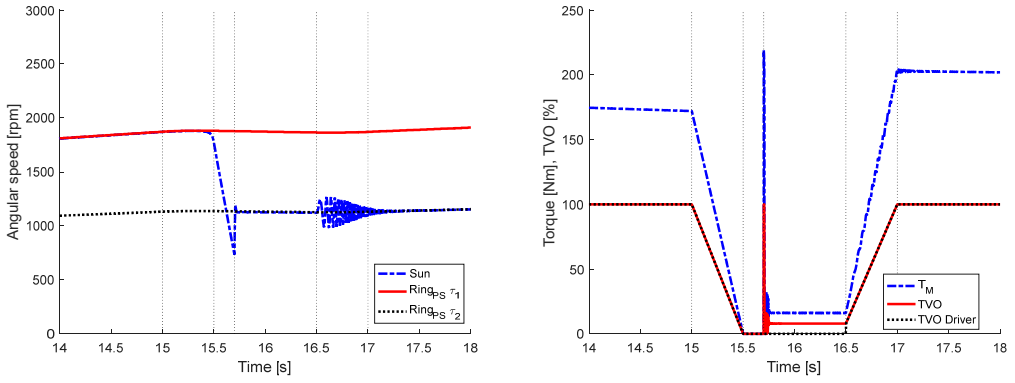

Figure 7.21 – Speeds (left) and torque (right) with increased proportional and integral gains of PID controller.

Instead, as regards the torque modulation inside the magnetic gearbox, reported in Figure 7.22, during the disengagement the transmitted torque is reduced with a linear decrement from the torque value provided by the electric motor to zero, then during both neutral and control phases it remains at a zero value and finally, during the engaging phase, it increases from zero to the torque necessary to rotate at the new speed, according to the electric motor torque characteristic.

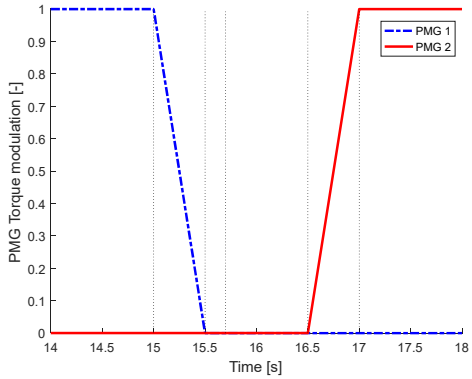

Figure 7.22 – Coefficients for PMG torque modulation

If a PI controller is used the time for the control phase, t_c, could be reduced from 0.8 s up to 0.1 s, as illustrated in Figure 7.23. Moreover, in this case, also the speed oscillations during the engaging phase are significantly reduced. Instead, the controller acts in an on/off way during time in which it is active.

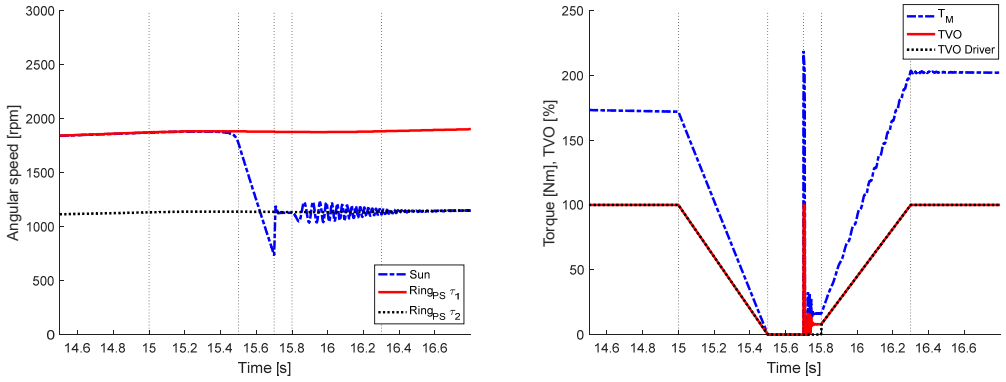

Figure 7.23 – Speeds (left) and torque (right) using PI controller and a $t_c = 0.1$ s.

Finally, if an only P controller is used, the control time should be enough long to avoid losing of synchronism during the engaging phase after the control phase.

7.4.2 Test # 2

During this test the time in neutral position is fixed to zero and thus the synchronisation with the new gear will be reached using only the control phase. In Table 7.4 all the timing parameters of the simulation are listed.

Table 7.4 – Time parameters during gearshift (test # 2).

Description	Parameter	Value
Starting time of gearshift	t_s [s]	15
Time in neutral position	t_N [s]	0
Time in control phase	t_c [s]	0.8
Time for disengaging+engaging	t_{CM} [s]	1

Firstly, as done for test # 1, an only proportional controller is used and results are reported in Figure 7.24. The following PID gains are considered: $\begin{bmatrix} K_p & K_i & K_d \end{bmatrix} = \frac{216}{400}\begin{bmatrix} 1 & 0 & 0 \end{bmatrix}$. As it is possible to notice from the figure, in the first part of the control phase, the controlled TVO is equal to zero. This time corresponds to the time necessary to decrease the electric motor speed to the appropriate velocity to engage with the second gear ratio, while in the second part of the control phase, the TVO assumes a constant value, which guarantees the equilibrium between motor torque and the dissipations due to the bearings of the driveline.

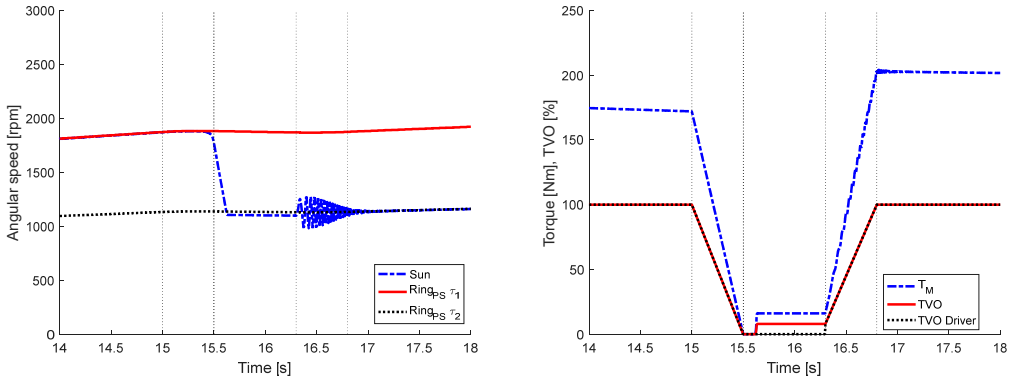

Figure 7.24 – Speeds (left) and torque (right) with only proportional gain.

After that, also the integral gain is considered, as reported in Figure 7.25, and thus the same PID gains of test # 1 are used: $\begin{bmatrix} K_p & K_i & K_d \end{bmatrix} = \frac{216}{400}\begin{bmatrix} 5 & 2 & 0 \end{bmatrix}$.

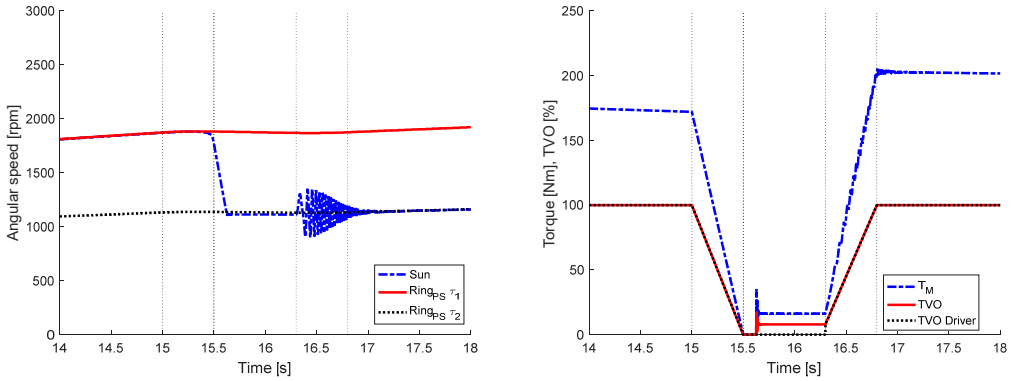

Figure 7.25 – Speeds (left) and torque (right) with PI gain.

The time for the control phase could be reduced from 0.8 s up to 0.2 s using both a P and a PI controller.

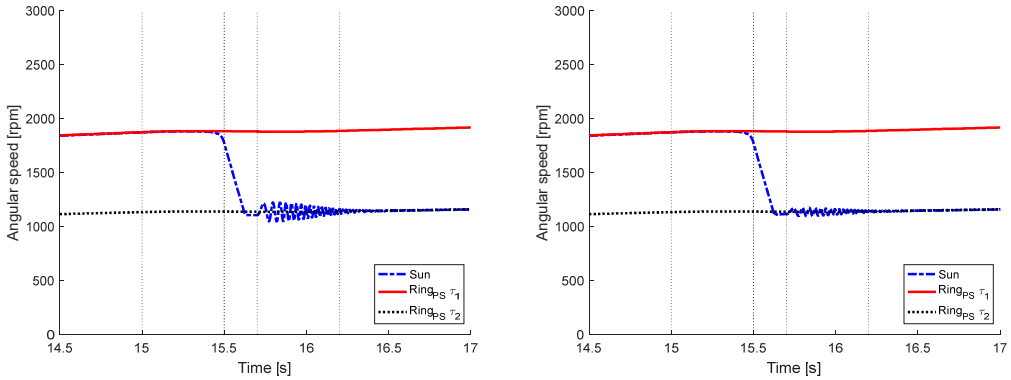

Figure 7.26 – Speeds with only P (left) and PI (right) controller and a $t_c = 0.2$ s.

As reported in Figure 7.26, the most perceivable effect of the control time reduction is the reduction of the oscillations in the motor speed during the engagement of the second PMG. Moreover, with a PI controller, this reduction is more evident than using an only proportional controller.

7.4.3 Test # 3

The main characteristic of this test is that the magnetic gearbox is in neutral condition for a certain time during the gearshift phase. Table 7.5 is used to define the gearshift timing, while Table 7.6 is used to clarify the several conditions, which happen during the gearshift phase.

Table 7.5 – Time parameters during gearshift (test # 3).

Description	Parameter	Value
Starting time of gearshift	t_s [s]	15
Time in neutral position	t_N [s]	0.4
Time in control phase	t_c [s]	0.4
Time to complete gearshift	t_{CM} [s]	1
Time for TVO modulation	t_{TVO} [s]	0.3

Table 7.6 – Gearshift events.

Event	Timing			
	$t_1 = t_s$	$t_2 = t_1 + t_{TVO}$	$t_3 = t_2 + t_N$	$t_4 = t_3 + t_{TVO}$
Disengaging TVO modulation				
Carrier disengaging				
TVO control phase				
Carrier in neutral position				
Carrier engaging				
Engaging TVO modulation				

According to values reported in the previous tables, the controller is overlapped to the neutral condition of the magnetic gearbox. In the first two tests it has been seen that oscillations on the speed on the sun rotor of the gearbox were mainly due to the engaging phase. Indeed, the TVO modulation between two different values must be properly managed, using a hyperbolic tangent trend instead of a linear increment/decrement. The position assumed by the carrier inside the magnetic gearbox during the simulation of this test is illustrated in Figure 7.27. The CAD model of magnetic gearbox used for these figures will be discussed in the following sections.

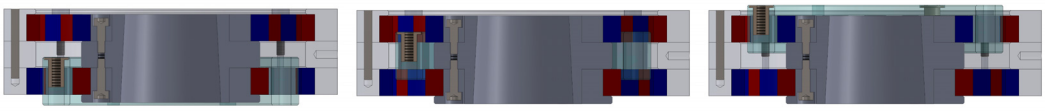

Figure 7.27 – Carrier position inside magnetic gearbox:
1st gear (left), neutral (centre), and 2nd gear (right)

The simulation results are reported in Figure 7.28, with a representation of the TVO, and in Figure 7.29, with the plot of speeds of transmission elements using an only proportional and a PID controller.

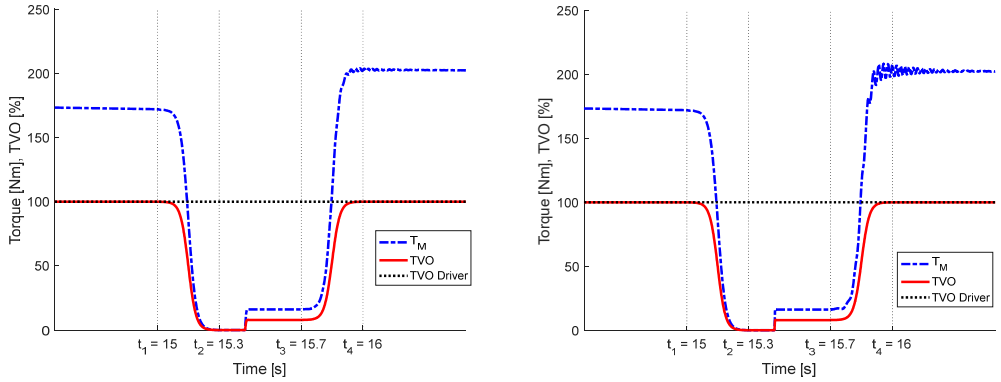

Figure 7.28 – Torque and TVO trends using a P (left) and PID (right) controller.

The values used for control gains in PID conditions are: $\begin{bmatrix} K_p & K_i & K_d \end{bmatrix} = \frac{216}{400}\begin{bmatrix} 5 & 2 & 0.1 \end{bmatrix}$, while for the only proportional control $\begin{bmatrix} K_p & K_i & K_d \end{bmatrix} = \frac{216}{400}\begin{bmatrix} 1 & 0 & 0 \end{bmatrix}$.

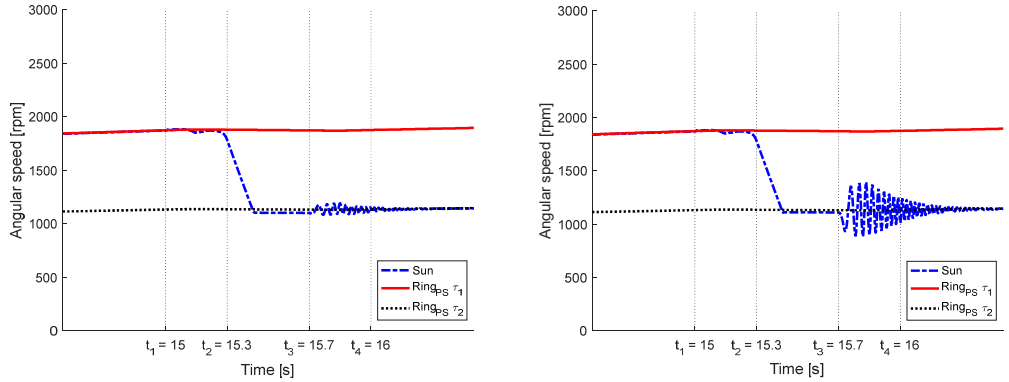

Figure 7.29 – Speed trends using a P (left) and PID (right) controller.

The torque transmitted by the planetary magnetic gear is modulated according to two different coefficients during the gearshift phase, since the ferromagnetic element, devoted to the modulation of the magnetic fields of inner and outer rotor, is subjected to an axial movement inside the magnetic gearbox. Their trend is reported in Figure 7.30.

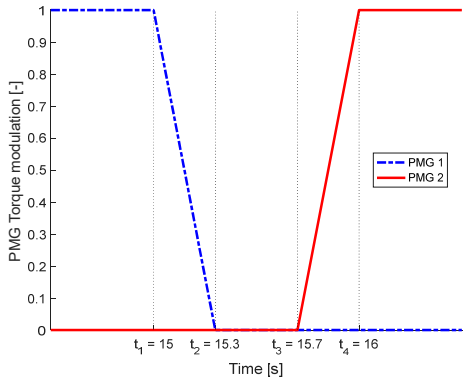

Figure 7.30 – Coefficients for PMG torque modulation.

As it is possible to notice from Figure 7.29, the oscillations on the sun speed during the engaging phase are still present, especially using an PID controller. This aspect is due to a small non-equilibrium condition between the end of the control phase and the beginning of the engaging phase. Moreover, the damping contribution on the transmission elements is a merely estimation. For this reason, this issue should be further investigated during the experimental activities on the magnetic gearbox prototype.

7.5 Magnetic gearbox prototype

All the analyses performed in the previous sections have been devoted to the study of the magnetic gearbox dynamic, especially in the transition phase between two different transmission ratios. However, the activities are not only simulative or analytic, since a functional demonstrator prototype, which has the purpose of being configurable with different power input / output solutions, has been realised. The prototype will allow, during the experimental campaign, to validate the high efficiency in terms of torque conversion in stationary gear ratio conditions, typical of magnetic gears and already demonstrated in simulations. Moreover, the optimal gearshift procedure between two different transmission ratios will be tested with an appropriate control strategy through dedicated sensors, which are mounted at input / output of the device. The magnetic gearbox prototype has been realised thanks to the participation in a Proof of Concept project for the development of the technology and an increment of the Technology Readiness Level (TRL) from 2 to 4, starting from a level in which the only the theoretical working principles of the technology were known to its experimental validation in the laboratory.

The main activities, aimed at the development of the invention, involved the design and construction of a two-stage (two-speed) magnetic gearbox prototype, to validate the patented idea, verifying the effectiveness of the system, evaluating the technological construction solutions, and highlighting any possible critical aspect in different kinematic and dynamic operative conditions.

Furthermore, the manufactured prototype is characterised by a functional parametricity, which allows to investigate different configurations concerning the transmission ratio, varying both its absolute value and its sign, thus allowing to reverse or not the direction of rotation between power input and output. In parallel with the realisation of the prototype, a devoted test bench was designed and built to explore and evaluate the magneto-mechanical characteristics of the prototype in different working conditions, through appropriate test protocols.

7.5.1 Prototype dimensions

The magnetic gearbox prototype can be considered as an evolution of the planetary magnetic gear prototype designed and proposed in § 6.2.2 as second release. Therefore, all the assumptions about prototype sizing, made in section § 6.2, remain valid.

Table 7.7 – Magnetic gearbox prototype dimensions and results.

Parameter	Value	Unit
Sun PM thickness $th_{PM,s}$	6.75	mm
Ring PM thickness $th_{PM,r}$	5	mm
Steel poles thickness th_{poles}	8.25	mm
Sun yoke thickness $th_{yoke,s}$	6	mm
Ring yoke thickness $th_{yoke,r}$	8.5	mm
Air gap	2	mm
Gear external radius R_{ext}	62.5	mm
Gear axial length L	10	mm
Sun PMs pole pairs n_s	$[5 \quad 7]$	-
Ring PMs pole pairs n_r	$[13 \quad 11]$	-
Carrier steel poles q	18	-
Gear transmission ratio $\tau_{s/r}$	$[-2.6 \quad -1.57]$	-
Results	**Value**	**Unit**
Torque inner rotor (sun) T_{sc}	$[2.57 \quad 3.46]$	Nm
Torque outer rotor (ring) T_{cr}	$[6.68 \quad 5.43]$	Nm
Torque carrier T_c	$[-9.25 \quad -8.89]$	Nm
Weight m_{PMG}	0.66 (one PMG)	kg
Torque density T_ρ	$[3.89 \quad 5.24]$	Nm/kg

All the information on the active part of the magnetic gearbox prototype, include two PMG with a common carrier, are reported in Table 7.7. The two transmission ratios depend on the number of PMs on the inner and outer rotor,

which are then connected to a common input shaft and a common output shaft, respectively. The proposed dimension allow to have not an higher torque on the rotors, with a maxim value less than 10 Nm, when the input shaft is connected to the carrier and the gearbox is working at the first transmission ratio.

After the appropriate sizing has been defined the magnetic gearbox has been designed using Solidworks software, as better illustrated in the next section.

7.5.2 CAD model of magnetic gearbox prototype

The magnetic gearbox prototype has been designed starting from the dimensions of the active part, discussed in the previous section, and reported in Figure 7.31. It is made of two PMG with a common carrier, which in the figure is placed along the first PMG. the PMs on the inner and outer rotors are glued on the corresponding yokes. Moreover, a neutral position is added to the gearbox with two different aims: the former is testing the gearshift manoeuvres with also this condition, while the latter is related to the efficiency of a PMG. Indeed, with a neutral position it is possible put in rotation the input and outer rotors of the prototype in order to evaluate bearing dissipations, to separate mechanical dissipations from magnetic dissipations, evaluating both a mechanical and a magnetic efficiency for the magnetic gearbox.

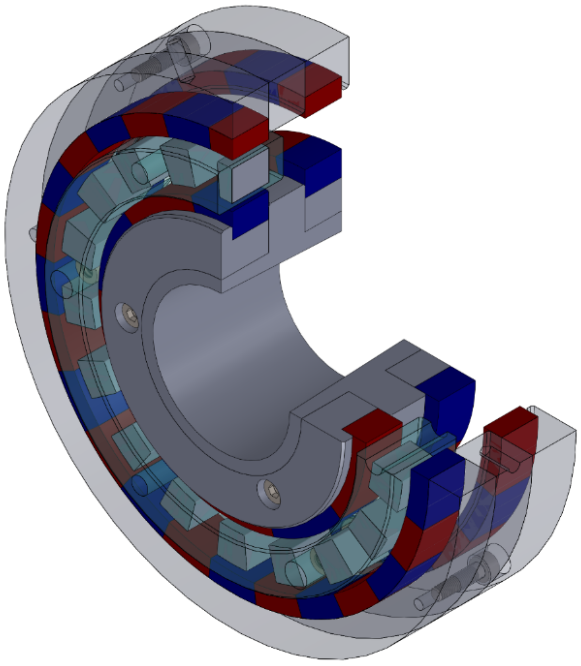

Figure 7.31 – Active part of magnetic gearbox prototype.

The yokes are then connected with screws both on inner and outer side, to have the whole active part, which in then mounted on the magnetic gearbox protype. This solution allow to have an active part, which could be replaced in case of failure, or two different transmission ratios are desired. Instead, the carrier is made of resin material, which structure houses the ferromagnetic poles.

The active magnetic gearbox is mounted on the passive structure of the magnetic gearbox protype, which is reported in Figure 7.32.

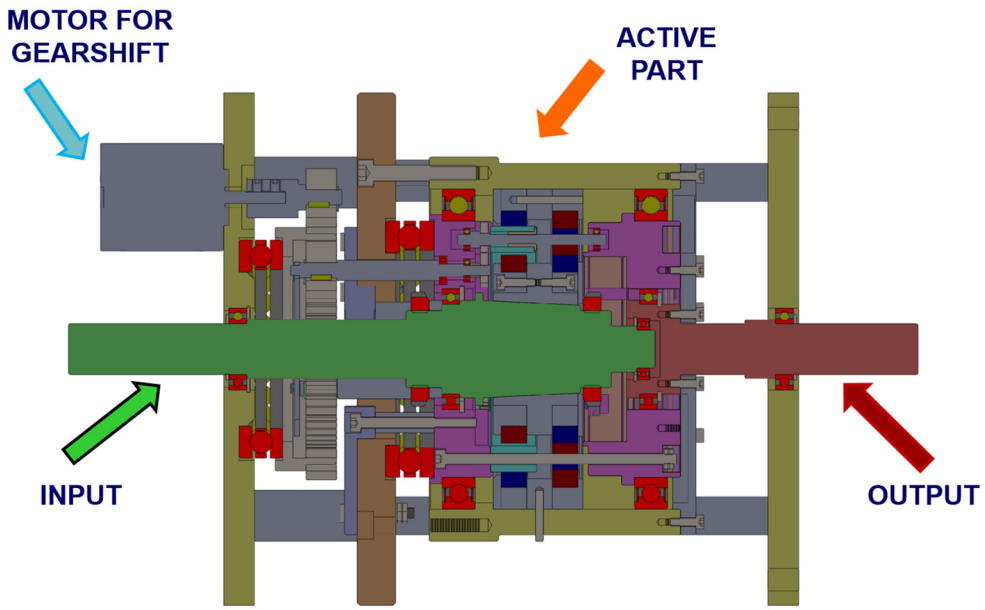

Figure 7.32 – CAD model of magnetic gearbox prototype.

The proposed solution is similar to the magnetic gear prototype reported in Figure 6.5. The slight differences are related to the active part and to the presence of an actuation system to axially move the carrier, allowing the engagement of a different transmission ratio. The carrier movement is made possible by a step motor, which is connected to a gear wheel. the actuation system for the carrier movement is reported in Figure 7.33. The rotation of the stepper allow the rotation of three different pin, connected to three planetary gears of an epicyclic system, which put in rotation three screws, inside the gearbox. These screws are then connected with three threaded bushings glued on the carrier.

The proposed magnetic gearbox consists of an external structure, which include the active part of magnetic gearbox. The idea to test the magnetic gearbox in a dual way, having different configurations for the input/output of external power, is maintained, hence the configuration modification is realised in a simpler way, just exchanging only some screw connections of the prototype.

The two possible configurations are reported in Figure 7.32 where on the top side the external ring is fixed to the supporting plate and the carrier is connected to the output shaft through a connecting flange. Likewise, on the bottom part, the carrier is fixed to the same plate and the ring rotates together with the output shaft. Moreover, the solution with a conical coupling is chosen to connect the input shaft of the prototype with the inner rotor of the active part of the magnetic gearbox. Meanwhile the outer rotor of the active part of gearbox is connected to the external ring by means of three parallel pins with interference fit.

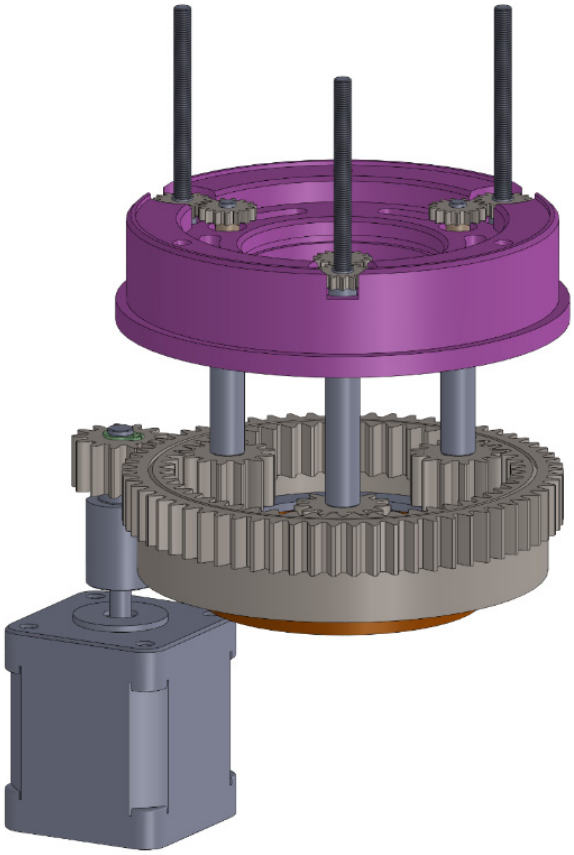

Figure 7.33 – Actuation system for carrier translation.

Moreover, an advantage is to have a magnetic gearbox prototype completely independent from the test bench, which has been realised using Bosh profiles with a modular solution, which guarantees a higher facility of mounting and dismounting, as reported in Figure 7.34.

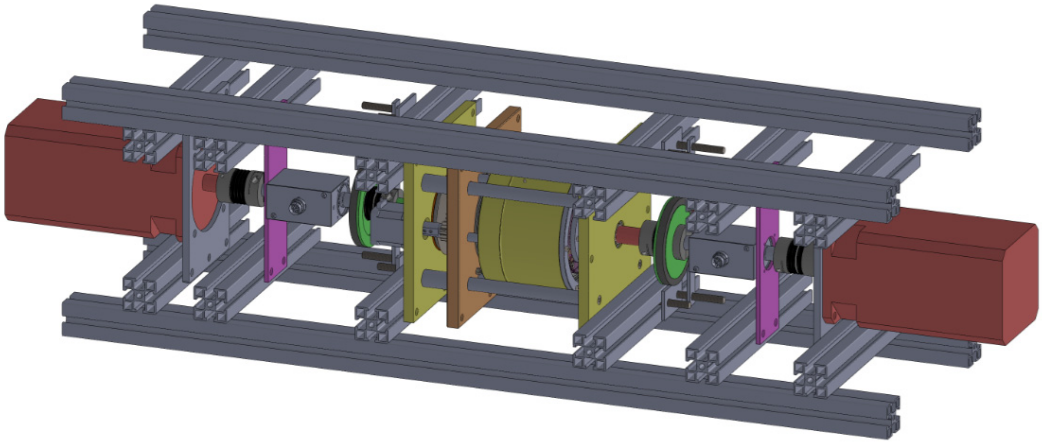

Figure 7.34 – Test bench with magnetic gearbox.

The modular structure of the test bench is completely symmetric with respect to the magnetic gearbox. Indeed, starting from the centre, the transmission driveline counts a first elastic joint (to connect the shaft of the prototype with the

torque sensor), the torque sensor itself, which can also evaluate the rotational speed, another elastic joint (to connect to torque sensor to the electrical motor) and the brushless motor. A solution with two electric motors is chosen, where the first one works as a motor, controlling it in torque, while the secondo one is controlled in speed and works as a brake. Moreover, it is possible to supply power from both sides, allowing the magnetic gearbox to be tested both as a torque multiplier or a speed multiplier.

On the other side, the presence of a higher number of radial and axial bearings causes more dissipation, reducing the mechanical efficiency between input and output of the system. For this reason, the presence of the neutral condition allows evaluating a mechanical efficiency which should be considered in the evaluation of the global efficiency of the magnetic gearbox prototype. In Figure 7.35 the operative bearings in the two possible configurations are highlighted.

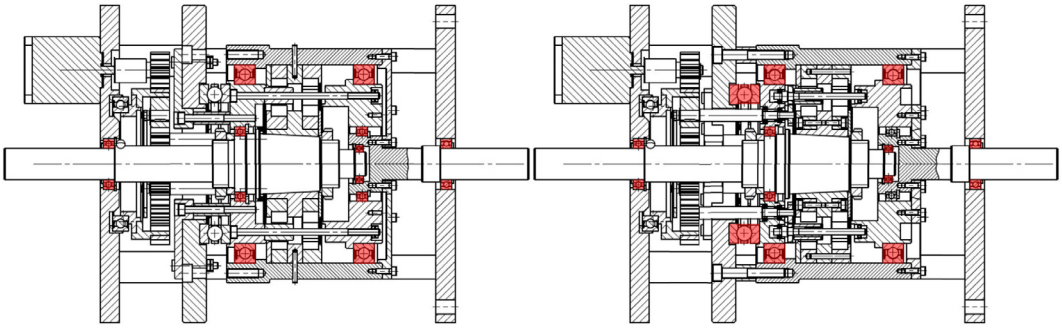

Figure 7.35 – Operative bearings in two different configurations:
carrier fixed (left) and ring fixed (right).

In the first configuration (carrier fixed), seven bearings (two of them are bigger than other five) are rotating, while in the second configuration (ring fixed), always seven bearings are in rotation, with greater dissipations since the largest bearings are three, instead of two in the previous case.

7.6 Magnetic FEM simulations

This section is devoted to the simulation analysis of electromagnetic quantities, namely magnetic flux, and magnetic induction, to compare them with the experimental data, measured on the first gear of the magnetic gearbox prototype, which will be discussed in the next chapter of this thesis.

The waveforms of the main magnetic properties, especially of magnetic flux and induction, have been simulated with static simulations, using FEMM software, changing the angular positions of inner and outer rotors of the magnetic gears, that compose the magnetic gearbox. These quantities are calculated at different distances in radial direction for each component which is part of the magnetic gearbox, namely at inner and outer yokes, on the inner and outer airgap, and on the ferromagnetic poles of the carrier.

A complete rotation of the sun is done with a degree step of $0.25°$, so on all the following figures five periods for each magnetic quantity can be seen, since the number of PMs pole pairs on the inner rotor is five. To be clear, all the angle positions analysed for the sun are reported in the vector $\vartheta_s = [0:0.25:360]°$, while for the ring the vector is $\vartheta_r = \left[\vartheta_{r,\max} : -0.25/\tau_1 : \vartheta_{r,\max} - 360/\tau_1\right]°$, where $\vartheta_{r,\max}$ is the angle position of the ring, which return the highest transmissible torque, while τ_1 is the transmission ratio of the analysed magnetic gear, that in this case is assumed equal to $\tau_1 = 2.6$. Therefore, in this way, during the different steps of simulation the transmissible torque of the PMG is almost the same, except for a torque ripple.

The induction quantities are evaluated using the function $B(x,y) = \text{mo\_getb}(x,y)$, while the magnetic flux is evaluated using the circuitry of the magnetic potential $A(x,y) = \text{mo\_geta}(x,y)$.

Finally, the voltage is evaluated during the post processing using the Faraday-Neumann-Lenz law of magnetic induction:

$$\Delta V = emf = -N\frac{d\Phi}{dt} \tag{7.24}$$

where $\Delta V = emf$ is the voltage or electromotive force at coil terminals, N is the number of coil turns, Φ is the magnetic flux, and t is calculated imposing a certain rotational speed to the rotors of the PMG.

7.6.1 Magnetic induction

The magnetic induction B in evaluated in radial and tangential direction in different elements of the magnetic gear.

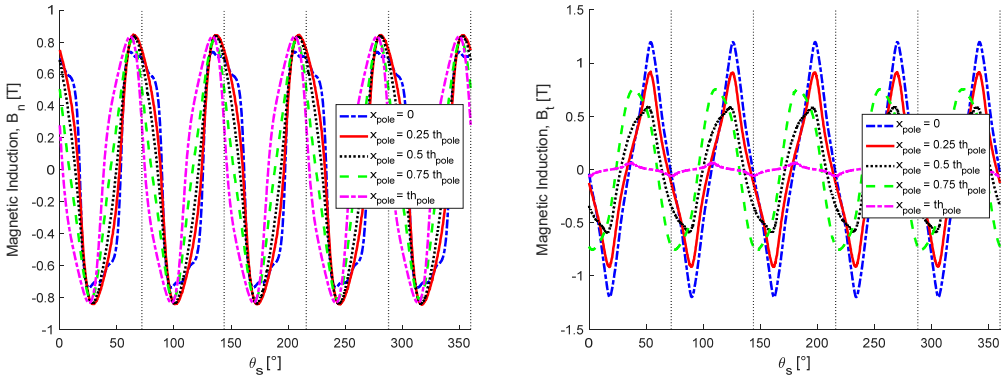

Figure 7.36 – Normal (left) and tangential (right) magnetic induction inside pole versus sun rotation.

Therefore, in Figure 7.36 the radial and tangential magnetic inductions inside the ferromagnetic pole are computed.

Five difference points in radial directions are assumed for this analysis. The first point at $x = 0$ corresponds to the inner point of the pole, namely the nearest point to the inner rotor, while the nearest point to outer rotor is considered, for $x = th_{pole}$.

The highest value for the normal magnetic induction is similar for all the points. This means that the magnetic induction has a prevalent contribution in the radial direction. Instead, as regards the tangential induction, the maximum value is evaluated for the point nearest the inner rotor with a contribution near to zero for the external point.

Instead, Figure 7.37 shows the magnetic induction in normal and tangential directions simulated in the inner and in the outer airgaps.

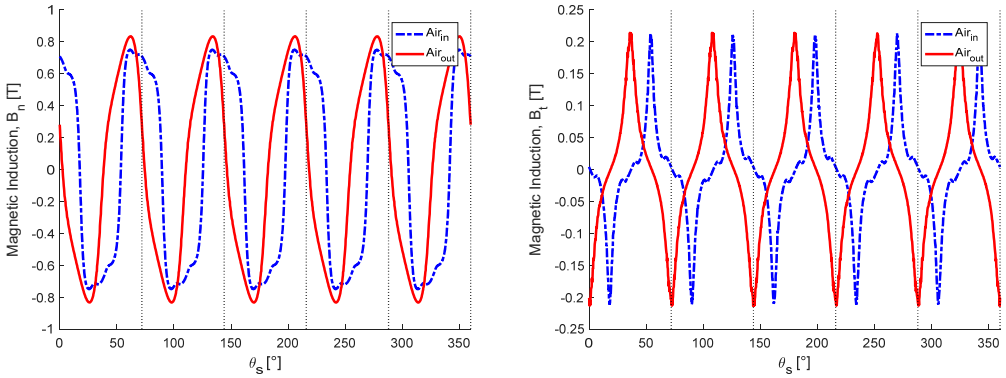

Figure 7.37 – Normal (left) and tangential (right) magnetic induction in the airgaps versus sun rotation.

Only the PMs on the inner rotor have been segmented in the simulation and the effect of segmentation is highly visible in the inner airgap at high values of the normal induction and at low values, near to zero, of the tangential induction.

The effect of segmentation is still evident in Figure 7.38, which show the magnetic induction in both directions.

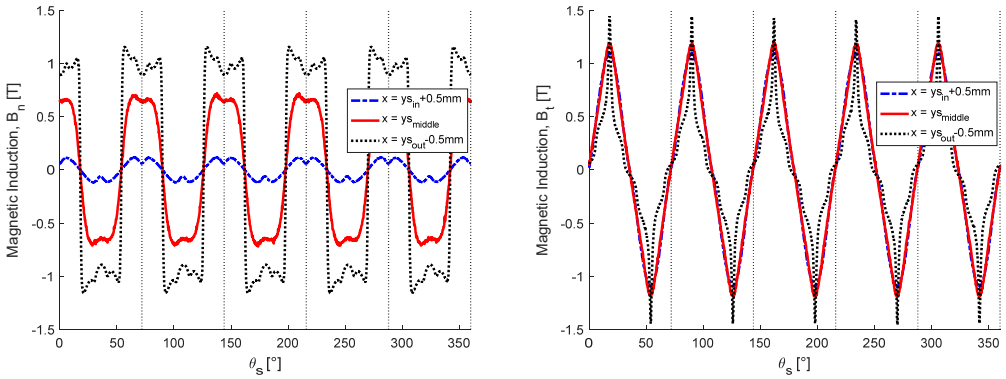

Figure 7.38 – Normal (left) and tangential (right) magnetic induction inside yoke sun versus sun rotation.

The magnetic inductions are evaluated at three different points of the yoke of the sun rotor. As it can be seen from the previous figures the magnetic inductions are higher at the outside of the yoke since this point is closer to the magnets. Instead, as regards the tangential induction, the highest values of the three waveforms are comparable. Moreover, the three lines are quite overlapped: this means that the induction in the tangential direction is equally distributed inside the inner yoke.

Finally, Figure 7.39 shows the magnetic induction in normal and tangential directions in three different points of the yoke of the ring rotor. As it can be seen from both figures the inductions are higher inside of the yoke because that point is closer to the PMs of the outer rotor. So, for the normal induction, the trend is similar for both inner and outer yokes, while for the tangential induction, the three waveforms are slightly different.

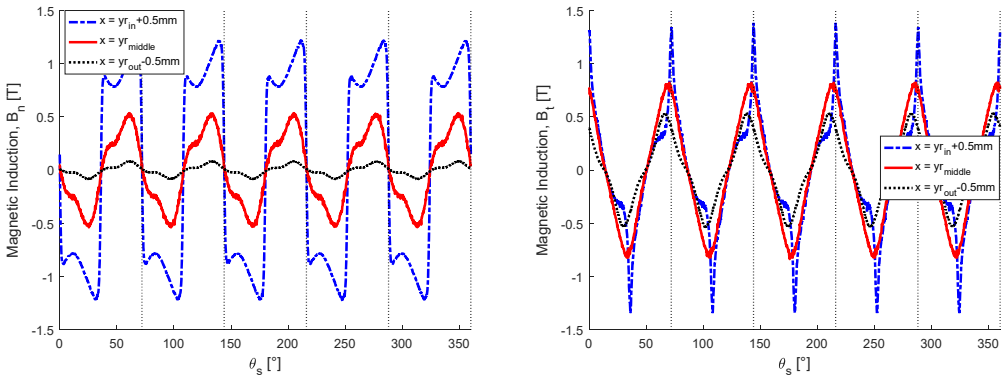

Figure 7.39 – Normal (left) and tangential (right) magnetic induction inside yoke ring versus sun rotation.

In all the previous figures the points in which evaluate the magnetic properties during the simulations, were fixed with a rotation of the inner and outer rotors. Hence, for a complete rotation of the high-speed rotor, namely the inner one, in all the plot it was possible to notice that the waveform has a replicability with a multiplicity of 5, which is the number of PMs on the inner rotor.

The other analysis on the magnetic induction waveforms is made selecting the same three points of the yokes rotating them of the same angle of the corresponding yokes. In this way it is possible to evaluate possible dynamic effects on the magnetic induction, comparing them with the experimental data.

For sake of clarity, the magnetic inductions in x and y direction are evaluated in FEMM for the points which were rotating in the several simulation steps. Then, in the post processing the inductions B_x and B_y are rotated of the appropriate angle, achieving B_n and B_t.

The induction in both directions, evaluated at the same three rotating points on the yoke of the sun are reported in Figure 7.40

The sign of normal induction is always the same during a complete rotation of the sun rotor, with a small ripple, while for the tangential induction the sign is still

the same. In this last case the ripple seems to be higher but the mean value in much less than the normal induction. Therefore, it can be said that the major component of the induction in the normal one. Certainly, a numerical noise affects the numerical simulation. Moreover, for both inductions the waveforms has a replicability with a multiplicity of 18, which is the number of ferromagnetic poles. This effect is perceivable since the carrier is fixed, hence also the ferromagnetic poles are fixed, and the observing points during a complete rotation of the inner rotor view a modification of the magnetic induction due to poles.

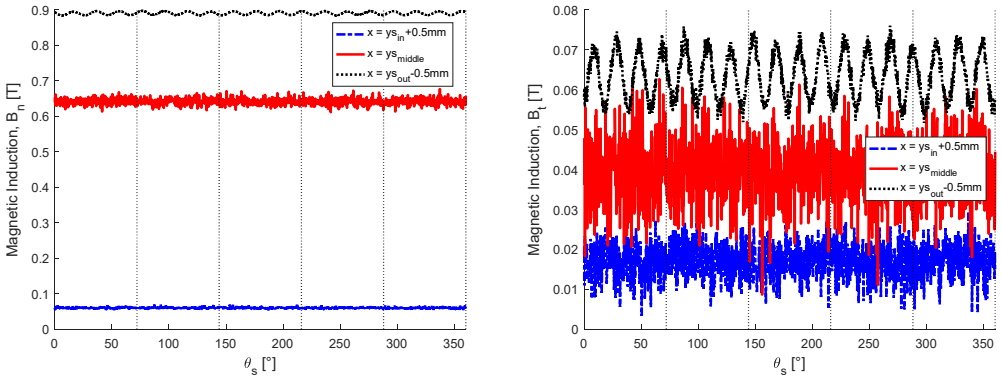

Figure 7.40 – Normal (left) and tangential (right) magnetic induction inside yoke sun (rotating points).

Instead, the inductions evaluated at the points on the yoke of the ring are reported in Figure 7.41.

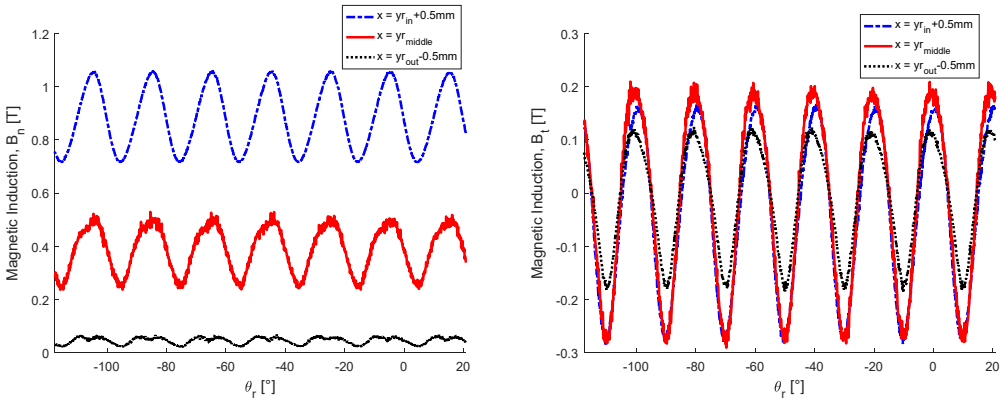

Figure 7.41 – Normal (left) and tangential (right) magnetic induction inside yoke ring (rotating points).

For the ring rotor it happens that the normal induction has the same sign during the ring rotation with a ripple higher than the sun normal induction. Instead, as regards the tangential induction, it has a sinusoidal trend during the ring rotation, with a non-zero mean value.

For the evaluation of dissipations due to eddy currents, it can be useful a plot of the normal induction versus the tangential one, as reported in Figure 7.42 for both inner and outer rotors.

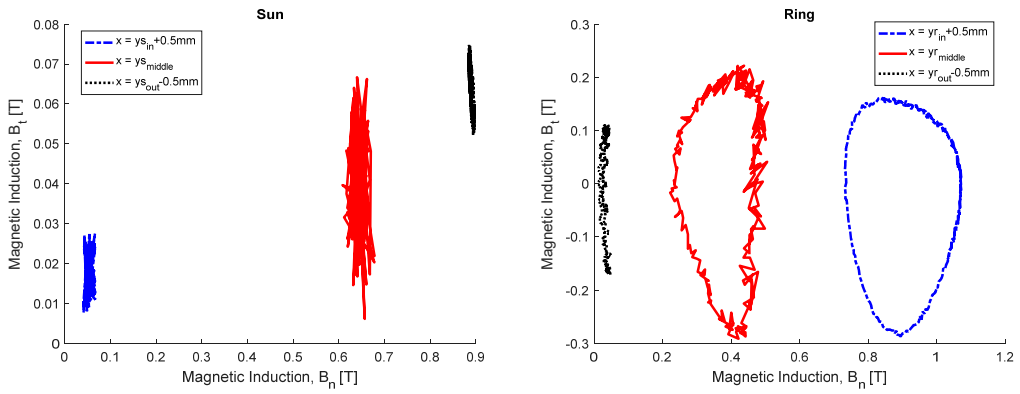

Figure 7.42 – Normal vs tangential induction inside yokes of sun (left) and ring (right).

As it is possible to notice from the previous figures, the loci of magnetic induction are not always elliptical due to harmonic distortion, geometrical effects, and numerical noise of the simulation. The numerical evaluation of the losses due to eddy currents will be discussed in future papers, but not in this PhD thesis.

7.6.2 Magnetic flux

As told before, the magnetic flux is evaluated knowing the magnetic potential in the ferromagnetic pole. Unlike for the magnetic induction, the magnetic flux is evaluated only in the centre of pole, using the circuitry of the magnetic potential, since the simulated flux will be compared with the experimental one in the next chapter. The radial and tangential magnetic fluxes are reported in Figure 7.43.

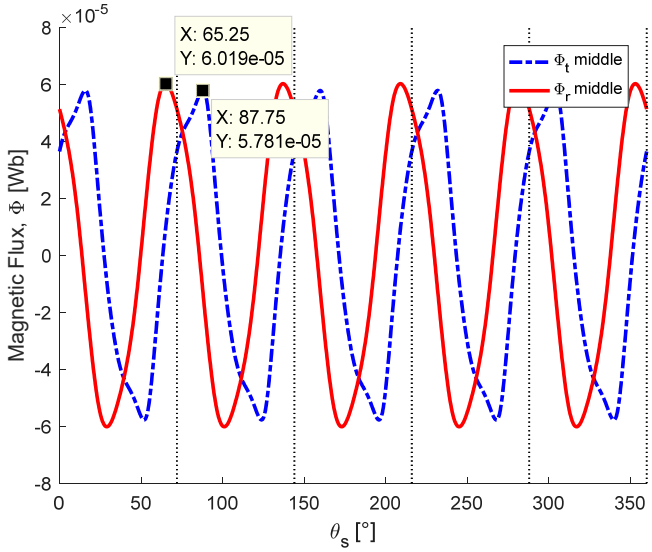

Figure 7.43 – Magnetic flux versus sun rotation.

The maximum value for the magnetic flux is around 6×10^{-5} Wb both for circumferential and radial fluxes. Moreover, with a counter-clockwise rotation of

the sun rotor, and a clockwise rotation of the ring during the simulation, the two waveforms have a phase shift of 22.5 °.

7.6.3 Voltage

If two different windings with a certain number of coils are placed in radial and tangential direction on the ferromagnetic pole, it is possible to evaluate experimentally the voltage at the ends of the windings. In this case the voltage is evaluated using Eq. (7.24) starting from the two numerical fluxes in radial and tangential directions.

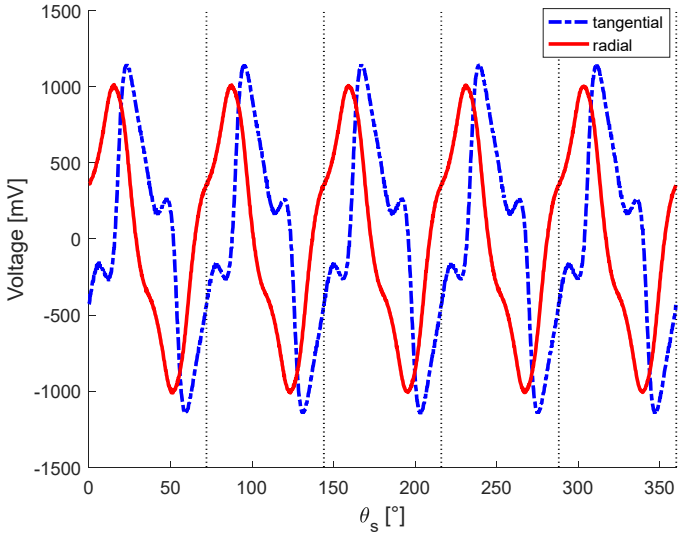

Figure 7.44 – Voltage versus sun rotation.

As it can be seen the induced voltage is not sinusoidal, this is due to the harmonics inside the magnetic flux. The highest value is around 1.000 mV, and it depends on the rotational speed of the rotors. Therefore, in order to perform a comparison with experimental data a rotational speed of 600 rpm for the low-speed side, namely for the ring, is assumed in the voltage evaluation during post processing.

7.6.4 Torque

The transmissible torque of the magnetic gear is computed through the Maxwell's stress tensor, as already explained in § 5.1.4. In Figure 7.45 the transmissible torque at the inner rotor T_{sc} is reported for a complete rotation of the sun rotor. There is a very little torque ripple, which has a multiplicity of 5, according to the number of PMs of the inner rotor.

The maximum transmissible torque is influenced by different constructional parameters of the magnetic gear but also by the residual magnetic induction of the PMs, which according to the datasheet is $B_r = 1.28$ T.

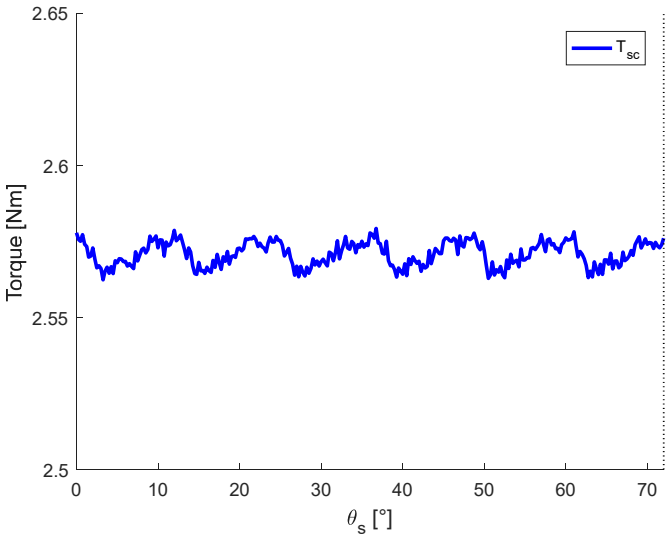

Figure 7.45 – Transmissible torque versus sun rotation.

Finally, it is important to state that the torque is computed using a 2D software as FEMM, so the maximum transmissible torque, which will be experimentally evaluated could be lower than the simulated value. This effect is probably due to boundary effects, since the axial length of each magnetic gear of the magnetic gearbox is only 10 mm.

7.7 Conclusions

The innovative technology of a magnetic gearbox has been proposed, proposing a complexity reduction of the transmission driveline with the integration of the clutch, of gearbox and eventually of the torque limiter in a more compact solution of magnetic gearbox, which solves the problem of gear engagement noise, allowing the torque transfer in contactless way.

Several solutions of magnetic gearbox, with different moving elements, sun, carrier, and ring, have been presented, pinpointing the slight constructional differences of each solution. Moreover, a double stage of magnetic gearbox has been proposed, with two translating carriers for the gear engagement: this kind of gearbox can regulate the transmission ratio both in series and in parallel configurations.

After that, an analytical model of a transmission driveline with a magnetic gearbox has been developed to study the gearshift procedure between two different PMG. The Simulink model of the previous chapter has been readjusted to simulate driveline dynamics with a magnetic gearbox, hence different control

logics have been developed and simulated to achieve the optimal gearshift procedure.

A CAD model of the magnetic gearbox prototype has been designed, together with its devoted test bench for contactless power transmission applications.

Finally, some simulative results on the magneto-mechanical properties of the gearbox prototype, which are obtained using FEMM, have been presented to be subsequently compared with the same experimental results, proposed in the following chapter.

Chapter 8

8. Development of a test rig for power transmission applications using a magnetic gearbox

This chapter deals with the development of a test rig for power transmission application to test the magnetic gearbox prototype, which CAD model has been already discussed in § 7.5. The test rig is integrated with a customised electrical panel, which include components for both the power supply to the electric brushless motors and for the acquisition system.

A dedicated project is under developing using LabView software to manage the control of the test bench and the acquisition of experimental data, through the sensors, namely torque sensors and magnetic incremental encoders, placed at both side of the magnetic gearbox prototype.

8.1 Prototype construction

One of the first steps for the assembly of prototype is the realisation of the active part of the magnetic gearbox, hence the assembling of components, which made the inner and outer rotors. In Figure 8.1 and Figure 8.2 the inner and outer rotors of the two magnetic gears of the gearbox are reported with the segmented PMs glued on the corresponding inner and outer yokes. Then the two inner rotors are assembled and mounted on the inner shaft of the prototype through the conical coupling and a lock nut as illustrated in Figure 8.3 (left), while the two outer rotors are connected by means of screws to the neutral position as reported in Figure 8.3 (right).

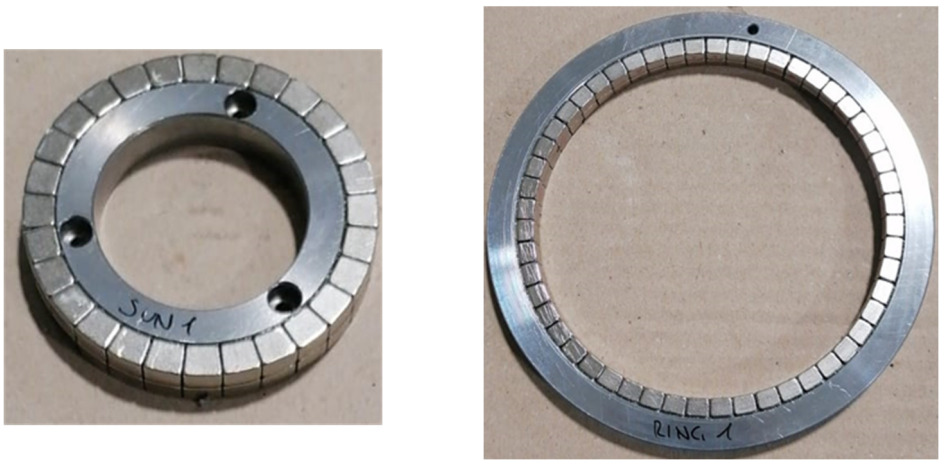

Figure 8.1 – Inner (left) and outer (right) rotors of 1st PMG with glued PMs.

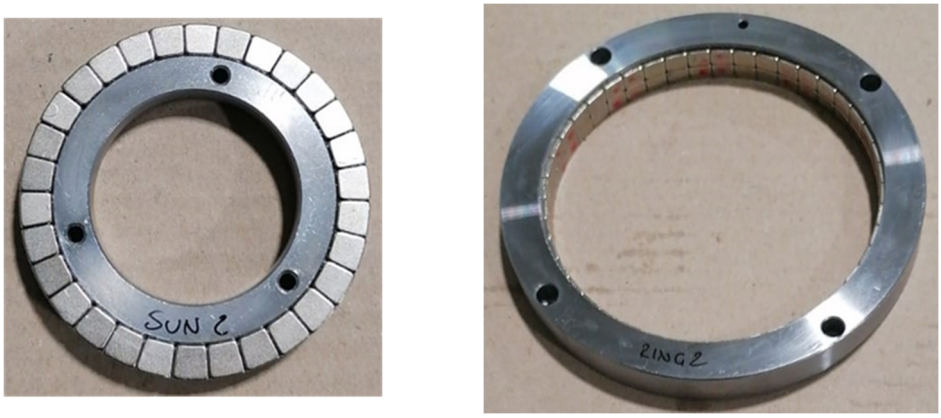

Figure 8.2 – Inner (left) and outer (right) rotors of 2nd PMG with glued PMs.

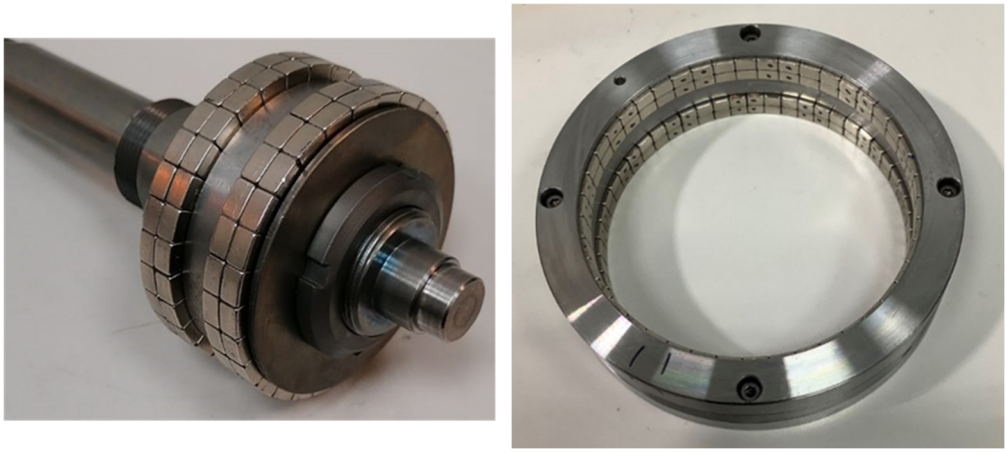

Figure 8.3 – Assembling of inner (left) and outer (right) rotors of the two PMGs.

Instead, as regards the intermediate element of the magnetic gearbox, namely the carrier, is made of resin and holds the ferromagnetic poles. As it is possible to notice from Figure 8.4, on 3 of the 18 poles there are 2 different windings, in radial and tangential directions with a certain number of coils, to evaluate the magnetic flux during torque transmission of the magnetic gearbox.

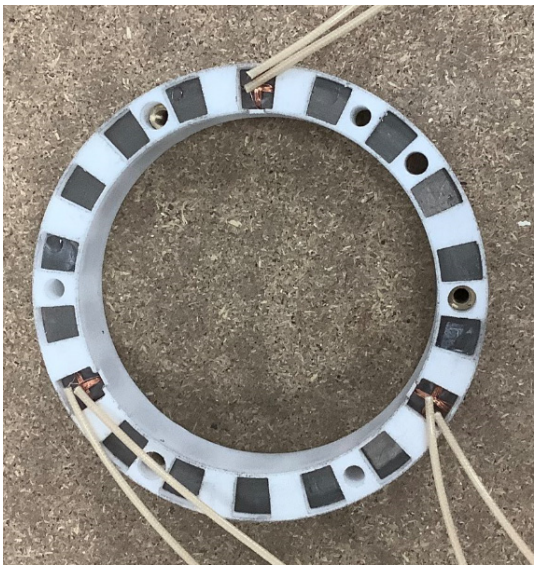

Figure 8.4 – Ferromagnetic poles inside carrier rotor with windings for magnetic flux evaluation.

In Figure 8.5 the prototype during the assembly phase is reported. it is possible to notice the carrier engaged with the 1st PMG. Meanwhile, it is possible to visualise the neutral stage and the PMs on the inner rotor of the 2nd PMG.

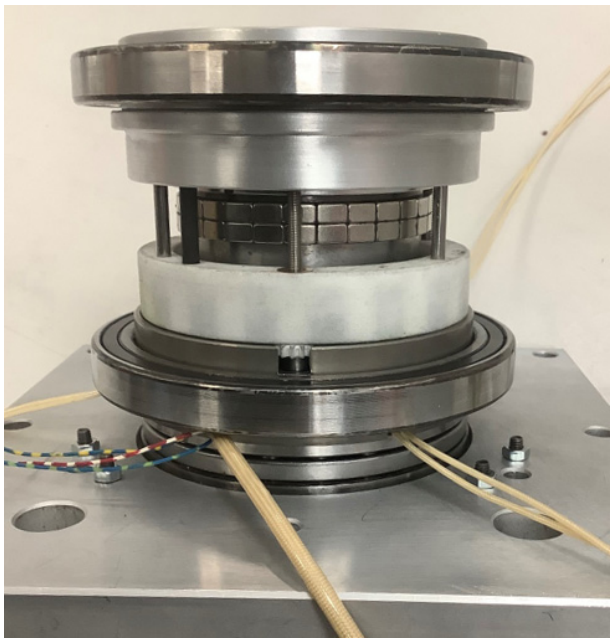

Figure 8.5 – Inner of gearbox prototype during assembly.

Moreover, two radial bearings are fitted with the lower and upper flanges, and an axial bearing is used to support all the prototype on the fixing plate on the bottom of the figure. Finally, the cable corresponds to the already mentioned coils for the measurement of the magnetic flux and to the cables of two micro-switches, which are used as end-stop for the carrier translation inside gearbox.

In Figure 8.6 the assembled magnetic gearbox prototype is reported. In details it is possible to detect on the left the step motor and the mechanical gears, which will eb used for the translation of the carrier.

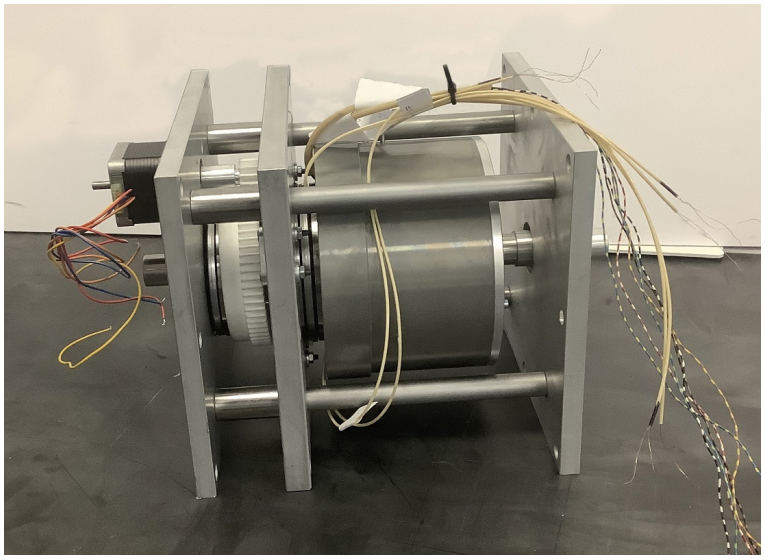

Figure 8.6 – Magnetic gearbox prototype.

The magnetic gearbox is then mounted on a dedicated test bench, already discussed in the CAD model, which be described in the next section together with the electrical panel.

8.2 Test rig and electrical panel

A global overview of the test bench for power transmission applications with a magnetic gearbox is reported in Figure 8.7, where on the left it is possible to notice the prototype on the customised modular structure, while on the left an electrical panel is placed.

Figure 8.7 – Assembled and instrumented test rig.

Different experimental test can be carried out on the test rig with magnetic gearbox technology, by exploiting its working principles as both magnetic gear and magnetic gearbox. In summary the possible tests are here listed:

- start-up test: the magnetic gearbox will be tested in a configuration with the same PMG (i.e., 1st gear), starting from a non-rotating system condition, to evaluate the motion transmission, vibrational behaviour during application of driving and resistive torques;
- test in stationary condition: the magnetic gearbox will be tested at fixed gear ratio, to check that the transmission ratio is kept constant during all the test, and to assess the presence of any torque ripple, not present in the simulation stage;
- test in overload condition: the prototype will be tested by applying a torque overload upstream or downstream of the system, to test its intrinsic function as a torque limiter, which allows to avoid damage to the transmission;
- test in neutral condition: the prototype will be tested in neutral condition to estimate its mechanical efficiency, which depends on the dissipations of bearings inside gearbox;
- test of transition conditions: the two-speed prototype is tested during the gearshift phase, analysing the kinematic quantities and dynamic variables, both in the upshift phase (gear increment), and in the downshift phase (gear reduction).

The development of the test rig also includes the realization of an electrical panel for both controlling and supplying power to the brushless motors and to the acquisition instruments mounted on the test bench. Five different voltage levels are considering during the design of the electrical panel, which are listed, here:

- 400 V (AC): to supply the rectifier;
- 540 V (DC): to supply the inverter;
- 230 V (AC): to supply the converters 230 V (AC) / 24 V (DC) or 230 V (AC) / 5 V (DC);
- 24 V (DC): to supply motor stepper for gearshift, torque sensors, acquisition system (Compact Rio), the auxiliaries of inverter and its heatsink;
- 5 V (DC): to supply incremental magnetic encoders.

A more detailed description of all components inside the electrical panel will be provided in the following section.

8.2.1 Electrical panel project

A five-core electrical plug, which is connected to the electrical grid with a five-core cable provides power to the electrical panel through the terminal blocks (squared in green) in Figure 8.8.

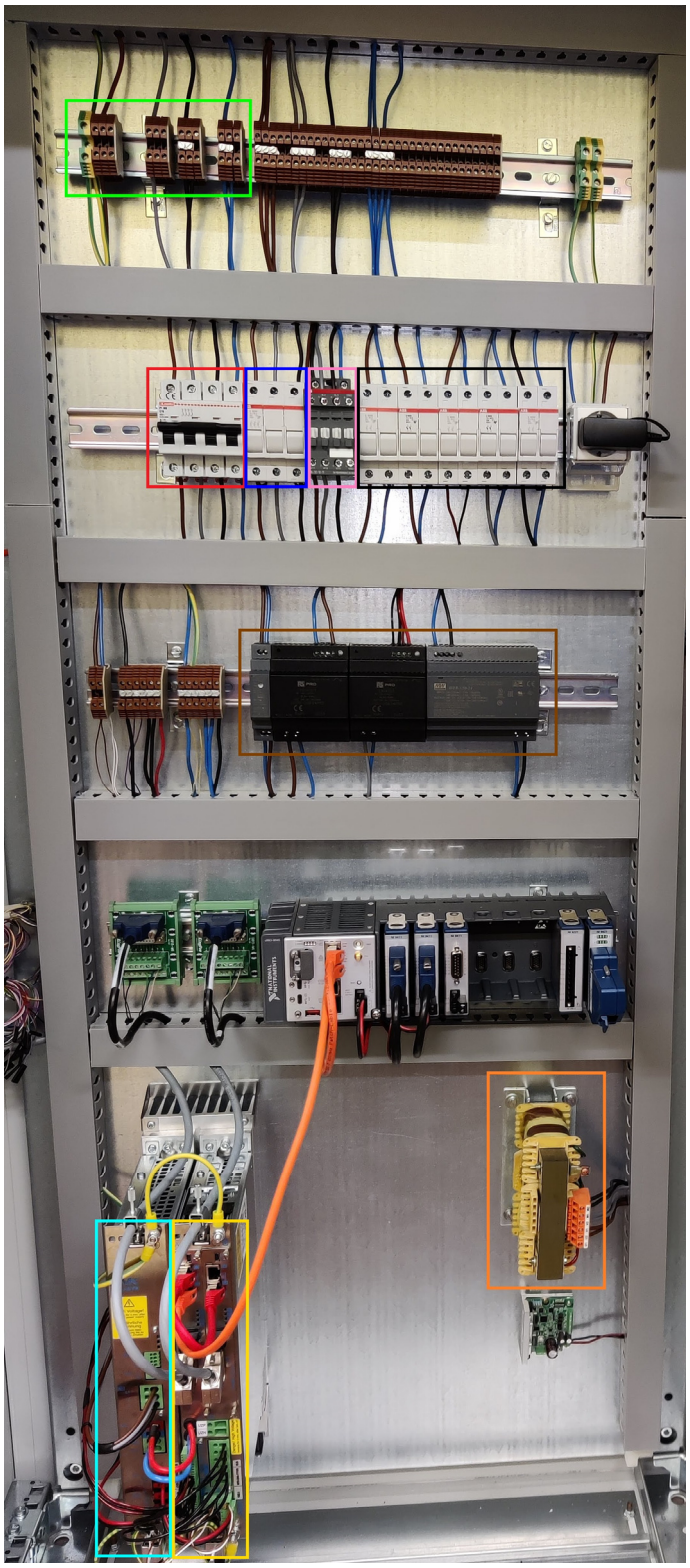

Figure 8.8 – Electrical panel.

The first component is the automatic circuit breaker (squared in red), which has the function of protect the entire electric line from overload and short circuits. After the automatic circuit breaker, the electric line is divided in five different sections, as indicated in the single line diagram of Figure 8.9.

The first section is the three-phases power supply of the motors. In this first line, proceeding in sequential order, the first component is the fuse disconnector (squared in blue), which has the function of protect the line from overcurrent. After that there is a contactor (squared in pink), with a coil supplied with the 24 V (DC), that allows to turn on the electric drive of the brushless motor, when a start button is pressed. Before the electric drive, there is the a particular component, called main choke (squared in orange), which has the function of filtering the current from power line disturbances. The electric drive is composed by two different modules, the KEN 5-0N rectifier (squared in light blue) which converts the voltage to 540 V (DC) and the KWD-5 inverter module (squared in yellow), with two different motor drivers.

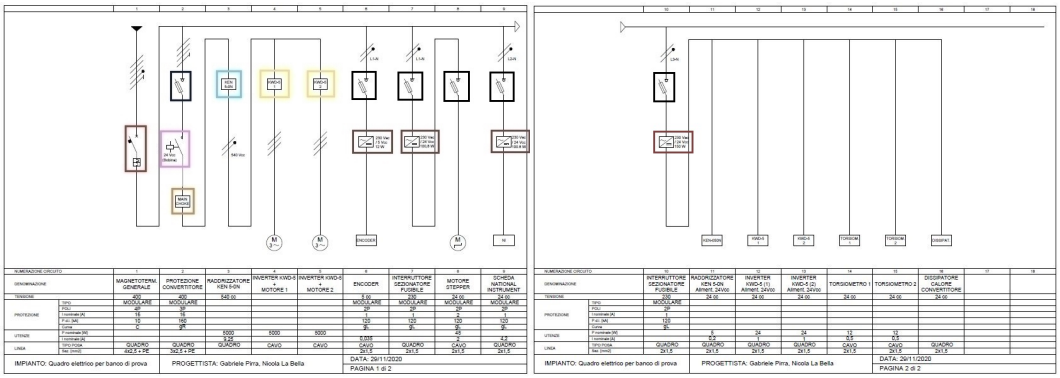

Figure 8.9 – Single line diagram.

Moreover, an emergency button stops the motors when a problem occur, acting on the inverter, which goes in an emergency state, hence opening the Insulated Gate Bipolar Transistor (IGBTs), to disconnect the power supply.

The nominal current is 16 A since, although the motors have a nominal power of 5 kW each, one of that is working in break mode, so the power is exchange from one motor to the other one without absorbing huge current from the line.

The other four sections deal with the low voltage lines: the conversion from 230 V (AC) to 24 V (DC) and 5 V (DC) was made with four converters (squared in brown). The loads have been equally sub-divided in order to keep the line balanced.

Finally, all the sections are protected by fuse disconnectors (squared in black), which have been sized in according with the nominal current absorbed by the respective section. The converters have a short circuit protection inside of them, so only the line that feeds the stepper motor has also a fuse disconnector after the converter, since the stepper driver is the only one component that can risk an overload.

The electric panel during the experimental tests remains closed and the interface with the external environment is ensured by its front end, reported in Figure 8.10.

Figure 8.10 – Commands on the panel front-end.

Starting from the top left, and proceeding in order, the commands on the electrical panel door are the following:

- a light to highlight the presence of voltage inside the electrical panel;
- a selector to switch on/off the electric drive, which is connect to a contactor;
- a stop emergency button, connected with the inverter, and to Analog Input (AI) module of the Compact RIO.
- an Ethernet port for connecting a PC to the Compact RIO system;
- a selector to switch on/off the stepper driver;
- a hand control unit with three buttons to manage the gearshift procedure of the magnetic gearbox;
- two electric sockets for PC and utilities.

At the present, the gearshift procedure is performed with the hand control unit, while in the future it will be integrated in the under developing LabView project, to have automated and replicable gearshift procedures.

8.2.2 Components inside electrical panel

In this section, all the connections inside the electrical panel will be explained in a more detailed way.

Electric drive

The electric drive is produced by AMK company, while the motors are produced by Servotecnica. They are brushless motors (model SVTM-A-03) with a

nominal power of 5 kW, and a nominal speed of 2900 rpm with a stall torque of 11.5 Nm.

Figure 8.11 – Electric drive.

The electric drive is composed by two modules which are mounted on the heatsink behind. The module on the left is the KEN 5-0N rectifier, while the module on the right is the KWD-5 which contain the two R25 inverter cards. As it can be seen from Figure 8.11, the electric drive has many connections to be done, which are listed below:

- the power supply to the motors (2 orange cables) is connected with the KWD-5. Each cable is composed by the three phases wires, the protection wire and other two wires which are connected to the thermal protection (white and brown cables);
- motor encoders (2 grey cables) are connect with the R25 inverter cards, for the control of the motors;
- Ethercat communication through an Ethernet cable between R25 and Compact RIO acquisition system;
- three-phase power supply is connected to the KEN 5-0N from the main choke;
- DC bus at 540 V (DC) connections between the two modules of the inverter (red and light blue cables);
- other connections with the twisted pair cable for 24 V (DC) power supply and the emergency connection with the stop button;
- 24 V (DC) to supply the heatsink.

Compact RIO

The Compact RIO is an acquisition system produced by National Instrument. It is programmed using LabView software, exploiting a real time communication with the electric drive for the motor control.

Input and output signals are managed through the acquisition module NI-9411 for measurements, and module NI-9421 to check emergency status and the operational condition of the motor stepper driver.

Moreover, the Compact RIO system requires a 24 V (DC) power supply.

Figure 8.12 – Compact RIO acquisition system.

As it is shown in Figure 8.12, the NI-9411 acquisition modules are connected with two specific terminal blocks on the left, which allows to have a more manageable connection with the terminals of encoders and torque sensors of the two sides of the test bench.

The encoders have 6 cables to be connected: A, B, Z signals and their corresponding denied signals. A resistance of 250 Ω is placed between each signal and its denied. A and B are square wave signals with a period T depending on the number of division n_{div} of the encoder according to Eq. (8.1):

$$T = \frac{2\pi}{n_{div}} \tag{8.1}$$

The two signals are phase-shifted by $T/4$ second, while Z signal counts only one step for each rotation of the encoder, as illustrated in Figure 8.13.

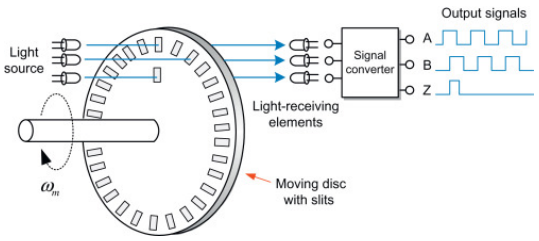

Figure 8.13 – Incremental encoder.

Instead, as regards the torque sensors, only two wires of the cable are connected, since only the torque is evaluated with these sensors, while the rotational speed is measured with the encoders.

The module NI-9421 on the right of Figure 8.12 is an AI module, which is connected to the emergency button in order to warn LabView if a problem occurs.

Finally, two Ethernet cables are used to communicate with the inverter and with the user's PC.

8.3 Experimental results: electromagnetic quantities

This section is the experimental counterpart of section § 7.6, where a simulation using FEMM of the 1st PMG of the magnetic gearbox has been performed, evaluating the electromagnetic quantities, as magnetic flux, magnetic induction. In this case, the electromagnetic quantities are evaluated in the opposite order, starting from the voltage. Moreover, experimental acquisition are made at different speeds of the ring rotor and on the three ferromagnetic poles of the carrier, in which the windings are present.

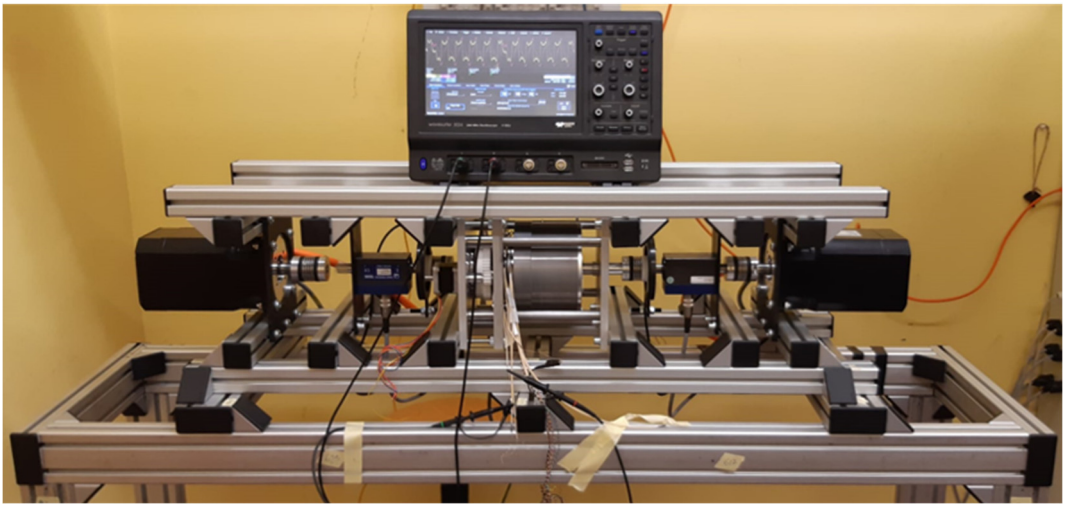

Figure 8.14 – Test bench during acquisitions with oscilloscope.

In Figure 8.14 the oscilloscope (model Teledyne LeCroy 3024z, 4 channels, 200MHz) for voltage acquisitions is reported, together with the test bench of magnetic gearbox.

8.3.1 Voltage

The acquired voltage values depend on the speed of the ring rotor. The higher is the rotational speed, the higher the maximum voltage value. The signals of the two windings in radial and tangential direction on the ferromagnetic pole are simultaneously acquired, while for the other poles the acquisition is repeated to have data redundancy, although the same results are expected. In Figure 8.15 –

Figure 8.17 the voltage acquisitions on the three poles are reported at different speeds of the external ring rotor.

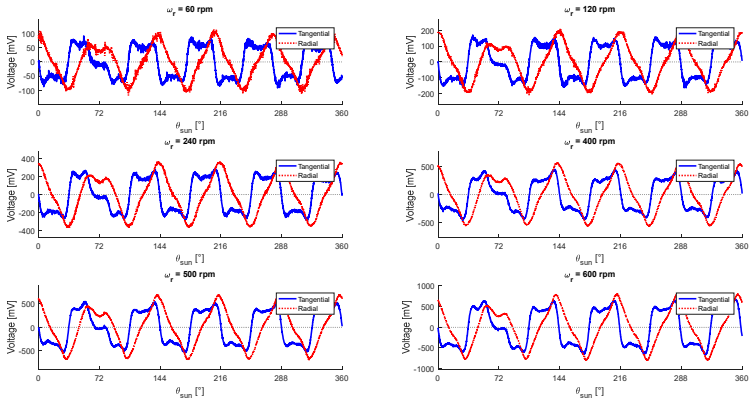

Figure 8.15 – Voltage of pole # 1 versus sun rotation.

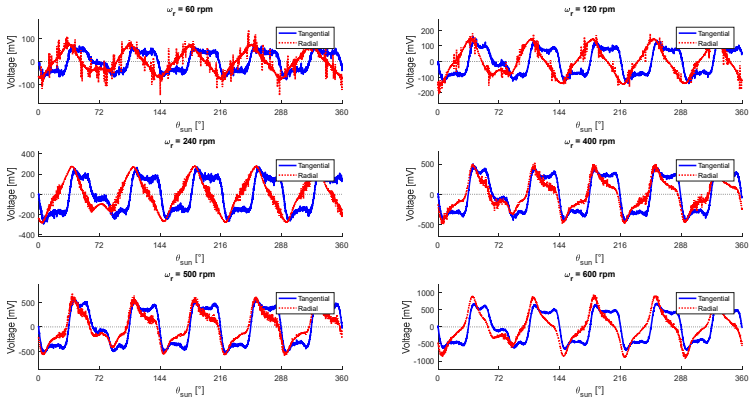

Figure 8.16 – Voltage of pole # 2 versus sun rotation.

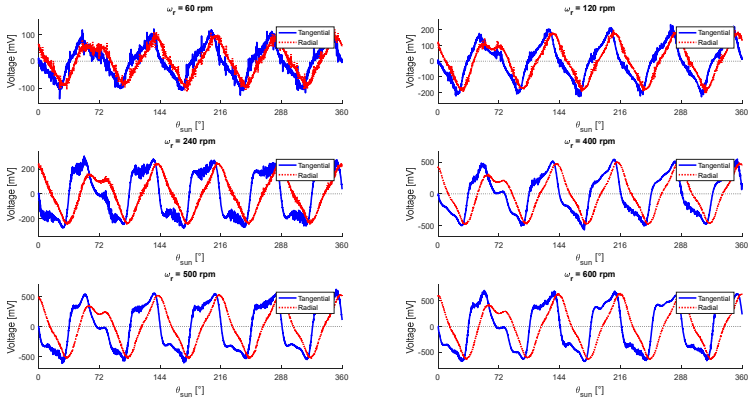

Figure 8.17 – Voltage of pole # 3 versus sun rotation.

For each waveform it is possible to observe a multiplicity of 5, for a complete rotation of the inner rotor, which corresponds to the number of PMs on the inner rotor. As it is possible to notice from the voltage waveforms, a magnet with wrong magnetisation direction is probably mounted on the inner rotor of the first gear of the prototype. This effect, which is still under investigation to detect which segmented magnet inside a pole pair has a wrong magnetisation, is clearly visible at all rotational speeds and for all the poles used for experimental acquisitions.

8.3.2 Magnetic flux

The magnetic flux is evaluated using the Eq. (7.24), reported in the section with simulative results. In Figure 8.18 the magnetic flux in both tangential and radial directions is reported.

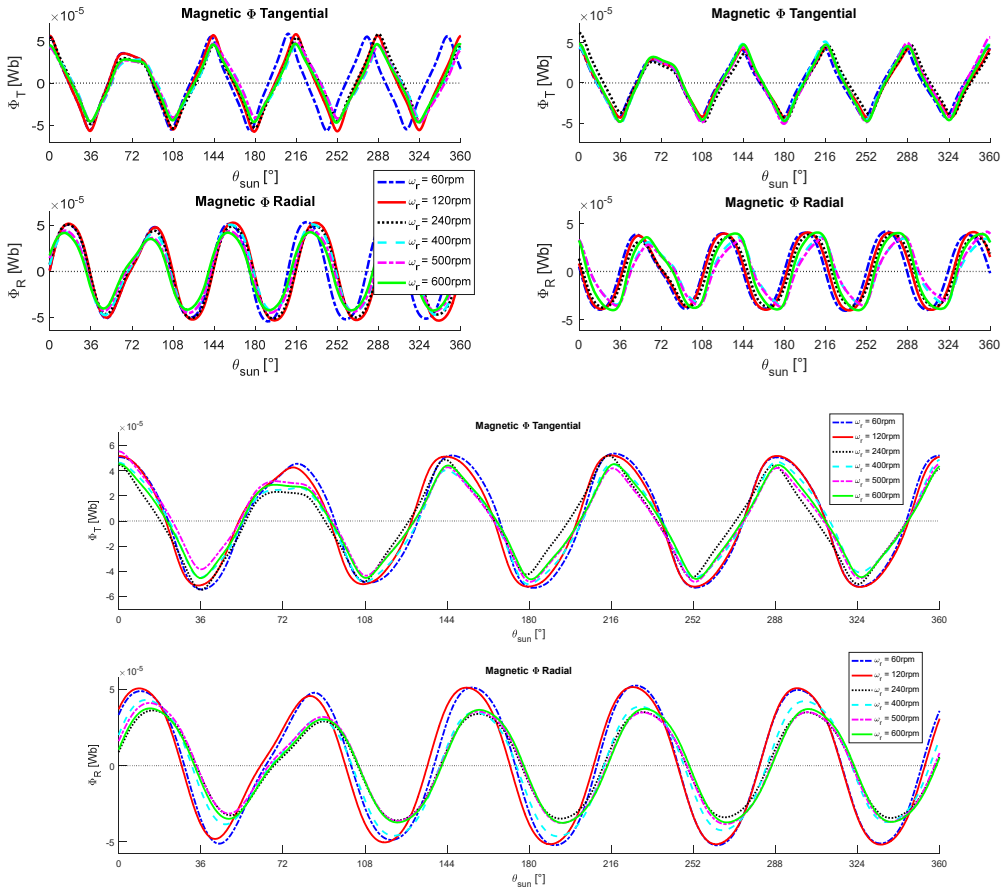

Figure 8.18 – Tangential and radial magnetic flux using pole # 1 (top-left), pole # 2 (top-right), and pole # 3 (bottom) acquisition of windings voltage.

As it is possible to notice from the acquisition on the third pole, the magnetic flux, especially in radial direction is influenced by the rotational speed, so non-linear effects are presented. For this reason, a 2D simulation on FEMM with static simulations at each different angle of the rotor, is a good strategy, especially as regards the computational costs, although it does not consider this dynamic effect.

Moreover, the magnetic flux in the first waveform is lower than the others due to the segmented magnet with wrong magnetisation direction.

A good correlation between simulated and experimental results has been highlighted, both in terms of phase shift and maximum value of Φ_T and Φ_R, which is around 5×10^{-5} Wb. The two fluxes, especially the radial one, present dynamic effects due to the rotational speed, whereas the first peak of the two waveform is lower than others for a wrong magnetisation of the segmented PMs on the inner rotor.

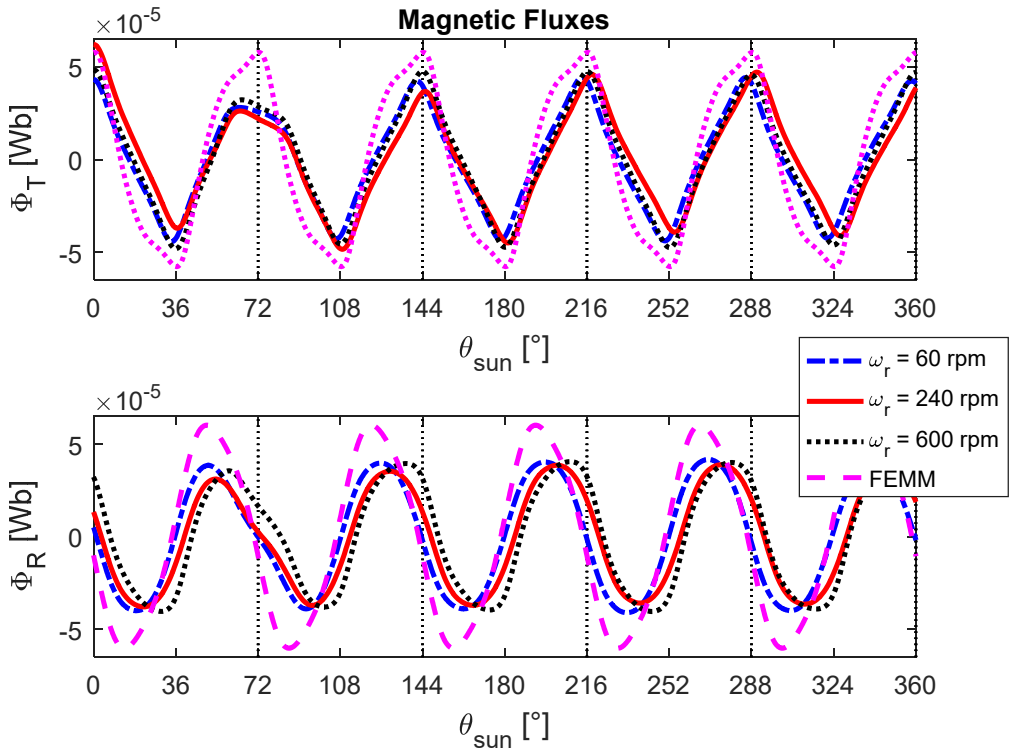

Figure 8.19 – Tangential and radial fluxes at different speed of ring rotor

8.3.3 Magnetic induction

The magnetic induction is evaluated using the dimensions of the ferromagnetic pole to calculate the section area of the coil in radial and tangential directions. The disposition of the two coils for the radial and tangential fluxes is reported in Figure 8.21.

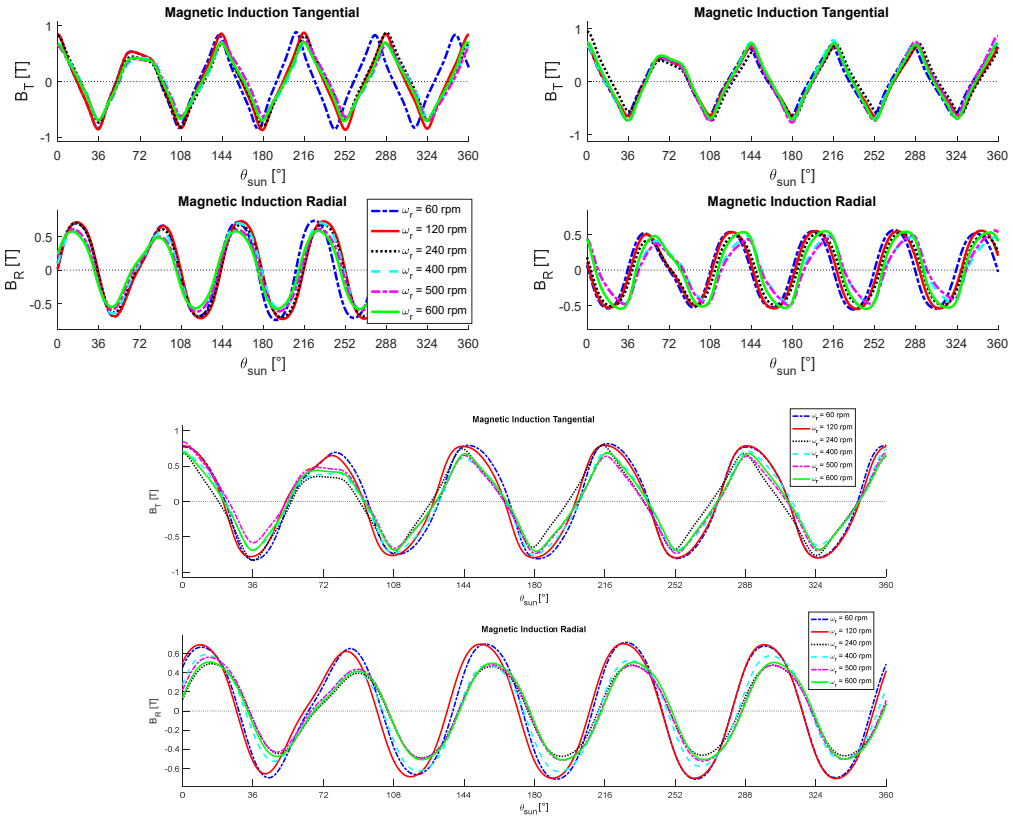

Figure 8.20 – Tangential and radial magnetic induction using pole # 1 (top-left), pole # 2 (top-right), and pole # 3 (bottom) acquisition of windings voltage.

As for the magnetic flux, also the magnetic induction is influenced by the rotational speed, so non-linear effects are presented, and the first waveform is lower than the others due to the segmented magnet with wrong magnetisation direction.

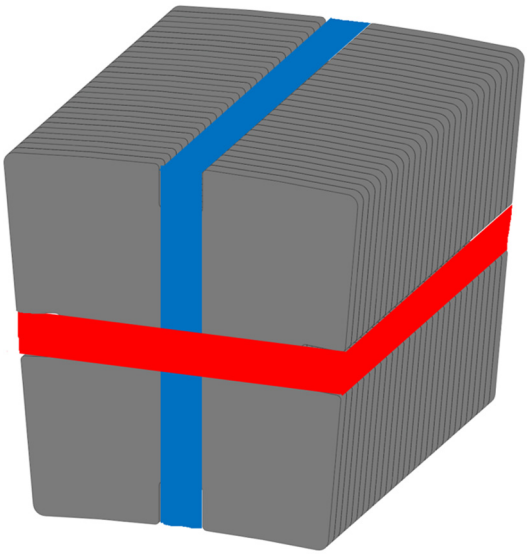

Figure 8.21 – Ferromagnetic pole with the two windings for tangential flux (blue) and radial (red) fluxes.

Finally, the experimental values of magnetic induction have to be compared with magnetic induction of the ferromagnetic poles, reported in § 7.6.1 in Figure 7.36. For the experimental tangential induction, the highest value is around 0.7-0.75 T, while for the numerical one at the centre of the pole it is of 0.6-0.65 T.

Instead, for the experimental radial induction the highest value is around 0.55 T, while for the numerical one it is of 0.75-0.8 T.

So, the comparison between experimental and numerical results is quite good, since the use of a 2D simulation in FEMM can influence the correctness of results.

8.4 Experimental results: mechanical quantities

The results reported in this section are obtained using the acquisitions of torque sensors and incremental encoders mounted on the test bench. During the experimental test, only one side of the prototype was connected to the electric motor, which the prototype in the 1st gear position. Hence, the power is supplied firstly from the outer rotor side, letting the prototype to work as a speed multiplier / torque reducer, while in the second set of tests the power input is the high-speed side, namely the sun shaft, ensuring the prototype to work as a torque multiplier / speed reducer. For this reason, the torque evaluated by the torque sensor, placed at the power input side, corresponds to the torque losses inside the magnetic gearbox, because of bearing dissipations. Instead, only the rotational speed is evaluated at the other side of gearbox transmission, since the torque measured at this side is equal to zero.

Moreover, during the experimental tests, an increment of the external temperature of the prototype has been perceived, because of two different possible phenomena: the former is the bearings overheating, the latter is instead related to thermal dissipations for eddy currents in the yoke on outer rotor. This last issue is strongly related to the magnetic induction value inside the yoke during its rotation. Infact, using the 2D simulation in FEMM, as reported in Figure 7.41 (right), the tangential induction has a sinusoidal trend during the ring rotation, with a non-zero mean value. This leads to thermal dissipations inside the yoke.

At the same time, the heating inside the prototype is responsible for the reduction of viscosity of the bearings lubricant oil. Therefore, higher the working temperature, better will be the performance of bearings with a consequential reduction of power losses inside the gearbox.

This effect is evident in Figure 8.22, where the torque measured by the input torque sensor is reported. Suppling power from the low-speed side, the reported torque loss corresponds to the mean value of torque during an acquisition of 5 s. All the different speeds, in the range $60 \div 660$ rpm, are tested in an incremental order during the test # 1, a decremental order in test # 2, and again in incremental order in test # 3.

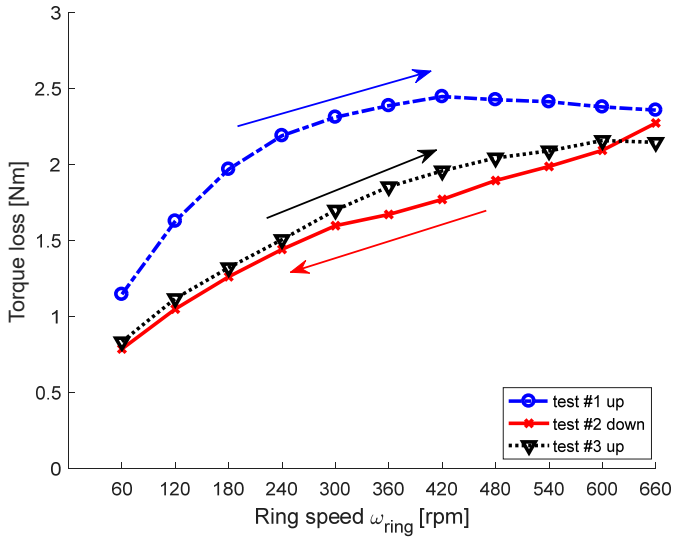

Figure 8.22 – Torque loss inside gearbox supplying power at low-speed side.

It is evident a reduction of power losses going on with the experimental acquisition. The values of dotted black lines were expected lower or equal to those of solid red line. For this reason, also other dynamic effects inside the transmission driveline should be taken into account in further future analyses.

The same set of experimental acquisitions are made supplying power from the high-speed side of the magnetic gearbox and testing all the rotational speeds, considering the transmission gear ratio. Hence, the rotational speeds of the inner rotor are in the range $2.6 * [60 \div 570]$ rpm, where 2.6 is the gear ratio of the 1st PMG inside the gearbox.

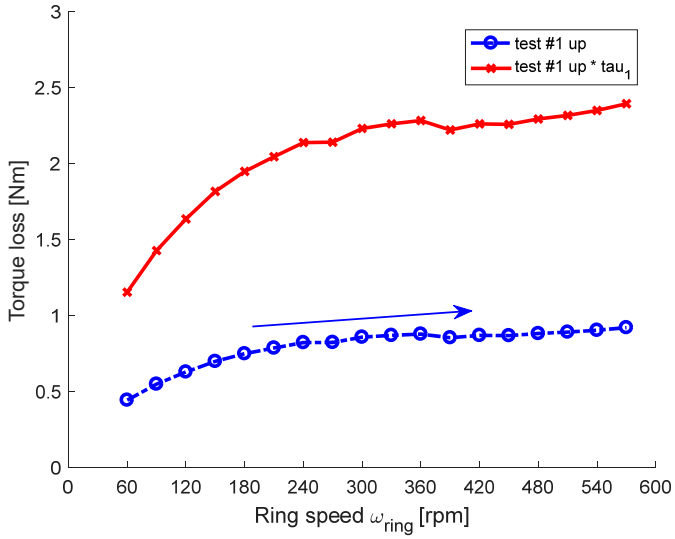

Figure 8.23 – Torque loss inside gearbox supplying power at high-speed side.

These results are reported in Figure 8.23, using the rotational speed of the ring rotor, obtaining lower value of dissipated torque than the previous case. This is due to the gear ratio, hence, to have a comparable result, it is necessary to

multiply the dissipated torque for 2.6. To be clear, the dash-dotted blue line is converted in the solid red one.

The comparison detween the two different configuration tests is reported in Figure 8.24, where it is possible to appreciate that the two curves are quite overlapped, especially at low rotational speeds. This means that the efficiency is similar in the two working conditions of torque amplifier and speed amplifier, in contrast with the traditional mechanical transmissions.

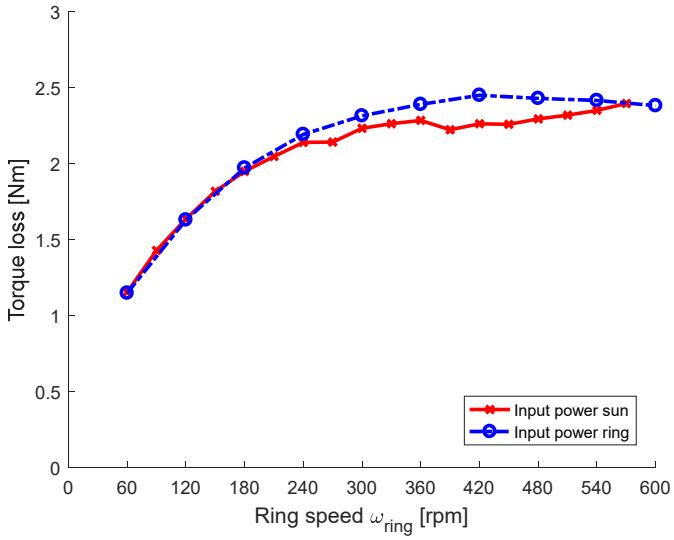

Figure 8.24 – Torque loss inside gearbox supplying power at high-speed side (sun rotor) and low-speed side (ring rotor).

The highest value of torque loss for bearing dissipations in consistent, near to 2.5 Nm at the low-speed side. For this reason, another further step, before continuing with the experimental activity is the substitution of the two bigger bearings, responsible for mechanical dissipations, with others.

Another important aspect that must be considered is the torque ripple. Indeed, this phenomenon depends firstly on the magnetic coupling between inner and outer rotor and on the modulation of the magnetic flux by the ferromagnetic poles and secondly on the torsional vibrations of the transmission driveline. Considering the first case, with power input at the low-speed side, in Figure 8.25 the trend of the torque dissipations at four different speeds of the ring are reported, for a complete rotation of the sun (high-speed side). Moreover, the mean value is reported for all the torques. The dotted vertical black lines define an angle amplitude which corresponds to the amplitude of a PMs pole pair on the sun rotor.

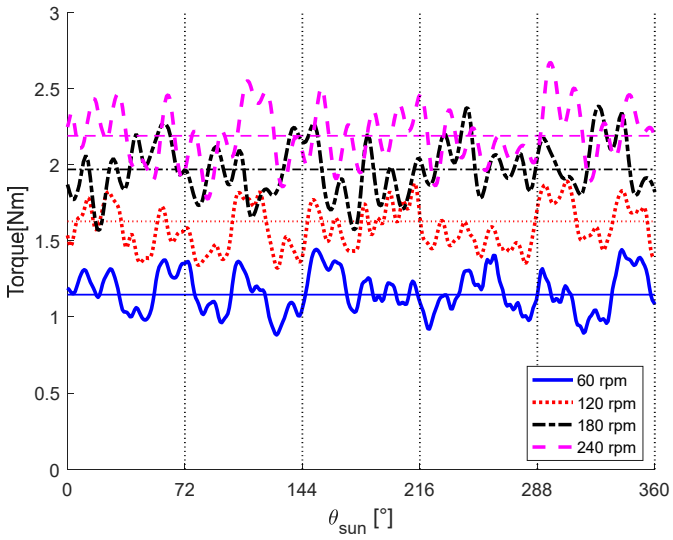

Figure 8.25 – Torque waveform supplying power at ring side.

Analysing the Fast Fourier Transform (FFT) of the torque signal in the range 0÷100 Hz, reported in Figure 8.26, and obtained using the torque acquisitions of 5 s, it is highlighted how the same harmonics are repeated for all the speeds tested.

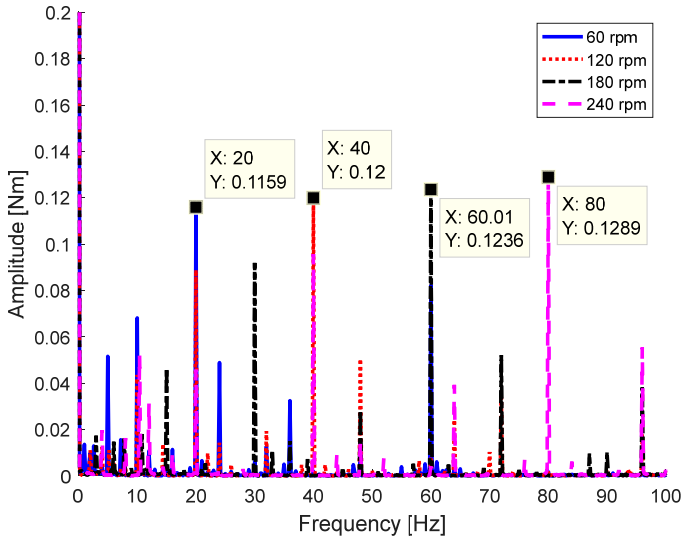

Figure 8.26 – FFT of torque waveform supplying power at ring side.

One of the highest harmonics, except for the mean contribution at 0 Hz, is found at 20 Hz, rotating at 60 rpm. Increasing the rotational speed, the frequency of this harmonic is increased, as well.

Moreover, the torque FFT for all the rotational speeds has been calculated. In Figure 8.27, the first eleven harmonics, namely the frequency of the first eleven highest peaks in terms of amplitude, for each speed are reported, with different marks. The dotted black lines have a slope equal to one and are traced starting the frequencies of harmonics computed at 60 rpm. Almost all the harmonics are

present also at higher rotational speeds, except for the region in the middle part of the figure, where certain harmonics are not crossed by the black lines, since they are not present at 60 rpm.

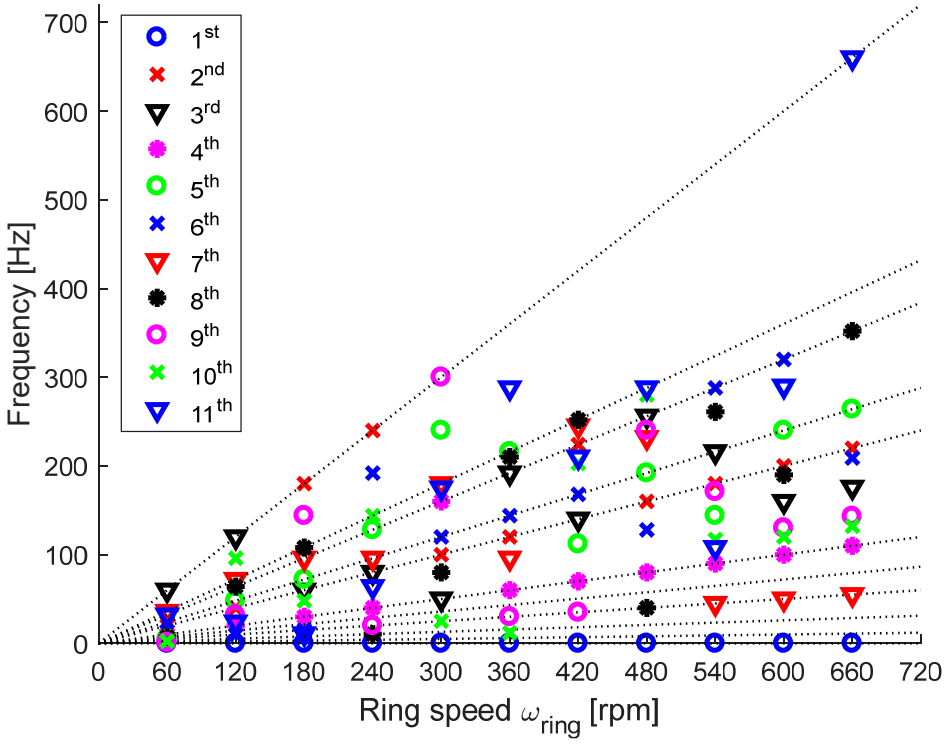

Figure 8.27 – Transmission order analysis supplying power at ring side.

Finally, from the previous figure it is evident that all the harmonics are related to the rotational speed, since all the marker of the harmonics follow a trend which depends on the slope of the black lines. Except for the first harmonic that is at 0 Hz for all the speeds, there are no other points which trace a line parallel to the x-axis. This means that there are no structural excitation frequencies of the test bench, or torsional resonances of the transmission driveline.

The same order analysis in made using the experimental acquisitions obtained supplying power from the high-speed side. In order to have comparable results with the previous case, in Figure 8.28, the rotational speed of the low-speed side is reported, while all the frequencies have been scaled of a factor equal to the transmission gear ratio $\tau_1 = 2.6$. Supplying power at the low-speed side the highest frequencies for the first eleven harmonics are found below 400 Hz, while providing power at the high-speed side, the highest frequencies are all below 200 Hz. This means that the mechanical properties of the system are changing since the two sides of transmission have different stiffnesses.

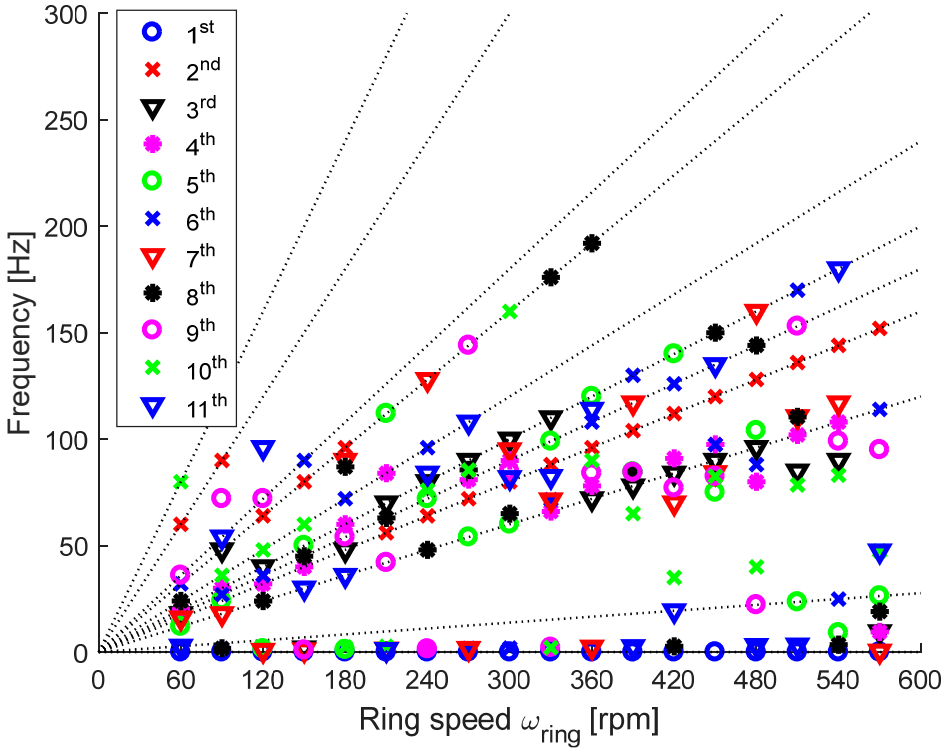

Figure 8.28 – Transmission order analysis supplying power at sun side.

Moreover, as regards the first order, only the harmonic at 60 rpm of ring is found, while for the other orders the trend is similar to the previous case.

The last analysis on the experimental data is made on ripple of the 1st transmission gear ratio of magnet gearbox. In Figure 8.29, the rotational speed of input and output shaft of gearbox are reported, during rotations at 60 rpm and 600 rpm of the low-speed side.

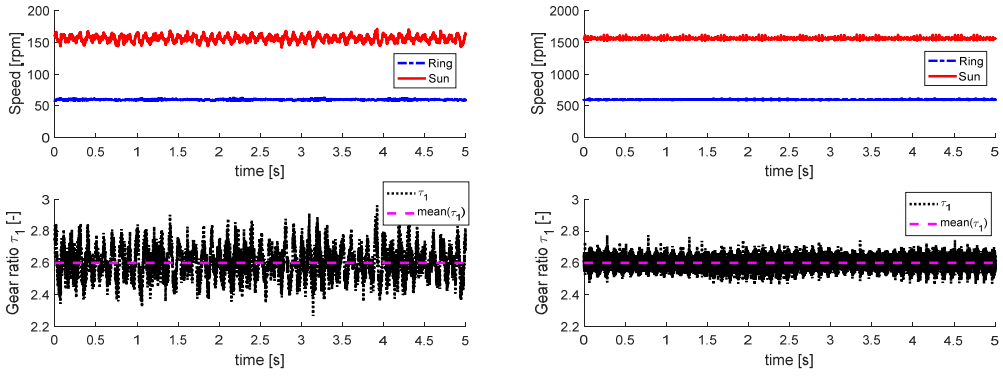

Figure 8.29 – Speed and transmission ratio trends supplying power at 60 rpm (left) and 600 rpm (right) at ring side.

The ripple on the gear ratio $\tau_1 = 2.6$, is higher at lower rotational speed, while the ripple on the speed velocity of inner and outer rotors is higher at high speed, in terms of speed range, and it is lower at high speed, in percentage terms w.r.t. the speed mean value.

Moreover, in Figure 8.29 (left), it is possible to observe a multiplicity of 5 in the ring speed, during an acquisition of 5 s. Hence, this phenomenon at 1 Hz is probably related to the rotational speed of the ring that is 60 rpm, namely 1 Hz. It is possible to do the same thinking also for the Figure 8.29 (right), where the multiplicity in the ring speed has a frequency of 10 Hz.

Finally, in Figure 8.30, the ripple on the gear ratio is reported for the two configurations at different speeds. This ripple is evaluated using Eq. (8.2):

$$ripple[\%] = \frac{\max(\tau_1) - \min(\tau_1)}{2 \cdot \text{mean}(\tau_1)} \cdot 100\% \tag{8.2}$$

where τ_1 is the transmission ratio and the ripple is evaluated as the semi-amplitude of the ratio range w.r.t. the mean value.

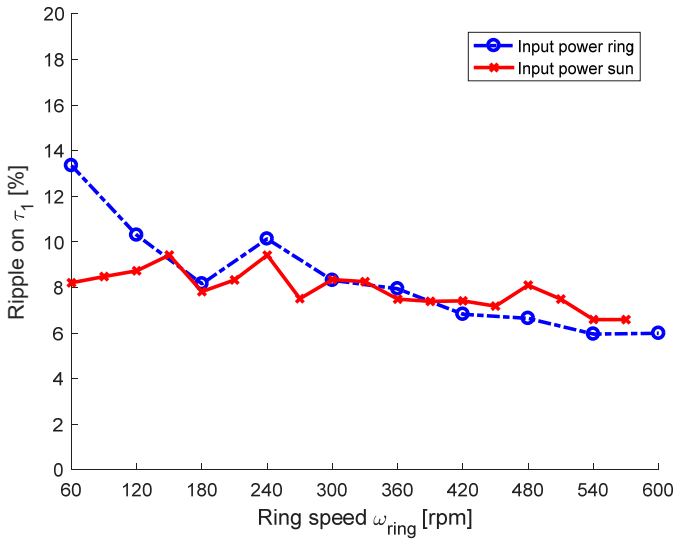

Figure 8.30 – Semi-ripple on gear ratio τ_1 w.r.t. mean value.

It is clear how the ripple decreases with an increment of the rotational speed. Moreover, the trend of two test configurations are a bit different since the ripple is almost constant supplying power at the high-speed side.

8.4 Conclusions

This chapter addressed the description of the magnetic gearbox prototype and its test rig to carry out the experimental campaign. Radial and tangential windings in 3 of 18 ferromagnetic poles have been realised to measure the magnetic flux inside the device to evaluate its magneto-mechanical performance.

A brief overview on the electrical panel project and realisation has been provided, presenting its main components and the system for the acquisition of experimental data.

The magnetic gearbox has been tested at fixed gear in no load condition supplying power at the two sides of transmission, to evaluate the torque losses due to the bearing dissipations, proving that the losses are quite similar letting the gearbox working as torque multiplier or speed multiplier.

Moreover, the acquired torque signals have been analysed, performing their FFT, in order to detect the main harmonics components inside the magnetic transmission, at different rotational speeds.

Finally, the speed ripple has been analysed at different rotational speeds, highlighting a ripple percentage decrement with an increment of the rotational speed at the two side of transmission.

Chapter 9

9. Conclusions

This dissertation has faced numerical, simulative, and experimental analyses of complex systems dedicated to power transmission that could be ground-breaking mainly in the automotive field, with the characteristics of traditional mechanical systems and with magneto-mechanical solutions.

The analysis of different deterministic and stochastic methods used to study uncertain systems and their dynamic responses, illustrated in Chapter 2, is part of the research activity carried out as visiting PhD student at the ISVR (Institute of Sound and Vibration Research) of Southampton University. Even if the covered topic is not strongly correlated to the power transmission systems, it has been a great opportunity to widen my technical knowledge in the field of mechanical description, identification, and active control. Mechanical systems with uncertainty have been faced from a dynamic point of view, analysing the effects of uncertain parameters on the frequency response functions of a mechanical system. Moreover, a basic overview on the active control of these system and on the variance of open-loop and closed-loop poles has been faced, although these results are not reported in this dissertation, since, at the moment, too far from the main topic.

The FFD and the LHD methods can be considered as the two correct approaches to deal with two or more factors, conducting a factorial experiment, in which the definition of an appropriate DOE is necessary to perform an accurate analysis. On the other side, complex interval analysis and complex affine analysis have demonstrated their advantage in the computational costs, with bad accuracy in FRF estimation over a certain percentage of uncertainty, depending on the number of uncertain parameters, which in case of 8 uncertain parameters is estimated around 1.5÷2 %.

Instead, the research activity, presented in Chapter 3 was dedicated to the modelling and experimental validation of powertrain components, to respond to the always increasing industrial needs to improve the NVH performance. As a first step, the model of a Dual Clutches Transmission gearbox has been developed

using Siemens/Amesim software, with a particular attention to synchronisers modelling, torsional and axial clearances and stiffness and contact damping between gear teeth of the gearbox. The model was validated comparing the simulated results with the experimental results of several test-runs, going to analyse the torsional backlashes of the transmission and the acceleration in a point of the gearbox external surface. A sensitivity analysis on different parameters of the model has been carried out to investigate possible improvements on NVH performance during the different gear engagements. Specifically, a methodology for the objective evaluation of the gearshift induce vibrations has been developed, evaluating the gearbox acceleration starting from the bearing forces. The more detailed is the model, the higher the computational costs are, hence if the analysis focuses on the gearshift phase a detailed model must be used, instead for the analysis of torsional dynamics during classical operational condition a simplified model can be used.

Starting from the main noise issues of classic mechanical transmissions, the possible adoption of passive magnetic gears was analysed, in Chapter 4, highlighting advantages and drawbacks with respect to traditional mechanical transmissions, such as the possibility of transferring torque contactless, avoiding gear wearing and their lubrication, and proposing their application in the automotive field. It has been concluded that a PMG can transmit the torque requested by a vehicle, but this could be done only if a complete redesign of the power transmission driveline is performed.

The further step in the topic of magnetic gears, in Chapter 5, has regarded the development of a magneto mechanical design with an analytical-dynamic approach, which has been integrated with a multi-objective optimisation of the designed magnetic gear, in which two different objective functions are used to deal with the maximisation of the torque density and the minimisation of moment of inertia of the rotating parts, for a better dynamic response of the PMG. Two different optimisation algorithms, namely “Pattern Search” and “fmincon” are carried out, proposing different points of view in the choice of appropriate constructional parameters for a PMG. Results given by the optimised PMG, in terms of torque maps for each angle position of the inner and outer rotors, together with their dynamic equations have been integrated in a model of transmission to validate the possible adoption of a magnetic transmission inside an automotive driveline.

The main focus of the activity proposed in Chapter 6 has been the design of a PMG prototype. Different arrangements for the PMG prototype are proposed, in order to achieve the best solution, in terms of compactness of the device and parametricity, which made possible to change the configuration, having different input/output solutions, hence having different working conditions as torque amplifier or speed amplifier.

The efforts in the constant research of an innovative application using magnetic transmissions has conducted to a patent application about a magnetic gearbox, presented in Chapter 7, which allows a complexity reduction of the transmission driveline integrating the functions of clutch, gearbox and of torque

limiter, solving at the same time the annoying issue of mechanical transmissions as gear engagement noise, torque interruption during gearshifts and failure or wearing of the mechanical components. Several patented constructional solutions of a magnetic gearbox, are proposed, varying the element used as modulator for the magnetic flux, which function can be assumed by the three elements of the planetary magnetic gearbox. A simplified control logic, with only proportional and integrative gains, has been applied in Matlab/Simulink environment to test the gearshift procedure of a magnetic gearbox transmission. For the automotive transmission analysed, the gearshift procedure can be completed in less than 0.5 s, which is a time strongly comparable with mechanical gearshift using the synchronisers in car gearboxes. Hence a CAD model of a magnetic gearbox prototype has been developed and an analysis on FEMM software is performed for the dimensioning of the prototype, evaluating its magneto-mechanical properties, responsible for its dynamic performance in steady-state and transient conditions.

The experimental activity reported in Chapter 8 can be considered as a preliminary stage of a more consistent experimental campaign, which should be carried on in the following months. Indeed, only tests at constant different speeds with no load on the other side of transmission have been performed.

The torque losses, due to bearing dissipations, are unfortunately comparable with the maximum transmissible torque of the gearbox, therefore it will be necessary to modify the magnetic gearbox prototype changing the bearings with highest dissipation. On the other side, also the 2nd gear of the magnetic gearbox must be tested for the complete characterisation of the magneto-mechanical properties. Instead, the analysis of the gearbox in neutral condition will be useful to characterise the mechanical dissipations, integrating a dissipation function in the torque map of the two electric motors, or considering it for an evaluation of a mechanical efficiency, different from the magnetic efficiency of the transmission.

Moreover, the gearshift procedure will be automated during the experimental tests, letting the magnetic gearbox changes the transmission ratio under specific operative conditions, both in upshifts and downshifts. Different control logics will be applied to the gearshift procedure to achieve the smoothest ever in terms of speed oscillation and the quickest one in terms of necessary time.

Finally, the magnetic gearbox will be tested in transient conditions during the run-up phase to evaluate the ripple on both torque and speed signals in a continuous way and not only at specific rotational speeds. In this way it will be possible to detect the critical regions in which torsional oscillations of the magnetic transmission are present or, in the same way, the excitation frequencies of the entire test bench.

10. List of publications

Journal publications

[3] E. Bonisoli, D. Lisitano, **L. Dimauro**, "Detection of critical mode-shapes in flexible multibody systems dynamics: the case study of a racing motorcycle", submitted to *Multibody System Dynamics*, March 2021.

[2] M. Filippini, P. Alotto, V. Cirimele, M. Repetto, C. Ragusa, **L. Dimauro**, E. Bonisoli, "Magnetic loss analysis in coaxial magnetic gears", *Electronics*, Vol. 8, Issue 11, 2019, paper n°1320, DOI: 10.3390/electronics8111320, pp. 1-15.

[1] V. Cirimele, **L. Dimauro**, M. Repetto, E. Bonisoli, "Multi-objective Optimization of a Magnetic Gear for Powertrain Applications", *International Journal of Applied Electromagnetics and Mechanics*, Vol. 60, Issue S1, 2019, DOI: 10.3233/JAE-191103, pp. S25-S34.

Book chapters

[2] E. Bonisoli, D. Lisitano, **L. Dimauro**, L. Peroni, "A proposal of dynamic behaviour design based on mode shape tracing: numerical application to a motorbike frame", *Dynamic Substructures*, Vol. 4, *Proceedings of the 37th IMAC*, A Conference and Exposition on Structural Dynamics, Conference Proceedings of the Society for Experimental Mechanics Series, 186 pp., Ch. 14, 2020, Springer, ISBN: 978-3-030-12183-9, Online ISBN: 978-3-030-12184-6, DOI: 10.1007/978-3-030-12184-6_14, pp. 149-158.

[1] E. Bonisoli, M. Casazza, D. Lisitano, **L. Dimauro**, "Parametric experimental modal analysis of a modern violin based on a Guarneri del Gesù model", *Rotating Machinery, Vibro-Acoustics & Laser Vibrometry*, Vol. 7, *Proceedings of the 36th IMAC*, A Conference and Exposition on Structural Dynamics, Conference Proceedings of the Society for Experimental Mechanics Series, 244 pp., Ch. 21, 2019, Springer, ISBN: 978-3-319-74692-0, Online ISBN: 978-3-319-74693-7, DOI: 10.1007/978-3-319-74693-7_21, pp. 219-230.

Conference proceedings

[3] **L. Dimauro**, V. Cirimele, E. Bonisoli, M. Repetto, "Electro-mechanical design of a magnetic gear prototype", *XXVI Symposium Electromagnetic Phenomena in Nonlinear Circuits*, *EPNC 2020*, April 7-9, 2021, Torino, Italy, Web conference, pp. 1-2.

[2] E. Galvagno, **L. Dimauro**, G. Mari, M. Velardocchia, A.D. Vella, "Dual Clutch Transmission vibrations during gear shift: a simulation-based approach for clunking noise assessment", *SAE Technical Paper*, 2019-01-1553, 2019, DOI: 10.4271/2019-01-1553, pp. 1-12.

[1] E. Bonisoli, D. Lisitano, **L. Dimauro**, "Experimental and numerical mode shape tracing from components to whole motorbike chassis", *International Conference on Noise and Vibration Engineering*, *ISMA*, 2018, Leuven, Belgium, September 17-19, pp. 3597-3604..

Patent submissions

[2] E. Bonisoli, D. Lisitano, **L. Dimauro**, "Smorzatore dinamico parametrico con funzionalità di sensore autoalimentato" ("Parametric dynamic absorber and self-power sensor"), Italian patent application n. 102020000030212, December 9, 2020.

[1] E. Bonisoli, **L. Dimauro**, A. Vigliani, M. Velardocchia, M. Repetto, V. Cirimele, P. Alotto, M. Filippini, "Cambio di tipo magnetico" ("Magnetic Gearbox"), Italian patent application n. 102020000017512, July 17, 2020.

11. References

[1] R. Fischer, F. Küçükay, G. Jürgens, R. Najork, B. Pollak, The automotive transmission book, Springer, 2015.

[2] G. Lechner, H. Naunheimer, Automotive transmissions: fundamentals, selection, design and application, Springer Science & Business Media, 1999.

[3] G.F. Heath, R.R. Filler, J. Tan, Development of Face Gear Technology for Industrial and Aerospace Power Transmission, (2002).

[4] H. Maas, A. Schamel, C. Weber, U. Kramer, Review of combustion engine efficiency improvements and the role of e-fuels, in: Int. Mot. 2016, Springer, 2016: pp. 463–483.

[5] J. Venkatesan, V.M. Praveen, V.K. Bhargav, B.B. Moorthy, Performance Improvement in Automotive Engines Using Vapour Absorption Refrigeration System for Air Conditioning, SAE Technical Paper, 2005.

[6] S.N. Doğan, G. HeNNiNG, T. Gödecke, M. Sommer, K. Fronius, M. Krohn, J. Kiesel, J. Dorfschmid, Advanced transmission technologies to improve vehicle performance, in: Altern. Fuels Adv. Veh. Technol. Improv. Environ. Perform., Elsevier, 2014: pp. 393–432.

[7] W. Novak, M. Stockmeier, B. Bertsche, Improvement of powertrain efficiency via CARF-Transmissions, in: DS 35 Proc. ICED 05, 15th Int. Conf. Eng. Des. Melbourne, Aust. 15.-18.08. 2005, 2005.

[8] N. Mutoh, O. Nishida, T. Takayanagi, T. Kato, K. Murakami, Driving torque distribution method for front-and-rear-wheel-independent-drive-type electric vehicles (FRID EVs) at the time of cornering, World Electr. Veh. J. 4 (2010) 558–566.

[9] F. Bucchi, B. Lenzo, F. Frendo, W. De Nijs, A. Sorniotti, The effect of the front-to-rear wheel torque distribution on vehicle handling: an experimental assessment, in: Dyn. Veh. Roads Tracks Vol 1 Proc. 25th Int. Symp. Dyn. Veh. Roads Tracks (IAVSD 2017), 14-18 August 2017, Rockhampton, Queensland, Aust., CRC Press, 2017: p. 31.

[10] J.S. Freeman, S.A. Velinsky, Design of Vehicle Power Transmission Systems, J. Mech. Des. 117 (1995) 113–120. https://doi.org/10.1115/1.2836443.

[11] I. Kolmanovsky, M. Van Nieuwstadt, J. Sun, Optimization of complex powertrain systems for fuel economy and emissions, in: Proc. 1999 IEEE Int. Conf. Control Appl. (Cat. No. 99CH36328), IEEE, 1999: pp. 833–839.

[12] M.J. Duty, M. Papke, Methods and systems for powertrain optimization and improved fuel economy, (2011).

[13] A.M. Lewis, J.C. Kelly, G.A. Keoleian, Vehicle lightweighting vs. electrification: Life cycle energy and GHG emissions results for diverse powertrain vehicles, Appl. Energy. 126 (2014) 13–20. https://doi.org/10.1016/j.apenergy.2014.03.023.

[14] X. Xu, P. Dong, Y. Liu, H. Zhang, Progress in Automotive Transmission

Technology, Automot. Innov. 1 (2018) 187–210. https://doi.org/10.1007/s42154-018-0031-y.
[15] M.S. Qatu, M.K. Abdelhamid, J. Pang, G. Sheng, Overview of automotive noise and vibration, Int. J. Veh. Noise Vib. 5 (2009) 1–35. https://doi.org/10.1504/IJVNV.2009.029187.
[16] M.S. Qatu, Recent research on vehicle noise and vibration, Int. J. Veh. Noise Vib. 8 (2012) 289–301. https://doi.org/10.1504/IJVNV.2012.051536.
[17] L.J. Adamson, S. Fichera, B. Mokrani, J.E. Mottershead, Pole placement in uncertain dynamic systems by variance minimisation, Mech. Syst. Signal Process. 127 (2019) 290–305. https://doi.org/10.1016/j.ymssp.2019.03.007.
[18] G. Manson, Calculating frequency response functions for uncertain systems using complex affine analysis, J. Sound Vib. 288 (2005) 487–521. https://doi.org/10.1016/j.jsv.2005.07.004.
[19] D. Moens, D. Vandepitte, An interval finite element approach for the calculation of envelope frequency response functions, Int. J. Numer. Methods Eng. 61 (2004) 2480–2507. https://doi.org/10.1002/nme.1159.
[20] K. Tsurumoto, S. Kikuchi, A new magnetic gear using permanent magnet, IEEE Trans. Magn. 23 (1987) 3622–3624.
[21] K. Atallah, D. Howe, A novel high-performance magnetic gear, IEEE Trans. Magn. 37 (2001) 2844–2846. https://doi.org/10.1109/20.951324.
[22] K. Atallah, S.D. Calverley, D. Howe, Design, analysis and realisation of a high-performance magnetic gear, IEE Proceedings-Electric Power Appl. 151 (2004) 135–143.
[23] X. Liu, K.T. Chau, J.Z. Jiang, C. Yu, Design and analysis of interior-magnet outer-rotor concentric magnetic gears, J. Appl. Phys. 105 (2009) 07F101.
[24] M. Filippini, P. Alotto, Coaxial Magnetic Gear Design and Optimization, IEEE Trans. Ind. Electron. 64 (2017) 9934–9942. https://doi.org/10.1109/TIE.2017.2721918.
[25] R.G. Montague, C.M. Bingham, K. Atallah, Magnetic gear dynamics for servo control, Proc. Mediterr. Electrotech. Conf. - MELECON. (2010) 1192–1197. https://doi.org/10.1109/MELCON.2010.5475900.
[26] M. Fukuoka, K. Nakamura, O. Ichinokura, Dynamic simulation of planetary type magnetic gear based on reluctance network analysis, Proc. 2011 14th Eur. Conf. Power Electron. Appl. EPE 2011. 47 (2011) 2414–2417.
[27] M. Desvaux, R. Le Goff Latimier, B. Multon, S. Sire, H. Ben Ahmed, Analysis of the dynamic behaviour of magnetic gear with nonlinear modelling for large wind turbines, Proc. - 2016 22nd Int. Conf. Electr. Mach. ICEM 2016. (2016) 1332–1338. https://doi.org/10.1109/ICELMACH.2016.7732697.
[28] O. Molokanov, P. Kurbatov, P. Dergachev, A. Alami, Dynamic model of coaxial magnetic planetary gear, 2015 18th Int. Conf. Electr. Mach. Syst. ICEMS 2015. (2016) 944–948. https://doi.org/10.1109/ICEMS.2015.7385171.
[29] A. Matthee, S. Gerber, R.J. Wang, A high performance concentric magnetic gear, in: Proc. South. African Univ. Power Eng. Conf. Johannesburg, South Africa, 2015: pp. 203–207.
[30] G. Jungmayr, J. Loeffler, B. Winter, F. Jeske, W. Amrhein, Magnetic gear: Radial force, cogging torque, skewing, and optimization, IEEE Trans. Ind. Appl. 52 (2016) 3822–3830.

[31] V. Cirimele, L. Dimauro, M. Repetto, E. Bonisoli, Multi-objective optimisation of a magnetic gear for powertrain applications, Int. J. Appl. Electromagn. Mech. 60 (2019). https://doi.org/10.3233/JAE-191103.
[32] S. Gerber, R.J. Wang, Evaluation of a prototype magnetic gear, Proc. IEEE Int. Conf. Ind. Technol. (2013) 319–324. https://doi.org/10.1109/ICIT.2013.6505692.
[33] K.K. Uppalapati, W. Bomela, J.Z. Bird, M. Calvin, J. Wright, Construction of a low speed flux focusing magnetic gear, 2013 IEEE Energy Convers. Congr. Expo. ECCE 2013. (2013) 2178–2184. https://doi.org/10.1109/ECCE.2013.6646976.
[34] C.G.C. Neves, M.F. Goettems, A.F.F. Filho, Construction of a Coaxial Magnetic Gear, 18th Int. Symp. Electromagn. Fields Mechatronics, Electr. Electron. Eng. (2017) 2–5.
[35] C.C. Huang, M.C. Tsai, D.G. Dorrell, B.J. Lin, Development of a magnetic planetary gearbox, IEEE Trans. Magn. 44 (2008) 403–412. https://doi.org/10.1109/TMAG.2007.914665.
[36] M. Filippini, P. Alotto, V. Cirimele, M. Repetto, C. Ragusa, L. Dimauro, E. Bonisoli, Magnetic loss analysis in coaxial magnetic gears, Electron. 8 (2019). https://doi.org/10.3390/electronics8111320.
[37] J. Druant, H. Vansompel, F. De Belie, P. Sergeant, Loss Identification in a Double Rotor Electrical Variable Transmission, IEEE Trans. Ind. Electron. 64 (2017) 7731–7740. https://doi.org/10.1109/TIE.2017.2698362.
[38] S.J. Kim, E.J. Park, S.Y. Jung, Y.J. Kim, Torque transfer efficiency estimation of the magnetic gear considering eddy current loss, 2016 IEEE Transp. Electrif. Conf. Expo, Asia-Pacific, ITEC Asia-Pacific 2016. (2016) 338–341. https://doi.org/10.1109/ITEC-AP.2016.7512974.
[39] K. Atallah, J. Wang, S.D. Calverley, S. Duggan, Design and operation of a magnetic continuously variable transmission, IEEE Trans. Ind. Appl. 48 (2012) 1288–1295.
[40] G. Genta, Vibration dynamics and control, Springer, 2009.
[41] D.J. Inman, Vibration with control, Wiley Online Library, 2006.
[42] S.G. Kelly, Fundamentals of Mechanical Vibrations Any text on mechanical vibrations, (2000).
[43] H.H. Khodaparast, J.E. Mottershead, K.J. Badcock, Propagation of structural uncertainty to linear aeroelastic stability, Comput. Struct. 88 (2010) 223–236. https://doi.org/10.1016/j.compstruc.2009.10.005.
[44] K.J. Badcock, S. Timme, S. Marques, H. Khodaparast, M. Prandina, J.E. Mottershead, A. Swift, A. Da Ronch, M.A. Woodgate, Transonic aeroelastic simulation for instability searches and uncertainty analysis, Prog. Aerosp. Sci. 47 (2011) 392–423. https://doi.org/10.1016/j.paerosci.2011.05.002.
[45] K.J. Badcock, H.H. Khodaparast, S. Timme, J.E. Mottershead, Calculating the influence of structural uncertainty on aeroelastic limit cycle response, Collect. Tech. Pap. - AIAA/ASME/ASCE/AHS/ASC Struct. Struct. Dyn. Mater. Conf. (2011). https://doi.org/10.2514/6.2011-1741.
[46] V.R. Franco, P.S. Varoto, Parameter uncertainties in the design and optimization of cantilever piezoelectric energy harvesters, Mech. Syst. Signal Process. 93 (2017) 593–609. https://doi.org/10.1016/j.ymssp.2017.02.030.
[47] P.S. Varoto, Effects of uncertainties on the dynamic response of an MDOF piezoelastic vibration energy harvester, Proc. ICEDyn. (2019) 1–17.

[48] M. Beyaoui, M. Tounsi, K. Abboudi, N. Feki, L. Walha, M. Haddar, Dynamic behaviour of a wind turbine gear system with uncertainties, Comptes Rendus - Mec. 344 (2016) 375–387. https://doi.org/10.1016/j.crme.2016.01.003.
[49] S. Wei, J. Zhao, Q. Han, F. Chu, Dynamic response analysis on torsional vibrations of wind turbine geared transmission system with uncertainty, Renew. Energy. 78 (2015) 60–67. https://doi.org/10.1016/j.renene.2014.12.062.
[50] A.H. Sayed, V.H. Nascimento, Design criteria for uncertain models with structured and unstructured uncertainties, Robustness Identif. Control. (2007) 159–173. https://doi.org/10.1007/bfb0109867.
[51] P.M. Patre, W. MacKunis, C. Makkar, W.E. Dixon, Asymptotic tracking for systems with structured and unstructured uncertainties, IEEE Trans. Control Syst. Technol. 16 (2008) 373–379. https://doi.org/10.1109/TCST.2007.908227.
[52] M.A. Djeziri, R. Merzouki, B.O. Bouamama, Robust monitoring of an electric vehicle with structured and unstructured uncertainties, IEEE Trans. Veh. Technol. 58 (2009) 4710–4719. https://doi.org/10.1109/TVT.2009.2026281.
[53] L. Wang, Mixed structured and unstructured uncertainty modeling method with application to Linear Tape-Open drives, University of California, San Diego, 2012.
[54] R.E. Moore, Interval arithmetic and automatic error analysis in digital computing, Stanford University, 1963.
[55] R.E. Moore, Interval analysis, Prentice-Hall Englewood Cliffs, 1966.
[56] J.L.D. Comba, J. Stolfi, Affine arithmetic and its applications to computer graphics. Anais do VII SIBGRAPI, 9–18, (1993).
[57] R. Boche, Complex interval arithmetic with some applications Lockheed Missiles & Space Company, (1966).
[58] D.C. Montgomery, Design and analysis of experiments, John wiley & sons, 2017.
[59] N.A. Heckert, J.J. Filliben, C.M. Croarkin, B. Hembree, W.F. Guthrie, P. Tobias, J. Prinz, Handbook 151: NIST/SEMATECH e-Handbook of Statistical Methods, (2002).
[60] J. Antony, Full Factorial Designs, Second Edi, Elsevier Ltd, 2014. https://doi.org/10.1016/b978-0-08-099417-8.00006-7.
[61] M.D. McKay, R.J. Beckman, W.J. Conover, A comparison of three methods for selecting values of input variables in the analysis of output from a computer code, Technometrics. 42 (2000) 55–61.
[62] M. Stein, Large sample properties of simulations using Latin hypercube sampling, Technometrics. 29 (1987) 143–151.
[63] J.C. Helton, F.J. Davis, Latin hypercube sampling and the propagation of uncertainty in analyses of complex systems, Reliab. Eng. Syst. Saf. 81 (2003) 23–69.
[64] D.M. Steinberg, D.K.J. Lin, A construction method for orthogonal Latin hypercube designs, Biometrika. 93 (2006) 279–288.
[65] A. Shapiro, Monte Carlo Sampling Methods, Handbooks Oper. Res. Manag. Sci. 10 (2003) 353–425. https://doi.org/10.1016/S0927-0507(03)10006-0.
[66] E. Bonisoli, LUPOS – LUmped Parameters Open Source FEM code, Politecnico di Torino, Tutorial v.2021-01-16, (2021).

[67] C. Mares, J.E. Mottershead, M.I. Friswell, Stochastic model updating: Part 1-theory and simulated example, Mech. Syst. Signal Process. 20 (2006) 1674–1695. https://doi.org/10.1016/j.ymssp.2005.06.006.
[68] J.E. Mottershead, C. Mares, S. James, M.I. Friswell, Stochastic model updating: Part 2-application to a set of physical structures, Mech. Syst. Signal Process. 20 (2006) 2171–2185. https://doi.org/10.1016/j.ymssp.2005.06.007.
[69] E. Galvagno, L. Dimauro, G. Mari, M. Velardocchia, A.D. Vella, Dual Clutch Transmission Vibrations during Gear Shift: A Simulation-Based Approach for Clunking Noise Assessment, SAE Tech. Pap. 2019-June (2019). https://doi.org/10.4271/2019-01-1553.
[70] D. Centea, H. Rahnejat, M.T. Menday, The influence of the interface coefficient of friction upon the propensity to judder in automotive clutches, Proc. Inst. Mech. Eng. Part D J. Automob. Eng. 213 (1999) 245–258.
[71] V. Niola, V. Avagliano, G. Quaremba, The gear whine noise, in: Proc. 4th WSEAS (World Sci. Eng. Acad. Soc. Int. Conf. Energy Dev. Environ., 2011: pp. 445–450.
[72] D. Le Guen, T. Weck, A. Balihe, B. Verbeke, Definition of gearshift pattern: Innovative optimization procedures using system simulation, SAE Int. J. Engines. 4 (2011) 412–431.
[73] M. Chen, D. Wang, H. Lee, C. Jiang, J. Xin, Application of CAE in design optimization of a wet dual cutch transmission and driveline, SAE Int. J. Passeng. Cars-Mechanical Syst. 7 (2014) 1128–1137.
[74] S. Shih, J. Yruma, P. Kittredge, Drivetrain noise and vibration troubleshooting, SAE Trans. (2001) 485–495.
[75] R. Brancati, E. Rocca, R. Russo, A gear rattle model accounting for oil squeeze between the meshing gear teeth, Proc. Inst. Mech. Eng. Part D J. Automob. Eng. 219 (2005) 1075–1083.
[76] R. Russo, R. Brancati, E. Rocca, Experimental investigations about the influence of oil lubricant between teeth on the gear rattle phenomenon, J. Sound Vib. 321 (2009) 647–661.
[77] H.H. Miyasato, V.G.S. Simionatto, M.D. Junior, Study of the gear rattle phenomena in automotive powertrain systems, in: Proc. COBEM, 2011: pp. 1–10.
[78] R. Brancati, E. Rocca, S. Savino, A gear rattle metric based on the wavelet multi-resolution analysis: experimental investigation, Mech. Syst. Signal Process. 50 (2015) 161–173.
[79] Z. Zhang, J. Pang, H. Li, X. Yang, L. Wang, Y. Li, Study Of Dual-Clutch Transmission Gear Rattle Under Low Speed Driving Condition, ICSV22, Florence (Italy). (2015) 12–16.
[80] E. Galvagno, G.R. Guercioni, A. Vigliani, Sensitivity analysis of the design parameters of a dual-clutch transmission focused on NVH performance, SAE Technical Paper, 2016.
[81] E. Galvagno, A. Tota, M. Velardocchia, A. Vigliani, Enhancing Transmission NVH Performance through Powertrain Control Integration with Active Braking System, SAE Technical Paper, 2017.
[82] P.D. Walker, N. Zhang, Investigation of synchroniser engagement in dual clutch transmission equipped powertrains, J. Sound Vib. 331 (2012) 1398–1412.
[83] S.T. Razzacki, J.E. Hottenstein, Synchronizer design and development for dual clutch transmission (DCT), SAE Technical Paper, 2007.

[84] H. Pacejka, Tire and vehicle dynamics, Elsevier, 2005.
[85] S.K.F. Group, SKF Rolling Bearings Catalogue, SKF Gr. Author. (2016).
[86] C.G. Armstrong, Power-transmitting device, 1901.
[87] H.T. Faus, Magnet gearing, (1941).
[88] J.T.B. Martin, Magnetic transmission, (1968).
[89] S. Rand, Magnetic transmission system, (1970).
[90] M. Hetzel, Low friction miniature gear drive for transmitting small forces, and method of making same, (1974).
[91] M. Hetzel, Low friction miniature gear drive for transmitting small forces, (1975).
[92] K. Ikuta, S. Makita, S. Arimoto, Non-contact magnetic gear for micro transmission mechanism, in: [1991] Proceedings. IEEE Micro Electro Mech. Syst., IEEE, 1991: pp. 125–130.
[93] S. Kikuchi, K. Tsurumoto, Design and characteristics of a new magnetic worm gear using permanent magnet, IEEE Trans. Magn. 29 (1993) 2923–2925.
[94] S. Kikuchi, K. Tsurumoto, Trial construction of a new magnetic skew gear using permanent magnet, IEEE Trans. Magn. 30 (1994) 4767–4769.
[95] P.M. Tlali, R.J. Wang, S. Gerber, Magnetic gear technologies: A review, in: 2014 Int. Conf. Electr. Mach., IEEE, 2014: pp. 544–550.
[96] Y.D. Yao, D.-R. Huang, C.C. Hsieh, D.Y. Chiang, S.J. Wang, T.F. Ying, The radial magnetic coupling studies of perpendicular magnetic gears, IEEE Trans. Magn. 32 (1996) 5061–5063.
[97] O.S. Chirilă, D. Stoia, M. Cernat, K. Hamayer, High-performance magnetic gears topologies, in: 2010 12th Int. Conf. Optim. Electr. Electron. Equip., IEEE, 2010: pp. 1091–1096.
[98] Y. Wang, M. Filippini, N. Bianchi, P. Alotto, A Review on Magnetic Gears: Topologies, Computational Models, and Design Aspects, IEEE Trans. Ind. Appl. 55 (2019) 4557–4566.
[99] M. Chen, K.T. Chau, W. Li, C. Liu, Development of non-rare-earth magnetic gears for electric vehicles, J. Asian Electr. Veh. 10 (2012) 1607–1613.
[100] D. Fodorean, M.A. Fakhfakh, State of the art of magnetic gears their design and characteristics with respect to EV application, Model. Simul. Electr. Veh. Appl. 3 (2016).
[101] B. McGilton, R. Crozier, A. McDonald, M. Mueller, Review of magnetic gear technologies and their applications in marine energy, IET Renew. Power Gener. 12 (2017) 174–181.
[102] R.-J. Wang, S. Gerber, Magnetically geared wind generator technologies: Opportunities and challenges, Appl. Energy. 136 (2014) 817–826.
[103] X. Li, K.-T. Chau, M. Cheng, W. Hua, Comparison of magnetic-geared permanent-magnet machines, Prog. Electromagn. Res. 133 (2013) 177–198.
[104] Z.Q. Zhu, D. Evans, Overview of recent advances in innovative electrical machines—With particular reference to magnetically geared switched flux machines, in: 2014 17th Int. Conf. Electr. Mach. Syst., IEEE, 2014: pp. 1–10.
[105] J. Wang, K. Atallah, W. Wang, Analysis of a magnetic screw for high force density linear electromagnetic actuators, IEEE Trans. Magn. 47 (2011) 4477–4480.
[106] S. Pakdelian, N.W. Frank, H.A. Toliyat, Analysis and design of the trans-

rotary magnetic gear, in: 2012 IEEE Energy Convers. Congr. Expo., IEEE, 2012: pp. 3340–3347.
[107] S. Pakdelian, N.W. Frank, H.A. Toliyat, Principles of the trans-rotary magnetic gear, IEEE Trans. Magn. 49 (2012) 883–889.
[108] S. Pakdelian, N.W. Frank, H.A. Toliyat, Magnetic design aspects of the trans-rotary magnetic gear, IEEE Trans. Energy Convers. 30 (2014) 41–50.
[109] F.T. Jørgensen, T.O. Andersen, P.O. Rasmussen, The cycloid permanent magnetic gear, in: Conf. Rec. 2006 IEEE Ind. Appl. Conf. Forty-First IAS Annu. Meet., IEEE, 2006: pp. 373–378.
[110] J.L.G. Schüssler, J. Lindner, Eccentric drive having magnetic torque transmission, 1995.
[111] J. Rens, K. Atallah, S.D. Calverley, D. Howe, A novel magnetic harmonic gear, IEEE Trans. Ind. Appl. 46 (2009) 206–212.
[112] S. Mezani, K. Atallah, D. Howe, A high-performance axial-field magnetic gear, J. Appl. Phys. 99 (2006) 08R303.
[113] K. Atallah, J. Wang, D. Howe, A high-performance linear magnetic gear, J. Appl. Phys. 97 (2005) 10N516.
[114] E. Gouda, S. Mezani, L. Baghli, A. Rezzoug, Comparative study between mechanical and magnetic planetary gears, IEEE Trans. Magn. 47 (2010) 439–450.
[115] M. Desvaux, B. Multon, H. Ben Ahmed, S. Sire, Behaviour comparison between mechanical epicyclic gears and magnetic gears, in: Int. Symp. Multibody Syst. Mechatronics, Springer, 2017: pp. 401–410.
[116] H.W. M-Uller, H.W. Müller, Epicyclic drive trains: Analysis, synthesis, and applications, Wayne State University Press, 1982.
[117] K. Atallah, J. Rens, S. Mezani, D. Howe, A novel "pseudo" direct-drive brushless permanent magnet machine, IEEE Trans. Magn. 44 (2008) 4349–4352.
[118] K. Atallah, J.J. Rens, Variable magnetic gears, (2015).
[119] L. Shah, A. Cruden, B.W. Williams, A variable speed magnetic gear box using contra-rotating input shafts, IEEE Trans. Magn. 47 (2010) 431–438.
[120] L. Jian, K.-T. Chau, Design and analysis of a magnetic-geared electronic-continuously variable transmission system using finite element method, Prog. Electromagn. Res. 107 (2010) 47–61.
[121] Y. Mao, S. Niu, Y. Yang, Differential evolution-based multiobjective optimization of the electrical continuously variable transmission system, IEEE Trans. Ind. Electron. 65 (2018) 2080–2089. https://doi.org/10.1109/TIE.2017.2733458.
[122] A. Emadi, K. Rajashekara, S.S. Williamson, S.M. Lukic, Topological overview of hybrid electric and fuel cell vehicular power system architectures and configurations, IEEE Trans. Veh. Technol. 54 (2005) 763–770.
[123] R.H. Staunton, C.W. Ayers, L.D. Marlino, J.N. Chiasson, B.A. Burress, Evaluation of 2004 Toyota Prius hybrid electric drive system, Oak Ridge National Lab.(ORNL), Oak Ridge, TN (United States), 2006.
[124] T.A. Burress, S.L. Campbell, C. Coomer, C.W. Ayers, A.A. Wereszczak, J.P. Cunningham, L.D. Marlino, L.E. Seiber, H.-T. Lin, Evaluation of the 2010 Toyota Prius hybrid synergy drive system, Oak Ridge National Lab.(ORNL), Oak Ridge, TN (United States). Power …, 2011.
[125] D. Meeker, Finite element method magnetics, FEMM. 4 (2010) 32.
[126] N. Niguchi, K. Hirata, Cogging torque analysis of magnetic gear, IEEE

Trans. Ind. Electron. 59 (2011) 2189–2197.
[127] Z.Q. Zhu, D. Howe, Influence of design parameters on cogging torque in permanent magnet machines, IEEE Trans. Energy Convers. 15 (2000) 407–412.
[128] M. Filippini, P. Alotto, An optimization tool for coaxial magnetic gears, COMPEL-The Int. J. Comput. Math. Electr. Electron. Eng. (2017).
[129] F. Henrotte, G. Deliége, K. Hameyer, The eggshell method for the computation of electromagnetic forces on rigid bodies in 2D and 3D, CEFC 2002. (2002) 16–18.
[130] P. Di Barba, Multiobjective shape design in electricity and magnetism, Springer Science & Business Media, 2009.
[131] M. Velardocchia, E. Bonisoli, E. Galvagno, A. Vigliani, A. Sorniotti, Efficiency of epicyclic gears in automated manual transmission systems, SAE Technical Paper, 2007.
[132] M. Velardocchia, N. D'Alfio, E. Bonisoli, E. Galvagno, F. Amisano, A. Sorniotti, Block-oriented models of torque gap filler devices for AMT transmissions, SAE Technical Paper, 2008.
[133] E. Bonisoli, L. Dimauro, A. Vigliani, M. Velardocchia, M. Repetto, V. Cirimele, P. Alotto, M. Filippini, Patent Magnetic Gearbox (Disclosure form), (2019) 1–20.
[134] J.W.P. Montgomery, H.L. Edwards, T.P. Offord, Variable gear ratio magnetic gearbox, (2013).
[135] L. Shah, A. Cruden, Magnetic gearbox_WO2010142962_A2_2010.pdf, n.d.
[136] K.H. Ang, G. Chong, Y. Li, PID control system analysis, design, and technology, IEEE Trans. Control Syst. Technol. 13 (2005) 559–576.
[137] I. Mizumoto, D. Ikeda, T. Hirahata, Z. Iwai, Design of discrete time adaptive PID control systems with parallel feedforward compensator, Control Eng. Pract. 18 (2010) 168–176. https://doi.org/10.1016/j.conengprac.2009.09.003.